Simulating Galaxy Evolution with Cosmic Rays: the Multi-frequency View

---

Maria Werhahn

Kumulative Dissertation
zur Erlangung des akademischen Grades
“doctor rerum naturalium”
(Dr. rer. nat.)
in der Wissenschaftsdisziplin Theoretische Astrophysik

eingereicht an der
Mathematisch-Naturwissenschaftlichen Fakultät
Institut für Physik und Astronomie
der Universität Potsdam
und
Leibniz-Institut für Astrophysik Potsdam (AIP)

Ort und Tag der Disputation: Universität Potsdam, Golm, 02.11.2022

Hauptbetreuer:	Prof. Dr. Christoph Pfrommer
Mentorin:	Dr. Else Starkenburg
Gutachter:	Prof. Dr. Christoph Pfrommer
	Prof. Dr. Marcus Brüggen
	Prof. Dr. Todd Thompson

Published online on the
Publication Server of the University of Potsdam:
https://doi.org/10.25932/publishup-57285
https://nbn-resolving.org/urn:nbn:de:kobv:517-opus4-572851

Abstract

Cosmic rays (CRs) constitute an important component of the interstellar medium (ISM) of galaxies and are thought to play an essential role in governing their evolution. In particular, they are able to impact the dynamics of a galaxy by driving galactic outflows or heating the ISM and thereby affecting the efficiency of star-formation. Hence, in order to understand galaxy formation and evolution, we need to accurately model this non-thermal constituent of the ISM. But except in our local environment within the Milky Way, we do not have the ability to measure CRs directly in other galaxies. However, there are many ways to indirectly observe CRs via the radiation they emit due to their interaction with magnetic and interstellar radiation fields as well as with the ISM.

In this work, I develop a numerical framework to calculate the spectral distribution of CRs in simulations of isolated galaxies where a steady-state between injection and cooling is assumed. Furthermore, I calculate the non-thermal emission processes arising from the modelled CR proton and electron spectra ranging from radio wavelengths up to the very high-energy gamma-ray regime. I apply this code to a number of high-resolution magneto-hydrodynamical (MHD) simulations of isolated galaxies, where CRs are included. This allows me to study their CR spectra and compare them to observations of the CR proton and electron spectra by the Voyager-1 satellite and the AMS-02 instrument in order to reveal the origin of the measured spectral features. Furthermore, I provide detailed emission maps, luminosities and spectra of the non-thermal emission from our simulated galaxies that range from dwarfs to Milk-Way analogues to starburst galaxies at different evolutionary stages. I successfully reproduce the observed relations between the radio and gamma-ray luminosities with the far-infrared (FIR) emission of star-forming (SF) galaxies, respectively, where the latter is a good tracer of the star-formation rate. I find that highly SF galaxies are close to the limit where their CR population would lose all of their energy due to the emission of radiation, whereas CRs tend to escape low SF galaxies more quickly. On top of that, I investigate the properties of CR transport that are needed in order to match the observed gamma-ray spectra.

Furthermore, I uncover the underlying processes that enable the FIR-radio correlation (FRC) to be maintained even in starburst galaxies and find that thermal free-free-emission naturally explains the observed radio spectra in SF galaxies like M82 and NGC 253 thus solving the riddle of flat radio spectra that have been proposed to contradict the observed tight FRC.

Lastly, I scrutinise the steady-state modelling of the CR proton component by investigating for the first time the influence of spectrally resolved CR transport in MHD simulations on the hadronic gamma-ray emission of SF galaxies revealing new insights into the observational signatures of CR transport both spectrally and spatially.

Zusammenfassung

Kosmische Strahlung (CR) ist ein essentieller Bestandteil des interstellaren Mediums (ISM) von Galaxien und spielt eine wichtige Rolle in deren Entwicklung. Insbesondere ist sie in der Lage, die Dynamik einer Galaxie zu beeinflussen, indem sie galaktische Ausflüsse treibt oder das ISM aufheizt und sich dadurch auf die Effizienz der Sternentstehung auswirkt. Um Galaxienentstehung zu verstehen ist es daher notwendig, diesen nicht-thermischen Bestandteil des ISM genau zu modellieren. Aber außerhalb unserer lokalen Umgebung innerhalb der Milchstraße haben wir keine Möglichkeit, um CRs in anderen Galaxien direkt zu messen. Allerdings gibt es viele Möglichkeiten, CRs indirekt über die Strahlung zu beobachten, die sie auf Grund ihrer Interaktion mit Magnetfeldern und interstellarer Strahlung sowie mit dem ISM emittieren.

In dieser Arbeit habe ich einen numerischen Code entwickelt, der die spektrale Verteilung der CRs in Simulationen von isolierten Galaxien berechnet, wobei ein stationäres Verhältnis zwischen Injektion und Kühlen angenommen wird. Des Weiteren berechnet er die nicht-thermischen Strahlungsprozesse, die aus den modellierten CR Protonen- und Elektronenspektren hervorgehen. Diese reichen von Radiowellenlängen bis hin zu hochenergetischer Gammastrahlung. Ich wende diesen Code auf eine Vielzahl von hoch aufgelösten, magneto-hydrodynamischen Simulationen von isolierten Galaxien an, die CRs beinhalten. Das ermöglicht es mir, ihre CR Spektren zu untersuchen und mit Beobachtungen des Voyager-1 Satelliten sowie des AMS-02 Instruments von CR Protonen- und Elektronenspektren zu vergleichen, um dem Ursprung von den gemessenen spektralen Besonderheiten nachzugehen. Außerdem lege ich detaillierte Emissionskarten, Leuchtkräfte und Spektren der nicht-thermischen Strahlung unserer simulierten Galaxien vor, die von Zwerggalaxien über Milchstraßen-ähnliche Galaxien bis hin zu Starburst-Galaxien bei verschiedensten Entwicklungsstadien reichen. Damit kann ich erfolgreich die beobachteten Zusammenhänge zwischen jeweils der Radio- und Gammastrahlungsleuchtkraft mit der Ferninfrarot (FIR) Strahlung der sternbildenden Galaxien reproduzieren, wobei die FIR Strahlung ein guter Indikator für die Rate der Sternentstehung ist. Dabei finde ich heraus, dass Galaxien mit einer hohen Rate an Sternentstehung sehr nah an dem Limit sind, in dem ihre CR Population all ihre Energie an die Produktion von Strahlung verlieren würde, während CRs dazu tendieren, Galaxien mit einer niedrigen Sternentstehungsrate schneller zu verlassen. Zusätzlich untersuche ich die Eigenschaften des Transports von CRs, die benötigt werden, um die beobachteten Spektren der Gammastrahlung zu reproduzieren.

Außerdem decke ich die zugrundeliegenden physikalischen Prozesse auf, durch die die Korrelation zwischen der FIR- und Radioleuchtkraft auch in Starburst-Galaxien aufrecht erhalten werden kann und finde heraus, dass die thermische Emission natürlicherweise die beobachteten Radiospek-

tren in Galaxien wie M82 und NGC 253 erklärt, wodurch sich das Rätsel der flachen Radiospektren löst, die scheinbar im Widerspruch zum beobachteten engen Zusammenhang zwischen der FIR- und Radioleuchtkraft standen.

Zuletzt hinterfrage ich die Annahme eines stationären Zustandes bei der Modellierung der CR Protonenspektren, indem ich zum ersten Mal den Einfluss von spektral aufgelöstem Transport von CR Protonen in magneto-hydrodynamischen Simulationen auf die hadronische Gammastrahlung von sternbildenden Galaxien untersuche, was neue Einblicke in beobachtbare Signaturen, sowohl spektral als auch räumlich, von CR-Transport ermöglicht.

Contents

1. Motivation and outline

The most energetic particles that have been detected at the Earth's atmosphere so far are ionized nuclei and electrons, so called cosmic rays (CRs). Their main constituents are protons (around 90%) and alpha particles (around 9%). The rest is made of heavier nuclei, electrons and also some antimatter, i.e. positrons and antiprotons. Most of these particles are highly relativistic, which means that they move with velocities close to the speed of light, such that their kinetic energy becomes much larger than their rest mass energy. Many interesting questions arise from their existence and observed properties. Where do they come from? how have they been accelerated to such high energies? and how do they propagate from their acceleration sites to us? In addition, Galactic CRs are observed to be in equipartition with the magnetic and turbulent energy densities of the interstellar medium (ISM) in the Milky Way and hence seem to represent an important component of the ISM (Boulares & Cox, 1990; Zweibel, 2013). This poses the question: what role do they play in the formation and evolution of galaxies?

One of the main puzzles in galaxy formation is still the observed and unexpected low efficiency of star formation, where only about 20% of the available matter is transformed into stars at the scale of approximately the Milky Way (e.g. Fukugita et al., 1998). On top of that, this efficiency has been found to decrease further towards small and very large galaxies, respectively, which requires the existence of so-called "feedback" processes that prevent star formation from happening as efficiently as expected (Moster et al., 2010). While stellar winds and photo ionization might be responsible for altering the star-formation efficiency towards smaller galaxies, the feedback from active galactic nuclei (AGN), i.e. actively accreting supermassive black holes in the centers of galaxies, might do the job in very large galaxies (see e.g. the reviews by Morganti, 2017; Girichidis et al., 2020a). But in addition to this, theory proposes that at astrophysical shocks such as at the remnants of supernovae (SNe) CRs are accelerated. This relates their occurrence directly to the star formation activity of a galaxy, where they represent an important energy component of the ISM, qualifying them as an additional candidate of feedback processes in SF galaxies (e.g. Zweibel, 2017). In fact,

simulations have shown that CRs can have an effect on the star formation efficiency in galaxies, e.g. by launching galactic winds (e.g. Breitschwerdt et al., 1991; Girichidis et al., 2016; Pakmor et al., 2016c; Ruszkowski et al., 2017; Dashyan & Dubois, 2020).

But how do we know that numerical simulations are reflecting what is actually going on with CRs in galaxies? Luckily, CRs do not just propagate 'invisibly' through a galaxy, but they interact with magnetic fields, interstellar radiation fields as well as the ambient gas of the ISM. These interactions lead to the emission of various kinds of photons, ranging from radio wavelengths up to very high-energy gamma-rays. As a consequence, these radiation processes give us the opportunity to observationally constrain the properties of CRs even in distant galaxies where we do not have the ability to directly measure their CR content. Hence, the goal is to calibrate feedback due to CRs in galaxy formation by properly modelling the physics of CRs, implementing this in simulations of galaxies and calculating the resulting emission. This eventually can be compared to a various observations of real galaxies and in turn enables us to constrain our theoretical modelling. Intriguingly, this approach additionally provides theoretical predictions for a plethora of future observations. These range from the radio, e.g. with the Low Frequency Array (LOFAR) or Square Kilometre Array (SKA), up to the the X-ray and gamma-ray regime, such with the Cherenkov Telescope Array (CTA) that will observe high-energy gamma-rays with unprecedented sensitivity in the upcoming years.

To this end, I developed a framework to calculate the non-thermal emission resulting from CRs in star-forming galaxies and applied it to MHD simulations of isolated galaxies that were performed with the moving-mesh code Arepo, which includes CRs self-consistently. The outline of this thesis is the following: First, we summarize the relevant theoretical background of this work in Chapter 2, where we introduce CRs in Section 2.1, review the underlying equations of MHD simulations in Section 2.2 and provide an overview of all relevant radiation mechanisms in Section 2.3.

Subsequently, the main part of this work is presented in Chapters 3, 4 and 5. These chapters constitute of the three published papers Werhahn et al. (2021a), Werhahn et al. (2021b) and Werhahn et al. (2021c) that we refer to as Paper I, II and III in the following, respectively.

Chapter 3 introduces our simulations and the modelling of the steady-state spectra of CR protons and electrons which we then compare to actual measured spectra by AMS-02 and Voyager-1. The resulting gamma-ray emission from our simulated galaxies is then analysed in Chapter 4 where we aim to understand the gamma-ray luminosities and spectra of observed star-forming galaxies. Chapter 5 is dedicated to the radio emission where we again confront our simulated galaxies and their modelled radio synchrotron and free-free emission with observations. We analyse in Chapter 6 the gamma-ray emission from MHD simulations of galaxies that include spectrally resolved CR

transport, where we identify the observational signatures of this novel treatment that turns out to be particularly important for predicting spatially resolved high-energy gamma-ray emission.

Furthermore, we briefly recap further publication that I contributed to as a co-author in Chapter 7. Finally, we conclude in Chapter 8 and provide an outlook into future work.

Throughout this work, the cgs system of units is adopted, if not explicitly stated otherwise.

2. Theoretical background

This chapter provides an overview of the theoretical background that constitutes the basis for this thesis. After giving an introduction to CRs in Section 2.1, in particular their acceleration and transport, we briefly review the MHD equations that are underlying the simulations performed with Arepo in this work in Section 2.2. Finally, we summarize all relevant thermal and non-thermal radiation mechanisms in Section 2.3.

2.1 Cosmic rays

Since their discovery more than a century ago, CRs and their spectrum have been observed in various ways (Gaisser, 1990; Gabici et al., 2019). It turns out that the spectrum ranges over 12 decades in energy and exhibits a number of distinct features. While the differential spectrum is a power law with a slope of -2.7 up to energies of 3×10^{15} eV, it softens to a slope of -3.1 at higher energies, which is often called the "knee" feature. Above the so-called "ankle" at around 10^{18} eV, the slope again changes to -2.6 and hence the spectrum is harder at these ultra-relativistic energies. As can be easily derived from the size of the gyroradii of CR particles with different energies, they must originate from different sources. At the energies of the "knee" feature, the typical gyroradius of a CR proton propagating in a magnetic field with $B = 5$ μG is around 1 pc and hence corresponds to the typical size of a SNR after 100 years of evolution. These are indeed believed to be the main accelerators of Galactic CRs. However, CRs with energies above the "ankle" have gyroradii of order 1 kpc and consequently, they must originate from extra-galactic sources. At low energies $\lesssim$ 1 GeV, all Earthbound observations of the CR spectrum are affected by solar modulations (see e.g. Potgieter, 2013, for a review). However, the observations by the Voyager-1 satellite have revolutionised our picture of low energy CRs: Because this satellite has eventually passed the heliopause in August 2012, it is able to measure the spectrum at low energies in unprecedented detail without the influence of the solar wind (Cummings et al., 2016). We will make use of these

observations in Chapter 3 (i.e. Paper I).

Because CRs and magnetic fields are observed to be in pressure equilibrium with the turbulence in the mid-plane of the Milky Way (Boulares & Cox, 1990), it has been concluded that they must represent an important constituent of the ISM. Indeed, the pressure forces of these highly relativistic particles have been found to drive powerful galactic outflows in a number of theoretical works (see Section 3.1 for references) and hence are effecting the star-formation efficiency in the ISM. It is therefore crucial to take CRs as a relevant, non-thermal component of the ISM into account when aiming for a comprehensive understanding of galaxy formation and evolution.

2.1.1 CR propagation

The propagation and transport of CRs can be described by the evolution of its phase space distribution function $f^{3D}(\boldsymbol{x},\boldsymbol{p},t)$, which relates to the number and energy density via

$$n_{\rm cr} = \int f^{3D}(\boldsymbol{x},\boldsymbol{p},t) 4\pi p^2 {\rm d}p, \tag{2.1}$$

$$\varepsilon_{\rm cr} = \int E_{\rm kin}(p) f^{3D}(\boldsymbol{x},\boldsymbol{p},t) 4\pi p^2 {\rm d}p. \tag{2.2}$$

The kinetic energy is related to the momentum as $E_{\rm kin} = (\sqrt{(p^2+1)}-1)mc^2$, where m is the mass of the CR species under consideration and $p = |\boldsymbol{p}|$ denotes the absolute value of the normalized particle momentum $\boldsymbol{p} = \boldsymbol{P}/(mc)$.

In addition to the velocity $\boldsymbol{v}$ of the background plasma that CRs get advected with, they can stream along magnetic fields with the streaming velocity $\boldsymbol{v}_{\rm st} = -\boldsymbol{v}_{\rm A}{\rm sgn}(\boldsymbol{B}\cdot\boldsymbol{\nabla}f)$, where the Alfvén velocity is given by $\boldsymbol{v}_{\rm A} = \boldsymbol{B}/\sqrt{4\pi\rho}$. The latter process originates from CR scattering off of Alfvén waves that have been excited due to the CR streaming instability by CRs that propagate faster than the Alfvén velocity, confining their velocity to the Alfvén velocity. Furthermore, the diffusion of CRs in real space or momentum space is quantified via the spatial and momentum diffusion coefficients, $\mathbf{D}_{xx}$ and D_{pp}, respectively. The evolution of the isotropic part of the distribution function f^{3D} can be described by the Fokker-Planck equation that reads (Skilling, 1975; Schlickeiser, 1989)

$$\frac{\partial f^{3D}}{\partial t} + (\boldsymbol{v}+\boldsymbol{v}_{\rm st})\cdot\boldsymbol{\nabla}f^{3D} = \boldsymbol{\nabla}\cdot[\mathbf{D}_{xx}\cdot\boldsymbol{\nabla}f] + \frac{p}{3}\frac{\partial f^{3D}}{\partial p}\boldsymbol{\nabla}\cdot(\boldsymbol{v}+\boldsymbol{v}_{\rm st}) + \frac{1}{p^2}\frac{\partial}{\partial p}\left[p^2 D_{pp}\frac{\partial f^{3D}}{\partial p}\right] + S(p), \tag{2.3}$$

where the source and sink terms are summarized in $S(p)$ as

$$S(p) = q(p) - \frac{1}{p^2}\frac{\partial}{\partial p}\left(p^2 \dot{p} f^{3\mathrm{D}}\right) - \frac{f^{3\mathrm{D}}}{\tau_\mathrm{c}}. \tag{2.4}$$

This comprises a source function $Q(p)$, losses due to a cooling term denoted as $\dot{p}$ and catastrophic losses that happen on a timescale τ_c. Note that in this work, we will make use of the 1D distribution function of CRs $f(\boldsymbol{x}, p, t) = 4\pi p^2 f^{3\mathrm{D}}(\boldsymbol{x}, \boldsymbol{p}, t)$, if not stated otherwise.

In a simplified picture where only advective and diffusive transport with a spatially constant diffusion coefficient D as well as injection and cooling are taken into account, the evolution of the particle distribution function $f(E) = f(p)\mathrm{d}p/\mathrm{d}E$ can by expressed in terms of the total particle energy E via the the diffusion-loss equation (e.g. Torres, 2004; Ginzburg & Syrovatskii, 1964)

$$-D\nabla^2 f(E) + \frac{f(E)}{\tau} - \frac{\mathrm{d}}{\mathrm{d}E}\left[f(E)b(E)\right] - q(E) = -\frac{\partial f(E)}{\partial t}, \tag{2.5}$$

where τ denotes the confinement timescale. To simplify this further, we will quantify the losses due to diffusion and advection through a timescale τ_diff and τ_adv, respectively, and define an escape timescale $\tau_\mathrm{esc}^{-1} = \tau_\mathrm{diff}^{-1} + \tau_\mathrm{adv}^{-1}$ (see Chapter 3). Furthermore, we will consider Eq. (2.5) in a steady-state, i.e. $\partial f(E)/\partial t = 0$, yielding

$$\frac{f(E)}{\tau_\mathrm{esc}} - \frac{\mathrm{d}}{\mathrm{d}E}\left[f(E)b(E)\right] = q(E). \tag{2.6}$$

2.1.2 Loss rates of CR protons and electrons

In the following, we give an overview of the loss rates of CR protons and electrons due to various cooling processes by presenting a slightly modified version of the summary that we published in Appendix A1 of Paper I, which we complement here by synchrotron and IC losses for completeness. We express the loss rates as a function of energy, i.e $b(E) = -\dot{E}$, which can be converted to the corresponding momentum loss rates via $\dot{p} = \dot{E}\,\mathrm{d}p/\mathrm{d}E = \dot{E}/(\beta mc^2)$, where $\beta = v/c$ denotes the velocity normalised by the speed of light.

Protons. CR protons with an energy above the threshold energy of pion production $E > E_\mathrm{th} = 1.22\,\mathrm{GeV}$ lose energy at a loss rate given by

$$b_\pi = K_\mathrm{p} T_\mathrm{p} c \sigma_\mathrm{pp} n_\mathrm{N}, \tag{2.7}$$

where the inelasticity of the pp-interaction is $K_\mathrm{p} = 1/2$ (Mannheim & Schlickeiser, 1994), T_p is the particle kinetic energy, σ_pp is the cross section of proton-proton collisions (given by Eq. 3.50) and $n_\mathrm{N} = n_\mathrm{H} + 4n_\mathrm{He} = (X_\mathrm{H} + 1 - X_\mathrm{H})\rho/m_\mathrm{p} = \rho/m_\mathrm{p}$ is the number density of target nucleons, where $X_\mathrm{H} = 0.76$ denotes the hydrogen fraction and ρ is the gas density.

Additionally, CR protons lose energy through Coulomb interactions (Gould, 1972a), given by

$$b_\mathrm{Coul,p} = \frac{3\sigma_\mathrm{T} n_\mathrm{e} m_\mathrm{e} c^3}{2\beta}\left[\ln\left(\frac{2\gamma m_\mathrm{e} c^2 \beta^2}{\hbar\omega_\mathrm{pl}}\right) - \frac{\beta^2}{2}\right] \equiv \frac{3\sigma_\mathrm{T} n_\mathrm{e} m_\mathrm{e} c^3}{2\beta} A_\mathrm{p}, \tag{2.8}$$

where $n_\mathrm{e} = n_\mathrm{H} + 2n_\mathrm{He} = (X_\mathrm{H} + (1 - X_\mathrm{H})/2)\rho/m_\mathrm{p} = 0.88\rho/m_\mathrm{p}$ is the electron number density, $\hbar$ is the reduced Planck constant, e the elementary charge, c the speed of light and the plasma frequency is defined as $\omega_\mathrm{pl} = \sqrt{4\pi e^2 n_\mathrm{e}/m_\mathrm{e}}$. Furthermore, $\sigma_\mathrm{T} = 8\pi r_0^2/3$ is the Thomson cross-section, where $r_0 = e^2/(m_\mathrm{e}c^2)$ denotes the classical electron radius, and A_p defines the Coulomb logarithm and the velocity correction term in the bracket. The Lorentz factor γ and the normalised velocities $\beta = v/c$ without subscripts refer to protons (electrons are denoted with a subscript e).

Electrons. High-energy CR electrons mainly lose energy when they interact with an ambient magnetic field B with an energy density of $\varepsilon_B = B^2/(8\pi)$, a radiation field with a photon energy density ε_ph and/or with ambient gas which leads to the emission of synchrotron, IC and/or non-thermal bremsstrahlung emission, respectively.

The loss rates due to synchrotron and IC emission from CR electrons that have a normalised velocity $\beta_\mathrm{e} = v_\mathrm{e}/c$ and a Lorentz factor γ_e can be written as (see e.g. Blumenthal & Gould, 1970)

$$b_\mathrm{syn} = \frac{4}{3}\sigma_\mathrm{T} c \beta_\mathrm{e}^2 \gamma_\mathrm{e}^2 \varepsilon_B, \tag{2.9}$$

and

$$b_\mathrm{IC} = \frac{4}{3}\sigma_\mathrm{T} c \beta_\mathrm{e}^2 \gamma_\mathrm{e}^2 \varepsilon_\mathrm{ph}. \tag{2.10}$$

The IC loss rate is given here in the Thomson-limit for IC scattering, which holds if $\gamma_\mathrm{e} h\nu \ll m_\mathrm{e}c^2$, where ν is the frequency of the incoming photon. Besides losses due to IC and synchrotron emission, CR electrons lose energy due to bremsstrahlung emission. Following Blumenthal & Gould (1970), this yields in the case of highly relativistic electrons the expression

$$b_\mathrm{brems} = 4\alpha r_0^2 c n_\mathrm{p} \beta_\mathrm{e} \gamma_\mathrm{e}\left[\ln(2\gamma_\mathrm{e}) - \frac{1}{3}\right] m_\mathrm{e} c^2. \tag{2.11}$$

where we assume a fully ionized medium with $n_\mathrm{p} = 0.88\rho/m_\mathrm{p}$ and α is the fine structure constant. Additionally, we take Coulomb losses of CR electrons into account. The expression for the energy loss rate has been derived by Gould (1972b) and reads

$$b_\mathrm{Coul,e} = \frac{3\sigma_T n_\mathrm{e} m_\mathrm{e} c^3}{2\beta_\mathrm{e}} \left[\ln\left(\frac{m_\mathrm{e} c^2 \beta_\mathrm{e} \sqrt{\gamma_\mathrm{e} - 1}}{\hbar \omega_\mathrm{pl}} \right) - \ln(2) \left(\frac{\beta_\mathrm{e}^2}{2} + \frac{1}{\gamma_\mathrm{e}} \right) + \frac{1}{2} + \left(\frac{\gamma_\mathrm{e} - 1}{4\gamma_\mathrm{e}} \right)^2 \right] \tag{2.12}$$

$$\equiv \frac{3\sigma_T n_\mathrm{e} m_\mathrm{e} c^3}{2\beta_\mathrm{e}} A_\mathrm{e}, \tag{2.13}$$

where A_e defines the Coulomb logarithm and various correction terms in the bracket.

2.1.3 CR acceleration

Galactic CRs are suggested to be mainly accelerated at the shocks of SNRs. These highly energetic explosions of a dying massive star drive strong shocks through the ISM, where diffusive shock acceleration occurs, which is also known as first order Fermi acceleration (Axford et al., 1977; Krymskii, 1977; Bell, 1978; Blandford & Ostriker, 1978). This process can only take place at collisionless shocks and the particles to be accelerated have to start with an energy that is already larger than the energy of the thermal pool. The resulting CR spectrum from diffusive shock acceleration can be derived in different ways. We will follow here the macroscopic approach as summarized in Drury (1983), which is based on the original works by Axford et al. (1977), Krymskii (1977) and Blandford & Ostriker (1978). In this macroscopic picture, we describe the particle ensemble by its 3D distribution function f^3D that follows Eq. (2.3) and that we will denote as f in this Section for better readability. Furthermore, we consider a shock front that is separating the upstream and downstream media and whose shock normal is parallel to the magnetic field lines. In the inertial frame of the shock, it lies in the $y-z$ plane at $x = 0$ and the fluid approaches it along the x axis in positive direction with an upstream velocity v_1 for $x < 0$, which changes to a downstream velocity v_2 for $x > 0$. If we neglect streaming and diffusion in momentum space (i.e. Fermi-II acceleration) as well as cooling and catastrophic losses, Eq. (2.3) describes the evolution of f in the local fluid frame as

$$\frac{\partial f}{\partial t} + v\frac{\partial f}{\partial x} = \frac{\partial}{\partial x}\left(D\frac{\partial f}{\partial x} \right) + \frac{p}{3}\frac{\partial f}{\partial p}\frac{\partial v}{\partial x} + v_1 q(p)\delta(x), \tag{2.14}$$

where we additionally accounted for a source $q(p)$ at the shock front, i.e. at $x = 0$ (Pfrommer, 2005). Since the flow of the background plasma is steady and we look for steady-state solutions

$\partial f/\partial t = 0$, the evolution equation further reduces upstream and downstream to

$$v\frac{\partial f}{\partial x} = \frac{\partial}{\partial x}\left(D\frac{\partial f}{\partial x}\right) + v_1 q(p)\delta(x). \tag{2.15}$$

A general ansatz for the solution of this equation is given by

$$f(x,p) = g_1(p)\exp\left(\int_0^x \frac{v(x')}{D}\mathrm{d}x'\right) + g_2(p), \tag{2.16}$$

with arbitrary functions $g_1(p)$ and $g_2(p)$. As a boundary condition at $x \to -\infty$, i.e. far upstream, we set $f(x,p) \to f_1(p)$ and require f to be finite far downstream. Furthermore, we assume a continuous distribution function at the shock front. These conditions yield the solution

$$f(x,p) = \begin{cases} f_1(p) + [f_2(p) - f_1(p)]\exp\left(-\int_x^0 \frac{v_1}{D}\mathrm{d}x'\right) & \text{for } x < 0, \\ f_2(p) & \text{for } x > 0. \end{cases} \tag{2.17}$$

At the shock front, we consider Eq. (2.14) with $\partial f/\partial t = 0$, integrate it across the shock from $-\epsilon$ to ϵ and consider the limit $\epsilon \to 0$. By introducing the shock compression ratio $r = v_1/v_2$, this yields a differential equation

$$(r-1)p\frac{\partial f_2}{\partial p} = 3r[f_1(p) + q(p) - f_2(p)]. \tag{2.18}$$

Hence, the solution for the downstream distribution function f_2 is given by

$$f_2(p) = \alpha p^{-\alpha}\int_0^p p'^{\alpha-1}[f_1(p') + q(p')]\mathrm{d}p', \tag{2.19}$$

with the spectral index $\alpha = 3r/(r-1)$. Considering an injection momentum p_{inj}, a source function $q(p) = q_0\delta(p - p_{\mathrm{inj}})$ and neglecting the far upstream spectrum leads to a downstream spectrum of the form

$$f_2(p) \propto \left(\frac{p}{p_{\mathrm{inj}}}\right)^{-\alpha}. \tag{2.20}$$

Hence, we finally obtain a spectrum that is given by a power law in momentum with a spectral index α that is solely determined by the shock compression ratio r. According to the Rankine-Hugoniot

jump conditions at the shock, it is related to the shock Mach number $\mathcal{M}$ and the adiabatic index γ of the plasma via

$$r = \frac{\gamma + 1}{\gamma - 1 + 2/\mathcal{M}^2}. \tag{2.21}$$

In the case of a strong shock ($\mathcal{M} \to \infty$) and a non-relativistic plasma with $\gamma = 5/3$, this ratio is $r = 4$ and thus, the spectral index for the 3D distribution function is given by $\alpha = 4$. For the 1D distribution function $f^{1\mathrm{D}} = 4\pi p^2 f^{3\mathrm{D}}$, this corresponds to a spectral index of $\alpha = 2$.

In practice, the accelerated spectrum of CR electrons can be described by a power law with a super-exponential cut-off. In particular, if synchrotron losses are assumed to dominate cooling at SNR shocks, an analytical formula can be derived (Zirakashvili & Aharonian, 2007; Blasi, 2010), yielding a spectrum that is $\propto p^{-\alpha} \exp\left[-(p/p_{\mathrm{cut}})^2\right]$ with a cut-off momentum p_{cut}.

2.1.4 Observations and simple models of CR transport in the Milky Way

The most fundamental constraints on CR transport can be inferred from observations of secondary nuclei that are produced as a result of spallation of heavier CR elements with interstellar hydrogen (see e.g. the reviews by Strong et al., 2007; Amato & Blasi, 2018; Gabici, 2022) and that are over-abundant in comparison to solar abundances. In particular, lithium, beryllium and boron are such secondary nuclei that are produced by spallation of heavier CR nuclei, i.e. carbon or oxygen, which are more abundant heavier nuclei in comparison to lithium, beryllium and boron. Since we can measure primary and secondary CRs at Earth, the ratio of boron to carbon in the composition of CR nuclei gives insights into the propagation and confinement of CRs.

To understand the dependence of the boron-to-carbon (B/C) ratio on the escape time of CRs, we consider an ISM with hydrogen number density n_{H} and CRs with average boron and carbon densities n_{B} and n_{C}. Following e.g. the considerations by Gabici (2022), we can express the source function of boron $q_{\mathrm{B}} \sim n_{\mathrm{H}} v(\sigma_{\mathrm{C}\to\mathrm{B}} n_{\mathrm{C}} + \sigma_{\mathrm{O}\to\mathrm{B}} n_{\mathrm{O}})$, where v is the speed of the nucleus and $\sigma_{\mathrm{C}\to\mathrm{B}}$ and $\sigma_{\mathrm{O}\to\mathrm{B}}$ denote the spallation cross sections for boron production of carbon and oxygen, respectively. This can be further simplified by noticing that the observed abundances of oxygen and carbon are almost identical, i.e. $n_{\mathrm{O}} \approx n_{\mathrm{C}}$. The produced boron can then either interact with nuclei from the ISM with a spallation cross section σ_{B} and produce lighter nuclei on a timescale $\tau_{\mathrm{B}} = (n_{\mathrm{H}} \sigma_{\mathrm{B}} v)^{-1}$, or it can escape the galaxy after a timescale τ_{esc}. Both effects compete with the steady production of new boron, which yields an equilibrium density of boron $n_{\mathrm{B}} = q_{\mathrm{B}} \tau_{\mathrm{eff}}$ with the effective timescale of escape and destruction $\tau_{\mathrm{eff}}^{-1} = \tau_{\mathrm{esc}}^{-1} + \tau_{\mathrm{B}}^{-1}$. As a consequence, the B/C ratio can be expressed as

(Gaisser, 1990)

$$\frac{n_{\mathrm{B}}}{n_{\mathrm{C}}} \approx \frac{n_{\mathrm{H}} v \tau_{\mathrm{esc}} (\sigma_{\mathrm{C}\to\mathrm{B}} + \sigma_{\mathrm{O}\to\mathrm{B}})}{1 + \frac{\tau_{\mathrm{esc}}}{\tau_{\mathrm{B}}}} = \frac{X_{\mathrm{esc}}}{1 + \frac{X_{\mathrm{esc}}}{X_{\mathrm{B}}}} \frac{\sigma_{\mathrm{C}\to\mathrm{B}} + \sigma_{\mathrm{O}\to\mathrm{B}}}{m_{\mathrm{p}}}, \tag{2.22}$$

where we defined the amount of traversed matter in a time τ_i, also called grammage, via $X_i = m_{\mathrm{p}} n_{\mathrm{H}} v \tau_i$. Since the spallation cross sections entering Eq. (2.22) are roughly energy independent at high energies (Tatischeff & Gabici, 2018), the energy dependence of the B/C ratio is set by the energy dependence of the escape timescale, τ_{esc}. A fit of the observed B/C ratio by the AMS collaboration revealed an energy dependence of $n_{\mathrm{B}}/n_{\mathrm{c}} \propto E^{-0.3}$ (Aguilar et al., 2016). This can be interpreted in two ways: either high energy CRs have a shorter escape time than low energy CRs, i.e. their propagation mechanism is energy dependent, or they simply probe different average gas densities n_{H}. Unfortunately, the observed B/C ratio can only constrain the product of average density and escape timescale. Furthermore, one has to keep in mind that the energy scaling of the B/C ratio does not directly trace the energy scaling of the grammage or escape timescale, since this would only be true if $\tau_{\mathrm{esc}} \ll \tau_{\mathrm{B}}$, which holds for high energies only. In fact, taking this into account results in a steeper energy dependence of $\propto E^{-0.5}$ (Gabici, 2022), which is comparable to more detailed studies of CR propagation (see e.g. Evoli et al., 2019; Génolini et al., 2019).

In order to understand qualitatively the main physics behind CR propagation in the Galaxy and how an energy dependent propagation can be interpreted, we briefly recap the well known leaky box model. In this simplified model, CRs are allowed to random walk freely in a cylindrical volume. In 1D, the transport equation of CRs can be described in this picture by a diffusion equation with a source term q_0 in the midplane ($z = 0$) that reads in steady-state

$$-\frac{\partial}{\partial z}\left[D(p)\frac{\partial f}{\partial z}\right] = q_0 \delta(z). \tag{2.23}$$

For $z > 0$ and a spatially constant diffusion coefficient, the solution can be easily written down as

$$f(p,z) = f_0(p)\left(1 - \frac{q_0}{2D(p)f_0} z\right) = f_0(p)\left(1 - \frac{z}{H}\right), \tag{2.24}$$

where we defined in the last step a scale height $H = \frac{2D(p)f_0(p)}{q_0}$ that fulfills $f(p,H) = 0$ and where $f(p,0) = f_0(p)$. Hence, if we consider an injection spectrum $q_0(p) \propto p^{-\alpha}$ and a momentum-dependent diffusion coefficient $D(p) \propto p^{\delta}$, the equilibrium spectrum in the midplane is given

by

$$f_0(p) = \frac{q_0(p)H}{2D(p)} \propto p^{-\alpha-\delta}, \tag{2.25}$$

where we additionally have to assume a momentum independent scale height $H \neq H(p)$. Let us now consider a spectrum of carbon nuclei given by Eq. (2.25) that spallate into boron, giving rise to a boron source function $q_B(p) \propto n_{\rm H}\sigma_{\rm C\to B}f_{\rm C}(p)$. This yields for the equilibrium spectrum of boron according to Eq. (2.25)

$$f_{\rm B} = \frac{q_B(p)H}{2D(p)} \propto \frac{f_{\rm c}(p)}{D(p)} \propto \frac{q_{\rm c}(p)}{D^2} \propto p^{-\alpha-2\delta}, \tag{2.26}$$

given a source function for carbon $q_{\rm c} \propto p^{-\alpha}$, which implies for the B/C ratio

$$\frac{f_{\rm B}}{f_{\rm C}} \propto D(p)^{-1} \propto p^{-\delta}. \tag{2.27}$$

This can be reconciled with our result from Eq. (2.22) for high energies, under the assumption that $n_{\rm B}/n_{\rm C}$ only depends on the escape timescale and that escape is due to diffusion, with $\tau_{\rm esc} \propto E^{-\delta}$. Consequently, from measuring both the spectrum of primary CRs that is $\propto p^{-\alpha-\delta}$ and secondary CRs that have a spectrum $\propto p^{-\alpha-2\delta}$ one can infer δ and hence also the spectral index α of the originally injected source function. Several studies revealed an energy dependence of the diffusion coefficient ranging from $\delta = 0.3$ to 0.6 (Strong et al., 2007), which yields in combination with the observed primary CR spectrum with a spectral index of ≈2.7 an injection spectral index of $\alpha = 2.1$ to 2.4.

In order to obtain an independent measure of the residence time of CRs in the Galaxy, another observable is needed. The radioactive decay of short lived isotopes of CR nuclei that are produced in the spallation of CR nuclei with the ISM can be used as cosmic ray clocks, i.e. to infer the lifetime of CRs in the Galaxy by comparing their abundance to stable isotopes. An ideal example for this is the ^{10}Be isotope that relatively quickly decays in comparison to the stable ^{9}Be isotope but that is still long-lived enough to be able to be measured at Earth (Hayakawa et al., 1958; Ptuskin & Soutoul, 1998).

As a summary, the propagation of CRs can be constrained by observations of secondary CRs. On the one hand, the comparison of stable secondary particles like boron to primary CRs like carbon enable us to infer the energy dependence of diffusive transport and hence draw conclusions on the injection spectrum of CRs, without assuming anything about the nature of CR sources. But

measuring the B/C ratio only enables us to constrain the product of the average density and the escape timescale. On the other hand, the ratio of radioactive isotopes to their stable counterparts depends on the escape timescale only, which is estimated to be a few tens of Myrs (Yanasak et al., 2001; Lipari, 2014). From both measurements, both the scale height and the diffusion coefficient can be constrained, where H is typically estimated to be a few kpc and $D \sim H^2/\tau_{\rm esc} \approx 10^{28}\,{\rm cm}^2/{\rm s}$ at around 1 GeV/nucleon (see e.g. the review by Strong et al., 2007).

2.2 MHD equations and simulations

In this section, we motivate the MHD equations, following e.g. Choudhuri & Choudhuri (1998), that represent the foundation of the simulations used in this work and adopt in this context the Heaviside-Lorentz system of units for simplicity. Furthermore, we introduce MHD with CRs and give a brief overview of the Arepo code.

2.2.1 Ideal MHD

The theory of ideal MHD describes an ideally conducting and collisional fluid whose quantities can be described on timescales that are longer than the inverse plasma frequency and which is considered on length scales that are much larger than the mean free path between collisions.

We first start with the Boltzmann equation, which determines the evolution of the distribution function of particles that interact via collisions

$$\frac{{\rm d}f(\boldsymbol{x},\boldsymbol{u},t)}{{\rm d}t} = \frac{\partial f}{\partial t} + \dot{\boldsymbol{x}}\cdot\boldsymbol{\nabla} f + \dot{\boldsymbol{u}}\cdot\boldsymbol{\nabla}_u f = \left.\frac{{\rm d}f}{{\rm d}t}\right|_c, \tag{2.28}$$

where the velocity $\boldsymbol{u} = \boldsymbol{v} + \boldsymbol{w}$ contains a random component $\boldsymbol{w}$ in addition to its mean $\langle \boldsymbol{u}\rangle \equiv \boldsymbol{v}$. In order to be able to describe the dynamics of a system in the fluid approximation, the mean free path between the collisions must be much smaller than the characteristic size of the system.

If we consider a system where the total mass $\int \rho {\rm d}V$ is conserved, it can only change if there is a mass flux entering or leaving the system, i.e.

$$\frac{\partial}{\partial t}\int \rho {\rm d}V = -\int_{\partial V} \rho \boldsymbol{v}\cdot {\rm d}\boldsymbol{s}, \tag{2.29}$$

where $\boldsymbol{s}$ is a vector perpendicular to the surface of the volume which is pointing outwards. Hence, the minus sign implies that the mass is reduced by an outward flux. By applying the Gauss theorem to

Eq. (2.29), we can rewrite the surface integral into a volume integral via $\int_{\partial V} \rho \boldsymbol{v} \cdot \mathrm{d}\boldsymbol{s} = \int_V \boldsymbol{\nabla} \cdot (\rho \boldsymbol{v}) \mathrm{d}V$. Since our considerations must hold for any volume V, we obtain

$$\frac{\partial \rho}{\partial t} + \boldsymbol{\nabla} \cdot (\rho \boldsymbol{v}) = 0, \tag{2.30}$$

which is the so-called continuity equation. It can also be obtained by integrating Eq. (2.28) over $\mathrm{d}^3 u$ after multiplying it by the mass m.

Similarly, we can consider the amount of the momentum's i-th component $\int \rho v_i \mathrm{d}V$ in a volume that can only change due to a momentum flux T_{ij} across the surface if there are no external forces. The latter is given by $T_{ij} = P\delta_{ij} + \rho v_i v_j$ if there is no contribution from viscosity taken into account and where P denotes the pressure. The change of momentum is hence given by

$$\frac{\partial}{\partial t} \int\limits_V \rho v_i \mathrm{d}V = - \int\limits_{\partial V} T_{ij} \cdot \mathrm{d}s_j = - \int\limits_V \frac{\partial T_{ij}}{\partial x_j} \mathrm{d}V, \tag{2.31}$$

where we again applied the Gauss theorem in the last step. Since this applies to any considered volume, we obtain the equation

$$\frac{\partial}{\partial t} (\rho \boldsymbol{v}) + \boldsymbol{\nabla} \cdot (\rho \boldsymbol{v}\boldsymbol{v}^T + P\mathbf{1}) = 0. \tag{2.32}$$

A multiplication of Eq. 2.28 by $m\boldsymbol{u}$ and an integration over $\mathrm{d}^3 u$ would have given us the same result under the same assumption, i.e. that there is no viscosity and no external forces are acting on the system. However, if we want to consider an additional force, this has to be added to the right-hand side of Eq. (2.32). If we aim to include magnetic fields into the equations, this additional force corresponds to the Lorentz force exerted by a magnetic field $\boldsymbol{B}$ on an electrically neutral but conducting fluid

$$\boldsymbol{F}_\mathrm{L} = \frac{\boldsymbol{j} \times \boldsymbol{B}}{c}, \tag{2.33}$$

where $\boldsymbol{j}$ is the current density. This equation can be rewritten using Ampère's law, i.e. $\boldsymbol{\nabla} \times \boldsymbol{B} = \boldsymbol{j}/c$, which then reads

$$\boldsymbol{F}_\mathrm{L} = (\boldsymbol{B} \cdot \boldsymbol{\nabla})\boldsymbol{B} - \frac{1}{2} \boldsymbol{\nabla} \boldsymbol{B}^2. \tag{2.34}$$

This yields the momentum equation with the magnetic pressure added to the total pressure, i.e.

$P = P_{\text{th}} + \boldsymbol{B}^2/2$, that is given by

$$\frac{\partial}{\partial t}(\rho \boldsymbol{v}) + \boldsymbol{\nabla} \cdot (\rho \boldsymbol{v}\boldsymbol{v}^T + P\mathbf{1} - \boldsymbol{B}\boldsymbol{B}^T) = \mathbf{0}. \tag{2.35}$$

Similarly to the considerations above about mass and momentum conservation, we now consider the energy in a volume that can only change due to inflow or outflow of energy as well as a pressure acting on the volume that reads

$$\frac{\partial}{\partial t}\int_V \left(\varepsilon_{\text{th}} + \frac{1}{2}\rho \boldsymbol{v}^2\right) \mathrm{d}V = -\int_{\partial V} \left(\varepsilon_{\text{th}} + \frac{1}{2}\rho \boldsymbol{v}^2 + P_{\text{th}}\right) \boldsymbol{v} \cdot \mathrm{d}A = \int_V \boldsymbol{\nabla} \cdot \left[\left(\varepsilon_{\text{th}} + \frac{1}{2}\rho \boldsymbol{v}^2 + P_{\text{th}}\right) \boldsymbol{v}\right] \mathrm{d}V. \tag{2.36}$$

In the last step, Gauss' theorem was applied once more and we obtain for any arbitrary volume the equation

$$\frac{\partial}{\partial t}\left(\varepsilon_{\text{th}} + \frac{1}{2}\rho \boldsymbol{v}^2\right) + \boldsymbol{\nabla} \cdot \left[\left(\varepsilon_{\text{th}} + \frac{1}{2}\rho \boldsymbol{v}^2 + P_{\text{th}}\right) \boldsymbol{v}\right] = 0. \tag{2.37}$$

Note that we could also have arrived at this equation by multiplying Eq. (2.28) by $m\boldsymbol{u}^2$ and integrating over d^3u. As a next step, we again want to add magnetic fields to the equation. To this end, we make use of Faraday's law

$$\boldsymbol{\nabla} \times \boldsymbol{E} + \frac{1}{c}\frac{\partial \boldsymbol{B}}{\partial t} = \mathbf{0} \tag{2.38}$$

as well as ideal Ohm's law (i.e. in the case of infinite conductivity)

$$\boldsymbol{E} + \frac{1}{c}(\boldsymbol{v} \times \boldsymbol{B}) = \mathbf{0}. \tag{2.39}$$

Combining these two equations yields the induction equation

$$\frac{\partial \boldsymbol{B}}{\partial t} = \boldsymbol{\nabla} \cdot \left(\boldsymbol{B}\boldsymbol{v}^T - \boldsymbol{v}\boldsymbol{B}^T\right). \tag{2.40}$$

This equation is the equation of the evolution of the magnetic field. Multiplying Eq. (2.40) with $\boldsymbol{B}$ and some further simplifications lead to the equation of the evolution of the magnetic energy

density given by

$$\frac{\partial}{\partial t}\left(\frac{1}{2}\boldsymbol{B}^2\right) + \boldsymbol{\nabla}\cdot\left[\boldsymbol{B}^2\boldsymbol{v} - \boldsymbol{B}(\boldsymbol{v}\cdot\boldsymbol{B})\right] = 0. \tag{2.41}$$

By redefining the total energy density as $\varepsilon = \varepsilon_{\mathrm{th}} + \rho\boldsymbol{v}^2/2 + \boldsymbol{B}^2/2$ as well as the pressure $P = P_{\mathrm{th}} + \boldsymbol{B}^2/2$, this eventually leads us to the energy equation

$$\frac{\partial \varepsilon}{\partial t} + \boldsymbol{\nabla}\cdot\left[(\varepsilon + P)\boldsymbol{v} - \boldsymbol{B}(\boldsymbol{v}\cdot\boldsymbol{B})\right] = 0. \tag{2.42}$$

Finally, the Euler equations can be written in a compact form as

$$\frac{\partial \boldsymbol{U}}{\partial t} + \boldsymbol{\nabla}\cdot\boldsymbol{F} = \boldsymbol{S}, \tag{2.43}$$

where the state vector $\boldsymbol{U}$, the flux function $\boldsymbol{F}(\boldsymbol{U})$ and the source vector $\boldsymbol{S}$ are defined as

$$\boldsymbol{U} = \begin{pmatrix} \rho \\ \rho\boldsymbol{v} \\ \varepsilon \\ \boldsymbol{B} \end{pmatrix},\ \boldsymbol{F}(\boldsymbol{U}) = \begin{pmatrix} \rho\boldsymbol{v} \\ \rho\boldsymbol{v}\boldsymbol{v}^T + P\boldsymbol{1} - \boldsymbol{B}\boldsymbol{B}^T \\ (\varepsilon + P)\boldsymbol{v} - \boldsymbol{B}(\boldsymbol{v}\cdot\boldsymbol{B}) \\ \boldsymbol{B}\boldsymbol{v}^T - \boldsymbol{v}\boldsymbol{B}^T \end{pmatrix},\ \boldsymbol{S} = \begin{pmatrix} 0 \\ 0 \\ 0 \\ 0 \end{pmatrix} \tag{2.44}$$

with $P = P_{\mathrm{th}} + \boldsymbol{B}^2/2$. The equations are closed by means of an equation of state for the thermal gas

$$P_{\mathrm{th}} = (\gamma_{\mathrm{th}} - 1)\varepsilon_{\mathrm{th}} \tag{2.45}$$

with an adiabatic index of $\gamma_{\mathrm{th}} = 5/3$.

2.2.2 MHD with CRs

If CRs are coupled to the plasma via frequent wave-particle scatterings, they can be included into the MHD equations as a relativistic fluid with an adiabatic index of $\gamma_{\mathrm{cr}} = 4/3$ that relates their pressure and energy density via

$$P_{\mathrm{cr}} = (\gamma_{\mathrm{cr}} - 1)\varepsilon_{\mathrm{cr}}. \tag{2.46}$$

The evolution equation of the CR energy density $\varepsilon_{\rm cr}$ is obtained by integrating Eq. (2.3) (see Pfrommer et al., 2017a)

$$\frac{\partial \varepsilon_{\rm cr}}{\partial t} + \boldsymbol{\nabla} \cdot [\varepsilon_{\rm cr}(\boldsymbol{v} + \boldsymbol{v}_{\rm str}) - \kappa_\varepsilon \boldsymbol{b}(\boldsymbol{b} \cdot \boldsymbol{\nabla}\varepsilon_{\rm cr})] = P_{\rm cr}\, \boldsymbol{\nabla} \cdot (\boldsymbol{v} + \boldsymbol{v}_{\rm str}) + \Lambda_{\rm cr} + \Gamma_{\rm cr}, \tag{2.47}$$

where κ_ε is the kinetic energy-weighted spatial diffusion coefficient and CR energy sources and losses are denoted by $\Lambda_{\rm cr}$ and $\Gamma_{\rm cr}$, respectively. This yields a modified vector of conserved variables $\boldsymbol{U}$ as well as modified flux and source functions, $\boldsymbol{F}$ and $\boldsymbol{S}$, of Eq. (2.43) that are now given by

$$\boldsymbol{U} = \begin{pmatrix} \rho \\ \rho\boldsymbol{v} \\ \varepsilon \\ \varepsilon_{\rm cr} \\ \boldsymbol{B} \end{pmatrix}, \quad \boldsymbol{F}(\boldsymbol{U}) = \begin{pmatrix} \rho\boldsymbol{v} \\ \rho\boldsymbol{v}\boldsymbol{v}^T + P\boldsymbol{1} - \boldsymbol{B}\boldsymbol{B}^T \\ (\varepsilon + P)\boldsymbol{v} - \boldsymbol{B}(\boldsymbol{v} \cdot \boldsymbol{B}) \\ \varepsilon_{\rm cr}\boldsymbol{v} + (\varepsilon_{\rm cr} + P_{\rm cr})\boldsymbol{v}_{\rm st} - \kappa_\varepsilon \boldsymbol{b}(\boldsymbol{b} \cdot \boldsymbol{\nabla}\varepsilon_{\rm cr}) \\ \boldsymbol{B}\boldsymbol{v}^T - \boldsymbol{v}\boldsymbol{B}^T \end{pmatrix}, \tag{2.48}$$

$$\boldsymbol{S} = \begin{pmatrix} 0 \\ \boldsymbol{0} \\ P_{\rm cr}\boldsymbol{\nabla} \cdot \boldsymbol{v} - \boldsymbol{v}_{\rm st} \cdot \boldsymbol{\nabla} P_{\rm cr} + \Lambda_{\rm th} + \Gamma_{\rm th} \\ -P_{\rm cr}\boldsymbol{\nabla} \cdot \boldsymbol{v} + \boldsymbol{v}_{\rm st} \cdot \boldsymbol{\nabla} P_{\rm cr} + \Lambda_{\rm cr} + \Gamma_{\rm cr} \\ \boldsymbol{0} \end{pmatrix}. \tag{2.49}$$

Here, the total pressure P and the energy density ε (excluding CRs) are defined as

$$P = P_{\rm th} + P_{\rm cr} + \frac{\boldsymbol{B}^2}{2}, \tag{2.50}$$

$$\varepsilon = \varepsilon_{\rm th} + \frac{\rho\boldsymbol{v}^2}{2} + \frac{\boldsymbol{B}^2}{2}. \tag{2.51}$$

2.2.3 The Arepo code

The Arepo Code (Springel, 2010; Pakmor et al., 2016a; Weinberger et al., 2020) deploys an unstructured mesh by performing a Voronoi tessellation of a set of mesh-generating points. On these discrete points, it adopts a finite-volume discretization of the Euler equations where the state of the fluid is discretized my means of the cells of the Voronoi mesh. For this purpose, for each

cell i the averaged conserved quantities $\boldsymbol{U}$ of the fluid are calculated as

$$\boldsymbol{Q}_{\rm i} = \int_{V_{\rm i}} \boldsymbol{U} {\rm d}V \tag{2.52}$$

that are then evolved in time according to the fluxes across the cell interfaces. Pakmor et al. (2016a) improved the original version of Arepo and adopted a second-order Runge-Kutta method to calculate the fluxes and least-square gradient estimates in order to achieve second-order accuracy of the code. The mesh-generating points are moved according to the local fluid velocity, which makes the dynamics Galilean invariant, while also adapting the spatial resolution automatically to the flow. In addition, it inherits the advantages of mesh-based Eulerian approaches by adopting the same finite-volume discretization of the Euler equations and the Godunov approach to estimate the fluxes across cell interfaces very accurately.

Furthermore, it simulates magnetic fields with ideal MHD (Pakmor et al., 2011; Pakmor & Springel, 2013) as discussed in Section 2.2.1.To ensure the solenoidal constraint of the magnetic field $\boldsymbol{\nabla} \cdot \boldsymbol{B} = 0$, the Powell scheme is used (Powell et al., 1999b), where additional terms are added in order to counteract unwanted sources of the magnetic field and thus ensure divergence free magnetic fields. Finally, the one-moment CR hydrodynamics algorithm has been introduced in Pakmor et al. (2016b) and Pfrommer et al. (2017a). Here, CRs are treated as a relativistic fluid with an effective adiabatic index of 4/3 as summarized in the previous Section 2.2.2.

2.3 Radiation mechanisms

This section aims to give an overview of the relevant thermal and non-thermal emission processes, which are implemented in a numerical framework Crayon+ (Cosmic RAY emissiON) that was used and described in Paper I, Paper II and Paper III. In addition to the calculation of steady-state spectra of primary and secondary CRs, it calculates the resulting multi-frequency emission spectra. These constitute emission from CR electrons that range from synchrotron emission in the radio band to the gamma-ray regime, where CR electrons contribute via inverse Compton (IC) and bremsstrahlung emission. In addition, CR protons interact hadronically with the ambient medium and produce pions, that decay further into gamma-ray photons if they are neutral in charge. On the other hand, if the pions are charged, they decay into muons and eventually into so-called secondary electrons and positrons, depending on the charge of the initial pion. We will discuss all processes leading to the emission in the gamma-ray regime in Section 2.3.1, while we leave the description of

the production of secondary electrons and positrons to Section 3.7, which we published in Paper I.

In the following, we present the summary of the radiation processes that we published in the appendices of Paper II and Paper III. This comprises the non-thermal emission processes in the gamma-ray regime in Section 2.3.1 (published in App. A of Paper II), radio synchrotron emission in Section 2.3.2 as well as thermal free-free emission in Section 2.3.3 (published in App. A1 and the first part of App. A2 of Paper III, respectively).

2.3.1 Radiative processes in the γ-ray regime

We describe in the following the relevant processes in the γ-ray regime. In this context, we use the following definitions. The production spectrum of N_γ photons or source function q_γ is defined in units of ph erg^{-1} s^{-1} cm^{-3} as

$$q_\gamma = \frac{\mathrm{d}N_\gamma}{\mathrm{d}E\mathrm{d}t\mathrm{d}V}, \tag{2.53}$$

where E is the energy of the emitted photon, t denotes the unit time and V is the unit volume. The production spectrum is connected to the different definitions of the emissivities via

$$j_E = E\frac{\mathrm{d}N_\gamma}{\mathrm{d}E\mathrm{d}V\mathrm{d}t} \tag{2.54}$$

$$j_\nu = E\frac{\mathrm{d}N_\gamma}{\mathrm{d}\nu\mathrm{d}V\mathrm{d}t} = hj_E, \tag{2.55}$$

where h denotes Planck's constant. The total luminosity in erg s^{-1} is obtained by integrating the emissivity from energy E_1 to E_2 and over the total source volume Ω, i.e.,

$$L_{E_1-E_2} = \int_\Omega \mathrm{d}V \int_{E_1}^{E_2} \mathrm{d}E\, E\, q_\gamma. \tag{2.56}$$

Observing the emitting object from a luminosity distance d yields an observed spectral flux

$$F_E = \frac{1}{4\pi d^2}\int_\Omega \mathrm{d}V\, q_\gamma \tag{2.57}$$

in units of ph erg^{-1} s^{-1} cm^{-2}.

γ-ray emission from neutral pion decay

The collisions of CR protons with protons and other nuclei in the ambient ISM give rise to the production of several secondary particles. In particular, inelastic proton-proton (pp) collisions produce mainly pions, that lead to the production of γ rays, secondary electrons/positrons and neutrinos:

$$\begin{aligned} \pi^{\pm} &\rightarrow \mu^{\pm} + \nu_{\mu}/\bar{\nu}_{\mu} \rightarrow e^{\pm} + \nu_{\mathrm{e}}/\bar{\nu}_{\mathrm{e}} + \nu_{\mu} + \bar{\nu}_{\mu}, \\ \pi^{0} &\rightarrow 2\gamma\,. \end{aligned}$$

These secondary particles contribute to the leptonic radiation processes in addition to the primary electrons, i.e. via IC and bremsstrahlung emission (which will be discussed in the subsequent paragraphs of this section) and radio emission (see Section 2.3.2).

The source function q_{γ} that results from the decay of neutral pions following a pp collision is given by

$$q_{\gamma}(E) = c n_{\mathrm{H}} \int_{E_{\mathrm{p,min}}}^{\infty} \mathrm{d}E_{\mathrm{p}} f_{\mathrm{p}}(E_{\mathrm{p}}) \frac{\mathrm{d}\sigma_{\gamma}(E, E_{\mathrm{p}})}{\mathrm{d}E}, \tag{2.58}$$

where f_{p} denotes the CR proton distribution, E_{p} is the total proton energy, m_{p} is the proton mass and c the speed of light. Furthermore, E is the energy of the emitted γ-ray photon and n_{H} the hydrogen number density. It yields an emissivity that we denote by $j_{\nu,\pi^0} = E q_{\gamma}$. In the following, we denote neutral pions with π, if not stated otherwise. The differential cross section of γ-ray production is given by

$$\frac{\mathrm{d}\sigma_{\gamma}(E, E_{\mathrm{p}})}{\mathrm{d}E} = 2 \int_{E_{\pi,\mathrm{min}}}^{E_{\pi,\mathrm{max}}} \mathrm{d}E_{\pi} \frac{\mathrm{d}\sigma_{\pi}(E_{\mathrm{p}}, E_{\pi})}{\mathrm{d}E_{\pi}} f_{\gamma,\pi}(E, E_{\pi}). \tag{2.59}$$

Here, the normalised energy distribution $f_{\gamma,\pi}(E, E_{\pi})$ gives the probability of the production of a γ-ray photon with energy E from a single pion energy E_{π} and the factor of 2 accounts for the decay of one neutral pion into two γ rays. Following e.g. Stecker (1971), the Green's function for neutral pion decay is

$$f_{\gamma,\pi}(E, E_{\pi}) = \frac{1}{\sqrt{E_{\pi}^2 - m_{\pi}^2 c^4}}, \tag{2.60}$$

where m_{π} denotes the rest mass of neutral pions. From investigating the relativistic kinematics of the pp-collision, one can find the proton's threshold of pion production (see e.g. Mannheim &

Schlickeiser, 1994). If the kinetic energy of the proton in the center-of-momentum system is larger than the pions rest mass energy, a pion can be created. Transforming this requirement back to the lab system yields the threshold energy for pion production. It reads

$$\frac{E_{\mathrm{p,min}}}{m_{\mathrm{p}}c^2} = 2\left[1 + \frac{m_\pi}{2m_{\mathrm{p}}}\right]^2 - 1 = 1.22\,\frac{\mathrm{GeV}}{m_{\mathrm{p}}c^2} \tag{2.61}$$

and corresponds to the lower limit of the integral in Eq. (2.58). Following Kafexhiu et al. (2014), in order to correctly define the limits of the integral in Eq. (2.59), we consider the following quantities. First, the total energy and momentum of the pion in the center-of-mass (CM) system are given by

$$E_{\pi,\mathrm{CM}} = \frac{s - 4m_{\mathrm{p}}^2c^4 - m_\pi^2c^4}{2\sqrt{s}} \tag{2.62}$$

and

$$P_{\pi,\mathrm{CM}} = \sqrt{(E_{\pi,\mathrm{CM}})^2 - m_\pi^2c^4}/c \tag{2.63}$$

where $s = 2m_{\mathrm{p}}c^2(T_{\mathrm{p}} + 2m_{\mathrm{p}}c^2)$ is the squared center-of-mass energy. From this, the Lorentz factor and velocities of the CM system are given by $\gamma_{\mathrm{CM}} = (T_{\mathrm{p}} + 2m_{\mathrm{p}}c^2)/\sqrt{s}$ and $\beta_{\mathrm{CM}} = \sqrt{1 - \gamma_{\mathrm{CM}}^{-2}}$. The maximum allowed energy for the created pion given in the lab frame is

$$E_{\pi,\mathrm{max}} = \gamma_{\mathrm{CM}}(E_{\pi,\mathrm{CM}} + cP_{\pi,\mathrm{CM}}\beta_{\mathrm{CM}}) \tag{2.64}$$

and corresponds to the upper limit in Eq. (2.59). The corresponding Lorentz factor and velocity are denoted by $\gamma_{\pi,\mathrm{LAB}} = E_{\pi,\mathrm{max}}/(m_\pi c^2)$ and $\beta_{\pi,\mathrm{CM}} = \sqrt{1 - (\gamma_{\pi,\mathrm{CM}})^{-2}}$.

To ensure that the photon energy is $E < E_{\mathrm{max}}$, i.e. the maximum allowed energy for the photon from kinematic considerations, we define

$$Y_\gamma = E + \frac{m_\pi^2c^4}{4E}, \tag{2.65}$$

$$Y_{\gamma,\mathrm{max}} = E_{\mathrm{max}} + \frac{m_\pi^2c^4}{4E_{\mathrm{max}}} \tag{2.66}$$

and

$$X_\gamma = \frac{Y_\gamma - m_\pi c^2}{Y_{\gamma,\mathrm{max}} - m_\pi c^2}. \tag{2.67}$$

Then, we require $0 < X_\gamma < 1$. Additionally, the lower limit of the integral in Eq. (2.59), $E_{\pi,\min}(E)$ is the minimum energy that is needed to produce a photon of energy E, i.e.

$$E_{\pi,\min} = \max\left(m_\pi c^2, E + \frac{m_\pi^2 c^4}{4E}\right). \tag{2.68}$$

There are different parametrizations for the required terms in Eq. (2.58) in the literature, valid in different energy ranges. Yang et al. (2018b) focused on proton energies near the threshold of pion production up to 10 GeV in order to accurately prescribe the pion decay bump. They give a parametrization for the normalised pion energy distribution $\tilde{f}(x, T_\mathrm{p})$ using the hadronic interaction model from the Geant4 Toolkit (Agostinelli et al., 2003; Allison et al., 2006), so that the differential cross section of pion production is given by

$$\frac{\mathrm{d}\sigma_\pi}{\mathrm{d}x} = \sigma_\pi \times \tilde{f}(x, T_\mathrm{p}), \tag{2.69}$$

where $x = T_\pi / T_{\pi,\max}$ is the ratio of the kinetic pion energy and σ_π is the total cross section of pion production, including charged and neutral pions. There exist experimental data for the total cross section σ_π below $T_\mathrm{p} \leqslant 2\,\mathrm{GeV}$. Based on that, Kafexhiu et al. (2014) provide parametrizations in the energy range below 2 GeV, where they include all neutral pion production channels, i.e., $\mathrm{pp} \rightarrow \mathrm{pp}\pi^0$, $\mathrm{pp} \rightarrow \mathrm{pp}2\pi^0$ as well as $\mathrm{pp} \rightarrow \mathrm{p}\pi^+\pi^0$ and $\mathrm{pp} \rightarrow D\pi^+\pi^0$. Above kinetic proton energies of 2 GeV, the inelastic cross section is expressed in terms of the total inelastic cross section and an average pion multiplicity, that they fit separately, i.e.

$$\sigma_\pi = \sigma_{\mathrm{pp,inel}} \langle n_\pi \rangle . \tag{2.70}$$

Here, $\langle n_\pi \rangle$ denotes the average pion multiplicity and the inelastic cross section is given by

$$\sigma_{\mathrm{pp,inel}}(T_\mathrm{p}) = \left[30.7 - 0.96 \log\left(\frac{T_\mathrm{p}}{T_{\mathrm{p,th}}}\right) + 0.18 \log^2\left(\frac{T_\mathrm{p}}{T_{\mathrm{p,th}}}\right)\right]\left[1 - \left(\frac{T_\mathrm{p}}{T_{\mathrm{p,th}}}\right)^{1.9}\right]^3 \mathrm{mbarn}, \tag{2.71}$$

where the threshold proton kinetic energy is $T_{\mathrm{p,th}} = 2m_\pi c^2 + m_\pi^2 c^4/(2m_\mathrm{p}c^2) \approx 0.2797\,\mathrm{GeV}$. Additionally, Kafexhiu et al. (2014) provide a parametrization of the differential γ-ray cross section in the following form

$$\frac{\mathrm{d}\sigma_\gamma(T_\mathrm{p}, E)}{\mathrm{d}E} = A_{\max}(T_\mathrm{p}) F(T_\mathrm{p}, E), \tag{2.72}$$

where they fit $A_{\max}(T_\mathrm{p}) = \max\left(\mathrm{d}\sigma_\gamma/\mathrm{d}E\right)$ separately from $F(T_\mathrm{p}, E)$ since the maximum value only depends on the proton kinetic energy T_p. It is a function of the total π^0-production cross section $\sigma_\pi(E_\mathrm{p})$, for which they also provide their own fits. In the high-energy regime, they divide the cross section into the inelastic part and the pion multiplicity, see Eq. (2.70), and use Eq. (2.71) for $\sigma_{\mathrm{pp,inel}}$. This matches new experimental data by Beringer et al. (2012) in the very high energy regime around $T_\mathrm{p} = 10^7$ GeV better than e.g., the one used by Kelner et al. (2006). They furthermore provide their own fit to the average pion multiplicity $\langle n_{\pi^0}\rangle$, that agrees well with the description used by Yang et al. (2018b), which refers to data from Golokhvastov (2001).

In our approach, we use the parametrization by Yang et al. (2018b) for $T_\mathrm{p} < 10\,\mathrm{GeV}$ and the model by Kafexhiu et al. (2014) at larger energies. We compare this to other models from the literature in App. B1 and B2 of Paper II (see Section 4.5). The relative deviation of the resulting total γ-ray luminosity, integrated from 0.1-100 GeV, of our model in comparison to the analytical approximation by Pfrommer & Enßlin (2004) and the parametrization by Kelner et al. (2006) is shown to be ~ 10 per cent, depending on the spectral index of the CR proton spectrum (see Fig. B2 in Paper II, i.e. Fig. 4.11 in this work).

So far, we have assumed that the ambient gas consists of protons only. The effect of relativistic protons interacting with nuclei heavier than hydrogen was studied by Yang et al. (2018b). At high energies these interactions can be described by a sequence of binary nucleon-nucleon collisions according to the Glauber's multiple scattering theory (Glauber, 1955; Franco & Glauber, 1966; Glauber & Matthiae, 1970). However, there are two additional processes at lower, sub-relativistic energies, for which there exists no self-consistent theory. On the one hand, intra-nuclear collisions can lead to the production of pions below the kinematic threshold, which is called sub-threshold pion production. On the other hand, so called direct photons are emitted, probably due to neutron-proton-bremsstrahlung during the early stage of the nuclear interaction. The cross sections for these processes have been parametrized by Kafexhiu (2016). Yang et al. (2018b) used these parametrizations to analyse the contribution from heavy nuclei to the γ-ray emission from hadronic interactions from Galactic CR protons with the interstellar gas and found a very similar spectral shape when including heavy nuclei in comparison to only considering pp-interactions, but found an overall increased emissivity by a nuclear enhancement factor of $a_{\mathrm{nucl}} = 1.8$. Using the definition of the number density of hydrogen $n_\mathrm{H} = X_\mathrm{H}\,\rho/m_\mathrm{p}$, the helium density $n_\mathrm{He} = (1 - X_\mathrm{H})/4 \times \rho/m_\mathrm{p}$ and the mass fraction of hydrogen $X_\mathrm{H} = 0.76$, the number density of target nucleons in the ISM is given by $n_\mathrm{N} = n_\mathrm{H} + 4n_\mathrm{He} = \rho/m_\mathrm{p}$. Hence, if we use n_N as the target density for hadronic interactions, we only need another factor of $1.8 \times X_\mathrm{H} \approx 1.37$ to account for the interactions of heavier nuclei, such as the sub-threshold pion production.

Inverse Compton emission

The CR electron population also contributes to the non-thermal γ-ray emission. Inverse Compton (IC) scatterings transfer some of the CR electron energy to low-energy ambient photons, boosting them to very high energies up to the γ-ray regime. The typical energy gain for the up-scattered photon is given by $E_{\rm max} \approx 4\gamma_{\rm e}^2 E_{\rm i}/3$, where $\gamma_{\rm e} = \sqrt{p_{\rm e}^2 + 1}$ is the Lorentz factor of the electron colliding inelastically with an incident photon of energy $E_{\rm i}$. Following Jones (1968) and Blumenthal & Gould (1970), one can derive the emitted spectrum due to IC scattering of an electron population off of an incoming radiation field of photons, denoted by $n_{\rm ph}$. Using the general expression for the cross section of IC scattering described in the Klein-Nishina formalism, we can derive the IC emissivity resulting from a CR electron spectrum $N_{\rm e}(E_{\rm e})$ to obtain

$$j_{\nu,\rm IC} = 2\pi h E r_0^2 c \int {\rm d}E_{\rm e} \frac{f_{\rm e}(E_{\rm e})}{\gamma_{\rm e}^2} \int_{q_{\rm min}}^{1} \frac{{\rm d}q}{q} n_{\rm ph}[q(\gamma_{\rm e}, E)]\, f[q(\gamma_{\rm e}, E)], \tag{2.73}$$

where $r_0 = e^2/(m_{\rm e}c^2)$ is the classical electron radius, e is the elementary charge, $m_{\rm e}$ the electron rest mass and

$$f(q) = 2q \ln q + (1+2q)(1-q) + \frac{1}{2}\frac{(\Gamma_{\rm e} q)^2}{1+\Gamma_{\rm e} q}(1-q). \tag{2.74}$$

Furthermore, the normalised quantities $\Gamma_{\rm e}$ and q are given by $\Gamma_{\rm e} = 4E_{\rm i}\gamma_{\rm e}/(m_{\rm e}c^2)$and $q(\gamma_{\rm e}) = E^* m_e c^2/(4E_{\rm i}\gamma_{\rm e}(1-E^*))$, where $E^* = E/(\gamma_{\rm e} m_{\rm e} c^2)$. The integration limits for q follow from the kinematic limitations for E^*, i.e. $E_{\rm i}/(\gamma_{\rm e} m_{\rm e} c^2) \leqslant E^* \leqslant \Gamma_{\rm e}/(1+\Gamma_{\rm e})$, where $\Gamma_{\rm e} = 4E_{\rm i}\gamma_{\rm e}/(m_{\rm e}c^2)$, so that $q_{\rm min} = \left[4\gamma_{\rm e}^2(1 - E_{\rm i}/(\gamma_{\rm e} m_{\rm e} c^2))\right]^{-1} \leqslant q \leqslant 1$.

The incident radiation field $n_{\rm ph}$ is assumed to consist of different components that can each be described by black body distributions of different temperatures T_j and weighting factors A_j, such that

$$n_{\rm ph}(E) = \sum_j A_j \frac{E_{\rm i}^2}{\pi^2(\hbar c)^3 \left(\exp\left(E/k_{\rm B}T_j\right) - 1\right)}, \tag{2.75}$$

where $\hbar$ is the reduced Planck constant and $k_{\rm B}$ is Boltzmann's constant. For a given photon energy density $\varepsilon_{\rm ph}$, the black body spectrum is weighted according to $A_j = \varepsilon_{\rm ph}/(a_{\rm rad} T_j^4)$, where $a_{\rm rad} = 8\pi^5 k_{\rm B}^4/(15h^3c^3)$ is the radiation constant. To speed up the numerical integration of Eq. (2.73), we pre-evaluate the integral over q for fixed momentum bins of the electron distribution, assuming two fixed black body temperatures, i.e. $T_{\rm CMB} = 2.73$ K and $T_{\rm FIR} = 20$ K. The latter results from the assumption that the UV emission of young stars is absorbed by dust (Calzetti et al., 2000) and re-emitted in the FIR. To obtain an estimate of the FIR flux in each cell of our simulation, we

adopt the relation between SFR and FIR luminosity, L_{FIR}, obtained by Kennicutt (1998):

$$\frac{\dot{M}_\star}{\mathrm{M}_\odot\,\mathrm{yr}^{-1}} = a_{\mathrm{SFR}}\,1.7\times10^{-10}\frac{L_{\mathrm{FIR}}}{L_\odot}. \tag{2.76}$$

The parameter $a_{\mathrm{SFR}} = 0.79$ follows from adopting a Chabrier (2003) initial mass function, see Crain et al. (2010). The resulting photon energy density of a cell is then the sum of CMB and stellar radiation,i.e. $\varepsilon_{\mathrm{ph}} = \varepsilon_{\mathrm{CMB}} + \varepsilon_\star$, where the latter is derived by summing up the flux arriving at each cell from all actively star-forming cells at a distance R_i, i.e. $\varepsilon_\star = \sum_i L_{\mathrm{FIR}}/(4\pi R_i^2 c)$. This flux is calculated using a tree code in order to speed up the calculation. If the considered cell is actively star forming, the distance is estimated from the cell's volume, $R_i = [3V_i/(4\pi)]^{1/3}$.

Bremsstrahlung

The second process contributing to the non-thermal γ-ray emission of CR electrons is relativistic bremsstrahlung, which results from their acceleration in the field of charged nuclei. In the classical picture of the method of virtual quanta, i.e. the Weizsäcker-Williams approach, it can be described as an IC scattering process in the rest frame of a relativistically moving electron. It sees the electrostatic field of the approaching nucleon with charge Ze as a pulse of electromagnetic radiation, of which it inelastically scatters off and consequently, emits radiation while losing some of its energy. Therefore, in that picture one can again apply the IC formalism in the general Klein-Nishina regime, but replacing the incident radiation field with the virtual quanta from the approaching nucleus as seen from the electron's rest frame and calculate the scattered photon field. The differential cross section for relativistic bremsstrahlung, $\mathrm{d}\sigma_{\mathrm{brems}}$, in the lab frame for an electron scattering off of a nucleon is thus given by $\mathrm{d}\sigma_{\mathrm{brems}} = \mathrm{d}\sigma_{\mathrm{IC}}\mathrm{d}N$. Inserting the Klein-Nishina cross section and the expression for the differential number of virtual quanta $\mathrm{d}N$, one has to integrate over the impact parameter (see Blumenthal & Gould, 1970). Eventually, a Lorentz transformation back to the lab frame yields

$$\mathrm{d}\sigma_{\mathrm{brems}} = 4\alpha r_0^2 Z^2\frac{\mathrm{d}\omega}{\omega}\left[\frac{4}{3}\left(1-\frac{\hbar\omega}{E_{\mathrm{e,in}}}\right)+\left(\frac{\hbar\omega}{E_{\mathrm{e,in}}}\right)^2\right]\ln\left(\frac{2E_{\mathrm{e,in}}E_{\mathrm{e,out}}}{m_{\mathrm{e}}c^2\hbar\omega}\right), \tag{2.77}$$

where α is the fine structure constant, ω is the angular frequency of the emitted photon and $E_{\mathrm{e,in}}$ denotes the energy of the incoming electron, whereas $E_{\mathrm{e,out}}$ is the energy of the outgoing electron after scattering, i.e., $E_{\mathrm{e,out}} = E_{\mathrm{e,in}} - \hbar\omega$. Since the argument of the logarithm is typically $\gg 1$, this is consistent with the cross section derived by Bethe & Heitler (1934) in the Born approximation

for non-screened (i.e. fully ionized) ions and for the case of highly relativistic electrons, i.e.

$$\mathrm{d}\sigma_{\mathrm{brems}} = 4\alpha r_0^2 Z^2 \frac{\mathrm{d}\omega}{\omega} \frac{1}{E_{\mathrm{e,in}}^2} \left(E_{\mathrm{e,in}}^2 + E_{\mathrm{e,out}}^2 - \frac{2}{3} E_{\mathrm{e,in}} E_{\mathrm{e,out}} \right) \left(\ln \frac{2 E_{\mathrm{e,in}} E_{\mathrm{e,out}}}{m_e c^2 \hbar \omega} - \frac{1}{2} \right). \tag{2.78}$$

As pointed out by Haug (1997), if we consider mildly and highly relativistic electrons, one can combine the non-relativistic cross section obtained by Heitler (1954) with the extreme relativistic case that is expanded up to 6th orders in initial and final electron momenta. Equation (2.78) has a relative deviation of order $< 10^{-3}$ for frequencies above 0.1 GeV, when comparing it to the extension of the semi-relativistic description in Haug (1997), that also includes an correction factor that accounts for the distortion of the electron wave function in the Coulomb field of the nucleus. Hence, we adopt this approximation in the following.

In addition to electron-ion bremsstrahlung, we also have to take into account electron-electron bremsstrahlung. While at low incident electron energies the quadrupole emission from the electron-electron interaction can be neglected in comparison to the electron-nucleus dipole emission, it can make a significant contribution for higher energy electrons and emitted photons (Haug, 1975b). The exact expression for the electron-electron bremsstrahlung cross section $\mathrm{d}\sigma_{ee}$ was first derived by Haug (1975a), for which Baier et al. (1967) provided a good approximation for ultra-relativistic electrons. It is given in terms of the normalised energy $\epsilon = E/(m_{\mathrm{e}}c^2)$, where E denotes the energy of the scattered photon, by

$$\mathrm{d}\sigma_{ee} = (\sigma_1 + \sigma_2) A(\epsilon, \gamma_{\mathrm{e}}) \mathrm{d}\epsilon, \tag{2.79}$$

where

$$\sigma_1 = \frac{4 r_0^2 \alpha}{\epsilon} \left[\frac{4}{3} \left(1 - \frac{\epsilon}{\gamma_{\mathrm{e}}}\right) + \left(\frac{\epsilon}{\gamma_{\mathrm{e}}}\right) \right] \left[\ln \frac{2\gamma_{\mathrm{e}}(\gamma_{\mathrm{e}} - \epsilon)}{\epsilon} - \frac{1}{2} \right] \tag{2.80}$$

and

$$\sigma_2 = \frac{r_0^2 \alpha}{3\epsilon} \begin{cases} 16(1 - \epsilon + \epsilon^2) \ln \frac{\gamma_{\mathrm{e}}}{\epsilon} - \frac{1}{\epsilon^2} + \frac{3}{\epsilon} - 4 + 4\epsilon - 8\epsilon^2 & \\ -2(1 - 2\epsilon) \ln(1 - 2\epsilon) \left(\frac{1}{4\epsilon^3} - \frac{1}{2\epsilon^2} + \frac{3}{\epsilon} - 2 + 4\epsilon \right), & \epsilon \leqslant \frac{1}{2} \\ \frac{2}{\epsilon} \left[\left(4 - \frac{1}{\epsilon} + \frac{1}{4\epsilon^2}\right) \ln 2\gamma_{\mathrm{e}} - 2 + \frac{2}{\epsilon} - \frac{5}{8\epsilon^2} \right], & \epsilon > \frac{1}{2}. \end{cases} \tag{2.81}$$

The factor $A(\epsilon, \gamma_{\mathrm{e}})$ is a middly-relativistic correction factor that was introduced by Baring et al.

(1999) and reads

$$A(\epsilon, \gamma_\mathrm{e}) = 1 - \frac{8}{3}\frac{(\gamma_\mathrm{e} - 1)^{1/5}}{\gamma_\mathrm{e} + 1}\left(\frac{\epsilon}{\gamma_\mathrm{e}}\right)^{1/3}.$$

According to them, the highly relativistic approximation combined with this factor yields an accuracy within 10 per cent in comparison to the exact expression by Haug (1975a). We finally arrive at the bremsstrahlung emissivity resulting from a CR electron population as

$$j_{\nu,\mathrm{brems}} = j_{\nu,\mathrm{ep}} + j_{\nu,\mathrm{ee}}, \tag{2.82}$$

where we take into account the contribution of electron-proton and electron-electron bremsstrahlung, which are calculated by

$$j_{\nu,\mathrm{ep/ee}} = c\, n_{\mathrm{p/e}} \nu h^2 \int \mathrm{d}p_\mathrm{e} f_\mathrm{e}(p_\mathrm{e}) \frac{\mathrm{d}\sigma_{\mathrm{ep/ee}}(p_\mathrm{e}, \nu)}{\mathrm{d}\epsilon}. \tag{2.83}$$

2.3.2 Synchrotron emission

Each relativistic electron with charge e that is accelerated by an ambient magnetic field $\boldsymbol{B}$ emits synchrotron radiation. The resulting power emitted per unit frequency ν is given by (Rybicki & Lightman, 1986)

$$P(\nu, \gamma_\mathrm{e}) = \frac{\mathrm{d}E}{\mathrm{d}\nu \mathrm{d}t} = \frac{\sqrt{3} e^3 B \sin\alpha_\mathrm{pitch}}{m_\mathrm{e} c^2} F(x), \tag{2.84}$$

where α_pitch is the pitch angle, i.e. the angle between the velocity of the electron and the magnetic field, $x = \nu/\nu_\mathrm{c}$, the critical frequency is $\nu_\mathrm{c} = 3/(4\pi)\, \gamma_\mathrm{e}^3 \omega_B \sin\alpha_\mathrm{pitch}$, and the frequency of gyration is $\omega_B = eB/(\gamma_\mathrm{e} m_e c)$. Furthermore, the dimensionless synchrotron kernel $F(x)$ is defined as

$$F(x) = x \int_x^\infty K_{5/3}(\xi)\mathrm{d}\xi, \tag{2.85}$$

where $K_{5/3}$ is the modified Bessel function of order 5/3. For a population of electrons with a distribution $f_\mathrm{e}(p)$, the total emissivity, i.e., the emitted energy per unit time, volume and frequency,

is obtained by integrating over the electron distribution:

$$j_\nu(\nu) = E\frac{\mathrm{d}N_\gamma}{\mathrm{d}\nu\mathrm{d}V\mathrm{d}t} = \frac{\sqrt{3}e^3 B_\perp}{m_e c^2}\int_0^\infty f_\mathrm{e}(p)F(x)\mathrm{d}p, \tag{2.86}$$

where $B_\perp$ is the component of the magnetic field perpendicular to the line of sight and the argument of the synchrotron kernel depends on the electron momentum via the dependence of the critical frequency on the Lorentz factor, $\gamma_\mathrm{e} = \sqrt{1+p^2}$. Since the integration over the modified Bessel function is numerically expensive, we use an analytical approximation by Aharonian et al. (2010), which reads

$$\widetilde{F}(x) \approx 2.15x^{1/3}(1+3.06x)^{1/6}\frac{1+0.884x^{2/3}+0.471x^{4/3}}{1+1.64x^{2/3}+0.974x^{4/3}}e^{-x}. \tag{2.87}$$

This function peaks at $x = 0.2858$ but its first moment lies at $x = 2.13$.

2.3.3 Thermal free-free emission and absorption

Thermal electrons are deflected in the Coulomb field of ions of charge Ze and emit thermal free-free emission. The resulting emissivity from a medium with electron density n_e, ion density n_i and temperature T is given by (Rybicki & Lightman, 1986)

$$j_{\nu,\mathrm{ff}} = \; 6.8\times10^{-38}\,\mathrm{erg\,s^{-1}\,cm^{-3}\,Hz^{-1}}\times Z^2\frac{n_\mathrm{e}\,n_\mathrm{i}}{\mathrm{cm^{-6}}}\,T_1^{-0.5}\,e^{-h\nu/(k_\mathrm{B}T)}\,\overline{g}_\mathrm{ff}, \tag{2.88}$$

where $T_1 = T/(1\,\mathrm{K})$, h is Planck's constant and k_B denotes Boltzmann's constant. The corresponding absorption coefficient of free-free absorption in the Rayleigh-Jeans regime, i.e. for $h\nu \ll k_\mathrm{B}T$, reads (Rybicki & Lightman, 1986)

$$\kappa_\mathrm{ff}(\nu) = 0.018\,T_1^{-1.5}\,Z^2\frac{n_\mathrm{e}\,n_\mathrm{i}}{\mathrm{cm^{-6}}}\left(\frac{\nu}{\mathrm{Hz}}\right)^{-2}\overline{g}_\mathrm{ff}\,\mathrm{cm^{-1}}. \tag{2.89}$$

Here, the mean Gaunt factor $\overline{g}_\mathrm{ff}$ in the "small-angle, classical region" is given by (Novikov & Thorne, 1973)

$$\overline{g}_\mathrm{ff} = \frac{\sqrt{3}}{\pi}\ln\left[\frac{1}{4\xi^{5/2}Z}\left(\frac{k_\mathrm{B}T}{h\nu}\right)\left(\frac{k_\mathrm{B}T}{13.6\,\mathrm{eV}}\right)^{0.5}\right], \tag{2.90}$$

where $\xi = \exp(\gamma_E) \approx 1.781$ and γ_E denotes Euler's constant. We assume a temperature of $T = 8000$ K for the warm ionized medium and approximate the electron density n_e by taking a constant fraction ξ_e of the electron density provided in our pressurised ISM model (Springel & Hernquist, 2003) to parametrize the effect of radiation feedback in the dense star-forming/bursting regions and further assume $n_e \approx n_i$ and $Z = 1$. The optical depth due to free-free absorption is calculated via the integral of the absorption coefficient along the line of sight, i.e.

$$\tau_{ff}(\nu, s_0, s_1) = \int_{s_0}^{s_1} \kappa_{ff}(\nu) \mathrm{d}s = 0.018\, T_1^{-1.5}\, Z^2 \left(\frac{\nu}{\mathrm{Hz}}\right)^{-2} \overline{g}_{ff} \int_{s_0}^{s_1} \left(\frac{n_e}{\mathrm{cm}^{-3}}\right)^2 \mathrm{d}s, \tag{2.91}$$

where $\mathrm{d}s = \sin\phi\, \mathrm{d}y + \cos\phi\, \mathrm{d}z$ and ϕ denotes the inclination angle. Because for a constant temperature, $j_{\nu,ff}/\kappa_{ff}$ is constant along the line of sight and the solution of the radiative transfer equation (e.g. Rybicki & Lightman, 1986) is straight forward and yields an observed intensity of free-free emission

$$4\pi I_{\nu,ff}(s_1) = \frac{j_{\nu,ff}}{\kappa_{ff}} \left\{1 - \exp[-\tau_{ff}(\nu, s_0, s_1)]\right\}. \tag{2.92}$$

Also, the emitted synchrotron spectrum is affected by free-free absorption, which is typically relevant at low frequencies, as well as synchrotron self-absorption (SSA). The absorption coefficient and the corresponding optical depth of SSA reads (Rybicki & Lightman, 1986)

$$\kappa_{SSA}(\nu) = -\frac{c^2}{8\pi\nu^2} \int_0^\infty \mathrm{d}p_e P(\nu, p_e) \left(1 + p_e^2\right) \frac{\partial}{\partial p_e} \left[\frac{f_e(p_e)}{\beta\left(1 + p_e^2\right)}\right] \tag{2.93}$$

and

$$\tau_{SSA}(\nu, s_0, s_1) = \int_{s_0}^{s_1} \kappa_{SSA}(\nu) \mathrm{d}s. \tag{2.94}$$

In order to calculate the absorbed synchrotron spectrum, we use the formal solution of the radiative transfer equation for an emissivity j_ν and the optical depth $\tau = \tau_{SSA} + \tau_{ff}$., i.e.

$$4\pi I_\nu(s_1) = \int_{s_0}^{s_1} j_\nu(s) \exp[-\tau(\nu, s, s_1)] \mathrm{d}s. \tag{2.95}$$

3. Cosmic rays and non-thermal emission in simulated galaxies - I. Electron and proton spectra compared to Voyager-1 data

This chapter is based on our work published in Werhahn et al. (2021a).

Current-day cosmic ray (CR) propagation studies use static Milky-Way models and fit parametrized source distributions to data. Instead, we use three-dimensional magneto-hydrodynamical (MHD) simulations of isolated galaxies with the moving-mesh code Arepo that self-consistently accounts for hydrodynamic effects of CR protons. In post-processing, we calculate their steady-state spectra, taking into account all relevant loss processes. We show that this steady-state assumption is well justified in the disc and generally for regions that emit non-thermal radio and gamma rays. Additionally, we model the spectra of primary electrons, accelerated by supernova remnants, and secondary electrons and positrons produced in hadronic CR proton interactions with the gas. We find that proton spectra above 10 GeV only weakly depend on galactic radius, while they acquire a radial dependence at lower energies due to Coulomb interactions. Radiative losses steepen the spectra of primary CR electrons in the central galactic regions while diffusive losses dominate in the outskirts. Secondary electrons exhibit a steeper spectrum than primaries because they originate from the transported steeper CR proton spectra. Consistent with Voyager-1 and AMS-02 data, our models (i) show a turn-over of proton spectra below GeV energies due to Coulomb interactions so that electrons start to dominate the total particle spectra and (ii) match the shape of the positron fraction up to 10 GeV. We conclude that our steady-state CR modeling in MHD-CR galaxy simulations is sufficiently realistic to capture the dominant transport effects shaping their spectra, arguing for a full MHD treatment to accurately model CR transport in the future.

3.1 Introduction

Relativistic particles (so called CRs) are extremely rare in the interstellar medium (ISM): only one in $\sim 10^9$ particles is a CR particle. The CR population is mostly composed of protons with a small admixture of heavier nuclei, electrons and positrons. Despite the rarity of these highly energetic particles in terms of number density, their energy density is comparable to the thermal, magnetic and kinetic counterpart (Boulares & Cox, 1990; Zweibel, 2013). Hence, they inevitably play a crucial role in galaxy formation and evolution, e.g., by driving galactic winds and regulating star formation. This has been suggested in several different settings, such as one-dimensional (1D) flux tube models (Breitschwerdt et al., 1991; Zirakashvili et al., 1996; Ptuskin et al., 1997; Everett et al., 2008; Samui et al., 2010; Recchia et al., 2016) or three-dimensional simulations of the ISM (Hanasz et al., 2013; Girichidis et al., 2016; Simpson et al., 2016; Farber et al., 2018). In addition, CR-hydrodynamic simulations of forming galaxies in isolation (Jubelgas et al., 2008; Uhlig et al., 2012; Booth et al., 2013; Salem & Bryan, 2014; Pakmor et al., 2016c; Ruszkowski et al., 2017; Pfrommer et al., 2017b; Jacob et al., 2018; Dashyan & Dubois, 2020) or in cosmological environments (Salem et al., 2014; Buck et al., 2020; Hopkins et al., 2020, 2021a) have shown the relevance of CRs in regulating the star formation rate (SFR) of galaxies and their ability to launch galactic winds. Up to PeV particle energies, CR protons are assumed to be mostly accelerated at the remnants of supernovae (SNe) and therefore of Galactic origin (e.g. Ginzburg & Syrovatskii, 1964; Jokipii & Morfill, 1985). The mechanism of diffusive shock acceleration leads to a distribution of CRs that can be expressed as a power law in momentum (Blandford & Eichler, 1987). However, the locally observed spectrum is different from the freshly injected one, in terms of spectral distribution as well as composition, enabling theorists to infer CR propagation and interactions throughout the ISM. In particular, the abundance of secondary particle species that are created via CR interactions with the ISM provide insight into the propagation mechanisms (Strong et al., 2007; Grenier et al., 2015).

The strong connection between CRs and the physical properties of a galaxy can be deduced from observations of their non-thermal emission in radio (van der Kruit, 1971; Condon, 1992; Bell, 2003) and gamma rays (Ackermann et al., 2012b; Rojas-Bravo & Araya, 2016; Linden, 2017) that tightly correlate with indicators of star formation. Since core-collapse SNe explode only $\sim 5 - 30\,\mathrm{Myr}$ after star formation, a fresh population of CRs is closely connected to the existence of a young stellar population, whose ultraviolet (UV) radiation typically gets absorbed by dust and re-emitted in the far-infrared (FIR). Thus, under the assumption of calorimetry, i.e. that CRs lose most of their energy due to emission before they can escape, the FIR luminosity of star forming galaxies

is expected to be strongly connected to the non-thermal emission arising from their CR population (Pohl, 1994; Völk, 1989; Lisenfeld et al., 1996). Indeed, the radio synchrotron emission from CR electrons is found to be linearly correlated with the FIR luminosity of star forming galaxies. The correlation holds over many orders of magnitude from dwarf galaxies up to strongly starburst systems with a remarkably low scatter. This challenges our understanding of the processes in place, and needs fine-tuning of several parameters in order to explain the observations (Lacki et al., 2010). In this context, the relevance of primary versus secondary electrons has been discussed, the latter being claimed to play an important role especially in highly star-forming galaxies.

Similarly, the gamma-ray luminosities are found to strongly correlate with the FIR luminosities of star forming galaxies, but deviate from this relation at low SFRs (Ajello et al., 2020). This has been attributed to non-radiative losses of CRs coming into play in low-density galaxies, where the calorimetric assumption can not be fulfilled (Thompson et al., 2007; Strong et al., 2010; Lacki et al., 2011; Pfrommer et al., 2017b; Kornecki et al., 2020).

There are a number of numerical propagation models in the literature, e.g. GALPROP (Strong & Moskalenko, 1998), DRAGON (Evoli et al., 2008), PICARD (Kissmann, 2014) and Usine (Maurin, 2020). They solve the CR propagation equation on a grid while parametrizing the distribution of supernova remnants (SNR) with various input parameters, while aiming to match all constraints given by the observations of CR nuclei, electrons and positrons, as well as the observed gamma-ray and synchrotron emission of our Galaxy. However, these models combine different models for the source distributions and independent inferences of the density and magnetic field of the Milky Way. As such, they are not self-consistently emerging from an MHD simulation, which limits their predictive power.

In an extra-galactic context, it is common to use one-zone leaky-box models of star-forming galaxies in order to explain various aspects of their observed non-thermal emission quantities (e.g. Torres, 2004; Lacki et al., 2010, 2011; Yoast-Hull et al., 2013). These models prescribe one galaxy with a characteristic scale height, a fixed magnetic field and gas density, motivated by observations. Additionally, Heesen et al. (2016) and Miskolczi et al. (2019) use 1D CR transport models in order to explain the observed radio emission in the halos of star-forming spiral galaxies. However, there is no contact made to CR propagation models in the Milky Way, that probe the same underlying physics, and these one-zone models require fitting a number of parameters that are observationally not constrained.

We aim to develop a complementary approach to previous models by performing three-dimensional MHD simulations of forming galaxies. These simulations include CR protons as a relativistic fluid that is dynamically coupled to the MHD equations in the advection-diffusion

Table 3.1: Overview of the different simulations.

M_{200} [$M_\odot$]	c_{200}	ζ_{SN}	B_0 [G]	notes
10^{12}	7	0.10	10^{-10}	
10^{12}	7	0.05	10^{-10}	fiducial galaxy
10^{12}	12	0.05	10^{-10}	

approximation. We inject CRs at SNe that trace the sites of active star formation in the simulations. The dynamical impact of CR protons is thus included in the evolution of these galaxies. The spectral details of the CR protons as well as the CR electron and positron physics are investigated in post-processing.

This paper is the first of a series of three papers. Here, we focus on studying the spectra of CR protons, primary and secondary electrons, that we assume to be in steady-state in each computational cell. Our approach is aimed to be predictive, since our source function is not tuned in order to exactly reproduce the observations, but results from modeling star-formation and CR physics self-consistently in our MHD simulations. Hence, we obtain observables that can be related to recent measurements of the Milky Way, such as the spectra of CR protons and electrons, as well as the fraction of positrons. The aspects of the resulting non-thermal emission will be studied in two following papers. Werhahn et al. (2021b, hereafter Paper II) provides insights into the gamma-ray emission from CRs in simulated galaxies, both in terms of total luminosities and spectral energy distributions and Werhahn et al. (2021c, hereafter Paper III) analyses the radio-synchrotron emission from the primary and secondary electron population.

We present our simulations in Section 3.2. The modeling of CRs is explained in Section 3.3, where we detail how we obtain the spectra of CR protons, primary electrons and model the production of secondary electrons and positrons. Our resulting maps and spectra are discussed in Section 3.4, where we compare the latter to observations. Finally, we summarise our findings in Section 3.5. Appendix 3.6 provides more details on the normalisation of primary electron and proton spectra. Additionally, in Appendix 3.7 we describe the production of secondary electrons and positrons, show our parametrization of the cross section of pion production, and compare the electron source function to an analytical approximation.

3.2 Simulations

We perform MHD simulations of isolated galactic discs with the moving mesh code Arepo (Springel, 2010; Pakmor et al., 2016a), which simulates magnetic fields with ideal MHD (Pak-

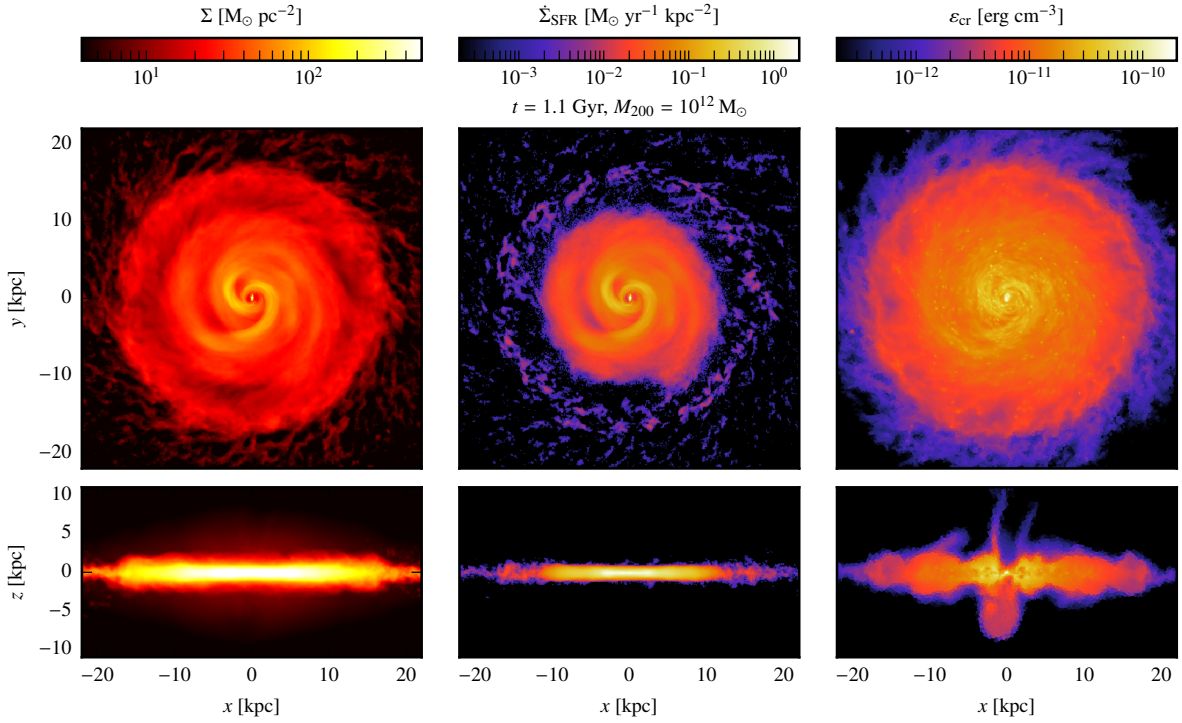

Figure 3.1: Left to right, we show projected maps of the gas surface density Σ, SFR density $\dot{\Sigma}_{\rm SFR}$ and slices of the cosmic ray energy density $\varepsilon_{\rm cr}$ at 1.1 Gyr. Shown are face-on views (top panels) and edge-on views (bottom panels) for a galaxy with a halo mass of $M_{200} = 10^{12}\,{\rm M}_\odot$, concentration $c_{200} = 7$, initial magnetic field $B_0 = 10^{-10}\,{\rm G}$ and CR acceleration efficiency $\zeta_{\rm SN} = 0.05$. In the following, we refer to this configuration as our fiducial galaxy.

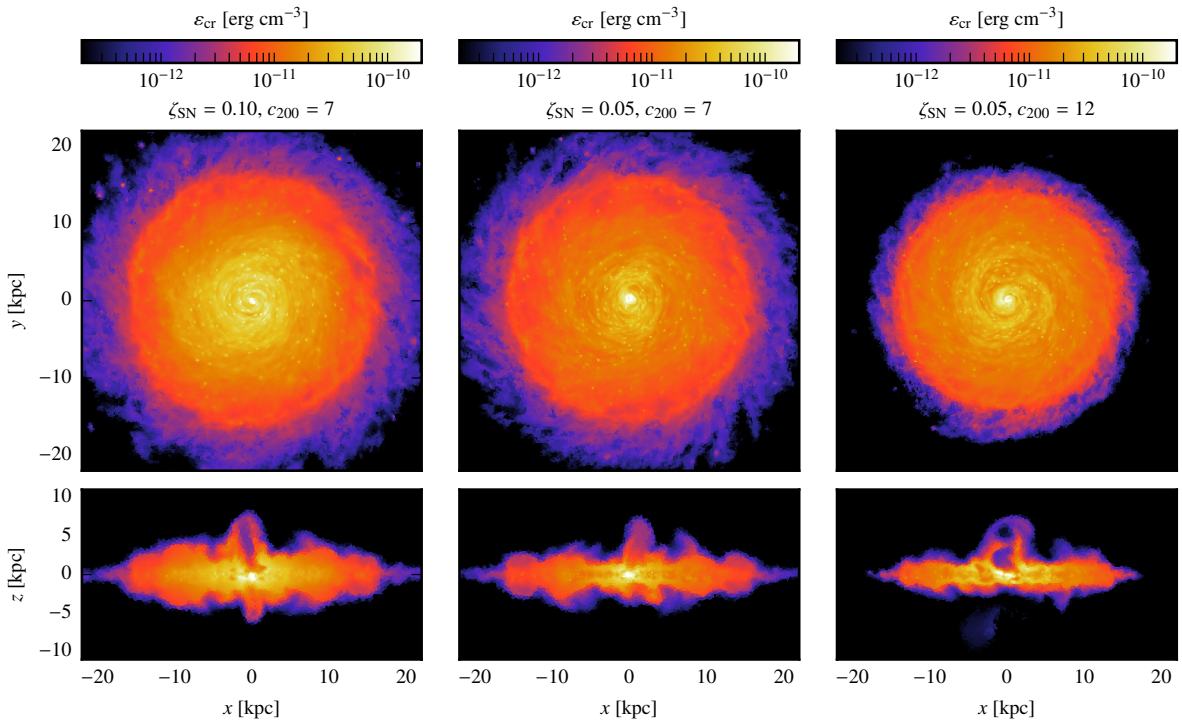

Figure 3.2: We show face-on views (top panels) and edge-on views (bottom panels) of slices of the CR energy density ε_{cr} through three different simulations with the same halo mass $M_{200} = 10^{12}\,M_\odot$ at 1 Gyr, but different concentration parameters c_{200} and injection efficiencies ζ_{SN} as indicated in the panels. The central panel shows our fiducial galaxy that we will analyse in the following.

mor & Springel, 2013). The simulations performed in this study are similar to those in Pfrommer et al. (2017b) and use the one-moment CR hydrodynamics algorithm (Pakmor et al., 2016b; Pfrommer et al., 2017a). In order to cover the entire mass spectrum of galaxies from dwarfs to Milky Way-like galaxies, we simulate dark matter halo masses ranging from $M_{200} = 10^{10}$ to $10^{12}\,\mathrm{M}_\odot$. The gas cloud is initially assumed to be in hydrostatic equilibrium with the halo. It contains 10^7 gas cells, each carrying a target mass[1] of $155\,\mathrm{M}_\odot \times M_{200}/(10^{10}\,\mathrm{M}_\odot)$, embedded in a dark matter halo that follows an NFW profile (Navarro et al., 1997). This is characterised by a concentration $c_{200} = r_{200}/r_\mathrm{s}$, where r_s is the characteristic scale radius of the NFW profile and the radius r_{200} encloses a mean density that corresponds to 200 times the critical cosmic density. We assume a baryon mass fraction of $\Omega_\mathrm{b}/\Omega_\mathrm{m} = 0.155$ and assign initial angular momentum to the halo, which is parametrized by a spin parameter $\lambda = j/(\sqrt{2}R_\mathrm{vir}V_\mathrm{vir}) = 0.05$, where $j = J/M$ is the specific angular momentum of the halo and R_vir and V_vir denote the virial radius and velocity of the halo, respectively. Our choice of the radial distribution of λ is in agreement with results from full cosmological simulations (Bullock et al., 2001). We switch on cooling at $t = 0$ which is fastest in the center. This causes loss of pressure support and infall of the gas while it conserves its specific angular momentum. As a result, a galactic disc starts to form from the inside out. While this problem set-up is axisymmetric, the simulation result is not axisymmetric due to the probabilistic star formation model that we will explain in the following.

The simulations follow a simplified model of star formation and instantaneous core-collapse SN feedback (Springel & Hernquist, 2003), in which regions above a critical threshold density are stochastically forming stars with an expectation value consistent with the observed Kennicutt (1998) law. CRs are instantaneously injected at the SNe, and obtain a fraction ζ_SN of the kinetic energy of the SN explosion. This implies that the CR energy gain of a cell with SFR $\dot{m}_\star$ is given by $\Delta E_\mathrm{CR} = \zeta_\mathrm{SN}\epsilon_\mathrm{SN}\dot{m}_\star\Delta t$, where $\epsilon_\mathrm{SN} = 10^{49}\,\mathrm{erg\,M}_\odot^{-1}$ is the released specific energy.

We adopt an initial seed magnetic field before collapse of the gas cloud of $B_0 = 10^{-10}\,\mathrm{G}$ and an injection efficiency of $\zeta_\mathrm{SN} = 0.05$ and 0.10. The injected CRs are advected with the gas, while adiabatic changes in the CR energy are taken into account. We also account for CR losses due to Coulomb interactions as well as hadronic losses as a consequence of inelastic collisions with the thermal ISM. Furthermore, we include anisotropic diffusion of CRs along the magnetic field, as described in Pakmor et al. (2016b) and adopt a parallel CR diffusion coefficient along the local magnetic field of $D = 10^{28}\,\mathrm{cm^2\,s^{-1}}$.[2] For halo masses of $10^{12}\,\mathrm{M}_\odot$, we adopt different values of the

[1] We enforce that the gas mass of all Voronoi cells remains within a factor of two of the target mass by explicitly refining and de-refining the mesh cells.

[2] This value is consistent with the recently discovered hardening of the logarithmic momentum slope of the CR proton spectrum at low Galactocentric radii, which is interpreted as a signature of anisotropic diffusion in the Galactic

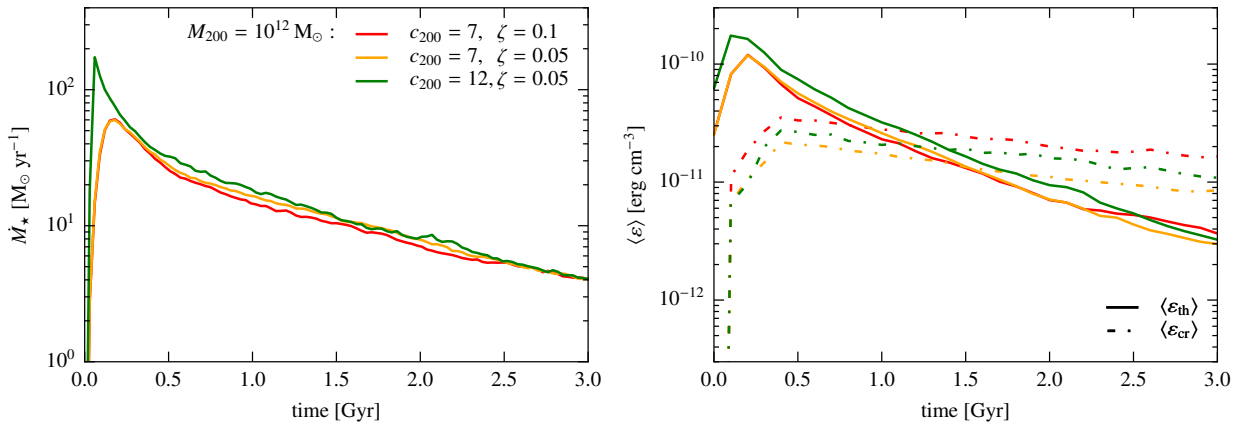

Figure 3.3: Time evolution of the SFR (left-hand panel) and the volume-averaged thermal and CR energy densities in a disk of radius 10 kpc and total height 1 kpc (right-hand panel) for our Milky Way-like galaxy with a halo mass of 10^{12} $M_\odot$. We vary halo concentration parameter $c_{200} = \{7, 12\}$ and CR energy acceleration efficiency $\zeta = \{0.05, 0.1\}$. Note that our fiducial galaxy is characterised by the combination $c_{200} = 7$ and $\zeta = 0.05$ (shown in yellow).

concentration parameter c_{200} for the dark matter halo.

Table 3.1 provides an overview of the different combinations of injection efficiency and concentration parameters that we use in our simulations of the 10^{12} $M_\odot$ halo, which we analyse here. We focus on this Milky Way-sized galaxy in this paper, whereas the smaller galaxies will be analysed in Paper II and Paper III. Figure 3.1 depicts a snapshot of the simulation with 10^{12} $M_\odot$ and $c_{200} = 7$ after $t = 1.1$ Gyr of evolution. The morphologies of the gas column density Σ and the SFR column density $\dot{\Sigma}_{\rm SFR}$, which are manifested by spiral structures, self-consistently determine the CR source distribution via our star formation model and hence give rise to a similar structure of the CR energy density. The CR pressure gradient was successful in driving an asymmetric outflow from the center that shows the largest SFR, which has evacuated underdense channels above and below the disc (visible in the column density map).

Despite the axisymmetric problem setup, we have seen that the emergent galactic winds are not symmetric with respect to the disc. In order to understand the reason for this asymmetric outflow morphology, we study the dependence of the CR distribution on various parameters in Fig. 3.2, which shows slices of the CR energy density. Prime among those parameter is i) the CR acceleration efficiency $\zeta_{\rm SN}$ that determines the amount of injected CR energy at SNe and hence

magnetic field (Cerri et al., 2017; Evoli et al., 2017). Using the flux of unstable secondary CR nuclei in recent AMS-02 data, which signals spallation processes in the ISM, the residence time of CRs inside the Galaxy can be constrained to yield identical values for the diffusion coefficient (Evoli et al., 2019, 2020a).

sets the CR gradient strength that is able to drive galactic winds and ii) the halo concentration c_{200} that determines the potential depth of the halo. Increasing values of c_{200} imply a larger density and hence a deeper dark matter potential. Indeed, Fig. 3.2 shows that larger values of c_{200} imply more compact discs and weaker outflows while larger values of $\zeta_{\rm SN}$ increase the outflow strengths. Hence, small changes in these parameters have large consequences on whether CRs can drive outflows in Milky Way-mass galaxies and shape the particular outflow morphologies. This is only possible because CR-driven winds are getting weaker towards the mass scale of Milky Way-mass galaxies (Uhlig et al., 2012; Jacob et al., 2018) so that the onset of a CR-driven wind represents an unstable phenomenon and critically depends on the acceleration strength (i.e., the CR gradient) and the gravitational attraction of the density of dark matter and the amount of stars, which increases with time and furthermore deepens the central potential. Hence, the asymmetry arises as an emergent phenomenon that is the result of the outflow taking the path of least resistance away from the galaxy, which may be blocked or obscured in one hemisphere of the galaxy.

Note that despite the different galactic outflow appearances and strengths, the global properties such as formed stellar mass or average thermal or CR energy are rather similar among these Milky Way-like models studied here. This is exemplified in Fig. 3.3 by analysing the SFRs (left-hand side) and volume-averaged thermal and CR energy densities in a disk of fixed radius and height for our three galaxies (right-hand side). The peak SFR increases by a factor of three when the halo concentration is increased from $c_{200} = 7$ to 12 due to the different compression upon the initial collapse, but this leaves little impact on the average thermal and CR energies. In particular, the latter quantity differs by approximately a factor of two, which exactly resembles the difference in energy injection efficiency at SNRs.

The time evolution of our simulations is exemplified in Figs. 3.4 and 3.5 for a simulation with $M_{200} = 10^{12}\,{\rm M}_\odot$, $c_{200} = 12$, $B_0 = 10^{-10}$ and $\zeta_{\rm SN} = 0.05$. In particular, maps of the gas density in Fig. 3.4 show the formation of a rotationally supported disc at a few hundred Myrs after the initial gas cloud has started to collapse. Because CRs are injected at remnants of SN explosions, they reside in the star-forming disc before they are transported through advection or diffusion. For the parameters chosen here, the CR pressure in the disc is sufficiently high after 600 Myrs in order to bend and open up the toroidal magnetic field, enabling them to diffuse into the halo and drive an outflow. Due to the decreasing SFR and hence decreasing CR injection rate, the CR gradient weakens over time and the outflow eventually dissolves another 300 Myrs later.

The initial collapse of the gas cloud results in a short starburst, followed by an exponentially declining SFR, see Figs. 3.3 and 3.5. Additionally in Fig. 3.5, we show the mean energy density of CR protons, primary and secondary electrons at different energies (10 GeV, 100 GeV and 1 TeV

respectively) as a function of time. They do not show any significant differences in the temporal evolution at the considered energies, but simply follow the evolution of the SFR. Here, we average over the radius, which includes 99 per cent of the hadronic gamma-ray emission, and the gas scale height h_ρ, where the gas density has dropped by an e-folding. The latter increases from $h_\rho = 0.13\,\mathrm{kpc}$ to $h_\rho = 0.83\,\mathrm{kpc}$ from $t = 0.1$ to $t = 2.3$ Gyr, before it approaches $h_\rho = 0.73\,\mathrm{kpc}$ at $t = 3$ Gyr. However, we note that our results do not depend on the specific choice of the averaging volume.

3.3 Cosmic ray modeling

For each snapshot of our simulations, we model the CR spectra in terms of a cell-based steady-state approximation, which assumes that the considered loss processes occur on a timescale shorter than the timescale of the total change in simulated CR energy density in each cell so that CR sources and losses balance each other.

3.3.1 Steady-state spectra

We separately solve three diffusion-loss equations (see e.g. Ginzburg & Syrovatskii, 1964; Torres, 2004) to obtain the equilibrium spectra for the spectral densities $f(E) = \mathrm{d}N/(\mathrm{d}E\,\mathrm{d}V)$, i.e. the number of particles per unit volume and unit energy, of CR protons, primary and secondary electrons, where E denotes the total particle energy. It assumes that the injection of CRs, given by the source term $q(E) = \mathrm{d}N/(\mathrm{d}E\,\mathrm{d}V\,\mathrm{d}t)$, the CR production rate per unit volume and unit energy, is balanced by cooling, i.e., energy losses $b(E) = -\mathrm{d}E/\mathrm{d}t$, and escape from the system. The latter includes advective and diffusive losses, which are combined in an energy-dependent escape timescale $\tau_\mathrm{esc} = 1/(\tau_\mathrm{adv}^{-1} + \tau_\mathrm{diff}^{-1})$. For each CR population, we solve the following equation

$$\frac{f(E)}{\tau_\mathrm{esc}} - \frac{\mathrm{d}}{\mathrm{d}E}\left[f(E)b(E)\right] = q(E), \tag{3.1}$$

which can be solved using the Green's function

$$G(E, E') = \frac{1}{b(E)} \exp\left(-\int_E^{E'} \mathrm{d}y \frac{1}{\tau_\mathrm{esc}(y)b(y)}\right). \tag{3.2}$$

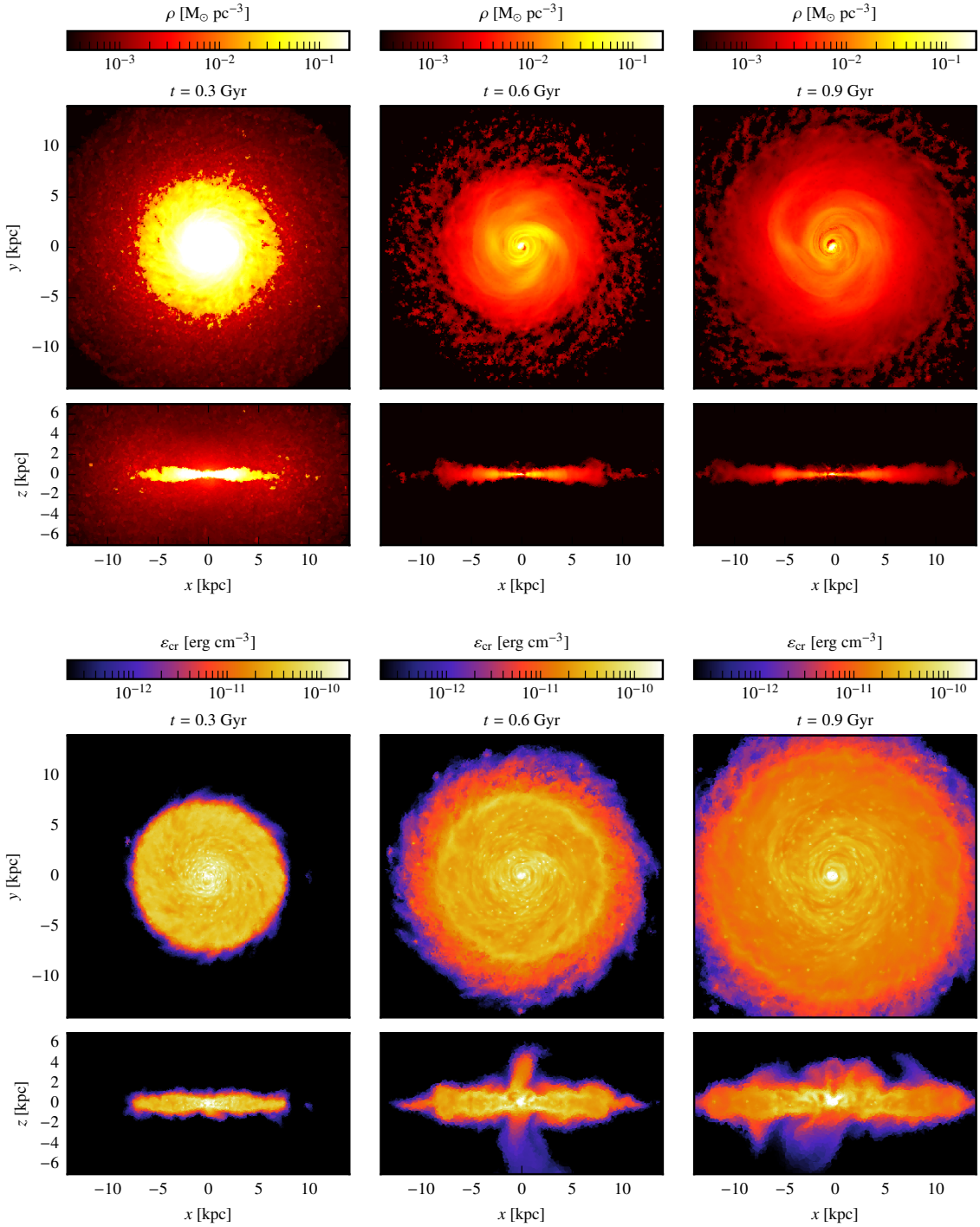

Figure 3.4: Temporal evolution of slices of the gas density ρ (top panels) and slices of the cosmic ray energy density $\varepsilon_{\mathrm{cr}}$ (bottom panels) for a galaxy with a halo mass of $M_{200} = 10^{12}\,\mathrm{M}_\odot$, concentration $c_{200} = 12$, initial magnetic field $B_0 = 10^{-10}\,\mathrm{G}$ and CR acceleration efficiency at SNe $\zeta_{\mathrm{SN}} = 0.05$. Each panel shows the face-on view on top of the edge-on view, respectively.

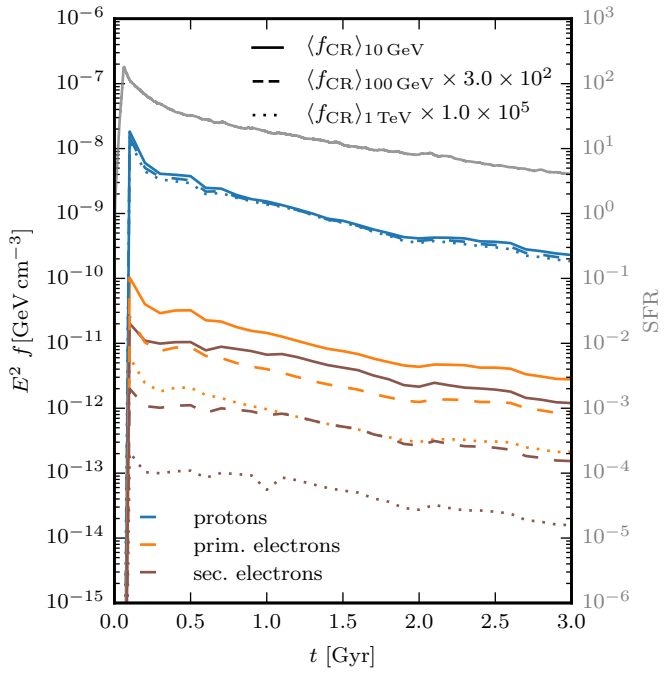

Figure 3.5: Evolution of the mean spectral energy density f of each CR species at 10 GeV, 100 GeV and 1 TeV over time for the simulation shown in Fig. 3.4. The spectra are averaged over the gas scale height and the radius which includes 99 per cent of the hadronic gamma-ray luminosity (see Paper II, for the calculation of the non-thermal emission processes). In addition, we show the SFR (grey line) as a function of time.

We obtain the steady-state distribution $f(E)$ in each cell from an injected source function of CRs, $q(E')$, by integrating over the initial energy E', i.e.,

$$f(E) = \int_E^\infty \mathrm{d}E' q(E') G(E, E'), \tag{3.3}$$

where $q(E) = q[p(E)]\mathrm{d}p/\mathrm{d}E$ and the injection spectra of CR electrons and protons are given in terms of a power-law in momentum,

$$q_i(p_i)\mathrm{d}p_i = C_i p_i^{-\alpha_{\mathrm{inj}}} \exp\left[-(p_i/p_{\mathrm{cut},i})^n\right]\mathrm{d}p_i, \tag{3.4}$$

where the normalised particle momentum is given by

$$p_i = \frac{P_i}{m_i c} = \sqrt{\left(\frac{E_i}{m_i c^2}\right)^2 - 1}, \tag{3.5}$$

the subscript $i = \mathrm{e}, \mathrm{p}$ denotes the CR species and $n = 1$ for protons and $n = 2$ for electrons (Zirakashvili & Aharonian, 2007; Blasi, 2010). The normalisation C_i is given in units of $\mathrm{s}^{-1}\,\mathrm{cm}^{-3}$. We assume that both protons and primary electrons share the same injection spectral index of $\alpha_{\mathrm{inj}} = 2.2$ (Lacki & Thompson, 2013) and assume cutoff momenta for protons, $p_{\mathrm{cut,p}} = 1\,\mathrm{PeV}/m_{\mathrm{p}}c^2$ (Gaisser, 1990), and electrons, $p_{\mathrm{cut,e}} = 20\,\mathrm{TeV}/m_{\mathrm{e}}c^2$ (Vink, 2012). While we inject CR protons at SNRs and transport their energy density with our MHD code (Pfrommer et al. 2017a, see also Section 3.2) the source term for the electrons is unspecified in our formalism and may include all relevant sources (SNRs, pulsar-wind nebulae, gamma-ray binaries). In principle, we could implement different source spectra for leptonic and hadronic CRs but leave the investigation of this degree of freedom to future work. In order to solve for the spectral energy distribution, in practice we discretise the spectrum in logarithmically equidistant momentum bins and integrate Eq. (3.2) for every momentum bin, before we perform the integration over the Green's function in Eq. (3.3) by using the trapezoidal rule.

Energy losses and timescales

The energy losses are evaluated locally in every cell, using the present physical properties of the cell. In order to separately solve Eq. (3.1) for CR protons and electrons, we have to consider the corresponding loss processes $b(E) = \dot{E}$ for each species.

The simulations already account for the CR proton losses. But in order to obtain a representation

of the spectral distribution of CRs, we assume a steady-state and solve the diffusion-loss equation for CR protons. This might give us a modified spectral index in comparison to the injection index $\alpha_{\rm p}$ if an energy-dependent loss process dominates the cooling. Finally, we re-normalise the steady-state distribution to the simulated CR energy density in each computational Voronoi cell. We consider the following energy-loss processes of CR protons.

Protons. CR protons lose energy due to (i) hadronic interactions with the ambient medium, which produce pions (Eq. 2.7) and (ii) through Coulomb interactions (Eq. 2.8), which heat the ISM. In order to avoid double-counting of adiabatic loss and gain processes we only account for this effect in our MHD simulations and neglect the spectral changes associated with this process. Modeling adiabatic spectral changes will require to follow the evolution of the spectral CR distribution in space and time in a galaxy simulation, which we postpone to future work (Girichidis et al., 2020b). Furthermore, we have to specify the characteristic timescale of losses due to escape. The residence time of CRs is determined by diffusion and advection, i.e.,

$$\tau_{\rm esc}^{-1} = \tau_{\rm diff}^{-1} + \tau_{\rm adv}^{-1}. \tag{3.6}$$

We estimate the diffusion timescale by

$$\tau_{\rm diff} = \frac{L_{\rm CR}^2}{D(E)} \propto E^{-0.5}, \tag{3.7}$$

with the energy-dependent diffusion coefficient $D(E) = D_0(E/E_0)^{0.5}$ as inferred from observed beryllium isotope ratios (Evoli et al., 2020a), where $D_0 = 10^{28}\,{\rm cm}^2\,{\rm s}^{-1}$, $E_0 = 3$ GeV, and we adopt the diffusion length in each cell, $L_{\rm CR} = \varepsilon_{\rm CR}/|\nabla\varepsilon_{\rm CR}|$. The characteristic timescale of advection is calculated as

$$\tau_{\rm adv} = \frac{L_{\rm CR}}{v_z}. \tag{3.8}$$

Assuming that in our cell-based steady-state approximation the azimuthal fluxes in and out of the cell compensate each other, we only take the velocity v_z of the cell in z-direction perpendicular to the disc into account for the estimation of the advection timescale. To justify this assumption, we show in Fig. 3.6 a map of the azimuthal velocity field v_ϕ in the disc that only varies smoothly on large scales. This is quantified by calculating the corresponding gradient map, $|\Delta v_\phi|_{\rm 2D}/v_\phi$. The latter visualises the small local relative deviations of the azimuthal velocity field, which are less

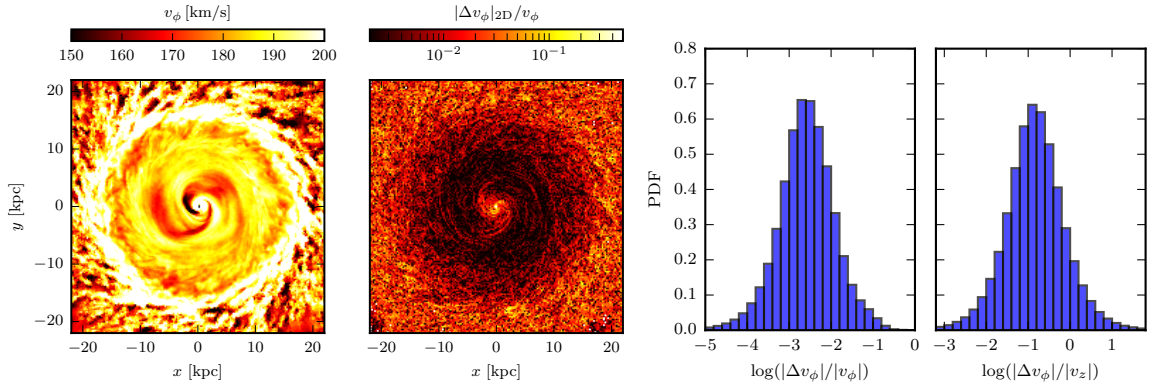

Figure 3.6: Face-on map of the azimuthal velocities v_ϕ within the disk of our fiducial galaxy at $t = 1.1$ Gyr (left-hand panel). The second panel shows the corresponding gradient map, where we multiply the absolute value of the gradient with the resolution of the 2D-map in order to obtain $|\Delta v_\phi|_{2D} = |\nabla v_\phi|\Delta x$. In addition, the two right-hand panels show histograms of the azimuthal velocity difference of each cell relative to the mean velocity of its neighbouring cells in three dimensions, $|\Delta v_\phi| = |v_\phi - \langle v_\phi \rangle_{\text{neighbours}}|$ relative to the absolute values of the azimuthal velocity ($|v_\phi|$, third panel) and vertical velocity, respectively ($|v_z|$, forth panel); see text for details.

than 10^{-2} for radii $r \lesssim 15$ kpc. Because this measure weakly depends on the plotting resolution, we complement this study by computing the azimuthal velocity difference of every cell to the mean of its neighboring cells in three dimensions. To this end, we construct a histogram of the difference $|\Delta v_\phi| = |v_\phi - \langle v_\phi \rangle_{\text{neighbours}}|$, which we normalise by $|v_\phi|$ and $|v_z|$, respectively (two right-hand panels in Fig. 3.6). Here, $\langle v_\phi \rangle_{\text{neighbours}}$ denotes the mean azimuthal velocity of the neighbouring cells within twice the radius of the cell. This histogram shows that the velocity of a computational Voronoi cell does not differ significantly from the mean azimuthal velocity value of the adjacent cells. On average, the deviation is of order $\sim 3 \times 10^{-3}$ times smaller than the azimuthal velocity of the cell itself. Similarly, $|\Delta v_\phi|$ typically amounts to 10 per cent of $|v_z|$, and the azimuthal velocity difference is below the absolute value of the vertical velocity in most cells ($|\Delta v_\phi| < |v_z|$) except for a small subset of cells at spiral density waves. Hence, this statistically justifies our assumption underlying Eq. (3.8).

Note that radial CR transport via advection and anisotropic diffusion is also strongly suppressed because of the largely toroidal magnetic field configuration in the disc (Pakmor & Springel, 2013; Pakmor et al., 2016c) and because circular rotation dominates the kinetic energy density (Pfrommer et al., 2021). Any residual CR fluxes not explicitly modeled in our steady-state approach need to be simulated by evolving the CR electron and proton spectra in our MHD simulations (Winner et al., 2019, 2020; Girichidis et al., 2020b).

Electrons. High-energy CR electrons lose mainly their energy via radiation processes. CR electrons with Lorentz factor γ_e and normalised velocity $\beta_\mathrm{e} = v_\mathrm{e}/c$ suffer synchrotron and IC losses at rates given by (see e.g. Blumenthal & Gould, 1970)

$$b_\mathrm{syn} = \frac{4}{3}\sigma_\mathrm{T} c \beta_\mathrm{e}^2 \gamma_\mathrm{e}^2 \varepsilon_B, \tag{3.9}$$

and

$$b_\mathrm{IC} = \frac{4}{3}\sigma_\mathrm{T} c \beta_\mathrm{e}^2 \gamma_\mathrm{e}^2 \varepsilon_\mathrm{ph}, \tag{3.10}$$

where $\varepsilon_B = B^2/(8\pi)$ is the magnetic energy density, B is the root-mean square magnetic field, and we assume the Thomson-limit for IC scattering, which holds if $\gamma_\mathrm{e} h\nu \ll m_\mathrm{e} c^2$, where ν is the frequency of the incoming photon. The photon energy density ε_ph includes photons from the CMB as well as stellar radiation. To account for the latter, we assume that the UV light emitted by young stellar populations is re-emitted in the FIR so that we are able to infer the FIR luminosity of each cell from its current SFR, where we adopt the relation obtained by Kennicutt (1998):

$$\frac{\mathrm{SFR}}{M_\odot\,\mathrm{yr}^{-1}} = \epsilon\, 4.5 \times 10^{-44} \frac{L_\mathrm{FIR}}{\mathrm{erg\,s}^{-1}} = \epsilon\, 1.7 \times 10^{-10} \frac{L_\mathrm{FIR}}{L_\odot}. \tag{3.11}$$

The parameter $\epsilon = 0.79$ follows from assuming a Chabrier (2003) initial mass function (Crain et al., 2010), yielding

$$\frac{L_\mathrm{FIR}}{L_\odot} = 7.4 \times 10^9 \frac{\mathrm{SFR}}{M_\odot\,\mathrm{yr}^{-1}}. \tag{3.12}$$

We assume a Planck distribution corresponding to the FIR regime, i.e. wavelengths ranging from $8 - 1000\,\mu\mathrm{m}$ with a typical warm dust temperature of $\sim 20\,\mathrm{K}$ (Calzetti et al., 2000). The evaluation of the energy loss rate in each cell is then performed by summing over the flux arriving from all other cells i with $\mathrm{SFR} > 0$ at a distance R_i, i.e.

$$\varepsilon_\star = \sum_i \frac{L_\mathrm{FIR}}{4\pi R_i^2 c} \tag{3.13}$$

and use $R_i = [3V_i/(4\pi)]^{1/3}$ as the distance if the considered cell is actively star forming, where V_i denotes the cell's volume. Because the computational cost of this sum would otherwise be proportional to the square of the cell number, we accelerate its computation with a tree code. We use $\varepsilon_\star$ as the incident radiation field in Eq. (3.10), together with the CMB, i.e., $\varepsilon_\mathrm{ph} = \varepsilon_\star + \varepsilon_\mathrm{CMB}$. For these assumptions, the effect of the Klein-Nishina suppression of the IC emission is expected to

be negligible because it is only relevant if the energy of the incoming photon becomes comparable to the electron rest mass. In the rest frame of the electron this amounts to $\gamma_e h\nu \simeq m_e c^2$. For IR photons ($h\nu \approx 10^{-2}$ eV), the Klein-Nishina suppression would thus only become relevant above $\gamma_e \approx 5 \times 10^7$ (or $E_e \sim 25$ TeV). Because this is larger than the cut-off in the primary electron spectrum, Klein-Nishina effects can only become relevant for secondary electrons, which can also be produced at higher energies. Additionally, including UV radiation for the incoming photon field, with typical temperatures around 10^4 K (or $h\nu \approx 2.4$ eV) would become relevant for electrons with $\gamma_e \approx 2 \times 10^5$ (or $E_e \sim 100$ GeV) and could change the detailed shape of the electron spectrum, as recently pointed out by Evoli et al. (2020b).

Third, for losses due to bremsstrahlung emission, we assume a fully ionized medium (see Eq. 2.11). Besides the energy loss processes that lead to the emission of photons, Coulomb interactions with the ambient medium have to be taken into account (see Eq. 2.13). They typically affect the low-energy part of the electron spectrum.

The discussed energy loss processes for CR electrons occur on characteristic timescales

$$\tau_{\rm loss} = \frac{E}{b_i(E)}, \tag{3.14}$$

where b_i denotes the various CR electron cooling rates. They allow us to determine the importance of each energy loss process for a given energy. In Fig. 3.7 we analyse our fiducial galaxy with a halo mass of 10^{12} $M_\odot$ at $t = 1.1$ Gyr (i.e., identical to the simulations shown in Fig. 3.1) and show maps of the ratio of different cooling timescales at an energy of $E = 10$ GeV, averaged over a thin slice around the mid-plane of the disc with a thickness of 500 pc. The total electron cooling timescale τ_e, which includes all electron cooling processes as discussed above, is shortest in the central kpc in the disc and increases outwards up to cooling times $\tau_e \sim 100$ Myr. Figure 3.7 shows that synchrotron losses of electrons only dominate in the very central regions, where the magnetic field is strongest. Otherwise, losses due to IC scattering occur on the shortest timescale in the disc and a few kpc above it, before escape processes take over and dominate over radiative losses.

In the case of CR protons, the shortest timescale within the disc is the hadronic timescale because of its dependence on gas density. It is acting on typical timescales of a few tens to a few hundred Myrs. In regions of lower gas density, in the vicinity of SNRs and in outflows, escape processes are faster than hadronic interactions. Comparing the two escape losses considered here, we find that losses due to advection are predominantly occurring within the outflow, where v_z is large and therefore $\tau_{\rm adv} < \tau_{\rm diff}$, while diffusion dominates elsewhere. Due to their energy dependence, we expect diffusion losses to gain importance at higher proton energies.

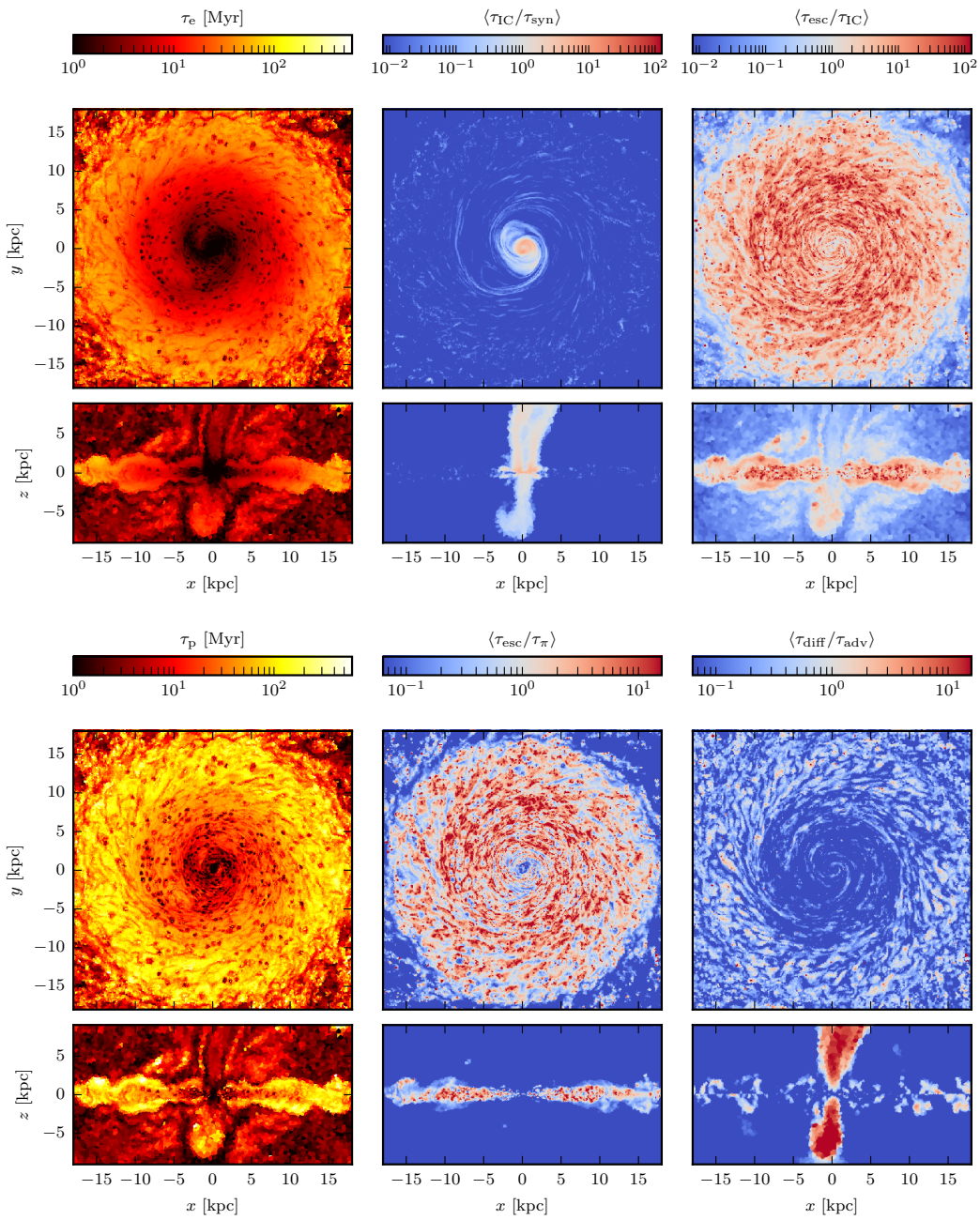

Figure 3.7: We show maps of characteristic timescales and their ratios at an energy of 10 GeV for our fiducial galaxy at a simulation time of 1.1 Gyr. The upper panels show the total electron cooling timescale τ_e (left), that includes all cooling processes. The middle and right panels show the IC-to-synchrotron cooling time and escape-to-IC cooling time. The lower panels show maps of the total cooling timescale of protons τ_p (left), the time scale ratios of escape-to-hadronic cooling (middle) and of diffusion-to-advection losses (right). All ratios are averaged over slices with a thickness of 500pc.

Normalisation of the CR spectra and the determination of $K_{\rm ep}^{\rm inj}$

After solving the spectral transport equation for CR protons and electrons (Eq. 3.3) in each Voronoi cell of our MHD simulation, we need to re-normalise the resulting steady-state spectra. The steady-state CR proton spectrum can be re-normalised to reproduce the simulated CR energy density in each cell. However, to obtain the correct normalisation of the primary electron spectrum, we need a relation between the source functions of primary electrons and protons, which we can apply in each cell. To this end, we normalise the simulated electron spectrum of a Milky Way-like galaxy, averaged around the solar galactocentric radius[3] to the observed electron-to-proton ratio at a kinetic energy of 10 GeV, which is given by $K_{\rm ep}^{\rm obs} = 10^{-2}$ (Cummings et al., 2016). We use this information to infer the corresponding injection spectrum of primary electrons, $Q_{\rm e}^{\rm prim}$, and the injection ratio $K_{\rm ep}^{\rm inj}$.

In this way, we obtain a ratio of injected electrons to protons in each cell. By construction, the mean of this distribution averaged around the Solar circle reproduces the observed value of the electron-to-proton ratio after taking into account all cooling processes. Naturally, for a specific value of $K_{\rm ep}^{\rm obs}$, we will thus get a distribution of injection ratios, $K_{\rm ep}^{\rm inj}$. The individual steps of this procedure are explained in detail in Appendix 3.6.

Assuming that this injection ratio is universal, we can then apply it to the remaining part of the galaxy and to other simulated galaxies with different masses. Note that conceptually, in this framework, injection relates to effective injection $q(E)$ into a computational Voronoi cell and should not be confused with instantaneous CR injection at an individual SNR. Therefore, we do not aim to reproduce observed ratios at SNRs with our resulting value for $K_{\rm ep}^{\rm inj}$.

In order to quantify this dispersion of $K_{\rm ep}^{\rm inj}$ in our simulated galaxy, we use Eq. (3.34), where we only consider CR spectra in a galacto-centric ring at the solar radius and re-normalise the proton injection function $q_{\rm p}$ to the CR energy density in each cell (see Eq. 3.26) and the primary electron injection function $q_{\rm e}^{\rm prim}$ to the observed value $K_{\rm ep}^{\rm obs}$ (see Eq. 3.32). Figure 3.8 shows a histogram of $K_{\rm ep}^{\rm inj}$, around the solar radius with $5\,{\rm kpc} < r < 11\,{\rm kpc}$ and $h < 1\,{\rm kpc}$, for two snapshots at 4 and 5 Gyr that exhibit global SFRs of $2.4\,{\rm M_\odot\,yr^{-1}}$ and $1.7\,{\rm M_\odot\,yr^{-1}}$, respectively. Hence, their SFRs are comparable to the observationally inferred galactic value of $1.9\,{\rm M_\odot\,yr^{-1}}$ (Chomiuk & Povich, 2011). Despite the rather short electron cooling timescales, we obtain a narrow distribution in $K_{\rm ep}^{\rm inj}$ with mean $\langle K_{\rm ep}^{\rm inj}\rangle \approx 0.02$ in both snapshots and apply this value to all evolutionary states of our simulated galaxies.[4] This enables us to obtain the normalisation of the primary electron spectrum

[3] In practice, we average over a torus-shaped region defined by $5\,{\rm kpc} < r < 11\,{\rm kpc}$ and $h < 1\,{\rm kpc}$ at 5 Gyr.

[4] We confirmed that this result is robust to variations of these parameters: the mean $\langle K_{\rm ep}^{\rm inj}\rangle$ varies from 0.017 to 0.024 if we average over $8\,{\rm kpc} \pm \Delta r$ with Δr ranging from 1 to 3 and h from 0.5 to 5 kpc.

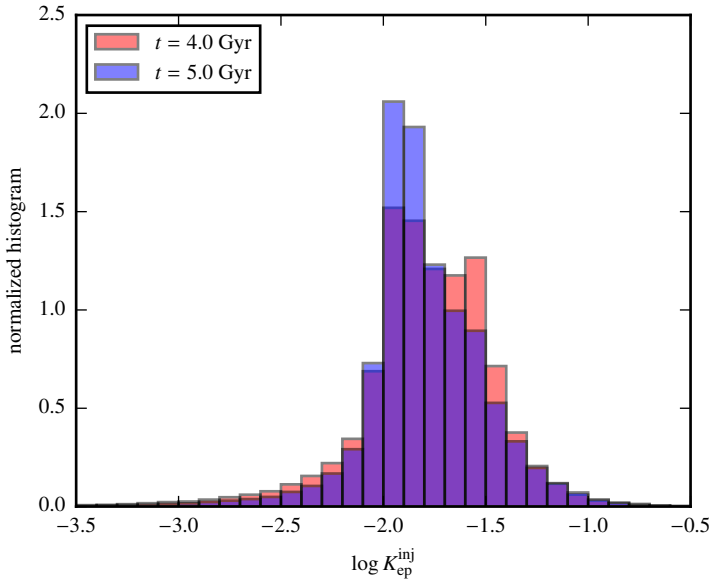

Figure 3.8: Histogram of the electron-to-proton injection ratio K_{ep}^{inj} for our fiducial galaxy with a halo mass of $10^{12}\,M_\odot$ at two times (indicated in the legend) so that the simulated SFRs at these times are both consistent with the Milky-Way value.

in other galaxies or outside the solar circle.

Applicability of the steady-state assumption

In order to scrutinise our steady-state assumption and identify its caveats, we compare the change of total CR energy density in each simulation cell over a global timestep (of 0.76 Myrs) and infer a corresponding timescale $\tau_{CR} = \varepsilon_{CR}/\dot{\varepsilon}_{CR}$, i.e., the characteristic timescale of the change in total energy density of CRs. The purpose of τ_{CR} is to provide an instantaneous time-scale (consistent with the numerical discretisation of the time integration used in the simulation) on which we report the relative change in CR proton energy density. Changes in this quantity on longer time intervals would probe CR evolution and would not represent instantaneous changes. On smaller time intervals, the hydrodynamic quantities would not represent a consistent state for Voronoi cells on the largest timesteps by construction. All cooling processes in the diffusion-loss equation should be of the same order or faster than that timescale, such that a steady state can be maintained, i.e., $\tau_{all} \lesssim \tau_{CR}$. Here, τ_{all} is the combined rate of all relevant cooling processes at a given energy and the diffusion loss rate, i.e., $\tau_{all}^{-1} = \tau_{cool}^{-1} + \tau_{diff}^{-1}$. As demonstrated in Fig. 3.7, the advection time-scale is larger than the diffusion time-scale with the exception of CR-driven galactic outflows. Thus, this

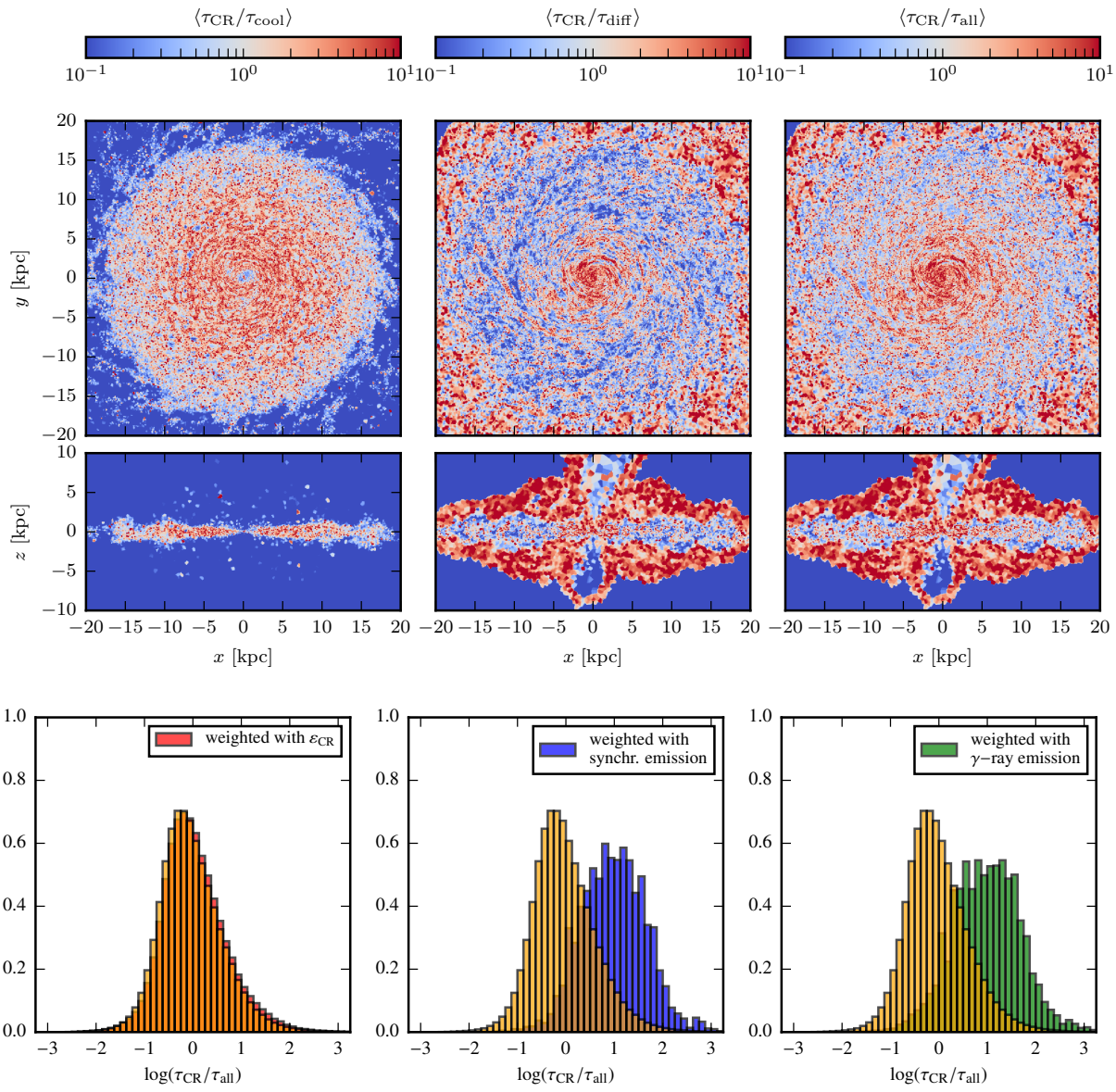

Figure 3.9: Face-on (top three panels) and edge-on (middle three panels) projections through a thin slice (0.5 kpc) of the ratio of the timescale of the change in total CR energy density $\tau_{\rm CR}$ to the CR cooling time (left), to the CR diffusion time (middle), and to the combined timescale of losses $\tau_{\rm all}$ (right) for our fiducial galaxy. Bottom panels: mass-weighted histograms of the cooling time ratio $\tau_{\rm CR}/\tau_{\rm all}$ (yellow), weighted with the CR energy density (left panel, red), the synchrotron emission (middle panel, blue) and the gamma-ray emission (right panel, green) of each cell.

justifies our neglect of considering the advection process in $\tau_{\rm all}$.

In Fig. 3.9 we show the ratio of these timescales at 10 GeV. The upper panel shows maps centered on the mid-plane of the disc, in which we average over slices with a thickness of 500 pc. We obtain $\tau_{\rm all} \lesssim \tau_{\rm CR}$, the condition for a steady-state, predominantly inside the disc. This is owing to the short hadronic timescales in regions of high gas density in combination with large diffusive losses in the central region. Still, there remain some areas, where the steady-state assumption breaks down. This occurs either in regions of low gas density, where hadronic losses are weak, and/or in the vicinity of SN explosions, where CRs are freshly injected, leading to a sudden change in the CR energy density and disturbing the steady-state configuration.

Nevertheless, the cells contributing predominantly to non-thermal emission processes respect the steady-state assumptions. This can be deduced from the lower panels of Fig. 3.9, where we show normalised histograms of the ratios $\tau_{\rm CR}/\tau_{\rm all}$ of all cells, weighted with the CR-energy density (left-hand panel), the synchrotron emission (middle panel) and the hadronic γ-ray emission resulting from neutral pion decay (right-hand panel), see Paper II and Paper III for the description of the emission processes. Clearly, weighting the timescale ratios by the non-thermal emission of each cell, either synchrotron or hadronic gamma-ray emission, leads to a shift in the ratios $\tau_{\rm CR}/\tau_{\rm all}$ towards higher values, indicating that the steady-state assumption is justified in cells that dominate the non-thermal emission. Yet, there is a non-negligible fraction of cells that do not obey the steady-state criterion and demand a more sophisticated treatment of the time evolution of CR spectra in three-dimensional MHD simulations, which we will examine in future work using new algorithms to follow CR electron and proton spectra (Winner et al., 2019; Girichidis et al., 2020b; Ogrodnik et al., 2021).

3.3.2 Secondary electrons and positrons

In addition to primary CR electrons that are accelerated at sources such as SNRs, pulsar-wind nebulae, or gamma-ray binaries, CR electrons can also be produced in inelastic collisions of CR protons with protons and other nuclei in the ambient ISM. Such hadronic reactions produce charged pions that decay into secondary electrons (and neutrinos) and the neutral pions into γ-rays.

For the calculation of the production spectrum of secondary electrons and positrons, parametrizations of the cross sections of pion production are required. In the following, we adopt the model by Yang et al. (2018b) for the low energy range $T_{\rm p} < 10\,{\rm GeV}$ (see equations 3.37, 3.38 and 3.41), the description by Kelner et al. (2006) for $T_{\rm p} > 100\,{\rm GeV}$ (see Eq. 3.42) and a cubic spline interpolation in between. We describe the calculation of the production spectrum of secondary particles in

Appendix 3.7.1 in more detail. Furthermore, we provide our own parametrization of the total cross section of charged pion production at low proton energies in Appendix 3.7.2. We compare our approach to an analytical approximation in Appendix 3.7.3, that will be useful in the following Section.

3.3.3 Ratio of primary to secondary electrons

To complement the numerical analysis of our work, we derive here an analytical approximation for the ratio of secondary electrons and positrons to primary electrons which helps to understand the physics underlying our simulation results. For simplicity, we assume that the injection spectral indices of CR electrons and protons are identical. Our analytical insight can be used to determine the relevance of each population to CR observables and quantify each contribution to the non-thermal emission, and eventually compare it to simulations. The steady-state spectrum after taking into account all cooling losses resulting from a source function q is approximately given by

$$f_{\mathrm{e/p}} = q_{\mathrm{e/p}}\,\tau_{\mathrm{e/p}}, \tag{3.15}$$

where $\tau_{\mathrm{e/p}}^{-1} = \tau_{\mathrm{esc}}^{-1} + \tau_{\mathrm{loss,e/p}}^{-1}$ and this equation is valid for protons, primary and secondary electrons in this analytical approximation. Furthermore, the spectrum of secondary particles (before undergoing cooling processes) is connected to the source function of secondary particles via

$$f_{\mathrm{e^{\pm},uncooled}}^{\mathrm{sec}} = q_{\mathrm{e^{\pm}}}^{\mathrm{sec}}\,\tau_{\pi}, \tag{3.16}$$

where τ_{π} is the characteristic timescale of pion production or hadronic interactions of CRs with the ISM (Eq. 3.54). Therefore, the steady-state spectrum of secondary electrons/positrons is given by

$$f_{\mathrm{e^{\pm}}}^{\mathrm{sec}} = q_{\mathrm{e^{\pm}}}^{\mathrm{sec}}\,\tau_{\mathrm{e}} = \frac{f_{\mathrm{e^{\pm},uncooled}}^{\mathrm{sec}}}{\tau_{\pi}}\,\tau_{\mathrm{e}}. \tag{3.17}$$

Consequently, the ratio of primary to secondary electrons can be expressed as

$$\frac{f_{\mathrm{e}}^{\mathrm{prim}}}{f_{\mathrm{e}}^{\mathrm{sec}}} = \frac{f_{\mathrm{e}}^{\mathrm{prim}}}{2 f_{\mathrm{e^{\pm},uncooled}}^{\mathrm{sec}}}\,\frac{\tau_{\pi}}{\tau_{\mathrm{e}}}, \tag{3.18}$$

where $f_{\mathrm{e}}^{\mathrm{sec}} = f_{\mathrm{e^{+}}}^{\mathrm{sec}} + f_{\mathrm{e^{-}}}^{\mathrm{sec}}$ is the total steady-state distribution of secondary electrons and positrons. Adopting the analytical approximation for $f_{\mathrm{e,uncooled}}^{\mathrm{sec}}/f_{\mathrm{p}}$ (Eq. 3.55) at a fixed physical momentum

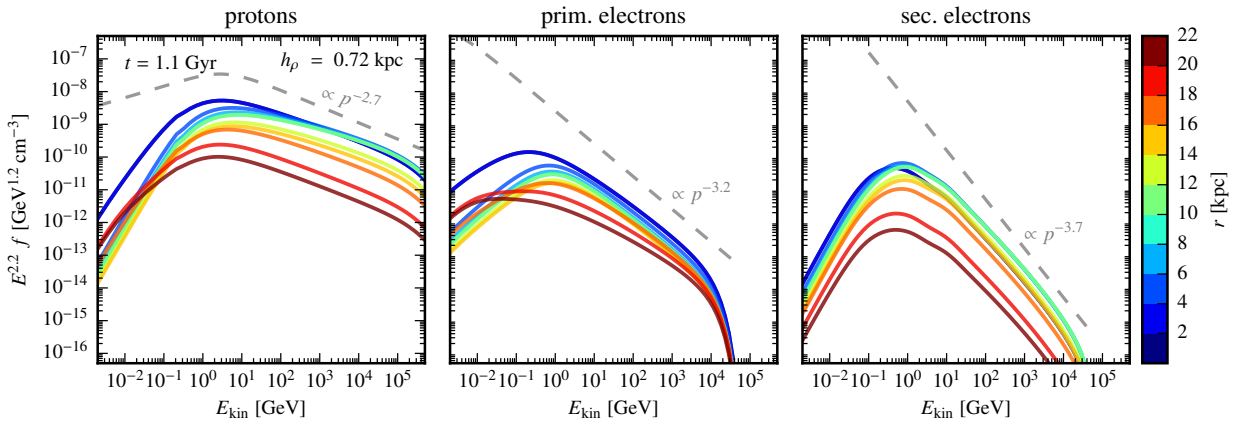

Figure 3.10: We show CR spectra of the different components (indicated in the titles) in radial bins as indicated by the colorbar of a simulation with halo mass $M_{200} = 10^{12}\,\mathrm{M}_\odot$, $c_{200} = 7$ and CR acceleration efficiency $\zeta_{\mathrm{SN}} = 0.05$ at 1.1 Gyr.

P_0, we get:

$$\frac{f^{\mathrm{sec}}_{\mathrm{e,uncooled}}[P_0/(m_\mathrm{e}c)]}{f_\mathrm{p}[P_0/(m_\mathrm{p}c)]} \simeq \frac{128}{3} 16^{-\alpha_\mathrm{p}} \frac{m_\mathrm{e}}{m_\mathrm{p}}. \tag{3.19}$$

Combining Eqs. (3.15), (3.18), and (3.19) and evaluating the spectra at 10 GeV, such that the primary electron and proton source functions are linked by $K^{\mathrm{inj}}_{\mathrm{ep}}$ (see Eq. 3.33), yields

$$\frac{f^{\mathrm{prim}}_\mathrm{e}}{f^{\mathrm{sec}}_\mathrm{e}} = K^{\mathrm{inj}}_{\mathrm{ep}} \frac{3}{128} 16^{\alpha_\mathrm{p}} \frac{\tau_\pi}{\tau_\mathrm{p}} \tag{3.20}$$

$$= K^{\mathrm{inj}}_{\mathrm{ep}} \frac{3}{128} 16^{\alpha_\mathrm{p}} \left(1 + \frac{\tau_\pi}{\tau_{\mathrm{esc}}}\right) \tag{3.21}$$

$$\approx 0.48 \left(1 + \frac{\tau_\pi}{\tau_{\mathrm{esc}}}\right) \quad \text{for} \quad \alpha_\mathrm{p} = 2.5 \tag{3.22}$$

and $K^{\mathrm{inj}}_{\mathrm{ep}} \approx 0.02$. Here, we assume that losses due to Coulomb interactions are negligible in comparison to hadronic losses, which is reasonable at and above the considered energies.

This implies in the fully calorimetric limit, where hadronic losses dominate over escape losses, i.e., $\tau_\pi \ll \tau_{\mathrm{esc}}$ (which is the case in the dense ISM, see Fig. 3.7), that the ratio of primary to secondary electrons depends only on $K^{\mathrm{inj}}_{\mathrm{ep}}$ and the spectral index of the cooled proton spectrum α_p. In particular, we find that in this limit, secondary electrons dominate above the primary electron

population. On the other hand, primary electrons dominate over secondary electrons as soon as escape losses are comparable to or larger than pionic losses, i.e., $\tau_\pi \gtrsim \tau_{\rm esc}$. In particular, as soon as (energy dependent) diffusive losses are important and steepen the proton spectra, the resulting secondary electron spectrum will be steeper than the primary one and hence, the ratio of secondaries to primaries will decrease at higher energies.

3.4 Results

3.4.1 CR spectra and maps

In order to obtain a representative spectrum of a certain region of our simulated galaxies, we average over our cell-based steady-state spectra. In Fig. 3.10 we show the CR proton spectra of our fiducial galaxy, as well as primary and secondary electrons averaged over galacto-centric rings with different radii as indicated by the colors. The height over which the spectra are averaged is the scale height of the gas density, which in this case is $h_\rho = 0.72\,\mathrm{kpc}$.

We assume an injection spectral index of $\alpha_{\rm inj} = 2.2$ for protons and electrons. Energy-dependent diffusion dominates CR transport at high energies. With our assumed diffusion coefficient $D \propto E_{\rm p}^{0.5}$, the *proton spectra* soften to an asymptotic spectral index of $\alpha_{\rm p} = 2.7$ (shown with a grey-dashed line in the left-hand panel of Fig. 3.10, where the spectral change at 1 GeV is due to the relativistic dispersion relation). While this asymptotic spectrum is realised at small and large galactic radii, it is not achieved at intermediate galactocentric radii. The dominant loss process of protons at low energies is Coulomb cooling that causes the spectra to turn down in comparison to a pure momentum power-law spectrum shown with a grey-dashed line in Fig. 3.10. This effect of Coulomb cooling below $\sim 1\,\mathrm{GeV}$ becomes more pronounced towards the denser central regions as evidenced by the stronger spectral cutoff.

While Coulomb interactions similarly affect the spectrum of *primary electrons* at energies $\lesssim 1$ GeV, diffusion plays a subdominant role in the central galactic regions at high energies where radiative losses due to synchrotron and IC interactions dominate. This causes the injection spectral index to steepen by one, to asymptotically arrive at the steady-state electron spectrum

$$f_{\rm e}^{\rm prim}(E_{\rm e}) \propto \frac{1}{b_{\rm IC} + b_{\rm syn}} \int_0^{E_{\rm e}} q_{\rm e}^{\rm prim}(E')\mathrm{d}E' \propto E_{\rm e}^{-(\alpha_{\rm inj}+1)}. \tag{3.23}$$

However, in contrast to CR protons, which only show mild spectral index variations with radius at energies larger than $\sim 10\,\mathrm{GeV}$ (see left-hand panel of Fig. 3.10), the primary electrons undergo

a change from the radiative loss-dominated regime in the centre to a more diffusion dominated regime in the outskirts of the galaxy which implies a hardening of the spectra by 0.5, yielding a spectral index of primary electrons $\alpha_{\rm prim,e} = 2.7$ (see middle panel of Fig. 3.10).

By contrast, $\alpha_{\rm sec,e}$, the spectral index of *secondary electrons*, is $\gtrsim \alpha_{\rm prim,\,e}$ because they originate from the steady-state CR proton population, which exhibits a steepened spectral index due to diffusive losses. After suffering radiative losses the high-energy spectral index of a steady-state secondary electron population asymptotically approaches $\alpha_{\rm sec,\,e} = 3.7$, independent of galactocentric radius (right-hand panel of Fig. 3.10).

We also show maps of the CR spectra at 10 GeV in the upper panels of Fig. 3.11, averaged over thin slices of 300 pc. Similarly, the lower panels in Fig. 3.11 show averages over 300 pc of the spectral index at 10 GeV of the different CR populations. We only consider cells that sum up to 99 per cent of the total energy density of the simulations in order to speed up the calculations.[5] Whereas the primary CR electrons reside in the same spatial regions as the CR protons, the secondary CR electron population is more concentrated towards the disc, where the gas density is large enough to yield a sufficiently large hadronic production rate. As expected, these regions coincide with those of short hadronic timescales shown in Fig. 3.7.

The spectral index analysis is performed at 10 GeV mainly for observational reasons: (i) hadronic interactions of 10 GeV protons produce $\sim$ 1 GeV photons resulting from the decay of neutral pions that are well observed by *Fermi* and (ii) because this is the typical electron momentum that contributes to the synchrotron radiation that is observed at 1.4 GHz, assuming typical magnetic field strengths of $\sim$ 1 μG. Figure 3.11 shows little variation in the proton spectral index which would translate into little variation of the gamma ray spectral index provided the pion decay is the dominant gamma-ray channel. We also observe a similar contribution of primary and secondary electrons in the galactic mid-plane implying an insignificant contribution of secondaries at higher energies because of their steeper spectra.

Moreover, secondary electrons show a more compact spatial distribution surrounding the mid-plane. Considering the more extended magnetic field distribution, we expect the primary synchrotron emission to match the secondary emission in the mid plane and to dominate over the secondary emission at higher frequencies and larger galactic heights. Similar arguments hold for the IC emission. For an incident radiation field that peaks at FIR frequency corresponding to a Planckian photon spectrum characterised by temperature 20 K, electrons with $p_{\rm e} \sim 10\,{\rm GeV}/(m_{\rm e}c^2)$ are able to Compton up-scatter these photons to $\sim$10 MeV, where we expect a similar contribution of secondaries in the mid-plane, but a subdominant contribution elsewhere because the radiation

[5]This includes all cells within the disc that are relevant for our results.

field is usually also more extended than the gas distribution. The spectral index of different CR species at 10 GeV (lower panels in Fig. 3.11) clearly show that the advection timescale dominates in the outflow regions (see also Fig. 3.7) so that the spectral index of protons and primary electrons reflects the index of the injected spectrum, $\alpha_{\rm inj} = 2.2$.

These considerations are summarised in Fig. 3.12 that demonstrates that the ratio of primary to secondary electrons is $\gtrsim 1$ so that primaries are dominant for most parts of the galaxy. Only within the disc where the gas density is high, secondary electrons are roughly three times more abundant than primary electrons at 10 GeV. This is in accordance with Eq. (3.21): using $K_{\rm ep}^{\rm inj} = 0.02$, $\alpha_{\rm p} = 2.2$ and assuming that $\tau_\pi \ll \tau_{\rm esc}$ ($\tau_\pi \simeq \tau_{\rm esc}$), which is required in order to produce secondaries efficiently, we obtain for the ratio in the analytical approximation $f_{\rm e}^{\rm prim}/f_{\rm e}^{\rm sec} \approx 0.2$ (0.4). A steeper spectral index of the cooled proton spectrum $\alpha_{\rm p} > 2.2$ would decrease the production rate of secondaries, which can be inferred both from our expression in Eq. (3.21) and from the fact that a steeper spectral index signals a dominant role of energy dependent diffusion losses in comparison to hadronic losses, making secondary production less efficient. Hence, at higher energies, the importance of primary versus secondary electrons decreases further (see middle and right-hand panel of Fig. 3.12).

3.4.2 Comparison to observations

Proton and electron spectra

Since crossing the heliopause in August 2012, Voyager 1 has been observing CRs in the local interstellar medium at energies below ~1 GeV, which are not subject to solar modulation effects (Cummings et al., 2016). Complementary, AMS-02 observed CR spectra at larger energies (Aguilar et al., 2014a, 2015). We see that CR proton spectra are affected by solar modulation at energies $\lesssim 10$ GeV (Potgieter, 2013).

In Fig. 3.13 we show both sets of observational data together with our spectra of CR protons and electrons of a Milky Way-mass galaxy ($M_{200} = 10^{12}\,{\rm M}_\odot$) at 5 Gyr, averaged over a ring at $r = 8 \pm 1$kpc to mimic the conditions of the galactocentric orbit of the Sun, and different heights above and below the midplane, i.e. $\pm h$, as indicated in the plot. We normalise our spectra to the observations at 10 GeV, which are unaffected by solar modulation (for details, see Table 3.2). This accounts for differences to the recent star formation history of our simulations and the Milky Way, which determines the CR injection rate and the fact that the Milky Way is under-luminous in gamma rays in comparison to the far infrared-gamma-ray relation by a factor 2.9 (using the relation of Ajello et al. 2020, but see also Ackermann et al. 2012b; Rojas-Bravo & Araya 2016; Pfrommer

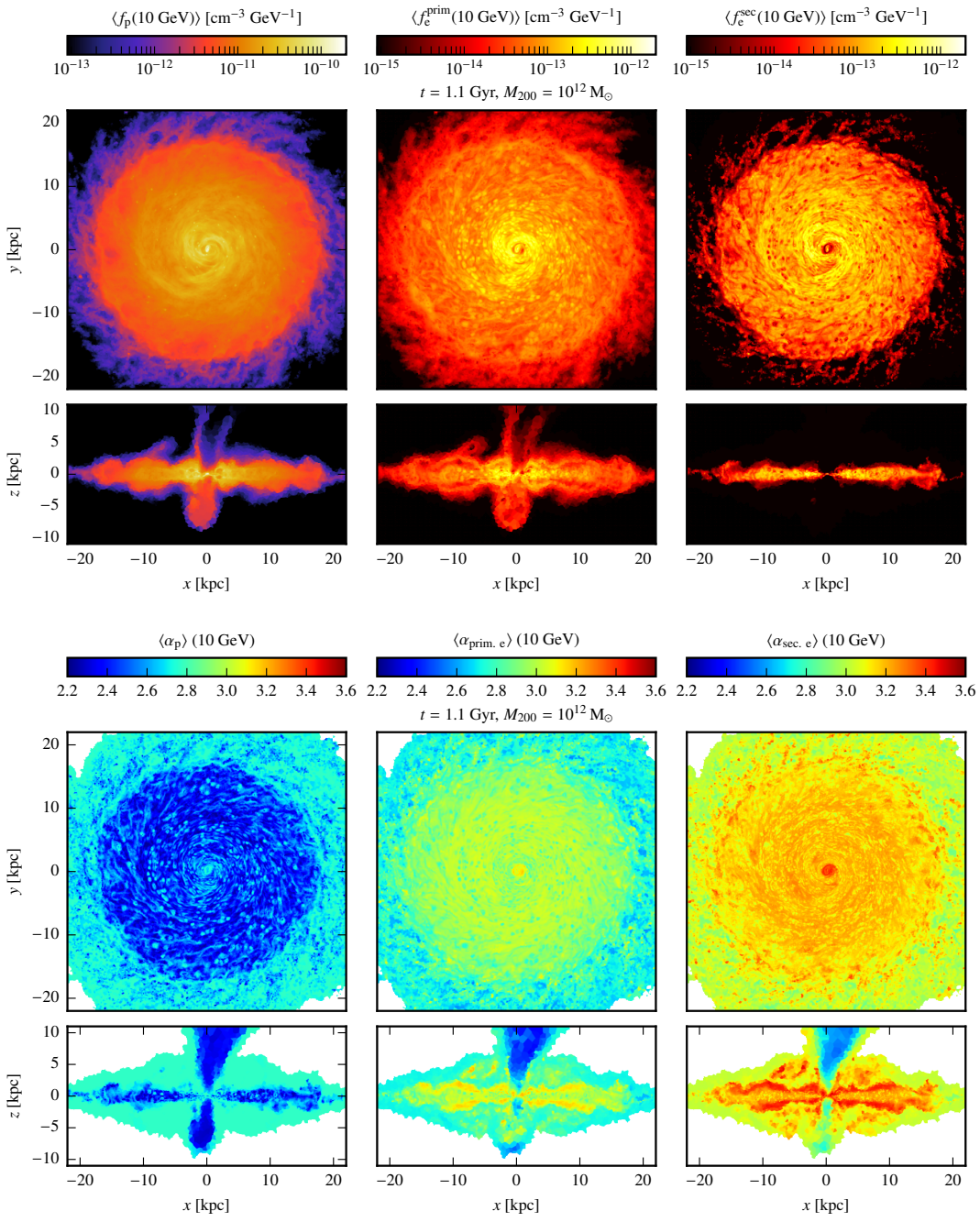

Figure 3.11: We show slices of the spectral CR density at 10 GeV (top six panels for protons, primary and secondary electrons from left to right) and spectral indices (lower six panels) of CR protons (α_p), primary and secondary electrons ($\alpha_{prim,e}$ and $\alpha_{sec,e}$), each averaged over thin (300 pc) slices for our fiducial galaxy (see Table 3.1).

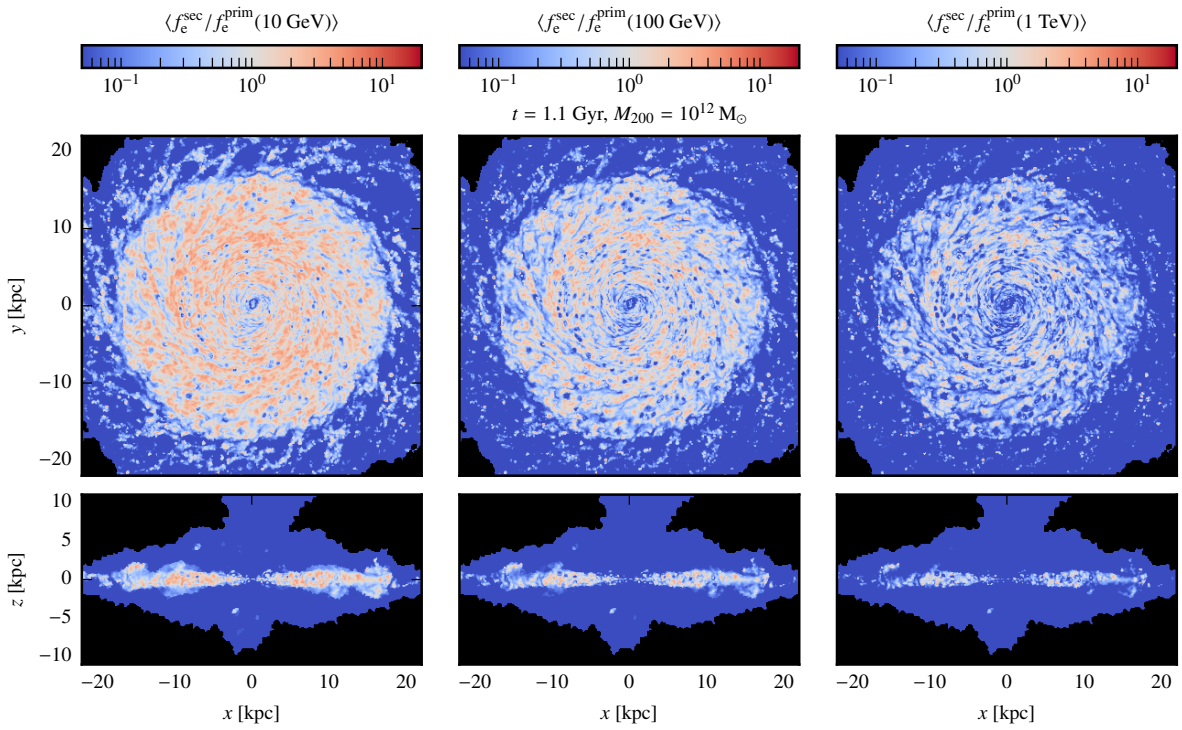

Figure 3.12: Face-on and edge-on maps of the ratio of secondary to primary electrons at 10 GeV, 100 GeV and 1 TeV averaged over a slice with thickness 300 pc, for our fiducial galaxy, i.e. the same snapshot that is shown in Figs. 3.1, 3.7 and 3.11.

et al. 2017b). The decreasing gas density with height over the disc causes Coulomb losses to be less efficient, elevating both electron and proton spectra at low energies with larger height.

The simulated steady-state spectra of protons and electrons provide an excellent match to the observed spectra throughout the range of energies shown if we average them over heights of ±1 kpc without the need of fine-tuning. In particular, the simulations nicely reproduce the observational finding that CR electrons dominate over the protons at low energies. This is due to effective Coulomb cooling at low energies, which causes a spectral flattening so that the proton-to-electron ratio approximately scales as

$$\frac{f_\mathrm{p}}{f_\mathrm{e}} \propto \frac{b_\mathrm{Coul,e}}{b_\mathrm{Coul,p}} = \frac{A_\mathrm{e}}{A_\mathrm{p}} \frac{\beta_\mathrm{p}}{\beta_\mathrm{e}} \approx \frac{\beta_\mathrm{p}}{\beta_\mathrm{e}}, \tag{3.24}$$

where we used Eqs. (3.23), (2.8), and (2.13), but limited the solution of the steady-state equation to Coulomb cooling only.[6] While the electron and proton spectra suffer from Coulomb cooling below 1 GeV, the proton spectrum experiences an additional β_p suppression at these energies (where electrons are still relativistic, i.e., $\beta_\mathrm{e} \approx 1$). This causes the electron spectrum to eventually dominate the total particle spectrum.

Still, we do not simultaneously match the spectra of electrons and protons when averaged over the same height. One possible explanation for this behavior are the different spatial regions in which we observationally probe electron and proton spectra. While the shape of the proton spectrum represents the average ISM conditions in the solar radius, the *observed* electron spectrum exclusively probes the shocked ISM between the Sun's bow shock and the heliosheath, in which the density is increased with respect to the ISM upstream of the bow shock. As a result, Coulomb losses are stronger, which causes an additional turn-over of the electron spectrum in comparison to the model spectrum that is averaged over heights of ±1 kpc. Note that while finite particle mean-free-path effects could potentially explain a small amount of solar modulation immediately upstream the heliosheath (Strauss et al., 2013), this is unlikely to be charge dependent and cannot explain the differing CR electron and proton spectra at low energies.

Furthermore, we obtain a somewhat harder CR proton spectrum for $E \gtrsim 50$ GeV in our model, over-predicting the observed spectrum at high energies, which is probably owing to our neglect of modeling CR streaming (Blasi et al., 2012; Evoli et al., 2018). This calls for an improved CR transport model in MHD simulations, which delivers a realistic (spatially and temporally varying) CR diffusion coefficient in the self-confinement picture (Thomas & Pfrommer, 2019; Thomas

[6]The deviation of the ratio $A_\mathrm{e}/A_\mathrm{p}$ from unity is below 1 per cent for the mean electron densities of interest here ($n_\mathrm{e} = 0.02 - 0.2\,\mathrm{cm}^{-3}$).

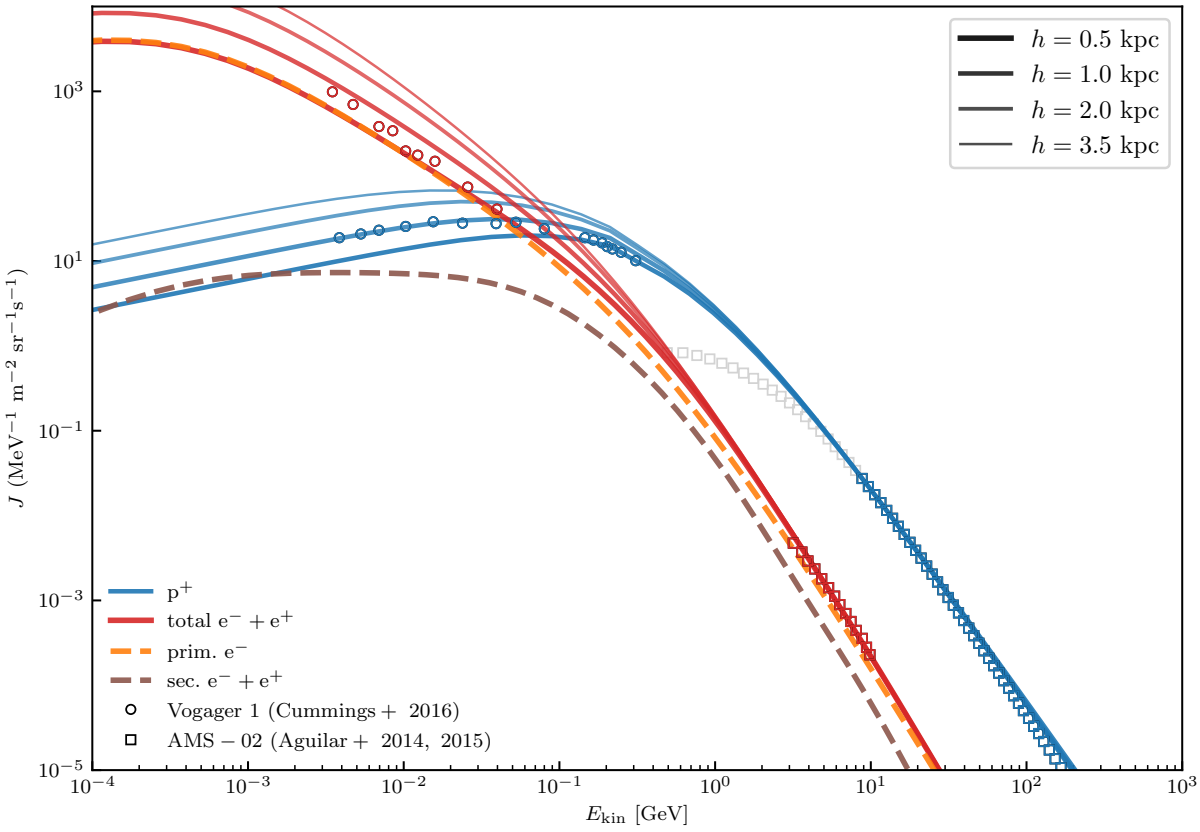

Figure 3.13: Spectra of CR protons and electrons at $t = 5$ Gyr, averaged over rings at $r = 8 \pm 1$kpc with different heights. For comparison, we show data of Voyager 1 (Cummings et al., 2016) and AMS-02 for electrons (Aguilar et al., 2014a) and protons (Aguilar et al., 2015). The AMS-02 data affected by solar modulation, i.e. below 10 GeV, is shown with grey symbols. The simulated CR spectra are normalised to the observations at 10 GeV to account for deviations of our simulated from the observed SFR (see Table 3.2 for details).

et al., 2020, 2021), which would also include the effect of a reduced CR diffusion coefficient around sources (Abeysekara et al., 2017). This could in turn signal the excitation of powerful CR-driven plasma instabilities (Shalaby et al., 2021).

In summary, the assumptions about the injected spectral index of protons and electrons, $\alpha_{\rm inj} = 2.2$, in combination with the observationally motivated energy dependence of the diffusion coefficient, $\propto E^{0.5}$ determine our spectrum at high energies. In addition, the modelling of $K_{\rm ep}^{\rm inj}$ yields the observed electron spectrum relative to that of protons at 10 GeV, per construction. However, the behaviour of the spectra at low energies is a prediction of our model and hence provides a physical explanation for the observed inversion of the spectra below ∼100 MeV.

Table 3.2: Summary of the normalisation factors used for the CR proton and electron spectra in Fig. 3.13, respectively, averaged over different heights h, in order to mach the data at 10 GeV.

h [kpc]	norm. factor protons	norm. factor electrons
0.5	0.18	0.20
1.0	0.21	0.26
2.0	0.25	0.37
3.5	0.31	0.50

Positron ratio

Several experiments reported the positron ratio that decreases with energy until $\sim$ 8 GeV at which point it starts to rise again, including TS93 (Golden et al., 1996), Wizard/CAPRICE (Boezio et al., 2001), HEAT (Beatty et al., 2004), AMS-01 (AMS-01 Collaboration et al., 2007), PAMELA (Adriani et al., 2009), *Fermi* (Ackermann et al., 2012a), AMS-02 (Aguilar et al., 2013, 2014b). If positrons solely arise from hadronic interactions of CR protons with the ISM, the positron fraction decreases with energy because of the steeper spectrum of secondaries in comparison to primaries. Thus, the observed rise of the positron fraction has been either attributed to annihilating/decaying dark matter particles (e.g. Yin et al., 2009; Cholis & Hooper, 2013; Feng et al., 2020), or local astrophysical sources such as pulsars or SNe (e.g. Serpico, 2012; Di Mauro et al., 2017; Hooper et al., 2009; Mertsch et al., 2020). We obtain in Fig. 3.14 the expected behaviour of a decreasing positron fraction with energy, coinciding with observations up to $\sim$ 8 GeV. The overall normalisation though depends on the height over which we average the CR electron spectra, as depicted in the legend. This is due to the fact that the decreasing gas density with height leads to a less efficient production of secondaries and therefore to a decrease in the fraction of positrons in comparison to all leptons, the latter being dominated by primary electrons.

Note that we do not simultaneously reproduce the observations of CR spectra and the positron fraction within one model, when averaged over the same height. This is consistent with the fact that we somewhat overproduce the proton spectrum at energies $\sim$ 100 GeV in comparison to the observations (see Fig. 3.13), which produces secondary electrons at around 6 GeV. In consequence, our positron fraction tends to be higher by a factor $\approx$ 1.9 in comparison to the observed values.

Another uncertainty in the calculation of the positron fraction is our assumption about the nuclear enhancement factor, that accounts for heavier nuclei in the composition of CRs and the ISM (see Appendix 3.7.1), for which we adopt the wounded nucleon model. However, Kafexhiu (2016) recently analysed the impact of different effects such as sub-threshold pion production on

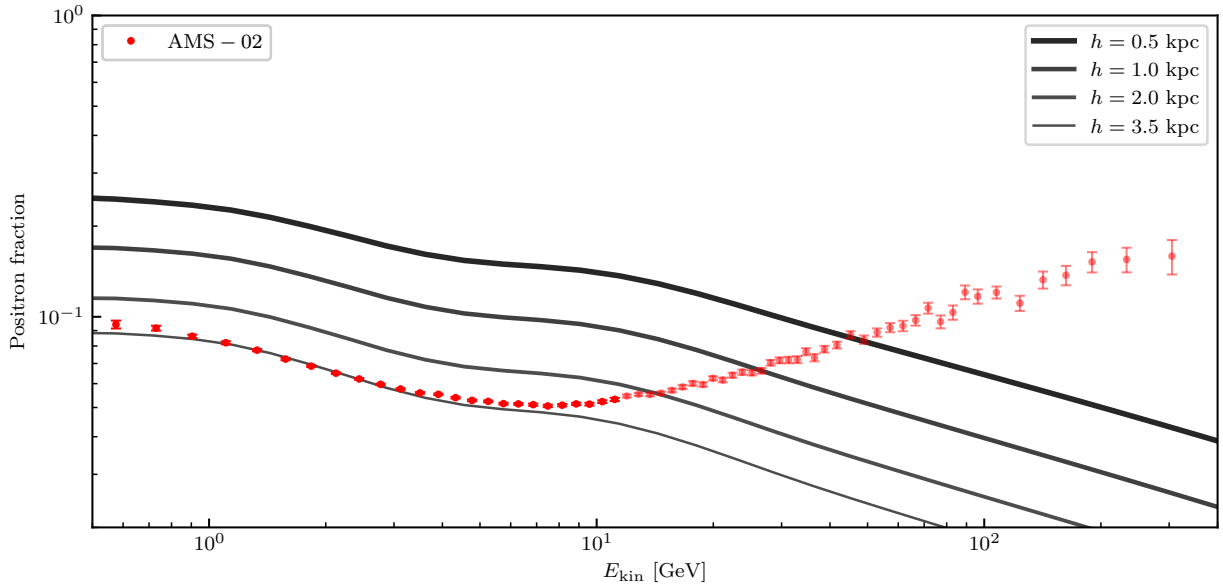

Figure 3.14: We show the positron fraction $f_{e^+}/(f_{e^+} + f_{e^-})$, averaged over different heights, at $t = 5$ Gyr (as in Fig. 3.13). The data points indicate observations performed by AMS-02 (Accardo et al., 2014). The rise of the the positron fraction above ~8 GeV is due to additional positron sources that are not modelled here (see Section 3.4.2).

the cross section of secondary particle production. In particular at low energies, the wounded nucleon model seems to break down. For example, in collisions of protons with carbon nuclei, electrons and positrons are shown to be created in equal amount, in contrast to pp-collisions, where more positrons than electrons are produced at low energies. Yang et al. (2018b) apply those considerations to solar abundances and quantify the effect on the gamma-ray spectrum. Still, the exact effect on the electron and positron spectra for solar abundances has (to our knowledge) not yet been analysed.

3.5 Summary and conclusions

For the first time, we calculate steady state CR spectra in three-dimensionsal MHD simulations that self-consistently include CRs. We model their spectra with a cell-based steady-state approximation, including hadronic and Coulomb losses for CR protons and radiative losses due to synchrotron, bremsstrahlung and IC losses for CR electrons. In addition, we estimate losses due to advection and diffusion, while assuming an energy-dependent diffusion coefficient. Furthermore, we carefully calculate the production of secondary electrons and positrons by combining existing models from

the literature (Yang et al., 2018b; Kelner et al., 2006) at intermediate energies and provide our own parametrization of the total cross sections of negatively and positively charged pion production, respectively (Eqs. 3.45 and 3.46).

Intriguingly, while our modelling of CR sources and transport in a self-consistently evolving galaxy does not involve fine-tuning of parameters, the emerging steady-state spectra convincingly reproduce observational CR features measured locally in the Milky Way. These include on the one hand measured CR proton and electron spectra in the ISM by AMS-02 (Aguilar et al., 2014a, 2015) and Voyager 1 (Cummings et al., 2016), for which we reproduce the inversion of proton and electron spectra so that the latter dominates the total particle spectrum at low energies. We attribute this to steady-state Coulomb cooling and analytically verify this behavior. On the other hand, our steady-state spectra also match the observed shape of the positron fraction up to energies of ~ 8 GeV, before the excess of positrons (attributed to additional sources such as pulsars) comes into effect. Solely the total normalisation of the CR spectra and positron fraction is not reproduced. However, this is not too surprising, considering the fact that our simulations are not designed to fully reproduce a realistic Milky Way analogue with a simultaneous match of current SFR, halo mass, as well as the potentially complex star-formation history. This could be addressed in future work by applying our model to cosmological simulations, where galaxies can be found that resemble the Milky Way in more detail. Summarising, the match of simulations and observational data indicates that our modelling apparently does not miss critical physics ingredients and is able to provide physics insights into observational findings that are very complementary to state-of-the-art approaches of CR transport analyses.

Our model enables us to obtain spatial and spectral information of CRs in simulated galaxies with different galaxy sizes and injection efficiencies of CRs. We use this approach as a starting point to analyse the non-thermal emission processes arising from CRs in star-forming galaxies in two accompanying publications. Paper II focuses on gamma-ray emission processes, examines the influence of CR transport models on the total gamma-ray luminosity and emission spectra, whereas Paper III is aimed towards understanding the radio emission of star-forming galaxies. In particular, our analytical modelling of the ratio of secondary-to-primary electrons enables us to constrain their relative contribution to the non-thermal emission processes.

3.6 Appendix: Normalization of CR spectra

In the following, we present Appendix A2 as published in Werhahn et al. (2021a), whereas Appendix A1 summarizing the loss rates of CR protons and electrons is given in Section 2.1.2.

In this section, we explain the detailed procedure of obtaining the normalisation of the primary electron and proton spectra, that allow us to infer an injected ratio of electrons to protons $K_{\rm ep}^{\rm inj}$.

A priori, we do not know the normalisation of the injection spectra in each cell so that we first assume $C_{i,0} = 1$ in Eq. (3.4), for protons and electrons. We calculate the steady-state spectrum $f_{\rm p,0}$ that results from a given injection spectrum and all energy loss processes, and then re-normalise the source function and spectral density via the CR energy density $\varepsilon_{\rm CR}$ in every cell:

$$f_{\rm p}(p_{\rm p}) = f_{\rm p,0}(p_{\rm p}) \frac{\varepsilon_{\rm CR}}{\varepsilon_{\rm CR,0}} \tag{3.25}$$

and

$$q_{\rm p}(p_{\rm p}) = q_{\rm p,0}(p_{\rm p}) \frac{\varepsilon_{\rm CR}}{\varepsilon_{\rm CR,0}}, \tag{3.26}$$

where

$$\varepsilon_{\rm CR,0} = \int T_{\rm p}(p_{\rm p}) f_{\rm p,0}(p_{\rm p}) {\rm d}p_{\rm p} \tag{3.27}$$

and $T_{\rm p}(p_{\rm p}) = \left(\sqrt{p_{\rm p}^2 + 1} - 1\right) m_{\rm p} c^2$. Similarly, for the primary electrons we calculate a steady-state spectrum $f_{\rm e,0}^{\rm prim}(p_{\rm e})$ from the injection spectrum $q_{\rm e,0}^{\rm prim}(p_{\rm e})$, and re-normalise it as

$$f_{\rm e}^{\rm prim}(p_{\rm e}) {\rm d}p_{\rm e} = A_{\rm norm} f_{\rm e,0}^{\rm prim}(p_{\rm e}) {\rm d}p_{\rm e}. \tag{3.28}$$

To identify $A_{\rm norm}$, we relate the steady state spectra of all electrons (primary plus secondary) to protons via the observed ratio of electrons to protons $K_{\rm ep}^{\rm obs}$ at a kinetic energy of 10 GeV, or equivalently at the corresponding normalised momenta, $p_{i,\rm 10GeV}$, i.e.

$$f_{\rm e}^{\rm prim+sec}(p_{\rm e,10GeV}) {\rm d}p_{\rm e} = K_{\rm ep}^{\rm obs} f_{\rm p}(p_{\rm p,10GeV}) {\rm d}p_{\rm p}. \tag{3.29}$$

Because we have already normalised the proton spectrum $N_{\rm p}$, we are able to obtain the primary

electron spectrum via

$$f_{\rm e}^{\rm prim}(p_{\rm e}) = A_{\rm norm} f_{\rm e,0}^{\rm prim}(p_{\rm e}), \tag{3.30}$$

$$A_{\rm norm} = \frac{K_{\rm ep}^{\rm obs} f_{\rm p}(p_{\rm p,10GeV}) \dfrac{m_{\rm e}}{m_{\rm p}} - f_{\rm e}^{\rm sec}(p_{\rm p,10GeV})}{f_{\rm e,0}^{\rm prim}(p_{\rm e,10GeV})}, \tag{3.31}$$

where we account for the normalised momenta $\mathrm{d}p_{\rm p} = \mathrm{d}p_{\rm e} m_{\rm e}/m_{\rm p}$ and use the fact that the normalised and un-normalised primary electron spectra are self-similar. Equivalently, we determine the normalisation of the electron injection spectrum $q_{\rm e}^{\rm prim}(p_{\rm e})$, that is linearly related to $f_{\rm e}^{\rm prim}(p_{\rm e})$:

$$q_{\rm e}^{\rm prim}(p_{\rm e}) = A_{\rm norm} q_{\rm e,0}^{\rm prim}(p_{\rm e}), \tag{3.32}$$

In order to infer the ratio of injected electrons to protons $K_{\rm ep}^{\rm inj}$, we compare the electron and proton injection spectrum at the same (physical) momentum P_0:

$$q_{\rm e}^{\rm prim}[P_0/(m_{\rm e}c)]\mathrm{d}p_{\rm e} = K_{\rm ep}^{\rm inj} q_{\rm p}[P_0/(m_{\rm p}c)]\mathrm{d}p_{\rm p}, \tag{3.33}$$

which yields after inserting our definition of the source functions the following expression:

$$K_{\rm ep}^{\rm inj} = \frac{q_{\rm e}^{\rm prim}[P_0/(m_{\rm e}c)]}{q_{\rm p}[P_0/(m_{\rm p}c)]} \frac{m_{\rm p}}{m_{\rm e}} = \frac{C_{\rm e}}{C_{\rm p}} \left(\frac{m_{\rm p}}{m_{\rm e}}\right)^{1-\alpha_{\rm p}}. \tag{3.34}$$

In this way, we obtain in each cell a ratio of injected electrons to protons that eventually reproduces the observed value after taking into account all cooling processes. If the electrons and protons cool on the same timescales (at the considered energy of 10 GeV), we obtain $K_{\rm ep}^{\rm inj} \simeq K_{\rm ep}^{\rm obs}$. On the other hand, $K_{\rm ep}^{\rm inj} < K_{\rm ep}^{\rm obs}$ ($K_{\rm ep}^{\rm inj} > K_{\rm ep}^{\rm obs}$) implies that the timescales of the hadronic cooling processes are smaller (larger) than the leptonic ones.

In the literature, the normalisation is often defined differently, in terms of injected energy into CR protons and electrons, i.e., $\varepsilon_{\rm e}^{\rm inj} = \zeta_{\rm prim} \varepsilon_{\rm p}^{\rm inj}$, such that

$$\zeta_{\rm prim} \int_0^\infty T_{\rm p}(p_{\rm p}) q_{\rm p}(p_{\rm p}) \mathrm{d}p_{\rm p} = \int_0^\infty T_{\rm e}(p_{\rm e}) q_{\rm e}^{\rm prim}(p_{\rm e}) \mathrm{d}p_{\rm e}. \tag{3.35}$$

Assuming the same injected spectral index of electrons and protons, $2 < \alpha_{\rm inj} < 3$, and a lower momentum cutoff that is much smaller than $m_{\rm p}c$ ($m_{\rm e}c$) for protons (electrons), it can be shown that

this is related to $K_{\rm ep}^{\rm inj}$ in the following way:

$$K_{\rm ep}^{\rm inj} = \zeta_{\rm prim} \left(\frac{m_{\rm p}}{m_{\rm e}}\right)^{2-\alpha_{\rm p}} \tag{3.36}$$

This implies that our approach, where we find $K_{\rm ep}^{\rm inj} \approx 0.02$, this corresponds to a primary electron-to-proton energy fraction of $\zeta_{\rm prim} \approx 9\%$ (assuming $\alpha_{\rm p} = 2.2$), which is consistent with the parameters used in other models, such as the one-zone steady-state models by Lacki et al. (2010).

3.7 Appendix: Electron source function and parametrization of the pion cross section

Here, we describe numerical algorithms for computing the electron source function and charged pion cross section in Appendix 3.7.1, before we detail our parametrization of the total cross section of pion production, σ_π, in Appendix 3.7.2. Finally, we derive an analytical approximation for the secondary electron source function in Appendix 3.7.3.

3.7.1 Production of secondary electrons and positrons

The minimum total proton energy required to produce a pion is $E_{\rm p}^{\rm min} = 1.22\,\mathrm{GeV}$. The production spectrum, i.e., the number of produced secondary particles per energy, time and volume, or source function q_s, of a secondary particle species $s = \gamma, \mathrm{e}^-, \mathrm{e}^+$ for a given CR proton distribution is given by

$$q_s(E_s) = c n_{\rm H} \int_{E_{\rm p}^{\rm min}}^{\infty} \mathrm{d}E_{\rm p} f_{\rm p}(E_{\rm p}) \frac{\mathrm{d}\sigma_s(E_s, E_{\rm p})}{\mathrm{d}E_s}. \tag{3.37}$$

The differential cross section of the secondary particle species s can be calculated by means of the differential cross section for the production of a pion with energy E_π from the collision of a proton with energy $E_{\rm p}$, i.e. $\mathrm{d}\sigma(E_{\rm p}, E_\pi)/\mathrm{d}E_\pi$. Then, we can solve the integral

$$\frac{\mathrm{d}\sigma_s(E_s, E_{\rm p})}{\mathrm{d}E_s} = \int_{E_\pi^{\rm min}}^{E_\pi^{\rm max}} \mathrm{d}E_\pi \frac{\mathrm{d}\sigma_\pi(E_{\rm p}, E_\pi)}{\mathrm{d}E_\pi} f_{s,\pi}(E_s, E_\pi), \tag{3.38}$$

where $f_{s,\pi}(E_s, E_\pi)$ is the normalised probability distribution for the production of a secondary particle s from a single pion energy E_π. Here, we are interested in electrons and positrons ($s = \mathrm{e}^-, \mathrm{e}^+$), and thus only in charged pions, while we will consider the production of neutral pions and gamma rays in Paper II. For the normalised electron/positron energy distribution $f_{\pi^\pm}(E_{\mathrm{e}^\pm}, E_\pi)$, we use the expressions derived by (Dermer, 1986b), assuming a mono-energetic, unpolarized, isotropic distribution of pions, to eventually calculate $\mathrm{d}\sigma_{\mathrm{e}^\pm}(E_{\mathrm{e}^\pm}, E_\mathrm{p})/\mathrm{d}E_{\mathrm{e}^\pm}$ from Eq. (3.38). In the literature, there are different parametrizations for the corresponding terms of Eq. (3.37). They relate to the definition of the pion source function in the following way

$$q_\pi(E_\pi) = cn_\mathrm{H} \int_{E_\mathrm{p}^\mathrm{min}}^{\infty} \mathrm{d}E_\mathrm{p} f_\mathrm{p}(E_\mathrm{p}) \frac{\mathrm{d}\sigma_\pi(E_\mathrm{p}, E_\pi)}{\mathrm{d}E_\pi}, \tag{3.39}$$

so that the source function of a secondary particle species is

$$q_s = \int_{E_\pi^\mathrm{min}}^{E_\pi^\mathrm{max}} \mathrm{d}E_\pi q_\pi(E_\pi) f_\pi(E_s, E_\pi). \tag{3.40}$$

The differential cross section of charged pion production or the electron source function can be obtained from simulations of pp-interactions, e.g. Pythia (Sjöstrand et al., 2006, 2008), SIBYLL (Fletcher et al., 1994), QGSJET (Kalmykov & Ostapchenko, 1993; Kalmykov et al., 1997; Ostapchenko, 2006) and Geant 4 (Agostinelli et al., 2003; Allison et al., 2006). At low proton energies near the kinematic threshold ($T_\mathrm{p} < 10\,\mathrm{GeV}$), we adopt the approach given by Yang et al. (2018b). They utilised the hadronic interaction model of the Geant 4 Toolkit (Agostinelli et al., 2003; Allison et al., 2006) to provide a parametrization for the normalised pion energy distribution $\tilde{f}(x, T_\mathrm{p})$, that reads

$$\frac{\mathrm{d}\sigma_\pi}{\mathrm{d}x} = \sigma_\pi \times \tilde{f}(x, T_\mathrm{p}). \tag{3.41}$$

Yang et al. (2018b) provide analytical formulae for $\tilde{f}(x, T_\mathrm{p})$, with $x = T_\pi / T_\pi^\mathrm{max}$. The parametrization of the total cross section of pion production σ_π is described in Section 3.7.2, where we provide our own fit to the data, shown by the solid lines in Fig. 3.15 and compare it to models in the literature.

In the high-energy range of protons with $T_\mathrm{p} > 100\,\mathrm{GeV}$, we use an analytical parametrization provided by Kelner et al. (2006), where they give production rate of secondary electrons from the SIBYLL code (Fletcher et al., 1994). It is given in terms of a distribution $F_{\mathrm{e}^\pm}(x, E_\mathrm{p})$, such that $F_{\mathrm{e}^\pm}(x, E_\mathrm{p})\mathrm{d}x$ describes the number of produced electrons and positrons per collision in the interval

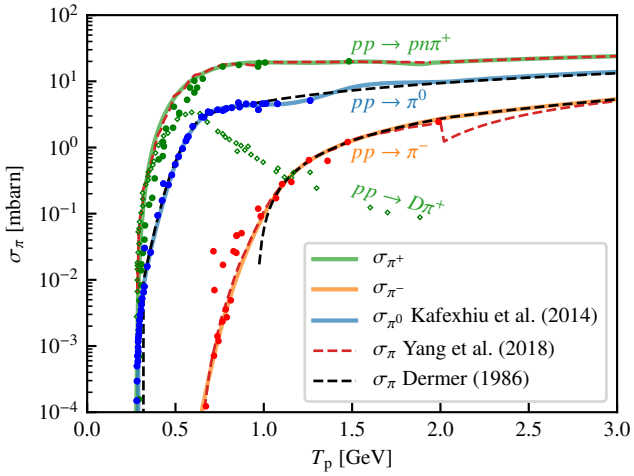

Figure 3.15: Total cross sections of π^0 and $\pi^\pm$ production with data points taken from the compilation in Yang et al. (2018b). The solid lines represent the parametrizations that are used here where we provide our own formulas for σ_{π^+} (green) and σ_{π^-} (orange) in Eqs. (3.45) and (3.46).

$(x, x + \mathrm{d}x)$ with $x = E_{\mathrm{e}^\pm}/E_\mathrm{p}$. Assuming that the production of secondary positrons is equal to the production of secondary electrons in this energy regime, the corresponding production rate is given by

$$q_{\mathrm{e}^\pm}(E_{\mathrm{e}^\pm}) = cn_\mathrm{H} \int_{E_{\mathrm{e}^\pm}}^{\infty} \sigma_\mathrm{pp}^\mathrm{inel}(E_\mathrm{p}) f_\mathrm{p}(E_\mathrm{p}) F_{\mathrm{e}^\pm}\left(\frac{E_{\mathrm{e}^\pm}}{E_\mathrm{p}}, E_\mathrm{p}\right) \frac{\mathrm{d}E_\mathrm{p}}{E_\mathrm{p}}. \tag{3.42}$$

Here, $\sigma_\mathrm{pp}^\mathrm{inel}$ is the total inelastic cross section parametrized by Kafexhiu et al. (2014) (see Eq. 3.44).

Figure 3.16 shows the parametrizations of the differential cross sections for different electron energies. We use a cubic spline to interpolate between the Yang et al. (2018b) model at low proton energies ($T_\mathrm{p} < 10\,\mathrm{GeV}$) and the Kelner et al. (2006) model at high proton energies ($T_\mathrm{p} > 100\,\mathrm{GeV}$).

So far, those parametrizations only consider pp-interactions. In addition, interactions of heavier CR nuclei with the ISM have to be taken in account. Following the wounded nucleon model (Białłas et al., 1976), one can rewrite the pion production so that it can be considered to be produced in pp-collision that are enhanced by a multiplicative factor (the 'nuclear enhancement factor'). Based on parametrizations by Lebedev et al. (1963) and Orth & Buffington (1976), Dermer (1986a) finds a value of 1.39, that increases to 1.45 if heavier nuclei than helium are included, whereas Stephens & Badhwar (1981) estimate it to 1.6 ± 0.1. Hence, we adopt the geometric mean of 1.5 and note on the relevance for studying those effects of heavier nuclei on the resulting spectrum of secondary electrons and positrons in more detail in the future (using e.g., the parametrizations of sub-threshold pion production given by Kafexhiu, 2016).

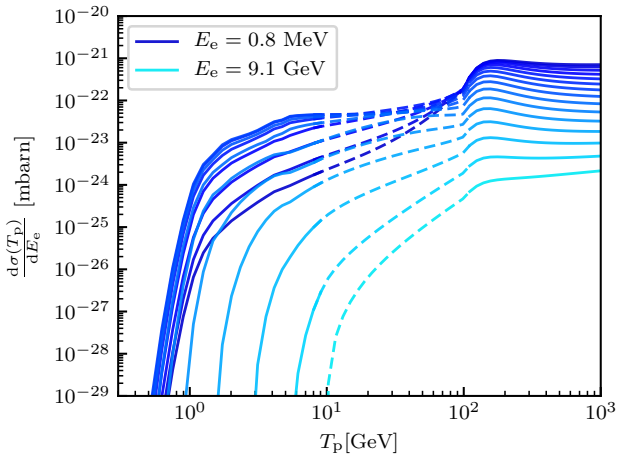

Figure 3.16: Interpolation (dashed lines) of the differential cross section $d\sigma_e(E_e, E_p)/dE_e$ as a function of kinetic proton energy T_p for fixed electron energies as indicated by different colors ranging from 0.8 MeV to 9.1 GeV (in steps of equidistant momentum bins in log-space). The parametrization below $T_p = 10$ GeV is given by Yang et al. (2018b), whereas above 100 GeV, we use Kelner et al. (2006).

3.7.2 Parametrizations for σ_π

For the total cross section of pion production, σ_π, Yang et al. (2018b) use their own fit to the experimental data below 2 GeV and a different prescription given in Golokhvastov (2001) at higher proton energies (see red dashed lines in Fig. 3.15). For $T_p > 2$ GeV, they express the cross section as

$$\sigma_\pi = \sigma_{pp}^{inel} \langle n_\pi \rangle \,. \tag{3.43}$$

Here, the pion average yield is parametrized as $\langle n_\pi \rangle = 0.78(w-2)^{3/4} w^{-1/4} - 1/2 + \varepsilon$ where $w = \sqrt{s}/m_p c^2$, s denotes the square of the total energy in the CMS, i.e. $\sqrt{s} = [2m_p c^2 (E_p + m_p c^2)]^{1/2}$, and $\varepsilon = 0$ for π^-, $1/3$ for π^0 and $2/3$ for π^+. This fit is based on experimental data by Golokhvastov (2001). The resulting curves of the total cross sections are shown in Fig. 3.15, where the red dashed lines show the parametrizations used in Yang et al. (2018b) and the points are the experimental data that they refer to. In the case of negative pions, one can clearly see the discontinuity at $T_p = 2$ GeV, where the description changes from a fit to the data at $T_p < 2$ GeV to the pion average yield by

Golokhvastov (2001) and the total inelastic cross section from Kafexhiu et al. (2014):

$$\sigma_{\mathrm{pp}}^{\mathrm{inel}}(T_{\mathrm{p}}) = \left[30.7 - 0.96 \log\left(\frac{T_{\mathrm{p}}}{T_{\mathrm{p}}^{\mathrm{th}}}\right) + 0.18 \log^2\left(\frac{T_{\mathrm{p}}}{T_{\mathrm{p}}^{\mathrm{th}}}\right)\right] \left[1 - \left(\frac{T_{\mathrm{p}}}{T_{\mathrm{p}}^{\mathrm{th}}}\right)^{1.9}\right]^3 \text{ mbarn}. \tag{3.44}$$

The black dashed line shows the approach by Dermer (1986b), that only starts at $T_{\mathrm{p}} = 0.95\,\mathrm{GeV}$ for σ_{π^-} and an extrapolation to lower energies would lead to an underestimate of the cross section in comparison to the experimental data. Because Yang et al. (2018b) do not provide an expression for their fit to the data points below 2 GeV, we determine our own fit to the data points up to $T_{\mathrm{p}} \leqslant 1.1\,\mathrm{GeV}$ and use the parametrization by Dermer (1986b) for higher proton energies, which leads to the orange solid line in Fig. 3.15. For the cross section of positively charged pion production, we fitted the curve from Fig. 4 in Yang et al. (2018b), that is a sum of all channels leading to the production of positively charged pions. In this case, it connects relatively smoothly to the description of the cross section for $T_{\mathrm{p}} > 2\,\mathrm{GeV}$ from Eq. (3.43). We fit the cross sections for charged pions as follows.

The total cross section for negatively charged pions is fit by $\sigma_{\pi^-}[\mathrm{mbarn}] = \exp(f_1(x))$ with

$$f_1(x) = a_1 \ln(x/c_1) + b_1 \ln^2(x/c_1), \tag{3.45}$$

where $x = T_{\mathrm{p}}/\mathrm{GeV}$, for $T_{\mathrm{p}} < 1.1$ GeV, which corresponds to a momentum of $P_{\mathrm{p}} = 1.8\,\mathrm{GeV/c}$. The parameters a_1, b_1, and c_1 are shown in Table 3.3. Therefore, we can use the parametrization by Dermer (1986b) for higher momenta, which is valid for values above $P_{\mathrm{p}} > 1.65\,\mathrm{GeV/c}$ but deviates from the data below $T_{\mathrm{p}} < 1.1$ GeV, see the black dashed line for σ_{π^-} in Fig. 3.15.

Furthermore, we provide our parametrizations for $\sigma_{\pi^+}[\mathrm{mbarn}] = f_2(x)$ by

$$\begin{aligned} f_2(x) = {} & [a_2 - b_2 \ln(x/c_2) + d_2 \ln^2(x/c_2)] \times (1 - (x/c_2)^2)^3 + \\ & [e_2 - f_2 \ln(x/c_2) + d_2 \ln^2(x/c_2)] \times (1 - (x/c_2)^{0.4})^3, \end{aligned} \tag{3.46}$$

where $x = T_{\mathrm{p}}/\mathrm{GeV}$, valid for $T_{\mathrm{p}} < 1.95$ GeV. For higher energies, we apply the parametrization by Yang et al. (2018b).

Table 3.3: Shown are the fit parameters for equations (3.45) and (3.46).

a_1	b_1	c_1
5.4868	-10.4440	1.3219
a_2	b_2	c_2
-1.5997×10^{-1}	-1.3570×10^{-1}	2.7219×10^{-1}
d_2	e_2	f_2
-2.9436×10^{-2}	-5.5311×10^{2}	-5.3490×10^{2}

3.7.3 Analytical approximation for the source function of secondary electrons

Following Pfrommer & Enßlin (2004), here we derive an analytical approximation for the source function of secondary electrons, which provides physical insight into our numerical approach of the hadronic reaction. Adopting a delta approximation for the production of pions, the differential cross section of pion production reads

$$\frac{\mathrm{d}\sigma(E_\pi, E_\mathrm{p})}{\mathrm{d}E_\pi} = \xi(E_\mathrm{p})\sigma_\mathrm{pp}^\pi(E_\mathrm{p})\delta(E_\pi - \langle E_\pi\rangle)\theta(E_\mathrm{p} - E_\mathrm{th}). \tag{3.47}$$

Assuming isospin symmetry, i.e., that the multiplicity of neutral pions is half that of charged pions, $\xi_{\pi^0} = (\xi_{\pi^+} + \xi_{\pi^-})/2$, this yields the pion source function

$$q_{\pi^+}(E_\pi) + q_{\pi^-}(E_\pi) = 2q_{\pi^\pm}(E_\pi) = \frac{2}{3}cn_\mathrm{H}\int \mathrm{d}E_\mathrm{p} f_\mathrm{p}(E_\mathrm{p})\frac{\mathrm{d}\sigma(E_\pi, E_\mathrm{p})}{\mathrm{d}E_\pi} \tag{3.48}$$

from a proton energy distribution $f_\mathrm{p}(E_\mathrm{p})$. At high energies, one can furthermore assume a constant pion multiplicity $\xi = 2$, following the model by Pfrommer & Enßlin (2004), as well as a mean pion energy $\langle E_\pi\rangle(E_\mathrm{p}) \simeq K_\mathrm{p}T_\mathrm{p}/\xi \simeq T_\mathrm{p}/(2\xi)$, where the inelasticity K_p was assumed to be $1/2$ (Mannheim & Schlickeiser, 1994). In the high-energy limit, the proton power-law distribution in momentum is also a power-law distribution in energy since $\gamma_\mathrm{p} = E_\mathrm{p}/(m_\mathrm{p}c^2) = \sqrt{1+p_\mathrm{p}^2} \approx p_\mathrm{p}$ for $p_\mathrm{p} \gg 1$ and furthermore, $T_\mathrm{p}/(m_\mathrm{p}c^2) = \gamma_\mathrm{p} - 1 \approx \gamma_\mathrm{p}$. If the energy distribution is given by a

power-law with spectral index α_p and normalisation factor $\tilde{C}_\mathrm{p}$,[7] we obtain the expression

$$\begin{aligned} q_{\pi^+}(E_\pi) + q_{\pi^-}(E_\pi) &= \frac{4}{3}\xi^{2-\alpha_\mathrm{p}} \frac{\tilde{C}_\mathrm{p}}{m_\mathrm{p}c} n_\mathrm{H} \sigma_\mathrm{pp}^\pi(\alpha_\mathrm{p}) \left(\frac{2E_\pi}{m_\mathrm{p}c^2}\right)^{-\alpha_\mathrm{p}} \\ &= \frac{16}{3} \frac{\tilde{C}_\mathrm{p}}{m_\mathrm{p}c} n_\mathrm{H} \sigma_\mathrm{pp}^\pi(\alpha_\mathrm{p}) \left(\frac{4E_\pi}{m_\mathrm{p}c^2}\right)^{-\alpha_\mathrm{p}}. \end{aligned} \tag{3.49}$$

In this approximation, the effective inelastic cross section σ_pp^π was modeled by Pfrommer & Enßlin (2004), which also accounts for kaon decay modes. It reads

$$\sigma_\mathrm{pp}^\pi(\alpha_\mathrm{p}) = 32 \times [0.96 + \exp(4.4 - 2.4\alpha_\mathrm{p})] \text{ mbarn}. \tag{3.50}$$

Transforming the distribution of pions into a distribution of electrons/positrons, i.e. $q_{\pi^\pm}\mathrm{d}E_{\pi^\pm} = q_{\mathrm{e}^\pm}\mathrm{d}E_{\mathrm{e}^\pm}$, and estimating the mean energy of the produced electrons or positrons from the decay channel $\pi^\pm \longrightarrow \mathrm{e}^\pm + 3\nu$ to be $\langle E_{\mathrm{e}^\pm}\rangle = \langle E_{\pi^\pm}\rangle /4$ (Mannheim & Schlickeiser, 1994) yields

$$q_{\mathrm{e}^\pm}^\mathrm{sec}(E_{\mathrm{e}^\pm}) = q_{\pi^\pm}\left[E_{\pi^\pm}(E_{\mathrm{e}^\pm})\right] \frac{\mathrm{d}E_{\pi^\pm}}{\mathrm{d}E_{\mathrm{e}^\pm}} = 4 q_{\pi^\pm}(4E_{\mathrm{e}^\pm}). \tag{3.51}$$

Combining this with Eq. (3.49) gives

$$q_\mathrm{e}^\mathrm{sec}(E_\mathrm{e}) = q_{\mathrm{e}^+}^\mathrm{sec}(E_\mathrm{e}) + q_{\mathrm{e}^-}^\mathrm{sec}(E_\mathrm{e}) = \frac{64}{3} n_\mathrm{H} \frac{\tilde{C}_\mathrm{p}}{m_\mathrm{p}c} \sigma_\mathrm{pp}^\pi(\alpha_\mathrm{p}) \left(\frac{16E_\mathrm{e}}{m_\mathrm{p}c^2}\right)^{-\alpha_\mathrm{p}}. \tag{3.52}$$

The resulting secondary electron/positron energy distribution can be inferred from the fact that the source function is a production rate that is acting on a characteristic timescale of pp-interactions τ_π:

$$f_{\mathrm{e}^\pm,\mathrm{uncooled}}^\mathrm{sec}(E_{\mathrm{e}^\pm}) = q_{\mathrm{e}^\pm}^\mathrm{sec}(E_{\mathrm{e}^\pm})\tau_\pi, \text{ where} \tag{3.53}$$

$$\tau_\pi = \frac{1}{c n_\mathrm{H} K_\mathrm{p} \sigma_\mathrm{pp}^\pi}, \tag{3.54}$$

provided there are no other cooling processes. Figure 3.17 shows the ratio of the resulting spectrum of secondary electrons plus positrons to the underlying proton spectrum as a function of energy, E,

[7] Note that $\tilde{C}_\mathrm{p}$ denotes the normalisation of the CR distribution function in units of cm^{-3} while C_p is the normalisation of the CR source function in units of $\mathrm{cm}^{-3}\ \mathrm{s}^{-1}$.

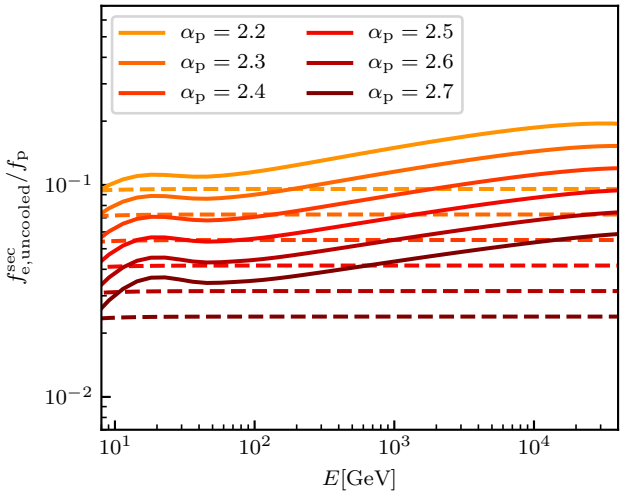

Figure 3.17: Ratio of secondary electrons and positrons to protons in our approach (solid lines) compared to the analytical model (dashed lines, Pfrommer & Enßlin, 2004), for different values of the spectral index of the proton spectrum α_p.

i.e. in the analytical model

$$\frac{f^{sec}_{e,uncooled}(E)}{f_p(E)} = \frac{2 f^{sec}_{e^{\pm},uncooled}(E)}{f_p(E)} = \frac{128}{3}\, 16^{-\alpha_p}. \tag{3.55}$$

4. Cosmic rays and non-thermal emission in simulated galaxies - II. γ-ray maps, spectra and the far infrared-γ-ray relation

This chapter is based on our work published in Werhahn et al. (2021b).

The γ-ray emission of star-forming (SF) galaxies is attributed to hadronic interactions of cosmic ray (CR) protons with the interstellar gas and contributions from CR electrons via bremsstrahlung and inverse Compton (IC) scattering. The relative importance of these processes in different galaxy types is still unclear. We model these processes in three-dimensional magneto-hydrodynamical (MHD) simulations of the formation of isolated galactic discs using the moving-mesh code Arepo, including dynamically coupled CR protons and adopting different CR transport models. We calculate steady-state CR spectra and also account for the emergence of secondary electrons and positrons. This allows us to produce detailed γ-ray maps, luminosities and spectra of our simulated galaxies at different evolutionary stages. Our simulations with anisotropic CR diffusion and a low CR injection efficiency at supernovae (SNe, $\zeta_{\rm SN} = 0.05$) can successfully reproduce the observed far infrared (FIR)-γ-ray relation. Starburst galaxies are close to the calorimetric limit, where CR protons lose most of their energy due to hadronic interactions and hence, their γ-ray emission is dominated by neutral pion decay. However, in low SF galaxies, the increasing diffusive losses soften the CR proton spectra due to energy-dependent diffusion, and likewise steepen the pionic γ-ray spectra. In turn, IC emission hardens the total spectra and can contribute up to $\sim$ 40 per cent of the total luminosity in low SF galaxies. Furthermore, in order to match the observed γ-ray spectra of starburst galaxies, we require a weaker energy dependence of the CR diffusion coefficient, $D \propto E^{0.3}$, in comparison to Milky Way-like galaxies.

4.1 Introduction

The emergence of CRs in SF galaxies can be inferred from their non-thermal emission. Besides synchrotron emission that arises from the CR electron population and is visible in radio wavelengths, we also expect γ-ray emission in the GeV-TeV range. On the one hand, inelastic collisions of CR protons with the ambient medium are responsible for creating neutral pions that decay further into γ-ray photons. On the other hand, the CR electron population produces γ rays either via bremsstrahlung, or by scattering off of photons from the cosmic microwave background (CMB) and other interstellar radiation fields, i.e. via IC scattering.

These processes have been predicted to occur in the nuclei of starburst galaxies, where SN rates, stellar wind powers and gas densities are expected to be large (Völk et al., 1996; Blom et al., 1999). These conditions imply an observable γ-ray flux from SF galaxies such as NGC 253, M82 and M31 (Romero & Torres, 2003; Persic et al., 2008; de Cea del Pozo et al., 2009; Rephaeli et al., 2010; McDaniel et al., 2019). Indeed, these galaxies have been detected at GeV and TeV energies by several experiments, e.g., by *Fermi* LAT (Ackermann et al., 2012b), the VERITAS Collaboration et al. (2009) and the H. E. S. S. Collaboration et al. (2018).

The γ-ray luminosities of a sample of SF galaxies have been found to correlate with their FIR luminosities (Ackermann et al., 2012b; Rojas-Bravo & Araya, 2016; Linden, 2017; Ajello et al., 2020), which traces the star formation rate (SFR). The ultra-violet (UV) light of young stellar populations gets absorbed by dust and re-emitted in the FIR, and at the same time, CRs are accelerated at remnants of supernova (SN) explosions. Hence, we expect a connection between these quantities if proton calorimetry holds (Pohl, 1994), similar to the well-known relation between radio and FIR luminosity (Völk, 1989; Lacki et al., 2010). Calorimeter theory describes the condition that inelastic collisions in the interstellar medium (ISM) occur on short timescales so that CR protons lose most of their energy before escaping the galaxy. However, the emergence of this relation over many orders of magnitude in SFRs and its non-linearity at low SFR has not been fully understood yet. In the case of starburst galaxies, the calorimetric assumption has been tested by modeling the spectra of individual galaxies with one-zone models (Lacki et al., 2011; Yoast-Hull et al., 2013). The departure from the linear relation at low SFRs has been attributed to the increasing relevance of non-radiative losses in those galaxies, e.g., adiabatic losses (Pfrommer et al., 2017b), diffusion and/or advection (Thompson et al., 2007; Strong et al., 2010; Lacki et al., 2011; Ackermann et al., 2012b; Martin, 2014; Kornecki et al., 2020). However, the small number of galaxies with low SFRs detected in γ rays makes it hard to constrain the relation in this regime. Furthermore, there might also be other contributions to the γ-ray emission of those SF galaxies, including a contribution

due to a population of high-energy pulsars in the SMC (Abdo et al., 2010; Lopez et al., 2018). Similarly, there might be pulsars and their nebulae or SN remnants contributing to the γ-ray flux of the LMC (Ackermann et al., 2016). Active galactic nuclei (AGN) can also contaminate the γ-ray flux, which has been postulated, e.g., for NGC 4945 (Wojaczyński & Niedźwiecki, 2017).

In previous one-zone models, the magnetic field strength, the CR electron and proton energy densities are considered to be free parameters that are fit to reproduce observed gamma-ray and radio emission spectra (Torres, 2004; Domingo-Santamaría & Torres, 2005; Persic et al., 2008; de Cea del Pozo et al., 2009; Lacki et al., 2010, 2011; Paglione & Abrahams, 2012; Yoast-Hull et al., 2013, 2015; Eichmann & Becker Tjus, 2016). Because this is an under-constrained system, a closure is assumed by either requiring that the CR proton and magnetic energy densities are in equipartition or by adopting a universal CR electron-to-proton ratio that is observed at the Solar radius in the Milky Way. More detailed one-dimensional flux-tube models (Breitschwerdt et al., 2002) and two-dimensional axisymmetric models (Martin, 2014; Buckman et al., 2020) make use of parametrized source functions, and/or prescribed density and magnetic field distributions.

Instead, here we will simulate the γ-ray emission attributed to the star formation activity in galaxies, i.e. due to the emergence of CRs, by using three-dimensional MHD simulations of the formation and evolution of isolated galactic discs. Note that neither the CR proton nor the magnetic energy densities are free parameters in our approach but a product of our MHD simulations. We will be using results from kinetic plasma simulations (Caprioli & Spitkovsky, 2014) in combination with a detailed modelling of multi-frequency emission maps and spectra of supernova remnant (SNRs) to determine the CR acceleration efficiencies (Pais et al., 2018, 2020; Pais & Pfrommer, 2020; Winner et al., 2020). Equivalently, our forming galaxy drives a turbulent magnetic dynamo that amplifies the field to observed field strengths (Pfrommer et al., 2021).

In addition to only accounting for CR protons and assuming a fixed spectral index for their energy distribution (Pfrommer et al., 2017b), we also account for possible changes in the spectral index due to energy dependent diffusion as well as cooling processes in this work. We revisit the production of secondary particles, such as γ rays, secondary electrons and positrons, and also consider leptonic emission processes in the γ-ray regime from secondary leptons and primary, shock-accelerated electrons at SNe. As such, we intend to gain new insights into the physical processes governing the γ-ray emission of SF galaxies.

This paper is the second paper of a series of three papers. It is based on the modeling of the steady-state spectra of CR electrons and protons as described in Werhahn et al. (2021a, hereafter Paper I). We recap our approach in Section 4.2. We present γ-ray emission maps resulting from different production channels of our simulated galaxies in Section 4.3, where we analyse the FIR-

γ-ray relation in Section 4.3.1 and compare our γ-ray spectra to observations in Section 4.3.2. A discussion of our results and a conclusion is presented in Section 4.4. In Section 2.3.1, we detail the non-thermal emission processes emerging in the γ-ray regime, i.e., γ-ray emission from neutral pion decay as well as the IC and bremsstrahlung emission.

4.2 Description of the methods

4.2.1 Simulations

Using the moving mesh code Arepo (Springel, 2010; Pakmor et al., 2016a), we simulate the formation of isolated galaxies from the collapse of a gas cloud that is initially in hydrostatic equilibrium with the dark matter halo as described in Paper I. The galaxies are embedded in dark matter halos that follow an NFW (Navarro et al., 1997) profile with a concentration parameter of $c_{200} = 12$ and masses of $M_{200}/\mathrm{M}_\odot = \{10^{10}, 10^{11}, 3\times10^{11}, 10^{12}\}$. Each halo contains 10^7 gas cells, each carrying a target mass of $155\,\mathrm{M}_\odot \times M_{200}/(10^{10}\,\mathrm{M}_\odot)$ and we enforce that the mass of all cells remains within a factor of two of the target mass by explicitly refining and de-refining the mesh cells.

The magnetic field evolution is prescribed by ideal MHD (Pakmor & Springel, 2013), which was shown to produce magnetic fields in cosmological simulations that match Milky Way observations (Pakmor et al., 2017, 2018, 2020). We adopt two different values for the initial seed magnetic field $B_0 = \{10^{-12}, 10^{-10}\}$ G that is oriented along the x axis. As the gas collapses, the magnetic field experiences adiabatic compression and grows exponentially via the emergence of a turbulent small-scale dynamo (Pfrommer et al., 2021). Conservation of specific gas angular momentum causes the gas to settle in a disc out of which a galaxy forms inside out, which continues to amplify and order the disc magnetic field.

CR protons are self-consistently included with the one-moment formalism (Pakmor et al., 2016b; Pfrommer et al., 2017a). We instantaneously inject CRs at the SNe with a fraction ζ_{SN} of the kinetic energy of the SN explosion and model CR transport in two different ways: we either only advect them with the gas or additionally account for anisotropic CR diffusion along the magnetic field with a constant parallel diffusion coefficient of $D = 10^{28}\,\mathrm{cm^2\,s^{-1}}$ or $D = 3\times10^{28}\,\mathrm{cm^2\,s^{-1}}$. In table 4.1, we give an overview of the different configurations of our simulations.

The relation between the isotropic CR diffusion coefficient D_{iso} and the coefficient along the magnetic field, D, depends on the exact magnetic field configuration. While a turbulent field implies $D_{\mathrm{iso}} = D/3$, pure CR transport along the homogeneous magnetic field yields $D_{\mathrm{iso}} = D$.

The latter situation is realised for active CR-driven wind feedback as CRs move along open field lines from the disc into the halo and the homogeneity of the magnetic field either results from the velocity shear of the outflow or the Parker instability. CR propagation within a turbulent spiral arm of the galaxy may prefer the situation with $D_{\rm iso} = D/3$. In fact, our adopted values for D are bracketing these two cases and are consistent with the recently discovered hardening of the logarithmic momentum slope of the CR proton spectrum at low Galactocentric radii, which is interpreted as a signature of anisotropic diffusion in the Galactic magnetic field (Cerri et al., 2017; Evoli et al., 2017). Analysing AMS-02 data of unstable secondary CR nuclei that result from spallation processes in the ISM yields the residence time of CRs inside the Galaxy that constrains identical values for the diffusion coefficient (Evoli et al., 2019, 2020a).

We vary the energy efficiency of CR acceleration and inject CR protons directly at the location of core-collapse SN explosions with $\zeta_{\rm SN} = 5$ per cent to 10 per cent of the canonical kinetic SN energy of 10^{51} erg. While the larger value is a canonical value adopted in CR studies, the low efficiency is motivated by taking the acceleration efficiency of ≈ 0.15 inferred by hybrid particle-in-cell simulations of proton acceleration at quasi-parallel shocks, in which the shock normal is close to the upstream magnetic field orientation (Caprioli & Spitkovsky, 2014) and averaging the result over the entire supernova remnant. This yields a CR proton acceleration efficiency of ≈ 0.05, independent of magnetic morphology (Pais et al., 2018). MHD simulations of expanding shell-type supernova remnants in the Sedov-Taylor phase that adopt such an efficiency for protons are able to match observational multi-frequency data (Pais et al., 2020; Pais & Pfrommer, 2020; Winner et al., 2020). We intend to assess the effect of varying those parameters and prescriptions of CR transport on the resulting γ-ray emission in our simulated galaxies.

4.2.2 Steady-state spectra

We follow the approach described in Paper I, where we calculate steady-state spectra $f(E) = {\rm d}N/({\rm d}E\,{\rm d}V)$ in each cell of our simulations by solving the diffusion-loss equation for CR protons, primary and secondary electrons, respectively. Following e.g., Ginzburg & Syrovatskii (1964) and Torres (2004), this reads

$$\frac{f(E)}{\tau_{\rm esc}} - \frac{\rm d}{{\rm d}E}\left[f(E)b(E)\right] = q(E), \tag{4.1}$$

where E denotes the CR energy. The injection spectrum $q(E) = q[p(E)]{\rm d}p/{\rm d}E$ is assumed to be a power law in momentum for CR protons as well as primary electrons, with the same spectral index $\alpha_{\rm inj} = 2.2$ (Lacki & Thompson, 2013). Furthermore, we assume an exponential cutoff in the

Table 4.1: Overview of the parameters of the different simulations with CR advection and anisotropic CR diffusion ('CR diff'): halo mass M_{200}, CR energy injection efficiency $\zeta_{\rm SN}$, initial magnetic field B_0 and parallel diffusion coefficient D. Note that in addition to these simulations, we also simulated all configurations with pure CR advection without accounting for diffusion ('CR adv').

M_{200} [$\mathrm{M}_\odot$]	$\zeta_{\rm SN}$	B_0 [G]	D [cm^2/s]
10^{12}	0.05	10^{-10}, 10^{-12}	1×10^{28}
3×10^{11}	0.05	10^{-10}, 10^{-12}	1×10^{28}
10^{11}	0.05	10^{-10}, 10^{-12}	1×10^{28}
10^{10}	0.05	10^{-10}, 10^{-12}	1×10^{28}
10^{10}	0.05	10^{-10}	3×10^{28}
10^{12}	0.10	10^{-12}	1×10^{28}
3×10^{11}	0.10	10^{-12}	1×10^{28}
10^{11}	0.10	10^{-12}	1×10^{28}
10^{10}	0.10	10^{-12}	1×10^{28}
10^{10}	0.10	10^{-12}	3×10^{28}

source functions given by

$$q_i(p_i)\mathrm{d}p_i = C_i p_i^{-\alpha_{\rm inj}} \exp\left[-(p_i/p_{{\rm cut},i})^n\right]\mathrm{d}p_i, \tag{4.2}$$

where $i = \mathrm{e}, \mathrm{p}$ denotes the CR species and $n = 1$ for protons and $n = 2$ for electrons (Zirakashvili & Aharonian, 2007; Blasi, 2010). The cutoff momenta are for protons $p_{\rm cut,p} = 1\,\mathrm{PeV}/m_{\rm p}c^2$ (Gaisser, 1990) and electrons $p_{\rm cut,e} = 20\,\mathrm{TeV}/m_{\rm e}c^2$ (Vink, 2012).

For CR protons, we consider energy losses, $b(E) = -\mathrm{d}E/\mathrm{d}t$, due to hadronic losses and Coulomb interactions. After also accounting for CR escape due to advection and diffusion we re-normalise the steady-state spectra to match the CR energy density in each cell. The escape losses include losses due to advection and diffusion, i.e.,

$$\tau_{\rm esc} = \frac{1}{\tau_{\rm adv}^{-1} + \tau_{\rm diff}^{-1}}. \tag{4.3}$$

The diffusion timescale is estimated using an estimate for the diffusion length in each cell, $L_{\rm CR} =$

$\varepsilon_{\rm CR}/|\nabla\varepsilon_{\rm CR}|$, via

$$\tau_{\rm diff} = \frac{L_{\rm CR}^2}{D}. \tag{4.4}$$

Furthermore, we assume an energy dependent diffusion coefficient $D = D_0(E/E_0)^\delta$, where we use $D_0 = 10^{28}$ and $3 \times 10^{28}\,{\rm cm^2\ s^{-1}}$ and $E_0 = 3\,{\rm GeV}$. The energy dependence of our diffusion coefficient is assumed to be $\delta = 0.5$ in our fiducial model, which has been obtained by fitting observed beryllium isotope ratios (Evoli et al., 2020a). We also study how modifying this parameter impacts the resulting γ-ray emission. We calculate the timescale of advection via

$$\tau_{\rm adv} = \frac{L_{\rm CR}}{v_z}, \tag{4.5}$$

where we only take into account cell velocities away from the disc in z-direction. This is justified because mass fluxes in and out of cells in the azimuthal direction nearly compensate each other (see figure 6 of Paper I, which corresponds to Fig. 3.6 in this work). Hence, in the cell-based approximation, only the advection perpendicular to and away from the disc is relevant in order to estimate the advection losses. Note that radial CR transport via advection and anisotropic diffusion is also strongly suppressed because of the largely toroidal magnetic field configuration in the disc (Pakmor & Springel, 2013; Pakmor et al., 2016c) and the dominant kinetic energy density associated with the toroidal velocity component (Pfrommer et al., 2021). Any residual CR fluxes not explicitly modeled in our steady-state approach need to be simulated by evolving the CR electron and proton spectra in our MHD simulations (Winner et al., 2019, 2020; Girichidis et al., 2020b).

In addition to escape losses, CR electrons can also lose energy due to the emission of radiation. Hence, their energy loss terms $b(E)$ additionally include synchrotron, IC and bremsstrahlung losses. The synchrotron and IC losses have the same dependence on energy, i.e. in the relativistic regime we obtain $b_{\rm syn} \propto B^2E^2$ and $b_{\rm IC} \propto B_{\rm ph}^2E^2$ (where B and $B_{\rm ph} = \sqrt{8\pi\varepsilon_{\rm ph}}$ are the strengths of the magnetic field and equivalent magnetic field of a photon distribution with an energy density $\varepsilon_{\rm ph}$, respectively), whereas bremsstrahlung losses scale as $b_{\rm brems} \propto n_{\rm p}E\ln(2E)$ (where $n_{\rm p}$ is the proton number density, see Paper I for details). Furthermore, the primary electron population is tied to the protons by means of an injected ratio of electrons to protons, i.e. $K_{\rm ep}^{\rm inj} = 0.02$, which is chosen so that it reproduces the observed value in the Milky Way at 10 GeV, when averaging over the CR spectra around the solar galacto-centric radius in a snapshot that resembles the Milky Way in terms of halo mass and SFR (see Paper I for a more detailed discussion).

Inelastic collisions of CR protons with the ISM generate a secondary population of CR electrons

and positrons. We calculate their production spectra using different approaches. For small kinetic proton energies, i.e., $T_\mathrm{p} < 10\,\mathrm{GeV}$, we use the model by Yang et al. (2018b) for the normalised pion energy distribution and combine it with our own parametrization of the total cross section for $\pi^\pm$ production that is provided in Werhahn et al. (2021a). At high energies, we adopt the description by Kelner et al. (2006) for $T_\mathrm{p} > 100\,\mathrm{GeV}$ and perform a cubic spline interpolation in the energy range in between.

In Paper I, we study the validity of the cell-based steady-state assumption. To this end, we calculate the characteristic timescale of the change in total energy density of CRs in our simulations, $\tau_\mathrm{CR} = \varepsilon_\mathrm{CR}/\dot{\varepsilon}_\mathrm{CR}$. In order to maintain a steady state, we require that all cooling or escape processes in the diffusion-loss equation are faster than that timescale, i.e., $\tau_\mathrm{all} \lesssim \tau_\mathrm{CR}$. Here, τ_all is the combined rate of all relevant cooling and diffusion processes at a given energy, i.e., $\tau_\mathrm{all}^{-1} = \tau_\mathrm{cool}^{-1} + \tau_\mathrm{diff}^{-1}$.[1] In figure 9 of Paper I (corresponding to Fig. 3.9 in this work), we find that the steady-state approximation breaks down in regions of low gas density, in regions surrounding SNRs that host freshly injected CRs, and in outflows: these are all situation that lead to fast changes in the CR energy density, which disturb the steady-state configuration and would require to dynamically evolve the spectral CR proton and electron distributions (Winner et al., 2019; Girichidis et al., 2020b; Ogrodnik et al., 2021). However and most importantly, weighting each Voronoi cell by the non-thermal radio synchrotron or hadronic gamma-ray emission reshapes the distribution in such a way, that the absolute majority of non-thermally emitting cells obey the steady-state condition: $\tau_\mathrm{all} \lesssim \tau_\mathrm{CR}$. This implies that the steady-state assumption is well justified in regions that dominate the non-thermal emission.

4.2.3 Non-thermal emission processes in the gamma-ray regime

We consider the following processes contributing to the emission of γ-rays from CRs:

$$j_E = E\frac{\mathrm{d}N_\gamma}{\mathrm{d}E\,\mathrm{d}V\,\mathrm{d}t} = j_{E,\pi^0} + j_{E,\mathrm{IC}} + j_{E,\mathrm{brems}}, \tag{4.6}$$

where N_γ denotes the number of produced photons with energy E per unit energy, volume and time. The first term arises from hadronic interactions of CR protons with the ISM, that produce neutral pions, that in turn decay further into two γ-ray photons. To calculate the resulting emissivity j_{E,π^0}, we adopt the parametrizations given by Yang et al. (2018b) for small proton kinetic energies

[1] Except for fast outflows, the advection timescale is larger than the diffusion timescale throughout the galaxy as is shown in figure 7 of Werhahn et al. (2021a) corresponding to Fig. 3.7 in this work. This justifies our neglect of advection in τ_all.

$T_\mathrm{p} < 10\,\mathrm{GeV}$ and the model by Kafexhiu et al. (2014) at larger energies. Furthermore, the primary and secondary CR electron populations give rise to two additional emission processes. In the presence of an ambient radiation field, low-energy photons can be up-scattered by CR electrons via IC scattering to gamma-ray energies. We calculate the emitted IC emissivity $j_{E,\mathrm{IC}}$ including the Klein-Nishina formalism, following Jones (1968) and Blumenthal & Gould (1970). For the incident radiation field scattering off of CR electrons, we take into account the radiation from the CMB and from stars. We assume that the latter is dominated by FIR emission, which is absorbed and re-emitted UV radiation from young massive stars that are enshrouded by dusty environments. The FIR emission is characterised by a black body temperature of $T = 20\,\mathrm{K}$ (see Appendix 2.3.1 for details). Additionally, the acceleration of CR electrons in the field of charged nuclei causes the emission of bremsstrahlung, denoted by $j_{E,\mathrm{brems}}$, that we describe in the Born approximation for non-screened ions and for highly relativistic electrons (Blumenthal & Gould, 1970). We detail our calculation of these radiation processes in Section 2.3.1 and compare it to two other models from the literature in Appendix 4.5.

4.3 Non-thermal gamma-ray emission from simulated galaxies

We now apply the prescriptions for the three main radiation processes in the γ-ray regime (Section 4.2.3) to our simulated galaxies. To calculate the γ-ray emission from neutral pion decay, we use the steady-state spectra of CR protons f_p in each cell and solve the integral of Eq. (2.58). Similarly, the cell-based leptonic steady-state spectra, f_e, consisting of primary and secondary contributions, enable us to determine the resulting IC and bremsstrahlung emission from Eq. (2.73) and (2.83). Here, we make use of the physical quantities in each cell, i.e. the gas density (for hadronic interactions and bremsstrahlung emission) and our approximation for the photon radiation field (for the IC emission). Those properties are shown in Fig. 4.1 for a snapshot of a simulation with a halo mass of $M_{200} = 10^{12}\,\mathrm{M}_\odot$ after $t = 2.3\,\mathrm{Gyr}$ that includes anisotropic diffusion of CR protons. This snapshot exhibits a SFR, γ-ray and radio luminosity similar to M82 (see Table 4.2). In addition, the halo mass of $M_{200} = 10^{12}\,\mathrm{M}_\odot$ seems to be a reasonable assumption for M82. The stellar mass can be derived from the K-band apparent magnitude, which we take from the Two Micron All Sky Survey (2MASS; Skrutskie et al., 2006) Extended Source Catalog (XSC) to be $m_K = 4.665$. Adopting a distance of 3.7 Mpc yields a total magnitude of $M_K = -23.176$, from which we estimate the stellar mass of M82 of $\log_{10} M_\star \approx 10.66$, using the relation obtained by Cappellari (2013). Adopting the Moster et al. (2010) relation between stellar and halo mass of galaxies yields a halo mass of $1.6 \times 10^{12}\,\mathrm{M}_\odot$.

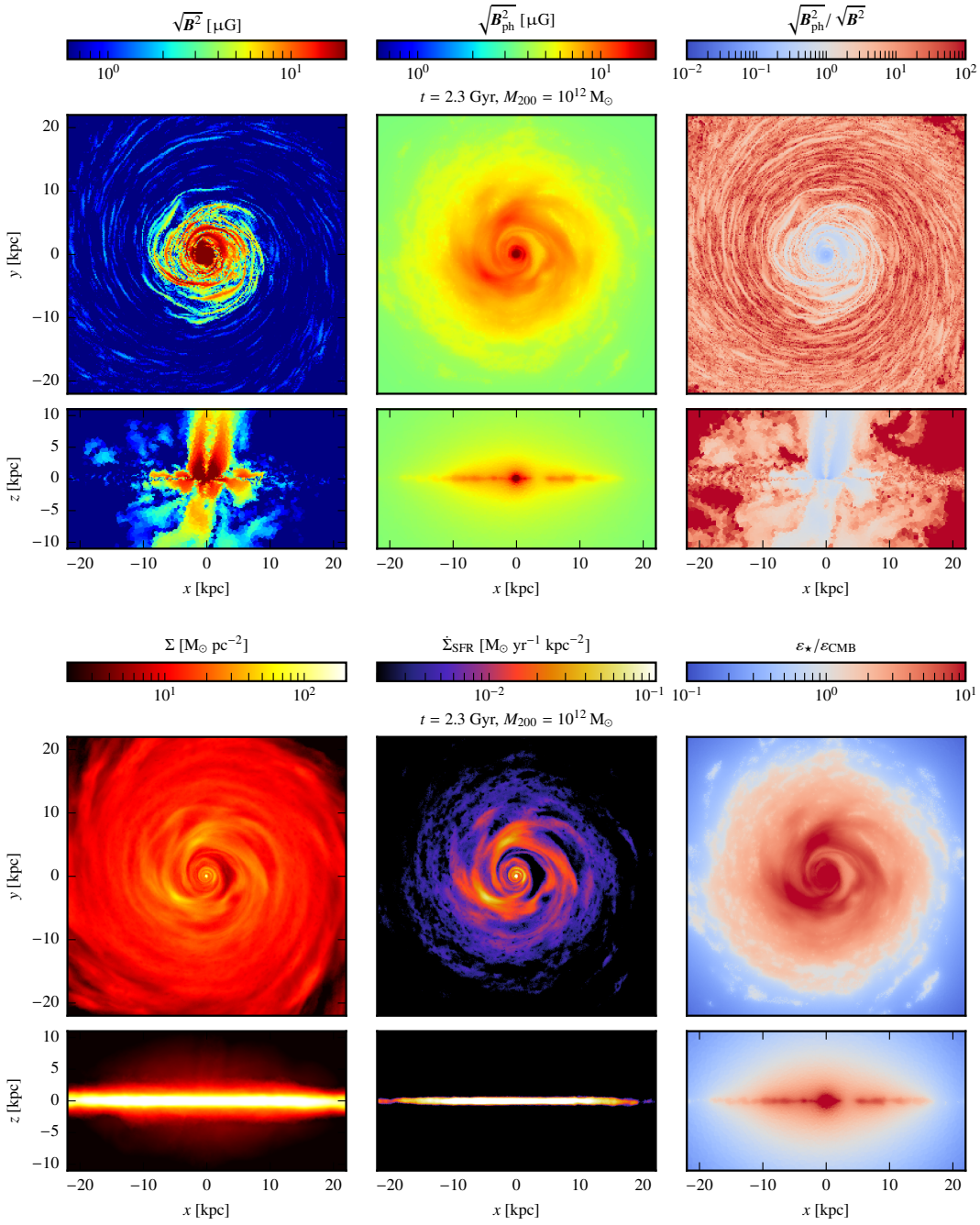

Figure 4.1: Face-on and edge-on maps of slices of the magnetic field, the equivalent magnetic field of the photon energy density, i.e. $B_{\rm ph} = \sqrt{8\pi\varepsilon_{\rm ph}}$, and their ratio (upper panels, from left to right). The lower panels show (from left to right) the projected gas surface density, the star-formation rate density and the ratio of the photon energy density from the stellar radiation field to the CMB.

Table 4.2: Overview of the individual observed galaxies, whose spectra are compared to simulated galaxies in Fig. 4.8. The SFRs have been calculated by Kornecki et al. (2020), using far UV (Gil de Paz et al., 2007; Cortese et al., 2012) and IRAS 25 µm data (Sanders et al., 2003). The observed γ-ray and FIR-luminosities are taken from Ajello et al. (2020). The FIR luminosities from our simulated galaxies are inferred using the Kennicutt (1998) relation.

Galaxy	SFR (obs./sim.) [$M_\odot$ yr^{-1}]	L_γ (obs./sim.) [erg s^{-1}]	$L_{\rm FIR}$ (obs./sim.) [$L_\odot$]	Simulation M_{200} [$M_\odot$], t [Gyr]
NGC 2146	14.0 ± 0.5[1]	8.86×10^{40}	1.17×10^{11}	-
	25.520	1.04×10^{41}	1.90×10^{11}	$M_{200} = 10^{12}$, $t = 0.7$
M82[2]	10.4 ± 1.6[1]	1.85×10^{40}	5.89×10^{10}	-
	6.457	2.62×10^{40}	4.81×10^{10}	$M_{200} = 10^{12}$, $t = 2.3$
NGC 253	5.03 ± 0.76[1]	1.16×10^{40}	2.75×10^{10}	-
	4.110	1.25×10^{40}	3.06×10^{10}	$M_{200} = 3 \times 10^{11}$, $t = 1.1$
SMC	0.027 ± 0.003[1]	1.38×10^{37}	7.24×10^{7}	-
	0.011	1.34×10^{37}	8.10×10^{7}	$M_{200} = 10^{10}$, $t = 2.3$

[1] Kornecki et al. (2020).
[2] See corresponding maps in Fig. 4.1 and 4.3.

The map of the magnetic field in Fig. 4.1 is shown after 2.3 Gyr of evolution and still traces the outflow that has already been launched at ~1 Gyr. At that time, the increasing CR pressure gradient sourced by the ongoing injection of CR protons at SN remnants within the disc launched a galactic outflow that eventually forced the magnetic field lines to open up. After 2.3 Gyrs, this feature is still imprinted in the morphology of the magnetic field, whereas the CR outflow has already dissolved due to the decreasing SFR and hence the decreasing CR injection over time.

Contrary to the peculiar morphology of the magnetic field, the galactic photon field that is composed of interstellar radiation and CMB as characterised by an equivalent magnetic field is rather homogeneously distributed, and persists well above and below the disc, where we also have CR electrons.[2] To order of magnitude, we can estimate the equivalent magnetic field of the stellar radiation energy density, $B_\star$. Using the SFR of 6.48 $M_\odot$ yr^{-1} of the 10^{12} $M_\odot$ model at 2.3 Gyr (shown in Fig. 4.1), this corresponds to a FIR luminosity of $L_{\rm FIR} = 4.8 \times 10^{10} L_\odot$ (see Eq. 2.75). Approximating the star formation as a uniform thin disk of radius r, we obtain

$$\frac{B_\star^2}{8\pi} = \frac{F_{\rm FIR}}{c} = \frac{L_{\rm FIR}}{2\pi r^2 c} \tag{4.7}$$

[2]For reference, the equivalent magnetic field of the CMB is 3.24 $(1+z)^2$ µG at cosmological redshift z, which at the present epoch corresponds to the light green colour in the top middle panel of Fig. 4.1.

and hence

$$B_\star \approx 5 \left(\frac{L_{\rm FIR}}{4.8 \times 10^{10} {\rm L}_\odot} \right)^{1/2} \left(\frac{r}{10 \text{ kpc}} \right)^{-1} \mu{\rm G}. \tag{4.8}$$

Adding the CMB equivalent magnetic field, we obtain the equivalent magnetic field of the galactic photon field, $B_{\rm ph} = \sqrt{B_\star^2 + B_{\rm CMB}^2}$, which ranges from $B_{\rm ph} \approx 6\,\mu$G at around 10 kpc to $B_{\rm ph} \approx 4\,\mu$G at around 20 kpc (see top-middle panel of Fig. 4.1). The bottom right-hand panel of Fig. 4.1 shows the stellar-to-CMB energy density ratio: the stellar radiation energy density dominates over that of the CMB inside a galactocentric radius of $r \lesssim 20$ kpc, which reinforces the need to reliably model this contribution as its morphology is imprinted into the IC gamma-ray emission.

The top panel on the right-hand side of Fig. 4.1 shows the ratio $B_{\rm ph}/B$ that indicates the relative importance of IC and synchrotron processes: while the central regions at $r \lesssim 5$ kpc has a dominant magnetic field with $B \gtrsim B_{\rm ph}$ so that synchrotron emission dominates over IC radiation, the situation is reversed at larger radii. Hence, we also expect the IC losses to be dominant over synchrotron losses at these larger radii $r \gtrsim 5$ kpc in the disc and outside the outflows in which synchrotron effects dominate because of the strong magnetic field.

In addition, in the bottom panels of Fig. 4.1 we show the gas column density and the SFR that closely traces the former. This is a consequence of our ISM, which is modelled with an effective equation of state (Springel & Hernquist, 2003). In this model, the star-forming gas is treated as a two phase medium in which star formation occurs in thermally unstable dense gas above a critical threshold density of $n_{\rm th} = 0.13\,{\rm cm}^{-3}$ in a stochastic manner with a probability that scales exponentially with time.

Figure 4.2 shows the spectral density of CR protons, primary and secondary electrons at 10 GeV. Each of these face-on maps reveal the close morphological correspondence of dense star-forming regions (in form of spiral structures) and the produced primary electrons and protons, see Fig. 4.1. Interestingly, the secondary CR electron maps exhibits low-density cavities that correspond to locations of SNR bubbles that form as a consequence of young stellar populations and which have freshly injected CR protons. The edge-on views of the different CR population reveal striking differences: while primary CR electron and proton maps are puffed up and show a CR-driven galactic wind,[3] the secondary CR electron map is tightly constrained to the dense ISM because its source function scales as $f_{\rm e}^{\rm sec} \propto n_{\rm N} f_{\rm p}$, where $n_{\rm N}$ denotes the number density of target nucleons in

[3]The morphology of primary CR electrons become progressively more uncertain in galactic outflows (at large distances from sources) where the steady-state condition is not fulfilled and because the source function does not anymore represent generic CR sources such as SNRs but net gains due to advection. We postpone simulations that explicitly follow the electron distribution in space and time (Winner et al., 2019, 2020) to future work.

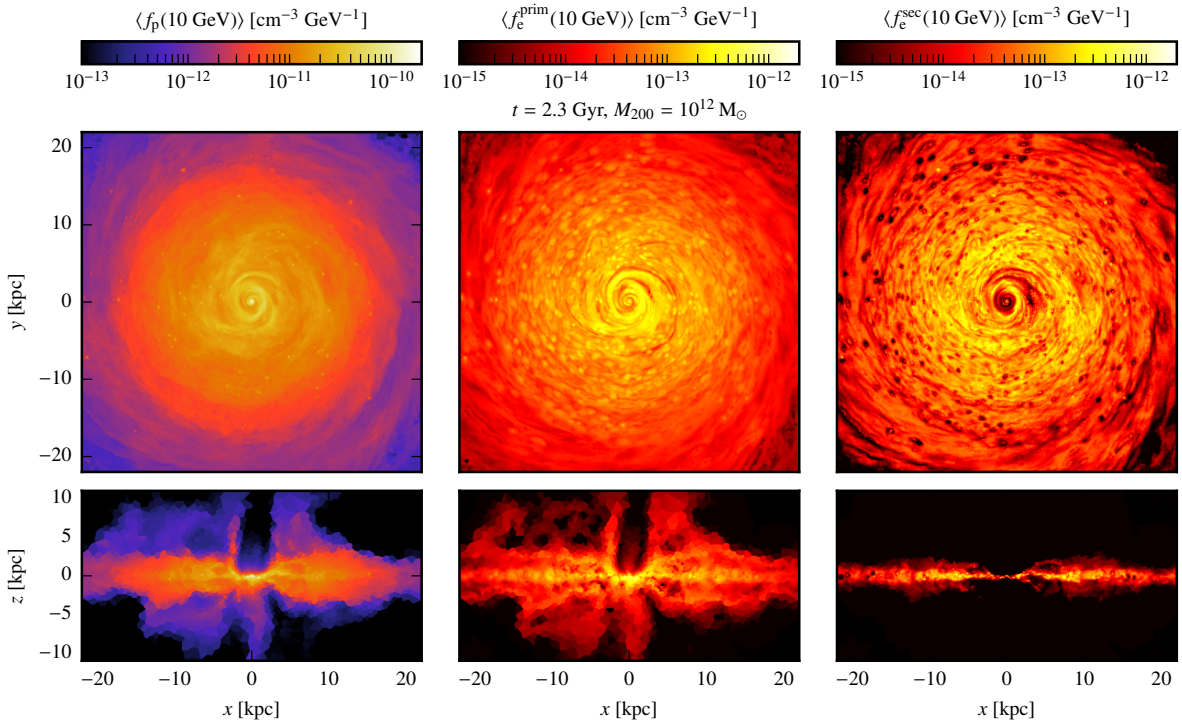

Figure 4.2: Face-on and edge-on maps of the spectral density of CR protons and primary and secondary CR electrons (at 10 GeV), averaged over a slice with thickness 0.3 pc, for the same halo as in Fig. 4.1.

the ISM, see Section 2.3.1.

The resulting maps of the different radiation processes at an energy of 1 GeV are shown in Fig. 4.3 for the different components. To this end, we project the emissivities along the line of sight to obtain face-on and edge-on views of the simulated galaxy. The IC emission is dominated by the emission resulting from primary CR electrons, that also reside outside the disc, where the photon radiation field acting as incoming photons for IC scattering is still strong. In contrast, secondary electrons can only be effectively produced within the disc, where the gas density is high (see column density panel in Fig. 4.1), which thus also confines their IC emission close to the mid-plane. Similarly, the γ-ray emission from neutral pion decay is strongest within the disc, where the gas and CR proton densities are both high. In contrast to the IC emission, the bremsstrahlung emission arising from primary and secondary electrons show similar strengths of their projected emissivities and in both cases, the emission approximately mimics the morphology of the gas density. This results from a similar occurrence of primary and secondary electrons in the disc (as discussed in Paper I) at 10 GeV and hence, their emitted bremsstrahlung is found to be comparably strong. Finally, the total emission at 1 GeV, that is shown in the lower right panel, is dominated by hadronic emission within the disc and the central regions of the galaxy, whereas IC emission from primary electrons is the main contributor to the total emission above and below the mid-plane.

4.3.1 The FIR-γ-ray-relation

Observations

As CRs are injected at SNRs, we expect a connection between the SFR and the γ-ray emission of SF galaxies. In fact, this as been found by Ackermann et al. (2012b) and Rojas-Bravo & Araya (2016). Recently, Ajello et al. (2020) revisited the γ-ray luminosity observed with *Fermi* LAT of 11 bona-fide γ-ray emitting galaxies. We plot their observations (black points) in the upper panels of Fig. 4.4, converting their FIR-luminosites to SFRs using Kennicutt (1998), except for the SMC, LMC and M33. It is well known that for those low-SFR galaxies, the Kennicutt (1998) conversion from FIR-luminosity to SFR does not hold anymore. This has been particularly pointed out by Kornecki et al. (2020), who discuss this effect in more detail. Hence, in the upper panels of Fig. 4.4 we plot the SFR (black points) and FIR luminosities (grey points) separately for the SMC, LMC and M33, where the deviations from the simple FIR-to-SFR conversion are expected to be the largest. The SFR of M33 was recently investigated by Thirlwall et al. (2020), who obtained a value of $0.28^{+0.02}_{-0.01}\,\mathrm{M_\odot\,yr^{-1}}$. Reconstructing the star formation history of the LMC, Harris & Zaritsky (2009) deduce a lower limit for its current SFR of $0.2\,\mathrm{M_\odot\,yr^{-1}}$. Consistently, Kornecki

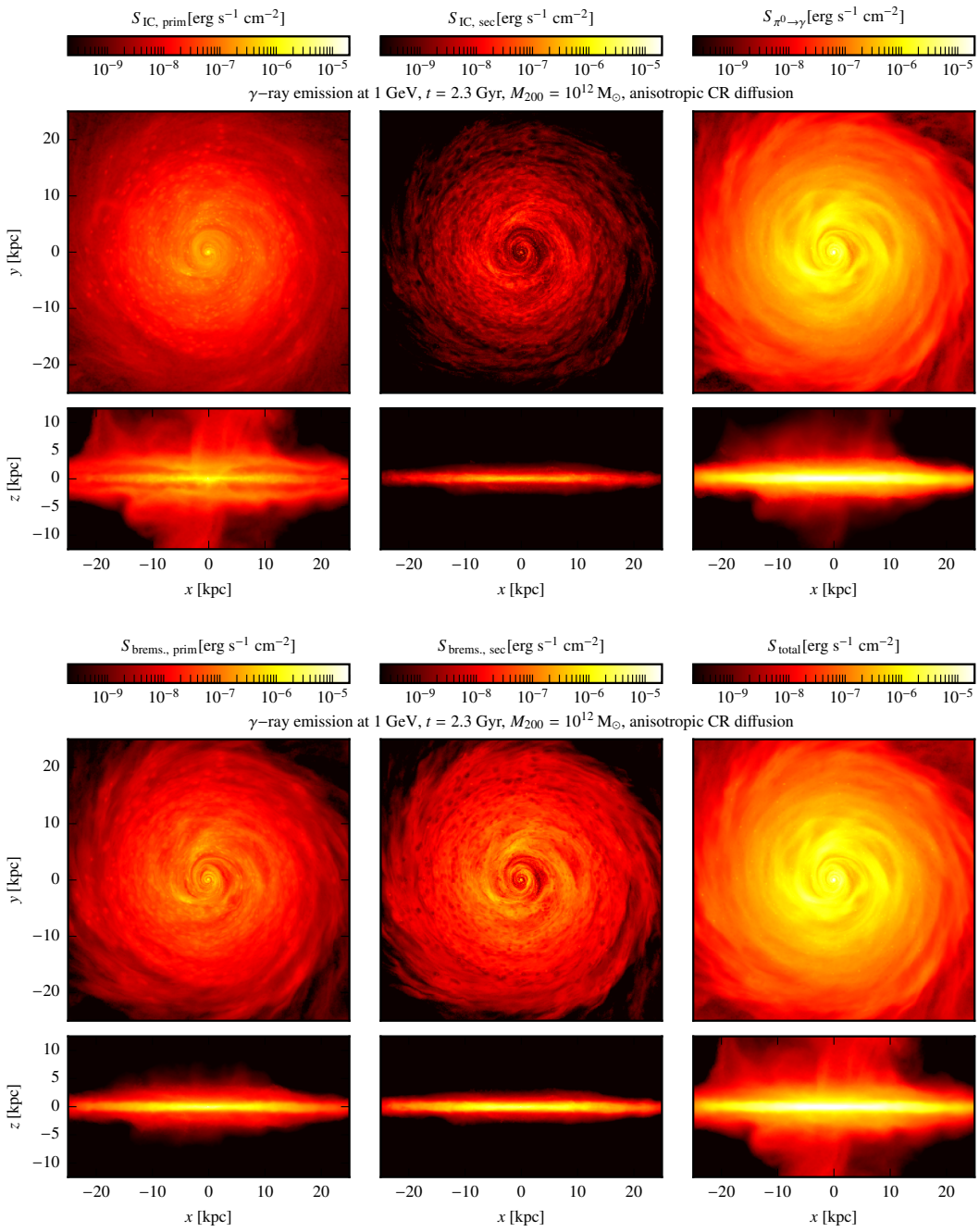

Figure 4.3: Projected maps of the γ-ray emission at 1 GeV from the same snapshot as shown in Fig. 4.1. From left to right, we show the different contributions, i.e. the primary and secondary IC emission, the emission from neutral pion decay in the upper panels and the primary and secondary bremsstrahlung as well as the total γ-ray emission in the lower panels.

et al. (2020) infer a SFR of $0.20 \pm 0.03\,M_\odot\,yr^{-1}$ from its observed far UV (Cortese et al., 2012) and IRAS 25 μm (Sanders et al., 2003) fluxes. In the same way, they obtain for the SMC a SFR of $0.027 \pm 0.003\,M_\odot\,yr^{-1}$.

It is important to keep in mind that the existing sample of SF galaxies that have been observed in γ rays is quite small, especially towards low SFRs, where the FIR-luminosity to SFR-conversion starts to break down. Hence, more observations of these galaxies with low SFRs are needed in order to better constrain the relation. In addition, there are still some galaxies included in the analysis of the FIR-γ-ray relation, that are suspected of hosting an AGN, that could give a significant contribution to the γ-ray luminosity, biasing the interpretation that the observed γ-ray emission is solely arising from SF processes in these galaxies.

Simulations

If we sum up the integrated emission from 0.1 to 100 GeV in each cell of our simulated galaxies, we get the total γ-ray luminosity, with contributions from the different radiation processes discussed above. In the upper panels in Fig. 4.4 we show the resulting FIR-γ-ray relation for our simulated galaxies with different halo masses (corresponding to different symbols) at different times, which corresponds to different star formation rates in the simulations. Starting from the time of the peak of the SFR, we chose for each simulation the snapshots where the SFR has approximately decreased by an e-folding. We show the model that only accounts for CR advection (violet) in comparison to the model that additionally includes anisotropic CR diffusion with a constant diffusion coefficient $D = 10^{28}\,cm^2\,s^{-1}$ (dark blue). Additionally, we show simulations with a higher diffusion coefficient of $D = 3 \times 10^{28}\,cm^2\,s^{-1}$ (light blue) for the smallest halo masses of $10^{10}\,M_\odot$. On top of that, we plot the observations (black symbols) and the upper limits detected by *Fermi* LAT from Ajello et al. (2020) and their best fit relation (orange line). We consider two different injection efficiencies $\zeta_{SN} = 0.05$ (top left-hand panel) and $\zeta_{SN} = 0.10$ (top right-hand panel).

Furthermore, we note that the influence of the choice of initial magnetic field ($B_0 = 10^{-10}$ or 10^{-12} G) on the resulting γ-ray emission is only marginal.[4] This is because gravo-turbulence driven by the initial infall of gas in our simulations results in a turbulent, small-scale dynamo that exponentially amplifies the seed magnetic field so that it saturates at a level close to equipartition with the kinetic turbulence at small scales, from where it is further amplified and ordered on larger scales (Pfrommer et al., 2021). As a result, the time of magnetic saturation and the launching of galactic winds vary among those models with a different seed magnetic field. This is shown in

[4]Pictured in the upper panels of Fig. 4.4 are the simulations with $B_0 = 10^{-10}$ G for $\zeta_{SN} = 0.05$ (left-hand panel) and $B_0 = 10^{-12}$ G for $\zeta_{SN} = 0.1$ (right-hand panel).

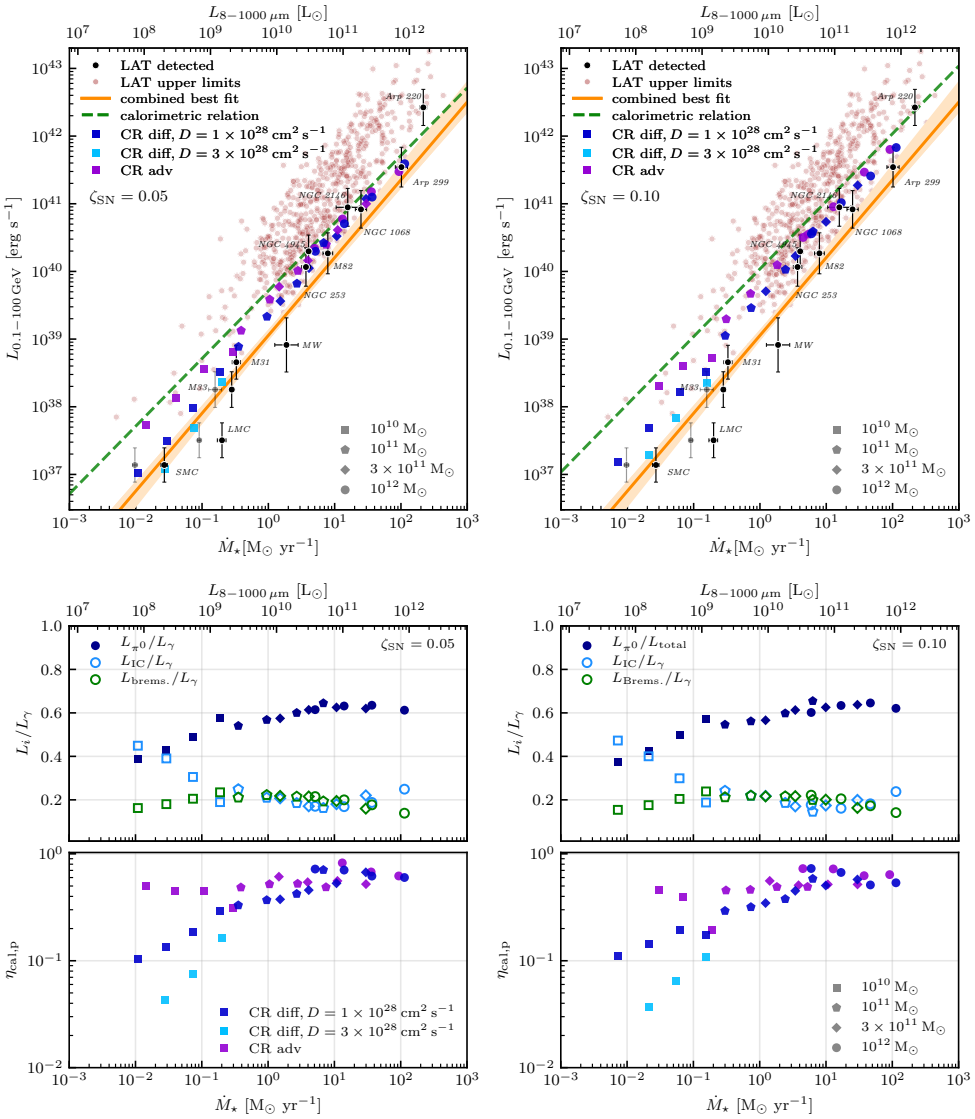

Figure 4.4: Upper panels: The FIR-γ-ray relation for our simulated galaxies, with $\zeta_{SN} = 0.05$ (left panel) and $\zeta_{SN} = 0.10$ (right panel). We contrast a model that only accounts for CR advection ('CR adv', purple) to the model that additionally includes anisotropic diffusion with different diffusion coefficients ('CR diff', dark and light blue). The calorimetric relation (dashed green line) is normalised to $L_\gamma/\eta_{cal,p}$ of the simulation with the highest SFR. Additionally, we show the FIR- and γ-ray luminosities obtained by Ajello et al. (2020), together with their fit to the data (orange line), that also includes the upper limits. For the SMC, LMC and M33, we show in addition to their FIR luminosity (in grey) also their SFRs as black points (see text for details). Middle panels: contributions of neutral pion decay (L_{π^0}), IC emission (L_{IC}) and bremsstrahlung ($L_{brems.}$) to the total γ-ray luminosity L_γ, integrated over 0.1-100 GeV, for $\zeta_{SN} = 0.05$ (left) and $\zeta_{SN} = 0.10$ (right) in our CR diffusion model. Lower panels: the calorimetric fraction $\eta_{cal,p}$ (see Eq. 4.10) as a function of SFR of our simulated galaxies. The calorimetric limit, where hadronic losses dominate ($\eta_{cal,p} \rightarrow 1$), is not reached by starburst galaxies.

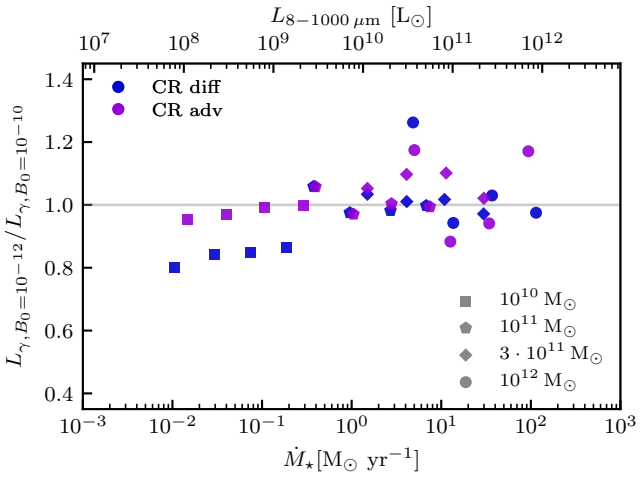

Figure 4.5: In order to evaluate the effect of changing the initial magnetic field B_0 in our simulations with $\zeta_{SN} = 0.05$ on the resulting gamma-ray emission, we show the ratio of the gamma-ray luminosity from our runs adopting $B_0 = 10^{-12}$ G relative to the gamma-ray luminosity from our runs with $B_0 = 10^{-10}$ G.

Fig. 4.5, where we quantify this effect on the total gamma-ray luminosity from our simulations with $\zeta_{SN} = 0.05$. When changing the initial magnetic field from $B_0 = 10^{-10}$ to 10^{-12} G, the difference in gamma-ray luminosities is less than 27 per cent and is below 10 per cent for three quarters of all analysed snapshots.

Two conclusions can be drawn from the upper panels in Fig. 4.4. First, we find that the smaller CR injection efficiency at SNR of $\zeta_{SN} = 0.05$ (upper left-hand panel) is preferred by the observations. Adopting a higher injection efficiency of $\zeta_{SN} = 0.10$ (upper right-hand panel) overestimates the observed relation for almost all combinations of halo masses and SFRs. Only the simulations with a higher diffusion coefficient of $D = 3 \times 10^{28}$ cm^2 s^{-1} manage to come close to the best-fit relation inferred from observations. Furthermore, even for the lower injection efficiency, the simulations that only account for advection of CRs (purple symbols) increasingly deviate from the observed relation for decreasing SFRs, where they produce significantly larger γ-ray luminosities in comparison to the observed galaxies (see also Pfrommer et al., 2017b).

To explain these trends in our simulations, we dissect the different contributions to the total γ-ray luminosity in Fig. 4.4 (middle panels), where we show the fractional contributions of neutral pion decay, IC emission and bremsstrahlung emission to the total γ-ray luminosity L_γ in our simulations for $\zeta_{SN} = 0.05$ and 0.10. The contribution of neutral pion decay to the total γ-ray emission decreases towards lower SF galaxies and is filled in by IC emission from CR electrons, whose contribution reaches up to ~ 40 per cent in galaxies with a small SFR of $\sim 10^{-2}$ $M_\odot$ yr^{-1}. The

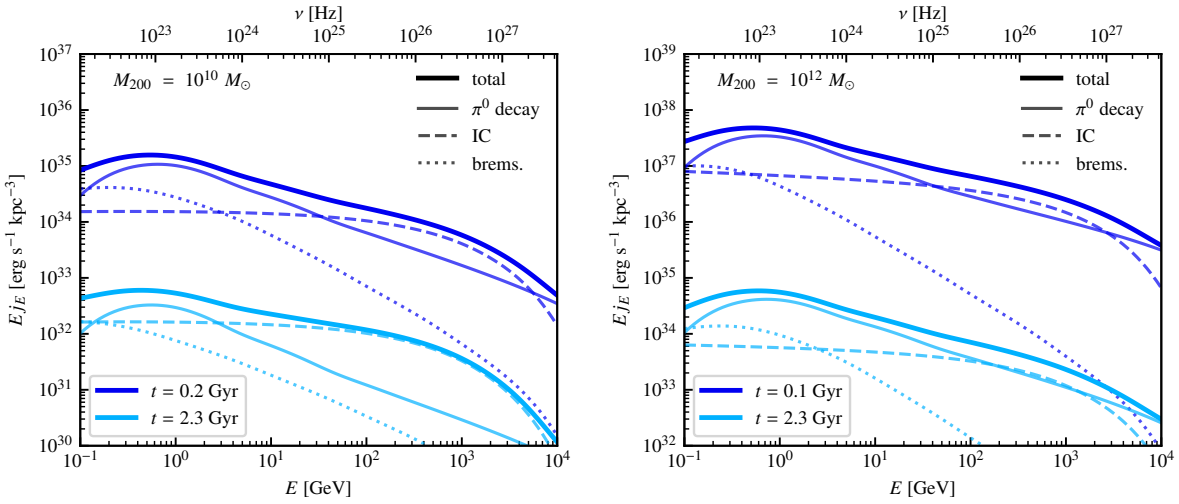

Figure 4.6: γ-ray spectra for halo masses $M_{200} = 10^{10}$ (left-hand panel) and $M_{200} = 10^{12}$ (right-hand panel) at the time of the peak of star formation and at a later time, when the SFR has decreased by two e-foldings. Shown are the contributions from neutral pion decay, IC and bremsstrahlung emission for each snapshot, as well as the total emitted spectrum (as indicated in the legend), respectively.

fractional contribution of bremsstrahlung contributes $\sim$ 20 per cent to the gamma-ray luminosity across all SFRs.

The smaller contribution of hadronic emission at small SFRs can be attributed to the decreasing gas density in those smaller galaxies, leading to less efficient hadronic losses of CR protons and allowing escape losses to dominate (see also e.g. Thompson et al., 2006, 2007; Strong et al., 2010; Lacki et al., 2010, 2011; Martin, 2014; Pfrommer et al., 2017b). This is underlined by Fig. 4.4 (lower panels), which we discuss in the following.

On average, a gamma-ray photon with an energy E can be produced by a proton with a kinetic energy of $T_\mathrm{p} \approx 8E$. In order to quantify the energy fraction of CR protons that are able to produce gamma-rays in the energy band ranging from E_1 to E_2, we define the bolometric energy fraction

$$\xi_\mathrm{bol} = \frac{\varepsilon_\mathrm{p}(p_1, p_2)}{\varepsilon_\mathrm{p}(0, \infty)} = \frac{\int_{p_1}^{p_2} q_\mathrm{p}(p_\mathrm{p})\, T_\mathrm{p}(p_\mathrm{p}) dp_\mathrm{p}}{\int_0^\infty q_\mathrm{p}(p_\mathrm{p})\, T_\mathrm{p}(p_\mathrm{p}) dp_\mathrm{p}} \approx 0.6, \tag{4.9}$$

where the normalised proton momenta p_1 and p_2 are given by $p_{1,2} = \sqrt{[8E_{1,2}/(m_\mathrm{p}c^2) + 1]^2 - 1}$ and we adopt $E_1 = 0.1$ GeV and $E_2 = 100$ GeV. This allows us to define the calorimetric fraction as the ratio of the luminosity of all pion-decay end products produced in hadronic collisions (L_π)

to the proton luminosity ($L_{\rm p}$) as

$$\eta_{\rm cal,p} = \frac{L_\pi}{\xi_{\rm bol} L_{\rm p}} \approx 1.7 \times \frac{\sum_i L_{\pi,i}}{\sum_i L_{{\rm p},i}}. \tag{4.10}$$

We estimate the total pion luminosity in each cell from the gamma-ray luminosity resulting from neutral pion decay, i.e. $L_{\pi,i} \approx 3L_{\pi^0,i} = 3L_{\gamma,i}$. The injected proton luminosity $L_{{\rm p},i}$ is computed from the SFR in each cell i via

$$L_{{\rm p},i} = \zeta_{\rm SN} \dot{M}_{\star,i}\, \epsilon_{\rm SN}\ , \tag{4.11}$$

where $\epsilon_{\rm SN} = E_{\rm SN}/M_\star = 10^{51}\,{\rm erg}/(100{\rm M}_\odot) = 10^{49}\,{\rm erg\,M}_\odot^{-1}$ quantifies the SN energy release per unit mass, under the assumption of a Chabrier (2003) initial mass function and assuming that stars with a mass above 8 $\rm M_\odot$ explode as SNe.

Hence, in the calorimetric limit, where hadronic losses dominate over escape losses, we obtain $\eta_{\rm cal,\,p} \rightarrow 1$. We find that highly SF galaxies with SFR $\gtrsim 1\,{\rm M}_\odot\,{\rm yr}^{-1}$ approach this limit, but level off at around 0.7. On average, we find that SF galaxies with SFRs ranging from ∼1 to 100 $\rm M_\odot\,yr^{-1}$ exhibit calorimetric fractions between 0.3 to 0.7. For starburst galaxies like NGC 253 and M82, this is roughly consistent with what has been previously found by Lacki et al. (2011), who estimated calorimetric fractions of NGC 253 and M82 ranging from about 0.2 to 0.4. Even though this means that highly SF galaxies lose a significant amount of energy due to hadronic interactions, we note that a calorimetric fraction of e.g., ∼40 per cent implies that the remaining 60 per cent of CR energy diffuses out of SF regions and is available for CR feedback in form of CR-driven galactic winds. In normally SF galaxies with SFR $\lesssim 1\,{\rm M}_\odot\,{\rm yr}^{-1}$, losses due to CR diffusion start to become dominant over hadronic losses, which leads to a decreasing calorimetric fraction. Consequently, the total γ-ray emission of these galaxies falls short of the calorimetric relation shown in the upper panels of Fig. 4.4 (dashed green line). Modeling a larger CR diffusion coefficient (of $D = 3 \times 10^{28}\,{\rm cm}^2\,{\rm s}^{-1}$, light blue symbols) thus results in an even larger deviation from calorimetry.

4.3.2 γ-ray spectra

In addition to the spatial information and the total γ-ray luminosity of our steady-state models of CR electrons and protons, we study the γ-ray spectra of our simulated galaxies and compare them to observational data.

Simulated γ-ray spectra

First, we investigate the effect of halo mass and temporal evolution of our simulations on the γ-ray spectra. In Fig. 4.6, we show the γ-ray spectra of two different halo masses $M_{200} = 10^{10}$ and $10^{12}\,\mathrm{M}_\odot$ at two different times, respectively. The time of the first snapshot is chosen at the time of the peak of the SF history, i.e., after 0.2 and 0.1 Gyr, respectively. At the second time shown here, the SFR has decreased by two e-foldings, i.e., at 2.3 Gyr in both cases. As the SFR decreases with time, the CR injection and thus its energy density drops, too. As a result, the total emitted spectrum is shifted downwards with time for both halo masses. While the IC emission in the smaller halo dominates the γ-ray emission above 40 GeV at early times and above a few GeV at later times, its contribution in the more massive halo decreases over time. In all cases, the bremsstrahlung emission plays a subdominant role above energies of 1 GeV and only becomes relevant at lower energies.

In Fig. 4.7 we assess the interplay between our steady-state CR spectra and the resulting γ-ray emission spectra. In the upper panels, we show the spectra of CR protons, primary and secondary electrons for three different halo masses ($M_{200} = 10^{12}$, 10^{11} and $10^{10}\,\mathrm{M}_\odot$) at the same time ($t = 2.3$ Gyr), which corresponds to SFRs of 6.48, 0.36 and 0.01 $\mathrm{M}_\odot\,\mathrm{yr}^{-1}$, respectively. The CR spectra are averaged over the gas scale-height, where the gas density has dropped by an e-folding (ranging from 0.6 to 0.9 kpc), and the radius, where 99 per cent of the gamma-ray luminosity is included. These range from $r = 9.5$ kpc in the low-mass halo to $r = 20.5$ kpc and $r = 27.5$ kpc in the middle and high-mass halos, respectively. Furthermore, the CR spectra of the lower mass halos are re-scaled by factors of 10 and 100 (as indicated in the legend) for visual purposes, which enables us to identify the differences in their spectral slopes. In the case of CR protons, smaller galaxies with lower SFRs exhibit steeper CR proton spectra, indicating that diffusive losses (that are assumed to be energy dependent) become increasingly important, which is consistent with our findings of Fig. 4.4 (bottom panels). Consequently, their CR proton spectra steepen by 0.5 due to energy dependent diffusion, which yields a spectral index of 2.7. This also results in a steeper γ-ray spectrum resulting from neutral pion decay with decreasing SFR (lower panels of Fig. 4.7).

By contrast, the primary CR electron spectrum steepens with higher SFR. This can be attributed to higher radiative losses of CR electrons under these conditions, which leads to a spectral index of the CR electron spectrum that is steeper by unity in comparison to the injected index, so that the cooled spectral index approaches 3.2. As radiation dominates over the magnetic energy density in most of the galaxy except for the very central regions of the galaxy (see Fig. 4.1), CR electrons mainly cool via IC interactions.

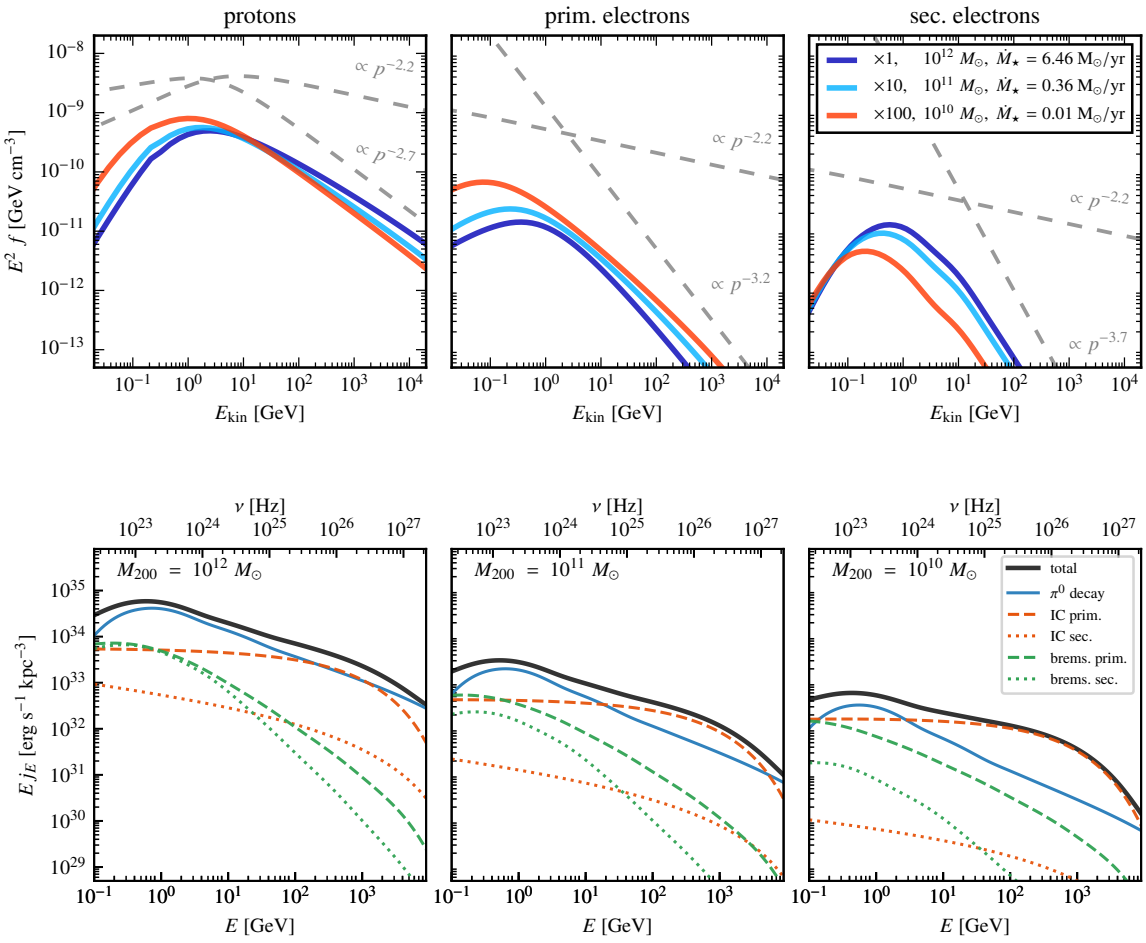

Figure 4.7: Upper panel: CR proton, primary and secondary electron spectra for three different halo masses, 10^{12}, 10^{11} and 10^{10} M$_\odot$, all at t = 2.3 Gyr, averaged over the gas scale-height and the radius that includes 99 per cent of the gamma-ray emission. For visual purposes, the CR spectra of the lower-mass halos are re-scaled as indicated in the legend. Lower panels: resulting γ-ray spectra of the same halos as shown above. The contribution to the IC and bremsstrahlung arising from the primary (dashed lines) and secondary (dotted lines) electron populations are shown separately.

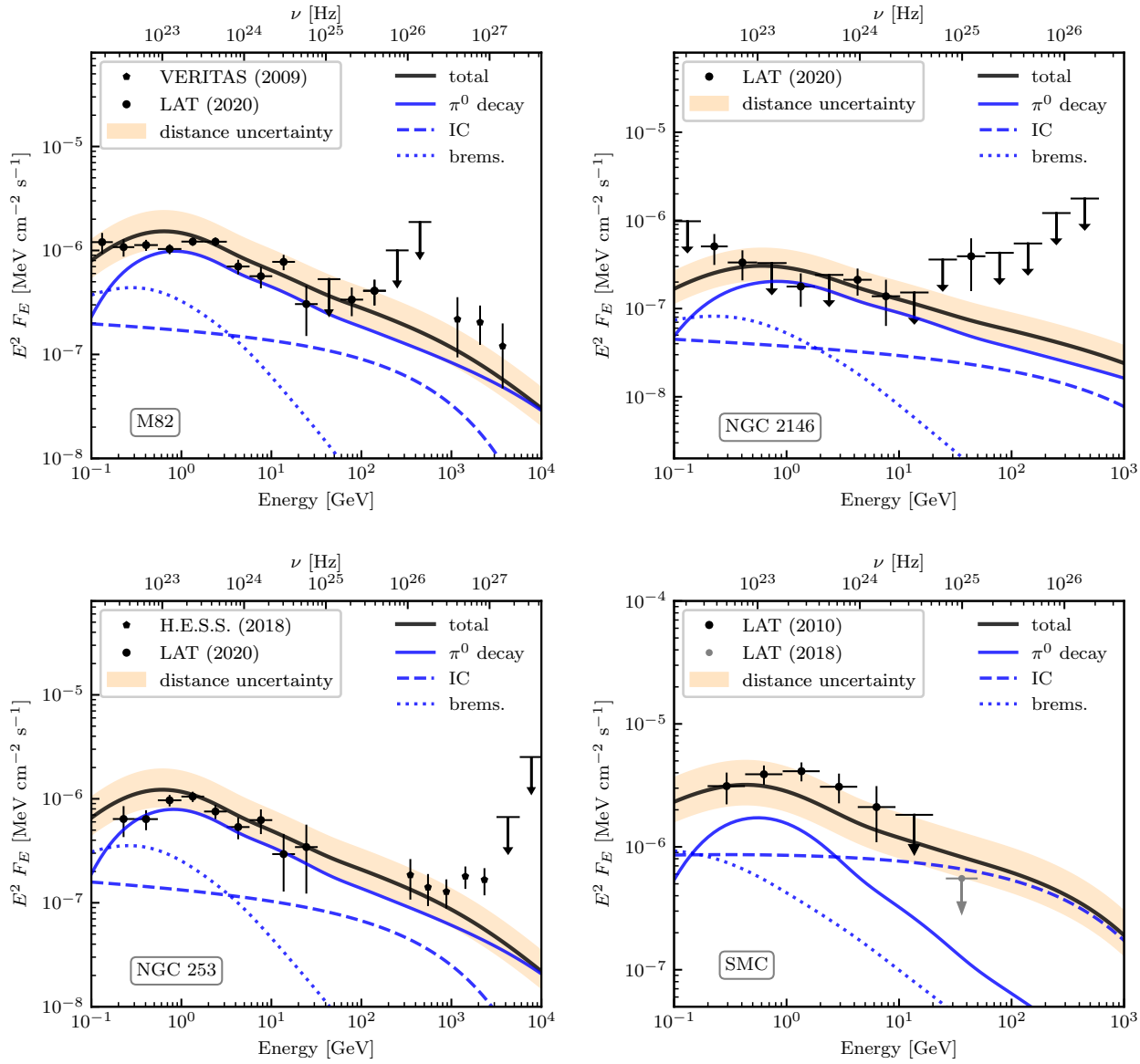

Figure 4.8: γ-ray spectra of the observed galaxies M82, NGC 2146, NGC 253 and SMC together with the emission of our simulated galaxies, which exhibit a similar total γ-ray luminosity and SFR. The simulated spectra are re-normalised to the corresponding observed total γ-ray luminosities for visual purposes (i.e. by factors of 0.71 to 1.03; see Table 4.2).

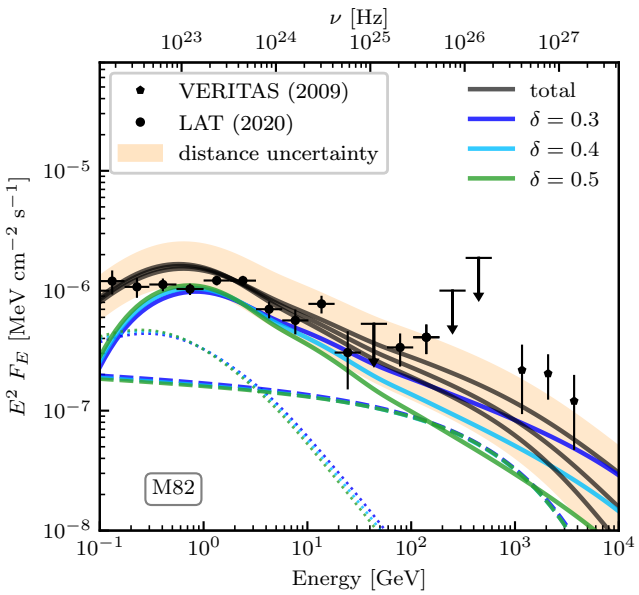

Figure 4.9: γ-ray spectrum of M82 (same as Fig. 4.8, upper left panel), together with our simulated spectra for three different values of the energy dependence of diffusion timescale, i.e. $t_{\rm diff} \propto E^{-\delta}$. A higher value of δ implies faster diffusion at higher energies, which results in steeper spectra of CR proton and γ rays from neutral pion decay.

The contribution of secondary electrons decreases with lower SFR as a consequence of the associated lower gas density. This is visible in the normalization of the spectra of secondary CR electrons in comparison to that of primary electrons, as well as the secondary bremsstrahlung and IC emission in comparison to the primary contributions, respectively. Hence, in the $10^{12}\,\mathrm{M}_\odot$ halo, which exhibits a higher SFR, secondary and primary bremsstrahlung contribute nearly equally. On the contrary, secondary bremsstrahlung is negligible in the $10^{10}\,\mathrm{M}_\odot$ halo. Similarly, the relevance of secondary IC emission decreases significantly from the 10^{12} to the $10^{10}\,\mathrm{M}_\odot$ halo. Furthermore, the secondary electron spectra are steeper in comparison to the primary ones because they result from the steady-state CR proton population, that exhibit spectral indices of $2.2 < \alpha_\mathrm{p} < 2.7$ due to energy dependent diffusion losses. After having cooled, secondary electron spectra are thus steepening further and approach spectral indices of $\alpha_\mathrm{e,sec} \gtrsim 3.2$, whereas the primary electron spectrum steepens at most by unity so that $\alpha_\mathrm{e,prim} \lesssim 3.2$. Overall, this leads also to steeper IC and bremsstrahlung spectra from the secondary CR electron population in comparison to primary electrons.

Comparison to observed γ-ray spectra

Looking at the upper panels in Fig. 4.4, we can easily find suitable snapshots of our simulations that correspond to individual observed galaxies in terms of their total γ-ray luminosity and their SFR. We consider the four galaxies NGC 2146, NGC 253, M82 and the SMC. In Table 4.2, we identify the corresponding snapshots that resemble the observed galaxies in terms of their SFR and total γ-ray luminosity, using our simulations with $\zeta_{\rm SN} = 0.05$ and $B_0 = 10^{-10}$ G. Even though the initial magnetic field does not influence the resulting γ-ray emission, we chose a value of $B_0 = 10^{-10}$ G in order to better reproduce the FIR-radio relation, which we discuss in Paper III. The γ-ray spectra of the individual galaxies are shown in Fig. 4.8, together with observations by LAT (Ajello et al., 2020). For M82, we additionally show VERITAS Collaboration et al. (2009) data, for NGC 253 H. E. S. S. Collaboration et al. (2018) data, and for the SMC, we show *Fermi*-LAT data (Abdo et al., 2010; Lopez et al., 2018). The distances to the galaxies are taken from Ajello et al. (2020) and references therein. The distance uncertainties are indicated by the orange band and are assumed to be 20 per cent, because typical distance uncertainties for galaxies within $\sim$ 25 Mpc are around 10-20 per cent (Freedman et al., 2001).

In case of starburst galaxies, i.e. for NGC 2146, NGC 253 and M82, we successfully match the observations at low energies. Only in the case of NGC 253, we slightly over-predict the data at 200-300 MeV which may indicate a too large leptonic bremsstrahlung contribution. In order to better match the data in the very high energy regime in these starburst galaxies, we need to assume the energy dependence of the diffusion timescale to scale as $E^{-\delta}$ with $\delta = 0.3$. This corresponds to a turbulent Kolmogorov spectrum (Strong et al., 2007). The effect of varying δ on the γ-ray spectrum is depicted in Fig. 4.9, where we show the γ-ray spectra for our M82 analogue adopting $\delta = \{0.3, 0.4, 0.5\}$. As expected, a higher value of δ leads to a steeper spectrum of CR protons and of the resulting neutral pion decay emission. In case of the SMC, we stick to our model with $\delta = 0.5$, which leads to a steeper spectrum at high energies that better agrees with the upper limit found by Abdo et al. (2010). However, we do not match the upper limit determined by Lopez et al. (2018). The resulting γ-ray luminosities given in Table 4.2 are calculated using $\delta = 0.3$ for NGC 2146, NGC 253 and M82 and are only $3-6$ per cent smaller, if we adopt $\delta = 0.5$.

4.4 Discussion and conclusions

In this paper, we evaluate the non-thermal γ-ray emission from MHD simulations of isolated galaxies with different halo masses. The emission processes include neutral pion decay resulting

from hadronic interactions of CR protons with the ISM, as well as IC and bremsstrahlung emission from CR electrons. We model the spectra of CR protons, primary and secondary electrons with a cell-based steady-state approximation in post-processing of our simulations, following the approach detailed in Paper I. This enables us to produce γ-ray maps of the emission processes as well as their energy spectra. Furthermore, we calculate a total γ-ray luminosity for each simulated galaxy and find that we better reproduce the observed correlation with the FIR luminosity if we adopt a low injection efficiency of CRs at SNe of $\zeta_{\rm SN} = 0.05$. Furthermore, the simulations only accounting for advection of CRs clearly overproduce the observed γ-ray luminosities at small SFRs and halo masses. Only the models with anisotropic CR diffusion agree with the observed deviation from calorimetry with decreasing SFRs.

Despite current belief, we find that the leptonic contribution to the total γ-ray emission in form of bremsstrahlung and IC emission is not negligible. While it is subdominant in comparison to the pion decay γ rays in starburst galaxies, it becomes progressively more important towards more moderate SF (and smaller) galaxies. On the other hand, this is also the regime where our assumption underlying the IC emission is weak, i.e. that the interstellar radiation field is dominated by the reprocessed UV light of young stellar populations, that gets re-emitted in the FIR by dust. Still, independent of the exact modeling of the incident radiation field for the IC emission, the pionic γ-ray emission in our model is not able to account for both the observed γ-ray luminosities as well as the spectral shapes of galaxies with low SFRs such as the SMC alone. As diffusive losses become more relevant in these low-density galaxies, this leads to a steepening of the CR proton spectra (depending on the exact energy dependence incorporated in the diffusion timescale). This necessarily results in steeper pion decay γ-ray spectra, which would be in conflict with the observations if this were the only relevant emission channel. Hence, a leptonic contribution to the γ-ray emission from IC scattering is indispensable in our models.

One of the arguments made in the literature in order to conclude a sub-dominant leptonic contribution to the total γ-ray emission depends on several underlying assumptions, that are only valid in the nuclear regions of starbursts, i.e. for high gas densities, magnetic field strengths and wind velocities. The magnetic field strength is either deduced from an energy equipartition argument, or from fitting several free parameters in one-zone models (see e.g., Torres, 2004; Lacki et al., 2010, 2011; Yoast-Hull et al., 2013) or axisymmetric two-dimensional models (Buckman et al., 2020) in order to simultaneously match the observations. The former approach assumes that the kinetic energy density $\varepsilon_{\rm kin} = \rho\, v^2/2$ is equal to the magnetic energy density, $\varepsilon_{\rm mag} = B^2/(8\pi)$. Assuming turbulent velocities of $\sim 20\,{\rm km/s}$ and gas densities of $n \sim 100\,{\rm cm}^{-3}$ yields in this approach magnetic field strengths of the order of 100 μG. The fast cooling of CR electrons due to

synchrotron emission in these strong magnetic fields has been proposed to be one of the reasons for suppressing the possible leptonic contribution to the γ-ray emission (Lacki et al., 2011). In contrast, γ-ray observations of the Galactic center suggest that CRs might not be able to penetrate into the densest regions and thus may be far from calorimetry (Crocker et al., 2011b,a).

However, those extreme properties are at most reached in the very central region of our simulated galaxies. Additionally, the energy density of the interstellar radiation field (or its equivalent magnetic field strength, see Fig. 4.1, upper panels) persists throughout the whole galaxy. The cooling of the electrons is hence not fully dominated by synchrotron cooling, enabling IC losses to be non-negligible, except in the very central regions of starburst galaxies. In particular, in the low density interstellar medium of dwarfs, we find that the IC emission might be able to contribute up to 40 per cent of the total γ-ray luminosity, as can be seen in Fig. 4.4 (middle panels). Still, our models of starburst galaxies M82 and NGC 253 (that are chosen to match the observed SFRs and L_γ) also match their observed radio luminosities at 1.4 GHz. We will address the radio emission of our simulated galaxies in Paper III in more detail.

Our findings suggest that SF galaxies are not reaching the calorimetric limit, and depart from this limit even further with smaller SFR and halo masses, which is due to the increasing relevance of diffusion losses. Hence, the contribution of neutral pion decay to the total γ-ray luminosity decreases at low SFRs, which is partly compensated by the larger contribution of leptonic IC γ-ray emission. Furthermore, the departure from calorimetry implies that there is still a considerable amount of CR energy left for feedback processes, even in highly SF galaxies.

4.5 Appendix: Comparison to hadronic interaction models

Here, we present Appendix B of Werhahn et al. (2021b), whereas the radiation processes in the gamma-ray regime (from Appendix A of Werhahn et al., 2021b) are presented in Section 2.3.1.

4.5.1 Analytical approximation by Pfrommer & Enßlin (2004)

Pfrommer & Enßlin (2004) derived an analytical expression for the γ-ray source function. They aimed for connecting the high energy limits for the γ-ray source function to the detailed physics near the threshold of neutral pion production that have been modeled with the COSMOCR code (Miniati, 2001), that is based on the isobaric model and also takes into account the contribution of kaon decay modes to the neutral pion production. The resulting analytical formula assumes a power-lar CR momentum distribution that extends below the kinematic threshold for the pp reaction

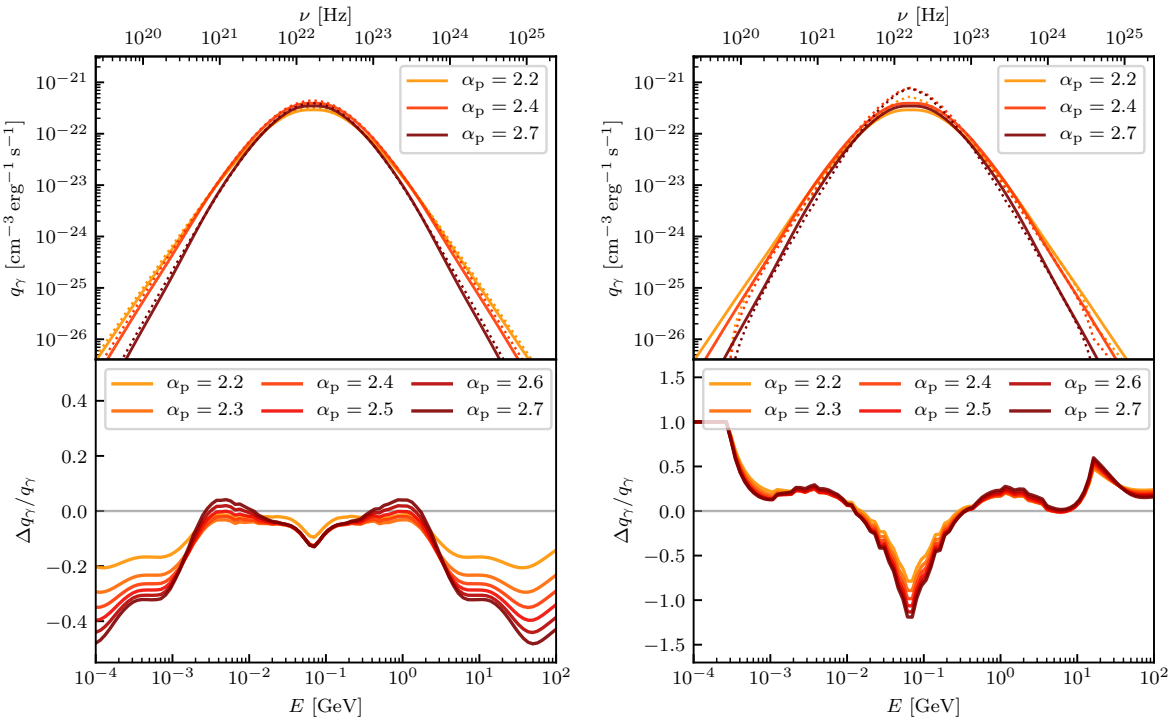

Figure 4.10: The γ-ray emissivity for a power-law distribution of protons with different spectral indices, normalised to $\varepsilon_{\rm CR} = 1\,{\rm eV\,cm^{-3}}$ and $n_{\rm N} = 1\,{\rm cm^{-3}}$, resulting from our approach (solid lines) and from the analytical approximation by Pfrommer & Enßlin (2004) (dotted lines, left panel), and the model by Kelner et al. (2006) (dotted lines, right panel). The lower panels shows their relative differences, respectively. Note the different scales in both panels.

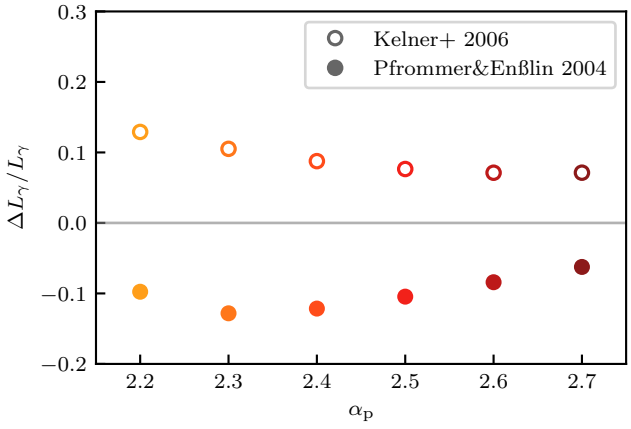

Figure 4.11: Relative deviation of the total luminosity L_γ between 0.1-100 GeV calculated from our model in comparison to Kelner et al. (2006) (open symbols) and Pfrommer & Enßlin (2004) (filled symbols) for different values of the proton spectral index $\alpha_{\rm p}$ (see legend in Fig. 4.10).

and reads (Pfrommer & Enßlin, 2004)

$$q_\gamma \simeq \sigma_{\rm pp}^{\pi} c n_{\rm N} \xi^{2-a_\gamma} C_{\rm p} \frac{4}{3a_\gamma} \left(\frac{m_\pi}{m_{\rm p}}\right)^{-a_\gamma} \times \left[\left(\frac{2E}{m_\pi c^2}\right)^{\delta_\gamma} + \left(\frac{2E}{m_\pi c^2}\right)^{-\delta_\gamma}\right], \tag{4.12}$$

where $n_{\rm N}$ denotes the target nucleon density, the pion multiplicity is assumed to be constant, $\xi = 2$, and $C_{\rm p}$ is the normalization of the proton momentum distribution at momentum $m_{\rm p}c$. The asymptotic slope of the γ-ray spectrum a_γ equals the spectral index of the proton population in the scaling model, that has also been adopted by Dermer (1986b). Furthermore, the parameter δ_γ and the total effective cross section $\sigma_{\rm pp}^{\pi}$ have been modeled by Pfrommer & Enßlin (2004) as

$$\delta_\gamma = 0.14 a_\gamma^{-1.6} + 0.44 \tag{4.13}$$

and $\sigma_{\rm pp}^{\pi}$ is given in Eq. (3.50). The analytical approximation by Pfrommer & Enßlin (2004) from Eq. (4.12) slightly over-predicts the resulting emission near the threshold of pion production, i.e. at $m_\pi c^2/2 \approx 67.5\,\mathrm{MeV}$(see Fig. 4.10), as well as at very high and very low γ-ray energies. However, the total γ-ray luminosity between 0.1-100 GeV is accurate to 10 percent in comparison to our approach (see Fig. 4.11).

4.5.2 Parametrization by Kelner et al. (2006)

Frequently used analytical expressions for the energy spectra of secondary particles in pp-collisions like pions, electrons, neutrinos and γ rays are provided by Kelner et al. (2006). They focus on the high energy regime, where $T_{\rm p} > 100\,\mathrm{GeV}$, and prescribe the production of γ rays in terms of the number of created photons in the interval $(x, x + \mathrm{d}x)$ per collision, denoted by $F_\gamma(x, E_{\rm p})$, with $x = E_\gamma/E_{\rm p}$. By convolving F_γ with the proton energy distribution $N_{\rm p}(\gamma_{\rm p})$ and the inelastic cross section of pp-interactions, one obtains the γ-ray production rate in the energy interval $(E_\gamma, E_\gamma + dE_\gamma)$ via

$$q_\gamma(E_\gamma) = c n_{\rm H} \int_{E_\gamma}^{\infty} \sigma_{\rm inel}(E_{\rm p}) f_{\rm p}(E_{\rm p}) F_\gamma\left(\frac{E_\gamma}{E_{\rm p}}, E_{\rm p}\right) \frac{\mathrm{d}E_{\rm p}}{E_{\rm p}}. \tag{4.14}$$

Fitting the numerical data with the SIBYLL code (Fletcher et al., 1994), they obtain the inelastic part of the total cross section of pp-interactions, $\sigma_{\rm inel}(E_{\rm p})/\mathrm{mb} = 34.3 + 1.88L + 0.25L^2$. In order to better match the experimental data in the low energy regime, they multiply this expression by a factor of $(1 - (E_{\rm th}/E_{\rm p})^4)^2$. For low proton kinetic energies ($T_{\rm p} < 100\mathrm{GeV}$), where their parametrization for $F_\gamma(x, E_{\rm p})$ is not valid, they suggest a δ-functional approach for the production

rate of pions. Hence, in this approximation, the production rate of pions is given by

$$\tilde{F}_\pi(E_\pi, E_\mathrm{p}) = \tilde{n}\delta\left(E_\pi - \frac{\kappa}{\tilde{n}}E_\mathrm{kin}\right), \tag{4.15}$$

where $\tilde{n} = \int \tilde{F}_\pi dE_\pi$ denotes the number of produced pions and κ is the fraction of kinetic energy transferred to γ rays by a proton with energy E_p. From this, they obtain the pion source function via

$$q_\pi(E_\pi) = \tilde{n}\frac{cn_\mathrm{H}}{K_\pi}\sigma_\mathrm{inel}\left(m_\mathrm{p}c^2 + \frac{E_\pi}{K_\pi}\right) f_\mathrm{p}\left(m_\mathrm{p}c^2 + \frac{E_\pi}{K_\pi}\right). \tag{4.16}$$

The parameter $K_\pi = \kappa/\tilde{n}$ prescribes the mean fraction of proton energy that is transferred to the produced neutral pion and is assumed to be $K_\pi = 0.17$, which agrees well with numerical Monte Carlo simulations (Mori, 1997), as demonstrated in Aharonian & Atoyan (2000). From this expression we can calculate the resulting γ-ray spectrum with

$$q_\gamma(E) = 2\int_{E_{\pi,\mathrm{min}}}^{E_{\pi,\mathrm{max}}} \mathrm{d}E_\pi \frac{q_\pi(E_\pi)}{\sqrt{E_\pi^2 - (m_\pi c^2)^2}}, \tag{4.17}$$

In comparison to our approach, which is shown by the solid lines in Fig. 4.10, the δ-function approximation by Kelner et al. (2006) for low proton energies can be recognized by a sharp peak around the pion-decay bump and hence overproduces the γ-ray emission at these energies in comparison to our approach by more than 100 per cent. The transition from the δ-approximation to their parametrization at higher proton energies > 100 GeV is visible in the γ-ray source function at energies around 10 GeV. The effect on the total γ-ray luminosity is depicted in Fig. 4.11. It shows that our approach yields an about 10% higher γ-ray luminosity in comparison to the approach by Kelner et al. (2006).

5. Cosmic rays and non-thermal emission in simulated galaxies - III. probing cosmic ray calorimetry with radio spectra and the FIR-radio correlation

This chapter is based on our work published in Werhahn et al. (2021c).

An extinction-free estimator of the star-formation rate (SFR) of galaxies is critical for understanding the high-redshift universe. To this end, the nearly linear, tight correlation of far-infrared (FIR) and radio luminosity of star-forming galaxies is widely used. While the FIR is linked to massive star formation, which also generates shock-accelerated cosmic ray (CR) electrons and radio synchrotron emission, a detailed understanding of the underlying physics is still lacking. Hence, we perform three-dimensional magneto-hydrodynamical (MHD) simulations of isolated galaxies over a broad range of halo masses and SFRs using the moving-mesh code Arepo, and evolve the CR proton energy density self-consistently. In post-processing, we calculate the steady-state spectra of primary, shock-accelerated and secondary CR electrons, which result from hadronic CR proton interactions with the interstellar medium. The resulting total radio luminosities correlate with the FIR luminosities as observed and are dominated by primary CR electrons if we account for anisotropic CR diffusion. The increasing contribution of secondary emission up to 30 per cent in starbursts is compensated by the larger bremsstrahlung and Coulomb losses. CR electrons are in the calorimetric limit and lose most of their energy through inverse Compton interactions with star-light and cosmic microwave background (CMB) photons while less energy is converted into synchrotron emission. This implies steep steady-state synchrotron spectra in starbursts. Interestingly, we find that thermal free-free emission flattens the total radio spectra at high radio frequencies and reconciles calorimetric theory with observations while free-free absorption explains the observed low-frequency

flattening towards the central regions of starbursts.

5.1 Introduction

The radio emission from star-forming galaxies is attributed to the interaction of CR electrons with an ambient interstellar magnetic field. These highly relativistic charged particles emit synchrotron radiation while gyrating around magnetic field lines, giving rise to a power-law spectrum at radio frequencies. Because CRs are accelerated at shocks of supernova (SN) remnants and because the lifetime of radio-emitting CR electrons in galaxies is shorter than tens of millions of years, their existence reveals ongoing star formation in a galaxy. Hence, a correlation between the radio synchrotron emission of star-forming galaxies and tracers of their star formation activity, such as the FIR luminosity, is expected. The latter traces ongoing star formation, because the ultra-violet (UV) light of a young stellar population is absorbed by dust and re-emitted in the FIR.

Indeed, a tight and nearly linear correlation has been observed between the radio and FIR luminosity of galaxies (van der Kruit, 1971; Helou et al., 1985; Condon, 1992; Yun et al., 2001; Bell, 2003; Molnár et al., 2021; Matthews et al., 2021). Due to the tightness of this relation across different types of star-forming galaxies and across five orders of magnitude in luminosity, the FIR-radio correlation (FRC) is widely used to estimate the SFR of galaxies from their radio luminosities (see e.g. Heesen et al., 2014, 2019; Vollmer et al., 2020). It has the notable feature of not being affected by dust extinction, which is one of the main uncertainties of other SFR estimators, which employ, e.g., the Hα and/or UV emission. This makes the FRC a favourable method for estimating SFRs in particular for high redshifts galaxies, where dust properties are unknown, and where accurate SFR estimators are critical for deciphering the cosmic star formation history. However, it is still unclear, whether the FRC evolves with redshift (Lacki & Thompson, 2010; Schleicher & Beck, 2013; Schober et al., 2016).

A linear FRC naturally emerges if CR electrons calorimetrically lose most of their energy to synchrotron emission (Völk, 1989; Lisenfeld et al., 1996). This requires that the corresponding timescale of synchrotron losses is shorter than all other loss processes that apply to CR electrons, i.e., losses due to inverse Compton (IC) and bremsstrahlung emission, as well as Coulomb losses and CR electron escape from the galaxy. The latter process arises due to advection and diffusion, and has been suggested to be relevant in galaxies with low SFRs (Thompson et al., 2006; Lacki et al., 2010). But highly star-forming galaxies, such as NGC 253 and M82, are expected to be calorimetric, due to high photon energy densities and magnetic field strengths. However, in this picture, the fully-cooled electron spectra would steepen by unity at high particle energies due to

the energy dependence of IC and synchrotron cooling. This would imply steep radio spectra with spectral indices at around 1.1, which is in contrast to observed values of 0.5–0.8. Hence, these flat radio spectra of star-forming galaxies pose a challenge to the calorimetric theory.

To gain insights into these processes, the radio and gamma-ray spectra of famous starburst galaxies such as M82 or NGC 253 have been analyzed with so-called one-zone models in which a galaxy is represented as a single entity and parametrized by average quantities (Torres, 2004; Lacki et al., 2010; Paglione & Abrahams, 2012; Yoast-Hull et al., 2013; Eichmann & Becker Tjus, 2016). One proposed solution for the problem of too steep radio spectra predicted from calorimetric theory has been bremsstrahlung and ionization losses in starburst galaxies (Thompson et al., 2006; Lacki et al., 2010; Basu et al., 2015), which could flatten CR electron spectra due to their shallower energy dependence in comparison to IC and synchrotron losses. However, at the same time, these additional processes open new energy loss channels for the radio-emitting CR electrons and thus diminish the resulting radio synchrotron luminosity. This would imply a sublinear FRC at high SFRs, which is in conflict with observations. To cure this problem, a second radio emission process has been proposed that fills in this missing radio emission in form of an increasing contribution of synchrotron emission from secondary electrons that are generated in hadronic CR proton interactions with the ambient interstellar medium (ISM, Thompson et al., 2006; Lacki et al., 2010), an efficient process in the dense centers of starbursts. This would successfully maintain the linear FRC, even at high SFRs. On the other hand, IC losses also compete with synchrotron losses that in turn might pose a challenge to use the FRC as SFR estimator, in particular at high redshifts, where IC losses due to scattering of CR electrons off CMB photons are expected to be larger. Thus, in addition to the question of calorimetry, understanding the relative importance of IC and synchrotron losses is essential.

To model these processes in more detail, we perform MHD simulations with the moving-mesh code Arepo, simulate the CR proton energy density and model the non-thermal CR spectra. This is the third and last paper of a series in which we present our results. The first paper (Werhahn et al., 2021a, hereafter Paper I) details the steady-state modeling of CRs in our simulations and compares the results to CR data. We find very good agreement for our CR electron and proton spectra as well as the positron fraction as a function of particle energy when compared to Voyager-1 and AMS-02 data. The resulting gamma-ray emission of star-forming galaxies is analysed in the second paper (Werhahn et al., 2021b, hereafter Paper II), where we successfully match the observed FIR-gamma-ray relation as well as observed gamma-ray spectra of star-forming galaxies. Here, we apply the same formalism as described in Paper I and study the resulting radio synchrotron emission from primary and secondary CR electrons. In a companion paper, Pfrommer et al. (2021)

investigate the origin of the global FRC. In particular, the role of the turbulent small-scale dynamo is identified and the processes leading to the observed scatter in the FRC are analyzed.

This paper is structured in the following way. In Section 5.2, we describe our simulations of isolated galaxies, the steady-state modeling of the CR proton, primary and secondary electron spectra, as well as the calculation of the resulting radio emission and absorption processes. Section 5.3 provides an overview of the timescales of the non-radiative and radiative losses of CR protons and electrons. We furthermore describe the modelling of the FRC in Section 5.4 where we analyse the primary and secondary contribution to the total radio luminosity, quantify the calorimetry of CR electrons and assess the processes that have been proposed to 'conspire' to maintain an almost linear FRC at high SFRs. Eventually, we scrutinise three possible mechanisms, that could be responsible for the observed flat radio spectra of star-forming galaxies such as NGC 253, M82 and NGC 2146 in Section 5.5, before we summarise our results in Section 5.6.

5.2 Description of the methods

5.2.1 Simulations

We perform simulations with the moving mesh code Arepo (Springel, 2010; Pakmor et al., 2016a) as described in Paper I and Paper II. Our simulations start from the gravitational collapse of a gas cloud embedded in a dark matter (DM) halo prescribed by an NFW (Navarro et al., 1997) profile, with masses ranging from $M_{200} = 10^{10}$ to $10^{12}\,\mathrm{M}_{\odot}$, in order to resemble realistic halo masses from dwarf to Milky Way (MW) sized galaxies. Subsequently, we simulate the formation of a rotationally supported disc that forms stars stochastically above a critical density threshold (Springel & Hernquist, 2003). After an initial burst of star formation, the SFR decreases exponentially over time. At SNe, CRs are instantaneously injected with an energy fraction ζ_{SN} of the kinetic energy of the SN explosion, which we vary from 5 to 10 per cent. The lower range of ζ_{SN} is inferred from a combination of kinetic plasma simulations at oblique shocks (Caprioli & Spitkovsky, 2014) and three-dimensional MHD simulations of CR acceleration at SN remnant shocks (Pais et al., 2018), which is followed by a detailed comparison of simulated radio, X-ray and gamma-ray emission maps and spectra to observational data (Pais et al., 2020; Pais & Pfrommer, 2020; Winner et al., 2020).

The ideal MHD prescription (Pakmor & Springel, 2013) governs the evolution of the magnetic field. Starting from an initial seed magnetic field B_0 permeating the gas cloud before collapse, the magnetic field is exponentially amplified by a small-scale dynamo, before it grows further via

Table 5.1: Overview of the simulations in this paper. Shown are (1) the halo mass M_{200}, (2) the CR transport model: in the 'CR adv' model we only account for CR advection with the gas whereas the 'CR diff' model additionally allows for anisotropic diffusion, (3) the initial magnetic field B_0, (4) the injection efficiency of CRs at SNRs, $\zeta_{\rm SN}$, and (5) the referenced figures.

$M_{200}[\mathrm{M}_\odot]$	CR model	B_0 [G]	$\zeta_{\rm SN}$	Figures
10^{10}	CR adv	10^{-10}	0.05	5.3, 5.6, 5.7, 5.12
10^{11}	CR adv / CR diff	10^{-10}	0.05	5.3, 5.6, 5.7, 5.12
3×10^{11}	CR adv / CR diff	10^{-10}	0.05	5.3, 5.6, 5.7, 5.12
10^{12}	CR adv / CR diff	10^{-10}	0.05	5.1 to 5.13
10^{10}	CR adv	10^{-12}	0.05	5.15
10^{11}	CR adv / CR diff	10^{-12}	0.05	5.15
3×10^{11}	CR adv / CR diff	10^{-12}	0.05	5.15
10^{12}	CR adv / CR diff	10^{-12}	0.05	5.15
10^{10}	CR adv	10^{-12}	0.10	5.15
10^{11}	CR adv / CR diff	10^{-12}	0.10	5.15
3×10^{11}	CR adv / CR diff	10^{-12}	0.10	5.15
10^{12}	CR adv / CR diff	10^{-12}	0.10	5.15

an inverse cascade until saturation (Pfrommer et al., 2021). We chose two different values for the initial magnetic field of $B_0 = 10^{-10}$ and 10^{-12} G, which represent the pre-amplified magnetic field in a proto-galactic environment. CRs are described as a relativistic fluid (Pakmor et al., 2016a; Pfrommer et al., 2017a) with adiabatic index of 4/3 and we account for adiabatic changes of the CR energy density as well as Coulomb and hadronic loses due to interactions with the ISM. Furthermore, CRs are advected with the gas (in our 'CR adv' models) and are additionally allowed to anisotropically diffuse along magnetic field lines (in our 'CR diff' models) with a parallel diffusion coefficient along magnetic field lines of $D_0 = 10^{28}\mathrm{cm}^2\,\mathrm{s}^{-1}$.

A summary of all simulations analysed in this paper is presented in Table 5.1. The concentration parameter of the NFW profile is given by $c_{200} = r_{200}/r_s = 12$ in all simulations, where the characteristic scale radius of the NFW profile is denoted by r_s and r_{200} is the radius enclosing a mean density that is equal to 200 times the critical density of the universe. We refer to the simulation in the 'CR diff' model with a halo mass of $M_{200} = 10^{12}\,\mathrm{M}_\odot$, $B_0 = 10^{-10}$ G and $\zeta_{\rm SN} = 0.05$ as 'fiducial halo' in the following.

5.2.2 CR steady-state spectra

In addition to the primary CR electron population that is accelerated at SNRs together with CR protons, hadronic interactions of CR protons with the ISM lead to the production of neutral and

charged pions. Pions decay further into muons and eventually to neutrinos and secondary electrons and positrons (hereafter referred to as secondary electrons).

In order to model the spectral distribution of CRs, we assume a steady state and solve the diffusion-loss equation (Ginzburg & Syrovatskii, 1964; Torres, 2004) in each cell for protons, primary and secondary electrons (see Paper I), which reads

$$\frac{f_i(E_i)}{\tau_{\rm esc}} - \frac{\mathrm{d}}{\mathrm{d}E_i}\left[f_i(E_i)b(E_i)\right] = q_i(E_i). \tag{5.1}$$

Here, E_i denotes the CR energy, the subscript $i = \mathrm{e,p}$ specifies the CR species and $f_i(E_i) = \mathrm{d}N_i/(\mathrm{d}V\mathrm{d}E_i)$ is the resulting equilibrium spectral density for either protons (denoted by p), primary or secondary electrons (denoted by e). We define the source function $q_i(E_i) = q_i(p_i)\mathrm{d}p_i/\mathrm{d}E_i$ in terms of a power-law in momentum with an exponential cut-off given by

$$q_i(p_i)\mathrm{d}p_i = C_i p_i^{-\alpha_{\rm inj}} \exp\left[-(p_i/p_{{\rm cut},i})^n\right]\mathrm{d}p_i, \tag{5.2}$$

where $p_i = P_i/(m_i c)$ denote normalised momenta, m_i is the proton/electron rest mass and c is the speed of light. We adopt $n = 1$ for protons and $n = 2$ for primary electrons (Zirakashvili & Aharonian, 2007; Blasi, 2010) in Eq. (5.2) and assume cutoff momenta for protons $p_{\rm cut,p} = 1\,\mathrm{PeV}/(m_{\rm p}c^2)$ (Gaisser, 1990) and for electrons $p_{\rm cut,e} = 20\,\mathrm{TeV}/(m_{\rm e}c^2)$ (Vink, 2012). Both, primary electrons and protons are injected with a spectral index of $\alpha_{\rm inj} = 2.2$. We discuss the source function of secondary electrons in Section 5.2.3.

The resulting steady-state distribution of CR protons is ensured to match the CR energy density in each cell, after all cooling processes have been taken into account. The energy loss processes are given by the cooling rate $b(E_i) = -\mathrm{d}E_i/\mathrm{d}t$, that comprise hadronic and Coulomb losses in the case of CR protons. Additionally, losses due to particle escape are quantified by the timescale $\tau_{\rm esc} = (\tau_{\rm adv}^{-1} + \tau_{\rm diff}^{-1})^{-1}$, where advection and diffusion losses are included. These are estimated via

$$\tau_{\rm diff} = \frac{L_{\rm CR}^2}{D} \tag{5.3}$$

and

$$\tau_{\rm adv} = \frac{L_{\rm CR}}{v_{\rm z}}. \tag{5.4}$$

Here, $L_{\rm CR} = \varepsilon_{\rm CR}/|\nabla\varepsilon_{\rm CR}|$ is an estimate for the diffusion length. For diffusion losses, we assume an energy dependence of the diffusion coefficient $D = D_0(E/E_0)^\delta$, where $D_0 = 10^{28}\mathrm{cm}^2\,\mathrm{s}^{-1}$,

$E_0 = 3$ GeV and $\delta = 0.5$, which can be inferred from observations of beryllium isotope ratios (Evoli et al., 2020a). However, we find in Paper II, that gamma-ray spectra of highly star-forming galaxies provide a better match for a shallower energy dependence of the diffusion coefficient with $\delta = 0.3$ and hence, we also adopt both values of δ here. For advection losses, only the verical velocity component v_z pointing away from the disc is taken into account, because we show in Paper I, that azimuthal fluxes in and out of a computational cell nearly compensate each other, so that advection predominantly happens in vertical direction.

The assumption of a cell-based steady state has been analyzed in Paper I, where we compare the timescale of the change in the total energy density of CRs over a global simulation timestep $\tau_{\rm CR}$ to the loss timescale that includes cooling and diffusion losses $\tau_{\rm all}$. We find that the requirement for a steady-state configuration, i.e. $\tau_{\rm all}/\tau_{\rm CR} < 1$ is reached in cells that contribute most to the non-thermal emission processes, i.e. both in the radio and gamma-ray regime. Hence, we consider this a good assumption for our study concerning the non-thermal emission processes. However, because the steady-state assumption breaks down in low density regions, in outflows and near SNRs, we aim towards a more accurate treatment of the time evolution of CR protons and electrons (Girichidis et al., 2020b; Winner et al., 2019) in future work.

5.2.3 Primary and secondary CR electrons

To obtain the steady-state distribution $f_{\rm e}$ of primary CR electrons, we adopt Eq. (5.2) as the source function and solve the steady-state equation, i.e., Eq. (5.1). The normalization of $f_{\rm e}$ is set by requiring the primary CR electrons to reproduce the observed ratio of electrons to protons, $K_{\rm ep}^{\rm obs}$, at 10 GeV in a snapshot of our simulations resembling the MW in terms of halo mass and SFR. To this end, we average over the cell-based steady-state spectra around the solar galacto-centric radius and re-normalise the spectra according to the observed electron to proton ratio. From this, we can infer the injected ratio of primary electrons to protons before cooling, $K_{\rm ep}^{\rm inj} \approx 0.02$, that is needed, in order to obtain the observed value of $K_{\rm ep}^{\rm obs} \approx 0.01$ at 10 GeV (Cummings et al., 2016) after cooling. We assume that the injected ratio of electrons to protons is universal and adopt it to the rest of the galaxy as well as all other simulated galaxies.

To calculate the production of secondary CR electrons and positrons, we adopt the parametrization of Kelner et al. (2006) for large kinetic proton energies $T_{\rm p} > 100$ GeV. Because Yang et al. (2018b) provide a more detailed modeling of the differential cross section of pion production near the threshold of pion production up to 10 GeV, we use their parametrization for small proton energies and perform a cubic spline interpolation in the intermediate energy range, combining it with

our own fit of the total cross section of pion production to the data (see equations B1, B5 and B6 in Paper I).

In addition to Coulomb and escape losses, CR electrons also suffer losses due to radiative processes, including synchrotron, bremsstrahlung and IC emission (see Section 5.3). In order to model the latter, we assume that the energy density of the incident radiation field is composed of the CMB and stellar radiation, i.e. $\varepsilon_{\rm ph} = \varepsilon_{\rm CMB} + \varepsilon_{\star}$. The stellar contribution can be approximated by the FIR emission that results from dust-reprocessed UV light from young stellar populations, which we approximate with a black body distribution characterised by a temperature $T = 20$ K (Calzetti et al., 2000). The resulting photon energy density in each cell is calculated as

$$\varepsilon_{\star} = \sum_i \frac{L_{{\rm FIR},i}}{4\pi R_i^2 c}, \tag{5.5}$$

where we infer the FIR-luminosity $L_{{\rm FIR},i}$ from the SFR in each cell (Kennicutt, 1998) and sum over the fluxes arriving from all other cells at a distance of R_i by using a tree-code. If a cell is itself actively star forming, we equate the distance with the cells' radius, which we derive from its volume V_i via $R_i = [3V_i/(4\pi)]^{1/3}$.

Of particular interest in this work is the relative importance of radio emission due to primary vs. secondary CR electrons. The ratio of their distribution functions at 10 GeV has been derived in Paper I using a simplified analytical approximation:

$$\frac{f_{\rm e}^{\rm prim}}{f_{\rm e}^{\rm sec}} = K_{\rm ep}^{\rm inj} \frac{3}{128} 16^{\alpha_{\rm p}} \left(1 + \frac{\tau_{\pi}}{\tau_{\rm esc}}\right), \tag{5.6}$$

where τ_{π} denotes the timescale of pion production via hadronic CR proton interactions with the ISM, $\alpha_{\rm p}$ is the spectral index of the CR proton distribution, and $f_{\rm e}^{\rm sec} = f_{\rm e^+}^{\rm sec} + f_{\rm e^-}^{\rm sec}$ is the total steady-state distribution of secondary electrons and positrons. Adopting $K_{\rm ep}^{\rm inj} = 0.02$ and calorimetric conditions for secondary electron production, i.e. $\tau_{\pi} \ll \tau_{\rm esc}$ ($\tau_{\pi} \simeq \tau_{\rm esc}$), which consequently implies $\alpha_{\rm p} = \alpha_{\rm inj} = 2.2$, Eq. (5.6) yields $f_{\rm e}^{\rm prim}/f_{\rm e}^{\rm sec} \approx 0.2$ (0.4). In fact, this can be interpreted as a lower limit, because as soon as escape losses become more important than hadronic losses, i.e. $\tau_{\pi} \gtrsim \tau_{\rm esc}$, secondary production ceases to be efficient and primary electrons will dominate over secondary electrons and positrons. Thus, we expect for simulations that only account for CR advection and neglect CR diffusion secondary electrons to dominate by a factor of ~ 5 at 10 GeV in the calorimetric limit. By contrast, if we also include energy dependent diffusion, we will obtain steeper CR proton spectra with $\alpha_{\rm p} \gtrsim 2.2$ as soon as diffusion losses become important. This increases the ratio of primary to secondaries at 10 GeV significantly and we can expect primary

electrons to dominate over secondaries.

5.2.4 Radio emission and absorption processes

Radio emission from star-forming galaxies is due to non-thermal synchrotron as well as thermal bremsstrahlung emission, i.e free-free emission. The modeling of these emission processes, together with the corresponding absorption processes, is summarised in the following.

Radio synchrotron emission

Using our steady-state CR electron population f_e, we calculate the radio synchrotron emissivity, $j_\nu = E\,\mathrm{d}N_\gamma/(\mathrm{d}\nu \mathrm{d}V \mathrm{d}t)$, in each computational cell following Rybicki & Lightman (1986), via

$$j_\nu = \frac{\sqrt{3} e^3 B_\perp}{m_e c^2} \int_0^\infty f_\mathrm{e}(p_\mathrm{e}) F(\nu/\nu_\mathrm{c}) \mathrm{d}p_\mathrm{e}, \tag{5.7}$$

where $B_\perp$ is the component of the magnetic field perpendicular to the line of sight, e denotes the elementary charge and we use an analytical approximation provided by Aharonian et al. (2010) for the dimensionless synchrotron kernel $F(\nu/\nu_\mathrm{c})$ (Eq. 2.85), where ν_c is the critical frequency (see Section 2.3.2 for details). The typical synchrotron emission frequency ν_syn is related to the electron Lorentz factor γ_e via[1]

$$\nu_\mathrm{syn} = 2\nu_c = \frac{3eB_\perp}{2\pi m_\mathrm{e} c} \gamma_\mathrm{e}^2 \simeq 1\ \mathrm{GHz}\ \frac{B_\perp}{1\ \mu\mathrm{G}} \left(\frac{\gamma_\mathrm{e}}{10^4}\right)^2. \tag{5.8}$$

This indicates that observations of synchrotron emission at a fixed frequency typically probe electrons with lower (higher) Lorentz factors in higher (lower) magnetic field strengths, which we refer to as the 'ν_c-effect' in the following. The specific radio synchrotron intensity I_ν at frequency ν (in units of erg cm^{-2} s^{-1} Hz^{-1} sterad^{-1}) is obtained by integrating j_ν along the line of sight (denoted by s) and the specific radio luminosity (in units of erg s^{-1} Hz^{-1}) is obtained by integrating j_ν over the entire galaxy, yielding

$$I_\nu = \frac{1}{4\pi} \int_0^\infty j_\nu \mathrm{d}s \qquad \text{and} \qquad L_\nu = \int j_\nu \mathrm{d}V. \tag{5.9}$$

[1]This relation can be derived by approximating the synchrotron kernel with a Dirac delta distribution, but see also App. 2.3.2.

Thermal free-free emission and absorption processes

In addition to non-thermal synchrotron emission, we also expect a contribution from thermal free-free emission in the radio band, which predominantly depends on the electron density and temperature. To model this accurately, a multi-phase model of the ISM with radiative transfer would be required. Since this is beyond the scope of this work, we adopt a simplified model here, where we assume a temperature of $T = 8000$ K for the warm ionized medium, which dominates this emission component. To estimate the corresponding electron density, we take a fixed fraction ξ_e of the electron density $n_e = x_e\, n_H$ that we calculate from the fraction of free electrons x_e provided by our simplified pressurised ISM model (Springel & Hernquist, 2003), that models the ISM with an effective equation of state, and leave ξ_e as a free parameter of order unity.

In addition, we account for free-free absorption and synchrotron self-absorption by means of the radiative transfer equation (see Eq. 2.95). To this end, we (i) rotate the simulation into a desired inclination of the disc with the line of sight, (ii) construct thinly-spaced slices through the simulation box perpendicular to the line of sight, from the front of the simulation volume to its back, and (iii) cumulatively add the optical depth, that is a sum of the optical depth of free-free absorption, τ_{ff}, and synchrotron self-absorption, τ_{SSA}. Because the electron density along the line of sight depends on galactic inclination, the resulting amount of free-free emission and absorption inherits this dependence and so does the shape of the radio spectrum. Whereas free-free absorption predominantly affects the low-frequency part of radio spectra (see Section 5.5.1), we find that synchrotron self-absorption has a negligible effect at radio frequencies studied here.

5.3 Timescales

This section will provide an overview of the timescales of all relevant processes, which we define as $\tau = E/\dot{E}$. Because we aim at explaining the FRC at 1.4 GHz, we compute the timescales at a fixed observational frequency. According to Eq. (5.8), electrons that emit synchrotron radiation at GHz frequencies in μG magnetic fields have a typical energy of $E_e = 10^4\, m_e c^2 \approx 5$ GeV. These electrons can be primary and secondary electrons while the latter have been hadronically created by CR protons with typical energies of $E_p \approx 16 E_e \approx 80$ GeV.

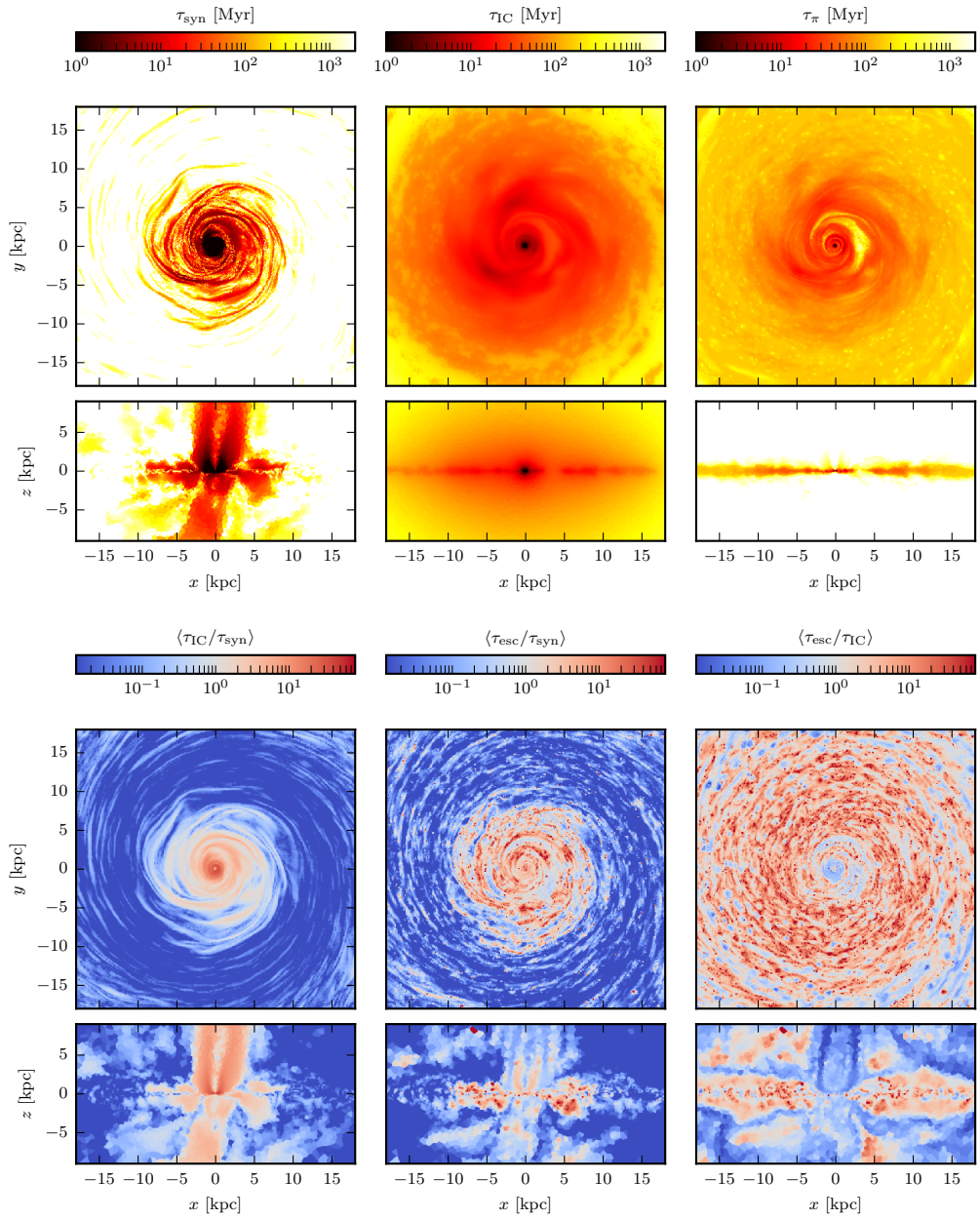

Figure 5.1: The upper panels show from left to right maps (slices) of the characteristic cooling timescales of synchrotron and IC cooling for CR electrons, as well as the timescale of hadronic interactions of CR protons, that is relevant for the production of secondary electrons. In the lower panels, we show the ratios of IC to synchrotron cooling, as well as the ratio of escape to synchrotron and to IC losses, respectively, where escape losses include losses due to CR advection and diffusion. The timescale ratios are averaged over thin slices with a thickness of 500 pc and the timescales are calculated at an energy of 10 GeV. All maps are shown for a snapshot with a halo mass of $M_{200} = 10^{12}\,\mathrm{M}_\odot$ at $t = 2.3$ Gyr.

5.3.1 Non-radiative processes

The injection timescale of secondaries corresponds to the timescale of hadronic interactions of CR protons with the ISM, and is given by

$$\tau_\pi = \frac{1}{c n_\mathrm{N} K_\mathrm{p} \sigma_\mathrm{pp}} \approx 240 \left(\frac{n_\mathrm{N}}{0.1\ \mathrm{cm}^{-3}}\right)^{-1} \mathrm{Myr}, \tag{5.10}$$

where the cross section of hadronic interactions is $\sigma_\mathrm{pp} \approx 44\,\mathrm{mbarn}$ for $\alpha_\mathrm{p} = 2.2$ (Pfrommer et al., 2017b), the inelasticity of hadronic interactions is given by $K_\mathrm{p} = 1/2$ (Mannheim & Schlickeiser, 1994), $n_\mathrm{N} = n_\mathrm{H} + 4n_\mathrm{He} = (X_\mathrm{H} + 1 - X_\mathrm{H})\rho/m_\mathrm{p} = \rho/m_\mathrm{p}$ is the number density of target nucleons in the ISM, where $X_\mathrm{H} = 0.76$ denotes the hydrogen fraction and ρ is the gas density. Consequently, the hadronic timescale directly traces the gas density, as can bee seen in the upper right panels in Fig. 5.1, which shows τ_π for our M82-like galaxy, see Table 5.2.

Coulomb interactions of CRs with the ambient medium of an electron number density n_e act on a timescale (Gould, 1972b)

$$\begin{aligned}\tau_\mathrm{Coul} &= \frac{2E_\mathrm{e}\beta_\mathrm{e}}{3\sigma_\mathrm{T} n_\mathrm{e} m_\mathrm{e} c^3}\left[\ln\left(\frac{m_\mathrm{e}c^2\beta_\mathrm{e}\sqrt{\gamma_\mathrm{e}-1}}{\hbar\omega_\mathrm{pl}}\right) - \ln(2)\left(\frac{\beta_\mathrm{e}^2}{2} + \frac{1}{\gamma_\mathrm{e}}\right) + \frac{1}{2} + \left(\frac{\gamma_\mathrm{e}-1}{4\gamma_\mathrm{e}}\right)^2\right]^{-1} \\ &\propto \frac{E_\mathrm{e}}{n_\mathrm{e}} \propto \frac{1}{B^{1/2} n_\mathrm{e}},\end{aligned} \tag{5.11}$$

where the normalised electron velocity is denoted by $\beta_\mathrm{e} = v_\mathrm{e}/c$, σ_T is the Thompson cross section, the plasma frequency is defined by $\omega_\mathrm{pl} = \sqrt{4\pi e^2 n_\mathrm{e}/m_\mathrm{e}}$ and we used in the last step the relativistic limit and Eq. (5.8) so that the last expression is only valid at fixed synchrotron emission frequency. Adopting an electron number density of $n_\mathrm{e} = 0.1\,\mathrm{cm}^{-3}$, Coulomb losses act on timescales of $\sim 2\,\mathrm{Gyr}$ for highly relativistic electrons with $\gamma_\mathrm{e} = 5\,\mathrm{GeV}/(m_\mathrm{e}c^2) \approx 10^4$, whereas middly-relativistic electrons with $\gamma_\mathrm{e} \sim 10$ cool on timescales of $\tau \approx 3\,\mathrm{Myr}$. Thus, Coulomb losses typically remove the low-energy part of the CR electron spectrum. Consequently, in order for radio-synchrotron emitting electrons (with typical Lorentz factors $\gamma_\mathrm{e} \sim 10^4$ for $B = 1\ \mu\mathrm{G}$ and $\nu_\mathrm{syn} = 1.4\,\mathrm{GHz}$) to be affected by Coulomb losses, very high densities are required.

5.3.2 Radiative processes

At high electron energies, radiative losses due to synchrotron, IC or bremsstrahlung emission are typically dominant. The loss timescale due to synchrotron emission is given by

$$\tau_{\rm syn} = \frac{3E_{\rm e}}{\sigma_{\rm T} c \beta_{\rm e}^2 \gamma_{\rm e}^2 \varepsilon_B} \propto \frac{1}{E_{\rm e} B^2} \propto B^{-3/2}, \tag{5.12}$$

where $\varepsilon_B = B^2/(8\pi)$ and we used Eq. (5.8) in the last step so that this dependence is only valid at fixed synchrotron emission frequency. For instance, in central regions of starburst galaxies with magnetic field strengths of $\approx 10\,\mu$G, where electrons with typical energies of $E_{\rm e} \approx 2$ GeV are responsible for radio synchrotron emission at GHz frequencies, the synchrotron cooling timescale is $\tau_{\rm syn} \approx 70\,$Myr. In starburst nuclei with up to $B \approx 50\ \mu$G, synchrotron cooling acts on even shorter timescales of $\tau_{\rm syn} \approx 6\,$Myr.

In an ambient radiation field with a photon energy density $\varepsilon_{\rm ph}$, CR electrons scatter off of these photons and lose energy on a timescale

$$\tau_{\rm IC} = \frac{3E_{\rm e}}{\sigma_{\rm T} c \beta_{\rm e}^2 \gamma_{\rm e}^2 \varepsilon_{\rm ph}} \propto \frac{1}{E_{\rm e} \varepsilon_{\rm ph}} \propto \frac{B^{1/2}}{\varepsilon_{\rm ph}}, \tag{5.13}$$

where the last step is only valid at fixed synchrotron emission frequency. Note that $\varepsilon_{\rm ph}$ is a sum of a stellar contribution ($\varepsilon_\star$, modeled by Eq. 5.5) and the CMB ($\varepsilon_{\rm CMB} \approx 4.16 \times 10^{-13}\,(1+z)^2\,{\rm erg\,cm^{-3}}$, where z is the cosmic redshift). The CMB is ubiquitous and independent of the local SFR (or $\varepsilon_\star$). For a photon energy density of $\varepsilon_{\rm ph} = 5\varepsilon_{\rm CMB}$, the IC cooling timescale ranges from ~ 40 Myrs to ~ 140 Myrs in regions with magnetic field strengths of 1 to $10\,\mu$G, where we again adopted Eq. (5.8). Because $\tau_{\rm syn}/\tau_{\rm IC} \propto B_{\rm ph}^2/B^2$, where $B_{\rm ph} = (8\pi\varepsilon_{\rm ph})^{1/2}$ is the equivalent magnetic field strength, IC losses will always dominate over synchrotron losses if $B_{\rm ph} > B$. Because the photon energy density of the CMB corresponds to $B_{\rm CMB} \approx 3\ \mu$G today, IC losses will be relevant as soon as the magnetic field drops below 3 μG, and correspondingly at larger magnetic field strengths if we additionally account for a stellar radiation field.

In a fully ionized medium with a proton number density $n_{\rm p}$, CR electrons lose energy due to the emission of bremsstrahlung on a timescale (Blumenthal & Gould, 1970)

$$\tau_{\rm brems} = \frac{E_{\rm e}}{4\alpha r_0^2 c n_{\rm p} \beta_{\rm e} \gamma_{\rm e} m_{\rm e} c^2} \left[\ln(2\gamma_{\rm e}) - \frac{1}{3}\right]^{-1} \propto \frac{1}{n_{\rm p} \ln E_{\rm e}}, \tag{5.14}$$

where α is the fine structure constant and r_0 denotes the electron radius. Again, adopting electrons

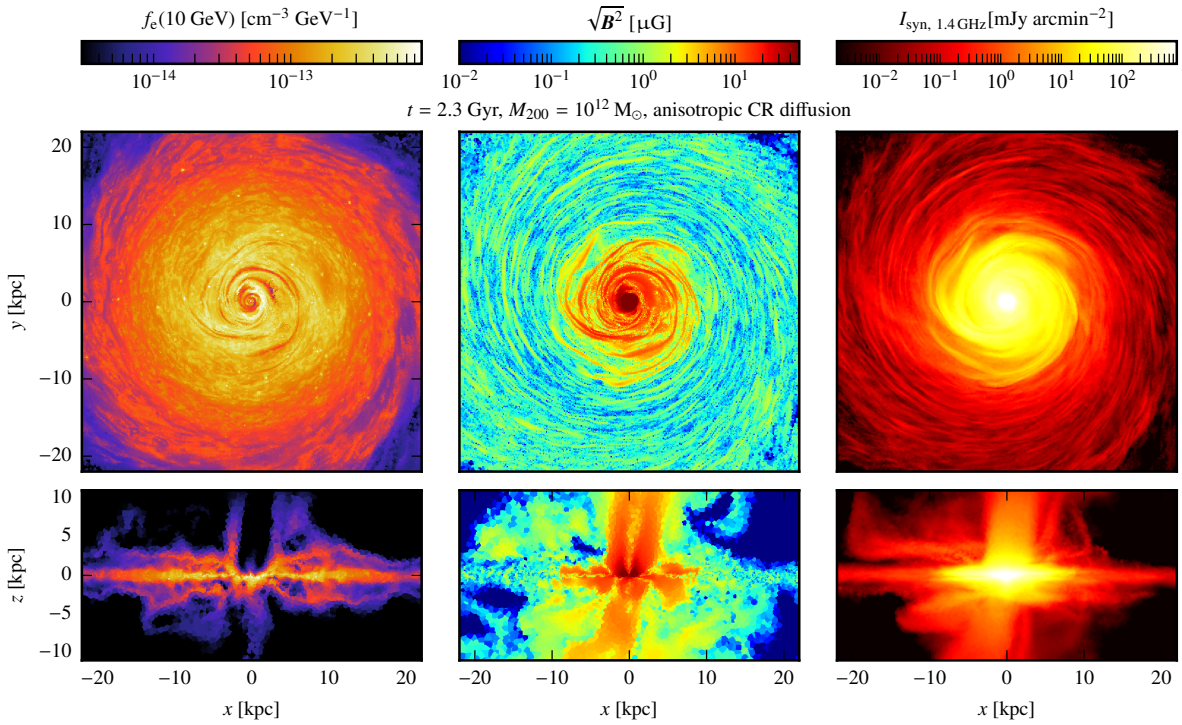

Figure 5.2: Face-on (upper panels) and edge-on (lower panels) maps of the CR electron distribution f_e at 10 GeV (left hand panels), the magnetic field strength (middle panels) and the total (primary and secondary) synchrotron intensity at 1.4 GHz (right hand panels) of a simulation with $M_{200} = 10^{12}\,\mathrm{M}_\odot$, $B_0 = 10^{-10}$ G and $\zeta_{\mathrm{SN}} = 0.05$ at $t = 2.3$ Gyr (i.e. the same snapshot as shown in Fig. 5.1).

with energies of 5 GeV, bremsstrahlung losses act in a medium with $n_{\mathrm{p}} = 0.1\,\mathrm{cm}^{-3}$ on timescales of $\tau_{\mathrm{brems}} \approx 480$ Myr. Consequently, high densities are required in order for bremsstrahlung losses to be able to compete with synchrotron or IC losses, as we will further discuss in Section 5.5.2.

5.3.3 Large dynamic range

The SFR-gas surface density relation, $\dot{\Sigma}_\star \propto \Sigma_{\mathrm{gas}}^{1.4}$, of star-forming and starburst galaxies suggested by Kennicutt (1998) is valid over a large dynamic range of five orders of magnitude in gas surface density. As a result, the CR cooling timescales that depend on gas density are expected to vary on a similarly large range of scales. Because the photon energy density is related to star formation, IC cooling strongly depends on the gas density via the Kennicutt (1998) relation, too. Similarly, the magnetic field strengths of star-forming galaxies are found to scale with gas surface density (Robishaw et al., 2008), resulting in a strong variation of the synchrotron cooling timescale with gas density as well. However, these cooling timescales are not only expected to significantly vary

among different types of galaxies, i.e. from dwarfs to starbursts, but also within a galaxy. In particular, the relative importance of the cooling and loss timescales is of relevance for shaping their spectra and determining their non-thermal emission properties.

This is exemplified in Fig. 5.1, where we show maps of the timescale of synchrotron and IC cooling of CR electrons and the hadronic timescale of CR protons, both at an energy of 10 GeV (upper panels), for our fiducial halo at $t = 2.3\,\mathrm{Gyr}$. As expected, the synchrotron cooling timescale traces the magnetic field (see Fig. 5.2) and varies from a few Myr in the very central regions with strong magnetic fields up to a few tens of Myr in the disc at around 5 kpc from the center. At larger radii, the synchrotron timescale increases with decreasing magnetic field as $\tau_{\mathrm{syn}} \propto B^{-2}$. By contrast, the IC cooling scales as $\tau_{\mathrm{IC}} \propto \varepsilon_{\mathrm{ph}}^{-1}$ and consequently, IC cooling remains important at larger radii, where the photon energy density is still high and approaches $\varepsilon_{\mathrm{CMB}}$. Consequently, IC dominates over synchrotron cooling beyond 5 kpc (see lower left panel in Fig. 5.1). Note that this ratio is independent of the electron energy, due to the identical energy dependence of IC and synchrotron losses. In those regions where synchrotron cooling dominates over IC cooling, the former is also faster than advection and diffusion losses, i.e. escape losses (lower middle panels in Fig. 5.1). However, in the outskirts of the galactic disc, IC losses dominate over escape losses and only within the outflows, advection losses become relevant.

5.4 The FIR-radio correlation

We will now describe our modelling of the FRC from our simulations, which allows us to dissect the contribution from primary and secondary electrons to the total radio synchrotron luminosity. Furthermore, we will assess calorimetry and analyse possible deviations from the calorimetric picture in starburst galaxies.

5.4.1 Modelling the FIR-radio correlation

Post-processing our simulations, we derive the steady-state CR electron distributions f_{e} (Eq. 5.1) in every resolution element. We show the sum of the primary and secondary electron equilibrium distribution at 10 GeV in the left-hand panels of Fig. 5.2 for our fiducial halo, i.e. a simulation with halo mass $M_{200} = 10^{12}\,\mathrm{M}_{\odot}$, after 2.3 Gyr. Together with the magnetic field of our MHD simulation (shown in the middle panels of Fig. 5.2), we can directly calculate the resulting radio synchrotron emission of the steady-state electron distribution, using Eq. (5.7). This is shown in the right-hand panels of Fig. 5.2 in terms of the specific radio synchrotron intensity I_ν at a frequency

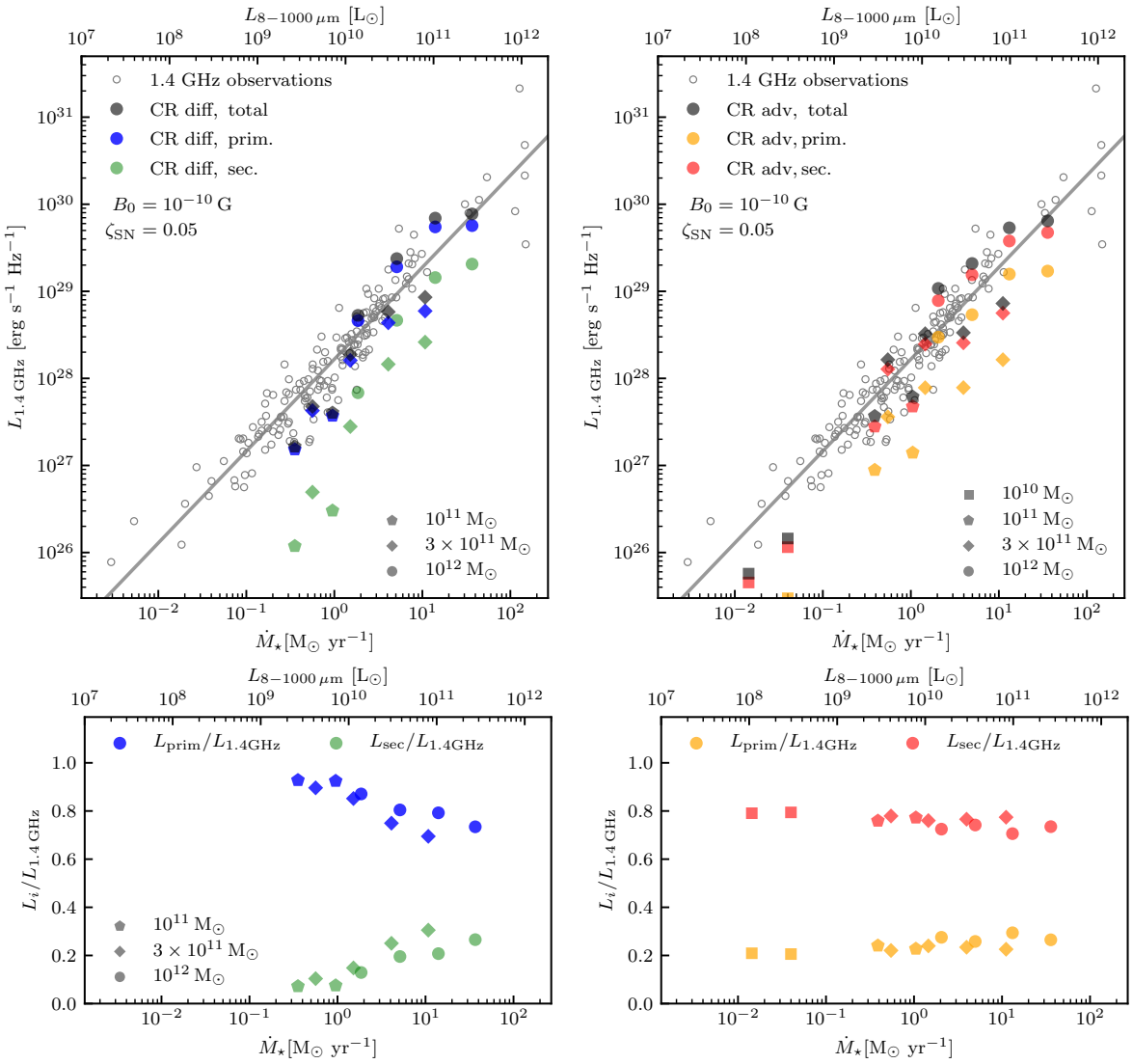

Figure 5.3: Top panels: we compare the observed FRC (Bell, 2003, open circles and a fit to the data, grey line) to our simulated FRC (black symbols for the total radio synchrotron luminosity) in our model that accounts for CR advection and diffusion ('CR diff', left-hand panels) as well as our CR advection-only model ('CR adv', right-hand panels) and assume face-on configurations for all galaxies. Colour coded are contributions from primary (blue and orange) and secondary (green and red) CR electrons and different symbols correspond to simulations with different halo masses (indicated in the legends). All simulations assume $B_0 = 10^{-10}$ G and $\zeta_{SN} = 0.05$. Bottom panels: we show the corresponding relative contributions to the total radio luminosity due to primary and secondary electrons, respectively. Note that the secondary emission dominates in our 'CR adv' model while the primary emission dominates in our 'CR diff' model.

of $\nu = 1.4$ GHz as it would be observed in a face-on (upper panel) or edge-on (lower panel) configuration. The radio emission in our projected maps is clearly dominated by the central region up to radii of ∼10 kpc, where the magnetic field is strong. Particular filamentary features are visible in the edge-on view of the radio emission. Those trace the morphology of the magnetic field, which reaches up more than 10 kpc above and below the disc, and which is shaped by a strong central outflow driven by the CR pressure gradient.

Because the radio synchrotron emissivity j_ν in Eq. (5.7) depends on the component of the magnetic field perpendicular to the line of sight and hence on the viewing angle, the calculation of the observed radio luminosity also depends on the observed orientation. For the FRC, we chose to calculate the radio luminosity for a face-on configuration of our galaxies. The corresponding edge-on luminosities are typically a factor of about two smaller, which introduces a natural scatter in the FRC (Pfrommer et al., 2021). We correlate the face-on radio synchrotron luminosities against the SFR ($\dot{M}_\star$) of our simulated galaxies with an initial magnetic field of $B_0 = 10^{-10}$ G and $\zeta_{\rm SN} = 0.05$ in Fig. 5.3. The corresponding FIR luminosities as derived from the SFRs using the Kennicutt (1998) relation are shown at the upper horizontal axis. For each simulated galaxy, we take snapshots at the peak of the SFR and at times when the SFR has successively decreased by an e-folding, which yields snapshots that are equally spaced in $\log \dot{M}_\star$. The effect of varying the initial magnetic field B_0 and the injection efficiency of CRs at SNRs, $\zeta_{\rm SN}$, on the FRC is discussed in App. 5.9. Note that we only show the radio synchrotron luminosities here and discuss possible contributions from thermal free-free emission in Section 5.5.1.

Our simulation models which only allow for CR advection ('CR adv', right-hand panel of Fig. 5.3) and where we additionally account for anisotropic CR diffusion ('CR diff', left-hand panel) match the observed FRC (Bell, 2003) over a broad range of SFRs. However, the radio luminosities of the smallest halos with $M_{200} = 10^{10}\,{\rm M}_\odot$ fall short of the FRC in our 'CR diff' model and are not visible within the range of radio luminosities shown in Fig. 5.3. As discussed in Pfrommer et al. (2021), these dwarf galaxies show a slower dynamo growth in comparison to the more massive halos. Additionally, they generate strong outflows that are launched due to the inclusion of anisotropic diffusion of CRs, enabling CRs to escape from the galactic disc, which further reduces the resulting radio emission. By contrast, in the 'CR adv' model, the small-scale dynamo efficiently amplifies the magnetic field and CRs accumulate in the galaxy because they cannot diffuse out of the disc by construction. Hence, our dwarf galaxies with $M_{200} = 10^{10}\,{\rm M}_\odot$ are able to reach the FRC in the 'CR adv' model (see Fig. 5.3, right-hand panel).

In addition to the total radio luminosity, Fig. 5.3 also shows the contributions arising from primary and secondary electrons separately, which are further analysed in the following section.

5.4.2 Secondary vs. primary synchrotron emission

Complementary to Pfrommer et al. (2021), here we aim to understand the individual contributions of primary and secondary electrons to the total radio synchrotron luminosity, which enables us to dissect the reasons for our successful reproduction of the observed FRC. First of all, in our approach, the injected CR proton luminosity is given by

$$L_{\rm p} = \zeta_{\rm SN} \dot{M}_\star \epsilon_{\rm SN} \,, \tag{5.15}$$

where $\epsilon_{\rm SN} = E_{\rm SN}/M_\star = 10^{51}\,{\rm erg}/(100\,{\rm M}_\odot) = 10^{49}\,{\rm erg\,M}_\odot^{-1}$ is the SN energy released per unit mass (see Pfrommer et al., 2017a), where we assume a Chabrier (2003) initial mass function. Adopting our fiducial injection efficiency of CR energy at SN remnants, $\zeta_{\rm SN} = 0.05$ (Pais et al., 2018), and using the Kennicutt (1998) relation between SFR and FIR luminosity, we obtain

$$L_{\rm p} \approx 5.5 \times 10^{-4} \left(\frac{\zeta_{\rm SN}}{0.05}\right) L_{\rm FIR}. \tag{5.16}$$

The primary electron population obtains a fraction $\zeta_{\rm prim}$ of the total luminosity of CR protons in our modeling that is given by (see Appendix A in Paper I)

$$L_{\rm prim-e} = \zeta_{\rm prim}\, L_{\rm p} = \left(\frac{m_{\rm p}}{m_{\rm e}}\right)^{\alpha_{\rm p}-2} K_{\rm ep}^{\rm inj}\, L_{\rm p}. \tag{5.17}$$

Using $K_{\rm ep}^{\rm inj} = 0.02$ and $\alpha_{\rm p} = 2.2$, this yields $\zeta_{\rm prim} \approx 0.09$.

On the other hand, hadronic interactions of CR protons with the ISM lead to the production of secondary electrons and positrons. Assuming that CR protons exclusively cool via hadronic interactions, the fraction of total proton luminosity injected into secondary electrons and positrons, i.e. $\zeta_{\rm sec} = L_{\rm sec-e}/L_{\rm p}$ can be estimated from the following consideration. Charged pions are produced in hadronic CR proton-proton interactions with a multiplicity 2/3 and on average, electrons/positrons obtain 1/4 of the pion energy, which yields a secondary fraction of about $2/3 \times 1/4 = 1/6$ of the total proton luminosity. Considering additionally the nuclear enhancement factor of 1.4 to 1.6, which accounts for heavier nuclei in the composition of CRs and the ISM (Białłas et al., 1976; Stephens & Badhwar, 1981), we arrive at an energy fraction of $\zeta_{\rm sec} \approx 0.25$. Hence, secondary electrons and positrons obtain a luminosity of

$$L_{\rm sec-e} = \eta_{\rm cal,p}\, \zeta_{\rm sec}\, L_{\rm p}, \tag{5.18}$$

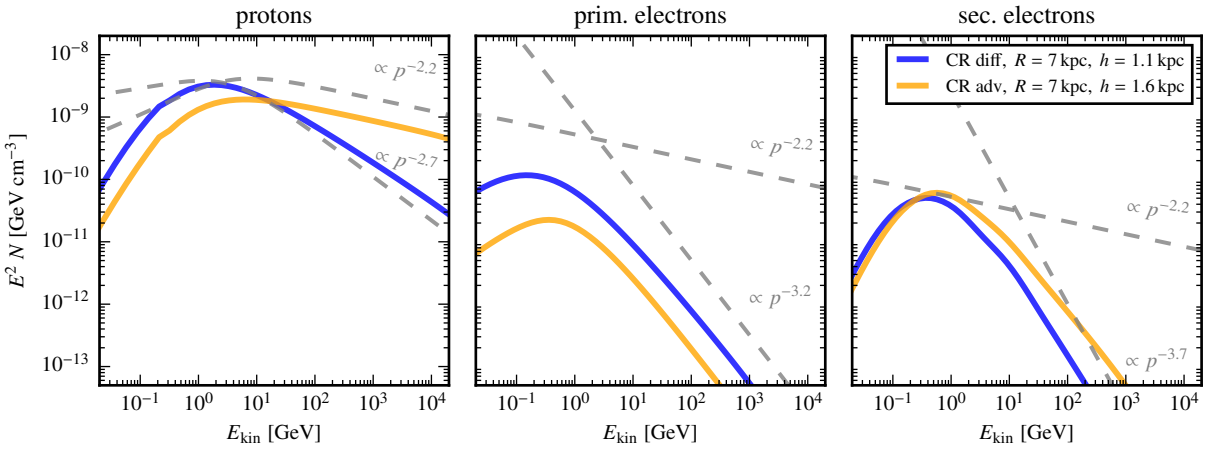

Figure 5.4: From left to right, we show CR proton, primary and secondary electron spectra of simulations with $M_{200} = 10^{12}\,\mathrm{M}_\odot$, $\zeta_{\rm SN} = 0.05$, $B_0 = 10^{-10}\,\mathrm{G}$. We contrast the CR spectra of snapshots at $t = 1.3\,\mathrm{Gyr}$ of a simulation that includes advection and anisotropic diffusion of CRs ('CR diff', blue) to a simulation that only accounts for CR advection ('CR adv', yellow). In both cases, we average the spectra over the radial range, that includes 99 per cent of the total radio luminosity at 1.4 GHz (i.e. $R \approx 7\,\mathrm{kpc}$ for both snapshots) and the height, where the magnetic field has decreased by an e-folding, as indicated in the legend. The grey dashed lines show momentum power-law spectra (with arbitrary normalisation to exemplify scaling properties) that are typical for the various transport and cooling processes (with indices indicated in the panels). These spectra account for the full proton/electron dispersion relation, which causes the mild downturn of the proton spectrum at energies $E_{\rm kin} \lesssim 1$ GeV.

where we additionally accounted for the calorimetric fraction of protons $\eta_{\rm cal,p}$. This factor quantifies the fraction of CR proton luminosity that is used for pion production, which reaches values up to $\eta_{\rm cal,p} \approx 0.8$ for highly star-forming galaxies (see Paper II). We assume a simple power-law momentum spectrum for the source function of CR electrons with a low-momentum cutoff $p_{\rm min}$ and calculate the volume-integrated injected electron source function via:

$$Q_{\rm e}(p_{\rm e}) = \frac{{\rm d}N_{\rm e}}{{\rm d}p_{\rm e}{\rm d}t} = \int q_{\rm e}(p_{\rm e}){\rm d}V = C_{\rm e} p_{\rm e}^{-\alpha_{\rm e,inj}} \theta(p_{\rm e} - p_{\rm min}), \tag{5.19}$$

where $\theta(p)$ denotes the Heaviside step function and $C_{\rm e}$ is the normalization. Assuming furthermore $\alpha_{\rm e,inj} > 2$, this enables us to define the total injected CR electron luminosity via

$$\begin{aligned} L_{\rm e} &= \int_0^\infty Q_{\rm e}(p_{\rm e})\, T_{\rm e}(p_{\rm e}) dp_{\rm e} = \frac{C_{\rm e}\, m_{\rm e} c^2}{\alpha_{\rm e,inj} - 1} \\ &\quad \times \left[\frac{1}{2} \mathcal{B}_{\frac{1}{1+p_{\rm min}^2}} \left(\frac{\alpha_{\rm e,inj} - 2}{2}, \frac{3 - \alpha_{\rm e,inj}}{2} \right) + p_{\rm min}^{1-\alpha_{\rm e,inj}} \frac{T_{\rm e}(p_{\rm min})}{m_{\rm e} c^2} \right] \end{aligned} \tag{5.20}$$

$$\equiv C_{\rm e}\, m_{\rm e} c^2 A_{\rm bol}(p_{\rm min}, \alpha_{\rm e,inj}), \tag{5.21}$$

where $T_{\rm e}(p_{\rm e}) = \left(\sqrt{1 + p_{\rm e}^2} - 1 \right) m_{\rm e} c^2$ is the kinetic electron energy and $\mathcal{B}_y(a, b)$ denotes the incomplete beta function (Abramowitz & Stegun, 1965). Assuming that the synchrotron cooling time of CR electrons is shorter than their escape time (Völk, 1989), the emitted synchrotron luminosity from a steady-state electron distribution $f_{\rm e}$ can be calculated as

$$\begin{aligned} \nu L_\nu({\rm GHz}) &= \frac{E_\gamma {\rm d}N_\gamma}{{\rm d}\ln\nu\, {\rm d}t} = \eta_{\rm syn} \frac{E_{\rm e} {\rm d}N_{\rm e}}{2\, {\rm d}\ln\gamma_{\rm e}\, {\rm d}t} \approx \eta_{\rm syn} \frac{\gamma_{\rm e}^{2-\alpha_{\rm e,inj}}}{2 A_{\rm bol}} L_{\rm e} \end{aligned} \tag{5.22}$$

$$\equiv \eta_{\rm syn}\, \zeta_{\rm bol}(p_{\rm min}, \alpha_{\rm e,inj}, \gamma_{\rm e})\, L_{\rm e}. \tag{5.23}$$

Here, we use ${\rm d}\ln\nu = 2{\rm d}\ln\gamma_{\rm e}$ (see Eq. 5.8) and Eq. (5.21), while assuming the relativistic limit ${\rm d}p_{\rm e} \approx {\rm d}\gamma_{\rm e}$ in Eq. (5.19). Furthermore, we define the bolometric electron fraction $\zeta_{\rm bol} = \gamma_{\rm e}^{2-\alpha_{\rm e,inj}}/(2A_{\rm bol})$, that accounts for the fraction of total electron luminosity that could potentially be converted into a specific synchrotron luminosity at frequency ν, given a magnetic field B and electrons with Lorentz factor $\gamma_{\rm e}(\nu, B)$ (Eq. 5.8). In addition, we introduce the calorimetric synchrotron fraction $\eta_{\rm syn}$, that quantifies the fraction of the available CR electron luminosity $\zeta_{\rm bol} L_{\rm e}$ that is actually converted into synchrotron emission, which will be discussed in more detail in Section 5.4.3.

Equations (5.19) to (5.23) can be separably adapted to primary and secondary electrons. Hence, we arrive at an FRC that reads for the specific luminosity as a function of FIR luminosity for each

CR electron population as

$$\nu L_{\nu,\mathrm{prim}}(\mathrm{GHz}) \approx 1.0\times10^{-7}\left(\frac{\eta_{\mathrm{syn,prim}}}{0.1}\right)\left(\frac{\zeta_{\mathrm{bol}}}{0.02}\right)L_{\mathrm{FIR}}, \tag{5.24}$$

and

$$\nu L_{\nu,\mathrm{sec}}(\mathrm{GHz}) \approx 1.3\times10^{-8}\left(\frac{\eta_{\mathrm{cal,p}}}{0.8}\right)\left(\frac{\eta_{\mathrm{syn,sec}}}{0.1}\right)\left(\frac{\zeta_{\mathrm{bol}}}{0.001}\right)L_{\mathrm{FIR}}, \tag{5.25}$$

where we use $\zeta_{\mathrm{SN}} = 0.05$. The 1.4 GHz radio luminosity as a function of SFR reads (using again Kennicutt, 1998),

$$L_{1.4\mathrm{GHz,prim}} \approx 2.0\times10^{27}\left(\frac{\eta_{\mathrm{syn,prim}}}{0.1}\right)\left(\frac{\zeta_{\mathrm{bol}}}{0.02}\right)\left(\frac{\dot{M}_\star}{\mathrm{M}_\odot\,\mathrm{yr}^{-1}}\right), \tag{5.26}$$

and

$$L_{1.4\mathrm{GHz,sec}} \approx 2.6\times10^{26}\left(\frac{\eta_{\mathrm{cal,p}}}{0.8}\right)\left(\frac{\eta_{\mathrm{syn,sec}}}{0.1}\right)\left(\frac{\zeta_{\mathrm{bol}}}{0.001}\right)\left(\frac{\dot{M}_\star}{\mathrm{M}_\odot\,\mathrm{yr}^{-1}}\right), \tag{5.27}$$

where we adopted $\gamma_{\mathrm{e}} = 6\times10^3$, which is the typical Lorentz factor of CR electrons emitting synchrotron radiation at 1.4 GHz in magnetic fields of 2 μG (see Eq. 5.8) and $\zeta_{\mathrm{bol}}(p_{\mathrm{min}} = 1, \alpha_{\mathrm{e,inj}} = 2.2, \gamma_{\mathrm{e}} = 6\times10^3) \approx 0.02$ for primary electrons, as well as $\zeta_{\mathrm{bol}}(p_{\mathrm{min}} = 1, \alpha_{\mathrm{e,inj}} = 2.7, \gamma_{\mathrm{e}} = 6\times10^3) \approx 0.001$ secondary electrons. This analytical estimate yields a synchrotron luminosity from secondary electrons that is a factor of ~ 10 smaller than the luminosity arising from primary electrons, if the assumptions $\eta_{\mathrm{cal,p}} = 0.8$, $\eta_{\mathrm{syn,prim}} = \eta_{\mathrm{syn,sec}} = 0.1$ and $\zeta_{\mathrm{bol}} = 0.02$ hold for primary electrons, whereas $\zeta_{\mathrm{bol}} = 0.001$ for secondary electrons. We will discuss the choice of these parameters in the following.

The primary and secondary contributions to the total synchrotron luminosity $L_{1.4\,\mathrm{GHz}}$ in our simulations (Fig. 5.3, dark-gray symbols) are separately shown in the upper panels of Fig. 5.3 with different colors, as indicated in the legend. The lower panels show the fraction of the primary and secondary luminosities, respectively. Whereas the primary luminosities fall short of the secondary emission in the 'CR adv' model (right-hand panels), the radio luminosity is strongly dominated by primary electrons in our 'CR diff' model (left-hand panels), with an increasing contribution from secondaries towards higher SFRs. This is due to the difference in both models in the parameters entering Eq. (5.27).

First, the calorimetric proton fraction $\eta_{\mathrm{cal,p}}$, representing the efficiency of secondary electron

production due to hadronic interactions, has been shown in Paper II to decrease with decreasing SFR in the 'CR diff' model from 0.7 in starburst galaxies, down to 0.1 in our dwarf galaxies. In the 'CR adv model', $\eta_{\rm cal,p}$ reaches values up to 0.8 and only typically varies by a factor of ~ 2. The reduced efficiency of pion production due to CR diffusion can be understood by the fact that CR diffusion is another CR proton loss process that competes with hadronic losses and thus lowers the secondary radio luminosity. However, the difference of $\eta_{\rm cal,p}$ for star-forming galaxies with $\dot{M}_\star \gtrsim 1\ {\rm M}_\odot\ {\rm yr}^{-1}$ is not significant enough to fully explain the discrepancy in $L_{\rm prim}$ vs. $L_{\rm sec}$ in our different CR transport models.

A more relevant effect for explaining the sub-dominant role of secondary electrons for the total radio luminosity in the 'CR diff' model is the effect of the steepening of the CR proton spectra due to energy-dependent diffusion. As an example, we show in Fig. 5.4 CR spectra of CR protons, primary and secondary electrons of a simulation with $M_{200} = 10^{12}\ {\rm M}_\odot$ for both CR transport models at $t = 1.3$ Gyr. The averaged CR spectra (shown with colours) are compared to momentum power-law spectra that are typical for the various transport and cooling processes (shown with grey-dashed lines), in which we account for the full proton/electron dispersion relation. This causes the mild downturn of the proton spectrum at energies $E_{\rm kin} \lesssim 1$ GeV. We can clearly see the effect of Coulomb-cooling, which suppresses the spectra in comparison to the momentum power-law spectrum and which is stronger for CR protons in comparison to primary electrons, due to the dependence of Coulomb-cooling on $\beta = v/c$ (see Eq. 5.11 and Paper I).

At high energies, the CR proton spectrum stays flat in the 'CR adv' model, i.e. $\alpha_{\rm p,adv} = \alpha_{\rm inj} = 2.2$, whereas the spectral index approaches $\alpha_{\rm p,diff} = 2.7$ in the 'CR diff' model, which accounts for energy-dependent diffusion, i.e. $D \propto E^{0.5}$. Because the steady-state proton distribution determines the source function of secondary electrons, $\alpha_{\rm sec-e,inj} = \alpha_{\rm p}$, the latter also exhibits a steeper steady-state spectrum in the model accounting for energy-dependent diffusion losses after accounting for the radiative steepening of the electron spectra due to IC and synchrotron interactions, $\alpha_{\rm sec-e} = \alpha_{\rm p,diff} + 1 = 3.7$. By contrast, the steady-state spectrum of primary electrons has a similar spectral shape in both models, with $\alpha_{\rm prim-e} = 3.2$ at high energies, where IC and synchrotron cooling dominate. Note that the spectra in Fig. 5.4 are averaged over the radii that include 99 per cent of the total radio luminosity in both snapshots, respectively, and a characteristic scale-height of the magnetic field (as indicated in the legend) so that we show representative CR spectra for explaining the radio synchrotron emission at 1.4 GHz.

This effect of steeper secondary CR electron spectra is entering Eq. (5.27) in the form of $\zeta_{\rm bol}$, that is a function of $p_{\rm min}$, $\gamma_{\rm e}(\nu, B)$ and $\alpha_{\rm e}$ (see Eq. 5.23). We exemplify these dependencies in Fig. 5.5, that shows the strong decrease of $\zeta_{\rm bol}$ with increasing spectral index $\alpha_{\rm e}$ of the CR electron

source function, which affects the available luminosity of primary and secondary electrons, that can be converted to radio synchrotron emission. As expected, steeper electron spectra imply a smaller amount of electrons available for synchrotron emission at a fixed frequency. While the low-momentum cut-off of the CR electron spectra does not have a significant impact on $\zeta_{\rm bol}$, the electrons' Lorentz factor $\gamma_{\rm e}$ naturally becomes increasingly more relevant for increasing spectral indices. As a result, $\zeta_{\rm bol}$ is affected by the $\nu_{\rm c}$-effect.

Consequently, we identify two main effects that can potentially be responsible for suppressing the radio luminosity via $\zeta_{\rm bol}$: (i) the steeper secondary CR electron source functions with the limiting value of $\alpha_{\rm sec-e,inj} = 2.7$ due to CR diffusion decrease $L_{\rm 1.4GHz,sec}$ (in comparison to primaries with $\alpha_{\rm prim-e,inj} = 2.2$ in both models and also secondaries with $\alpha_{\rm sec-e,inj} = 2.2$ in the 'CR adv' model), and (ii) the $\nu_{\rm c}$-effect, i.e., synchrotron emission at a fixed frequency in a lower magnetic field strength is generated by higher-energetic electrons, which are less abundant. This implies a smaller value of $\zeta_{\rm bol}$, which leads to a lower observed radio luminosity. The second effect is subdominant for primary CR electrons in both CR transport models and for secondary CR electrons in the 'CR adv' model because $\zeta_{\rm bol}$ does not significantly depend on $\gamma_{\rm e}$ for $\alpha_{\rm e,inj} = 2.2$. However, with increasingly larger $\alpha_{\rm e,inj}$, $\zeta_{\rm bol}$ is reduced by up to a factor of 5, when we increase $\gamma_{\rm e}$ by an order of magnitude. This is in fact the case within our simulations: As pointed out by Pfrommer et al. (2021), our simulations exhibit saturated magnetic field strengths of 0.1 μG to 14 μG for SFRs of 0.01 to 30 $\rm M_\odot\ yr^{-1}$ in our 'CR diff' model. This implies typical Lorentz factors of electrons emitting at 1.4 GHz that range from $\gamma_{\rm e} \approx 3.5 \times 10^4$ to $\gamma_{\rm e} \approx 3.5 \times 10^3$. As a result the $\nu_{\rm c}$-effect indeed plays an important role and is particularly strong for secondary electrons: as we move from starburst to dwarf galaxies the saturated magnetic field strengths decrease and imply increasing Lorentz factors of CR electrons, which diminishes the total radio luminosity (if it is observed at a fixed frequency). But in the case of our 'CR diff' model, diffusive losses become increasingly more important towards lower star-forming galaxies (Paper II), which steepens $\alpha_{\rm p} = \alpha_{\rm inj,sec.e}$ and hence, the secondary contribution to the total radio luminosity experiences an additional suppression, which explains the decreasing fraction of secondary radio luminosity with decreasing SFR, as shown in the lower left-hand panel in Fig. 5.3 for our 'CR diff' simulations.

5.4.3 Testing electron calorimetry

In order to quantify electron calorimetry of our simulated galaxies as a function of SFR and halo mass, we first define the calorimetric synchrotron fraction following Eq. (5.23) as

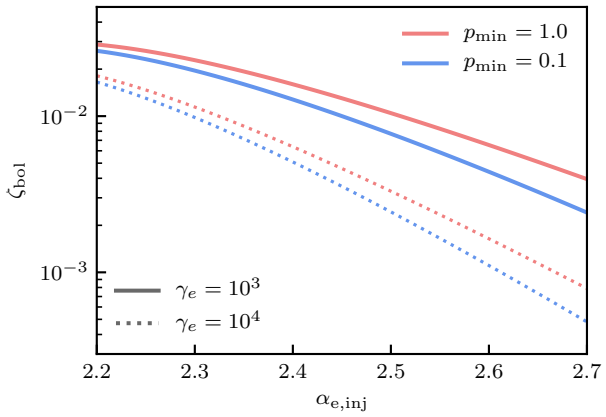

Figure 5.5: We show the bolometric electron fraction $\zeta_{\rm bol}$ as implicitely defined in Eq. (5.23). It quantifies the fraction of the total electron luminosity (from a CR electron source function approximated by a power law with injection spectral index $\alpha_{\rm e,inj}$ and low-momentum cutoff $p_{\rm min}$, see Eqs. 5.19 and 5.20) that is available for synchrotron emission at a frequency $\nu(\gamma_{\rm e}, B)$. For instance, in an ambient magnetic field of $B = 2$ µG, electrons with a Lorentz factor $\gamma_{\rm e} = 10^4$ radiate synchrotron emission at GHz frequencies (see Eq. 5.8).

$$\eta_{\rm syn,prim/sec} = \frac{\nu L_{\nu,\rm prim/sec}}{\zeta_{\rm bol} L_{\rm e}} = \frac{\sum_i \nu L_{\nu,\rm prim/sec,i}}{\sum_i \zeta_{{\rm bol},i} L_{{\rm e},i}}, \tag{5.28}$$

where in each cell i, we define the fraction of the total CR electron luminosity that radiates synchrotron emission at a frequency ν, given a magnetic field B_i within a cell i,

$$\zeta_{{\rm bol},i} = \frac{[\gamma_{\rm e}(B_i, \nu)]^{2-\alpha_{\rm e,inj}}}{2A_{\rm bol}}, \tag{5.29}$$

and $L_{\rm e} = L_{\rm prim-e} + L_{\rm sec-e}$ denotes the electron luminosity. For simplicity, the calorimetric synchrotron fractions of primary and secondary electrons $\eta_{\rm syn,prim/sec}$, are defined in such a way that they add up to a total calorimetric synchrotron fraction

$$\eta_{\rm syn} = \eta_{\rm syn,prim} + \eta_{\rm syn,sec} = \frac{\nu L_\nu}{\zeta_{\rm bol} L_{\rm e}}. \tag{5.30}$$

To fulfill this condition of additivity, we assume $\alpha_{\rm e,inj} = 2.2$ in all cells for both primary and secondary electrons. This implies that $\eta_{\rm syn,sec}$ represents in our definition a lower limit for the calorimetric synchrotron fraction of secondary electrons, since they can exhibit steeper injected

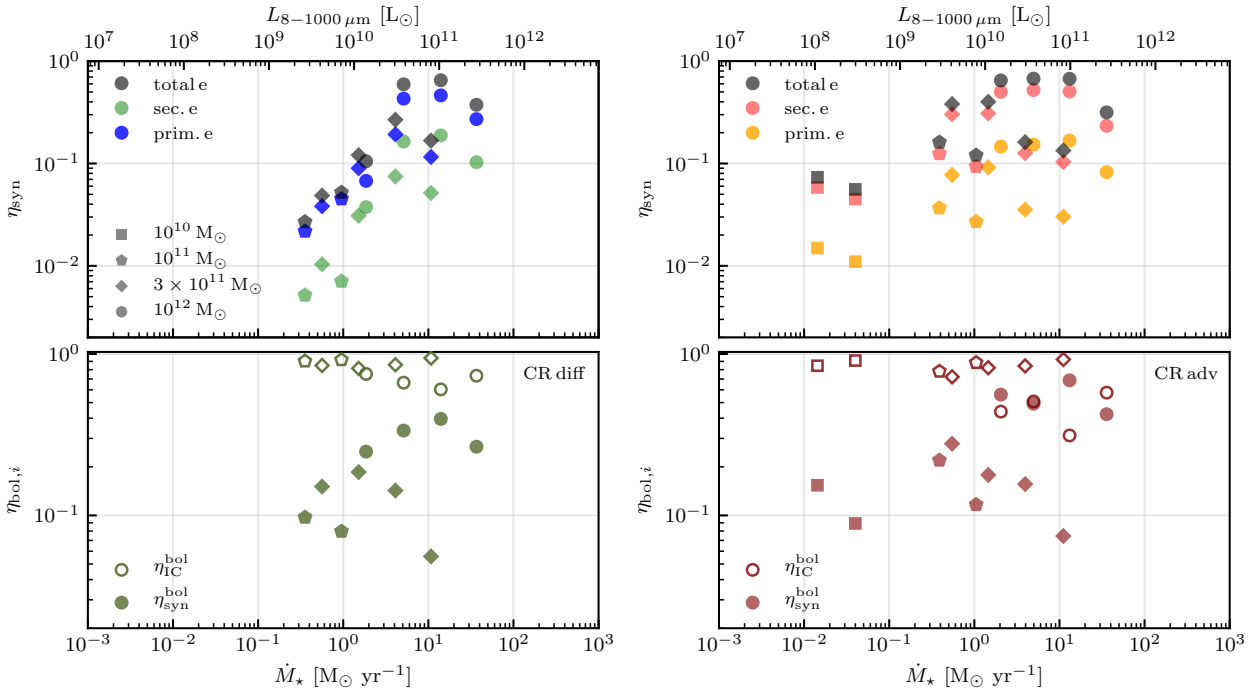

Figure 5.6: Top panels: we show the the calorimetric synchrotron fraction (see Eq. 5.28) for our CR diffusion (left-hand panel) and advection model (right-hand panel) as a function of SFR. In addition to the total fraction including primary and secondary electrons (black), we also show the fractions for primaries and secondaries separately (colour coded as indicated in the legend). Bottom panels: here, we show the bolometric fractions of synchrotron (filled symbols) and IC emission (open symbols) defined in Eqs. (5.31) and (5.32) which add up to unity by construction. The different symbols correspond to simulations with different halo masses as indicated in the top left-hand panel.

spectral indices $\alpha_{\mathrm{sec.e,inj}} > 2.2$, if energy dependent CR diffusion is included, as discussed in Section 5.4.2.

To calculate these calorimetric synchrotron fractions of our simulations, we estimate the available proton luminosity from the SFR using Eq. (5.15) in each cell,[2] and use this to compute the electron luminosities from Eq. (5.17) and (5.18). In the upper panels of Fig. 5.6, we show the calorimetric synchrotron fractions of our simulated galaxies (the same snapshots as shown in Fig. 5.3) for primary and secondary electrons, as well as the total calorimetric fraction. These range from 0.03 to 0.65 in our 'CR diff' models and from 0.06 to 0.67 in our 'CR adv' models. This partly explains the large scatter that we obtain in our FRC in Fig. 5.3. In particular, there is a difference in the calorimetric synchrotron fraction for different halo masses at the same SFR, that leads to a spread in radio luminosities. This is a result of the growth of the magnetic dynamo that continues to amplify magnetic fields at large disc radii of the galaxies, after saturation of the small-scale magnetic dynamo (Pfrommer et al., 2021).

Furthermore, we observe a global trend towards higher calorimetric fractions with higher SFRs, which is particularly strong in the 'CR diff' models. It remains to be seen whether an improved model for the ISM in global (dwarf) galaxy simulations with explicit SN-driven turbulence (Semenov et al., 2018; Gutcke et al., 2021) in a cosmological setting can further amplify the magnetic field in the outskirts of the disc via a small-scale dynamo. This would increase the values of η_{syn} at low SFRs in dwarfs over what is found in our models, where fast CR diffusion in the 'CR diff' model in low-mass halos efficiently quenches the small-scale dynamo and hence suppresses the calorimetric synchrotron fractions.

So far, we only considered the fraction of the injected electron luminosity that can potentially be converted to synchrotron emission at a fixed frequency, i.e. we only selected electrons with a certain Lorentz factor $\gamma_{\mathrm{e}}(\nu, B)$ that emits into a given frequency window. But in addition to that, we are also interested in comparing the total (bolometric) amount of energy that is radiated via synchrotron emission in comparison to IC scattering. To extend these considerations over the whole energy range, we define bolometric fractions of synchrotron and IC emission according to

$$\eta_{\mathrm{syn}}^{\mathrm{bol}} = \frac{\sum_i B_i^2 V_i}{\sum_i (B_i^2 + B_{\mathrm{ph},i}^2) V_i} \tag{5.31}$$

[2]Note that this implies that we only sum over cells with a SFR $\dot{M}_\star > 0$.

and

$$\eta_{\mathrm{IC}}^{\mathrm{bol}} = \frac{\sum_i B_{\mathrm{ph},i}^2 V_i}{\sum_i (B_i^2 + B_{\mathrm{ph},i}^2) V_i}. \tag{5.32}$$

These definitions are derived from the synchrotron and IC loss rates, which depend on the energy density of the magnetic field $\varepsilon_B \propto B^2$ and the photon energy density $\varepsilon_{\mathrm{ph}} \propto B_{\mathrm{ph}}^2$, respectively (see Eqs. 5.12 and 5.13). Per definition, $\eta_{\mathrm{IC}}^{\mathrm{bol}} + \eta_{\mathrm{syn}}^{\mathrm{bol}} = 1$, and hence, these fractions provide a measure of the fraction of the total electron luminosity that is lost to IC or synchrotron emission (at all possible frequencies) if we only consider these two radiative loss processes. To be consistent with the calculation of η_{syn}, we again only sum over all cells with SFRs $\dot{M}_\star > 0$ and show the resulting bolometric fractions of IC and synchrotron emission in the lower panels of Fig. 5.6. In almost all analysed snapshots, we find that $\eta_{\mathrm{IC}}^{\mathrm{bol}} > \eta_{\mathrm{syn}}^{\mathrm{bol}}$, which implies that IC losses are usually dominating synchrotron losses for CR electrons. For our small halos with $M_{200} = 10^{10}\,\mathrm{M}_\odot$ and $M_{200} = 10^{11}\,\mathrm{M}_\odot$, this is not surprising: Pfrommer et al. (2021) found that the magnetic field in these small halos saturate below the energy density of the CMB and hence, IC-cooling via scattering off of the CMB alone already dominates over synchrotron cooling. There are only three cases for which $\eta_{\mathrm{IC}}^{\mathrm{bol}} \leqslant \eta_{\mathrm{syn}}^{\mathrm{bol}}$, which represent highly star-forming galaxies with $M_{200} = 10^{12}\,\mathrm{M}_\odot$ in the 'CR adv' model. They saturate at the highest magnetic field strengths in comparison to all other shown simulations (Pfrommer et al., 2021) and hence, result in the highest bolometric fractions of synchrotron emission, that manage to dominate over IC emission.

5.4.4 'Conspiracy' at high gas densities

We found in Section 5.4.2, that there is an increasing contribution of secondary emission to the total radio luminosity toward larger SFRs in our 'CR diff' model. If this trend holds, the question arises of how to maintain the almost linear behaviour of the FRC. As proposed by Lacki et al. (2010), in addition to the larger contribution of secondary electrons to the radio luminosity in high-density starburst galaxies, one would also expect more losses due to Coulomb interactions and bremsstrahlung emission due to their dependence on gas density, see Eqs. (5.11) and (5.14). Furthermore, IC losses are expected to increase with higher SFRs due to the higher photon energy densities from young stellar populations. Consequently, in order to maintain an almost linear FRC, those effects have to 'conspire' to (approximately) cancel each other (Lacki et al., 2010).

To quantify deviations from the FRC and to test the relative contributions of the proposed effects, we utilise the ratio of total IR (TIR) to radio synchrotron emission as defined by Helou et al.

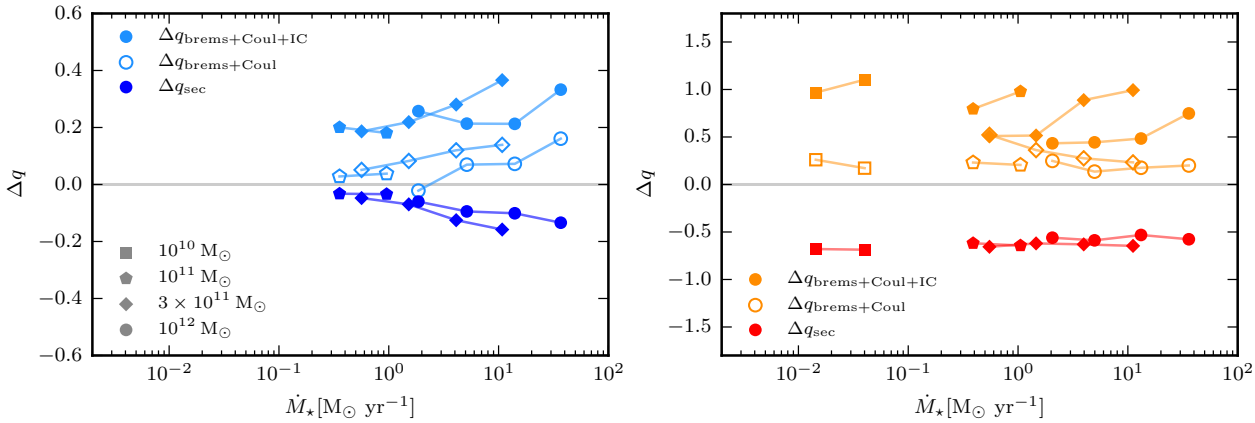

Figure 5.7: We show the change in the FIR-to-radio luminosity ratio, quantified by q (see Eq. 5.33), for our 'CR diff' (left-hand panel) and 'CR adv' models (right-hand panel). Here, we study how individual cooling processes modify the FRC: the effect of neglecting bremsstrahlung and Coulomb losses, that both depend on gas density, is shown via $\Delta q_{\rm brems+Coul}$ (Eq. 5.35) in light blue (orange) with open symbols in our 'CR diff' ('CR adv') models, whereas the effect of additionally neglecting IC losses, $\Delta q_{\rm brems+Coul+IC}$, is shown by the corresponding full symbols. Changes in q that result from disregarding the secondary radio emission are denoted by $\Delta q_{\rm sec}$ (Eq. 5.34) and are shown in dark blue (red). Different symbols correspond to different halo masses as indicated in the left-hand panel. Note that both panels have different ranges on their vertical axes.

(1985):

$$q = \log_{10}\left(\frac{L_{\mathrm{TIR}}}{L_{1.4\,\mathrm{GHz}}}\right) - 3.67, \tag{5.33}$$

where the TIR luminosity is given by $L_{\mathrm{TIR}} \approx 1.75 L_{\mathrm{FIR}}$ (Calzetti et al., 2000). We define the deviation from a given FRC via the difference Δq that results from comparing the full and a modified FRC for which we exclude different contributions to the total synchrotron emission. This enables us to study the impact of individual processes in modifying the slope of the FRC and whether these processes pose a challenge to the observed quasi-linearity of the FRC.

First, we assess the effect of neglecting the contribution of secondary electrons to the total radio luminosity $L_{1.4\,\mathrm{GHz}}$, and denote the corresponding parameter with $q_{\mathrm{no\ sec}}$. This is expected to be larger than q, where primary and secondary contributions are included. Hence, the difference

$$\Delta q_{\mathrm{sec}} = q - q_{\mathrm{no\ sec}} \leqslant 0 \tag{5.34}$$

enables us to quantify the contribution of secondary radio emission to the FRC.

Second, we consider the case of disregarding losses due to bremsstrahlung and Coulomb interactions to infer their effect on the radio emission and define the resulting difference as

$$\Delta q_{\mathrm{brems+Coul}} = q - q_{\mathrm{no\ brems+Coul}}. \tag{5.35}$$

To calculate $q_{\mathrm{no\ brems+Coul}}$, we compute the radio luminosity in Eq. (5.33) from steady-state spectra that we obtain by setting $b_{\mathrm{Coul}} = b_{\mathrm{brems}} = 0$. If these losses are significant in shaping the steady-state distribution, we expect $q_{\mathrm{no\,brems+Coul}} \leqslant q$ because fewer losses due to processes other than synchrotron emission potentially give rise to a larger radio luminosity. Similarly, we calculate the change in q from neglecting all non-synchrotron cooling processes, i.e. bremsstrahlung, Coulomb and IC cooling, which is denoted by

$$\Delta q_{\mathrm{brems+Coul+IC}} = q - q_{\mathrm{no\ brems+Coul+IC}}. \tag{5.36}$$

Figure 5.7 shows the deviation from a linear FRC when excluding secondary radio emission or bremsstrahlung and Coulomb losses. In our 'CR diff' runs, both effects become relevant in galaxies with SFRs $\dot{M}_\star \gtrsim 1\ \mathrm{M}_\odot\,\mathrm{yr}^{-1}$. In these star-forming and star-bursting galaxies, the missing radio emission from excluding secondary CR electrons is compensated by the additional radio emission, resulting from the neglect of bremsstrahlung and Coulomb losses. As a consequence,

the deviation from calorimetry that would be expected in starbursts, due to the increasing relevance of bremsstrahlung and Coulomb interactions in these high-density galaxies, seems to be counterbalanced by including the contribution of secondary radio emission.

IC losses elevate q across all SFRs and show an almost constant shift of q for our 'CR diff model', indicating that the IC emission does not significantly modify the slope of the FRC in this model. While IC losses become increasingly more relevant toward high SFRs for every individual galaxy simulation in our 'CR adv' model, on average the distribution of $\Delta q_{\mathrm{brems+Coul+IC}}$ is an elevated version of $\Delta q_{\mathrm{brems+Coul}}$ with an increased scatter. Hence, in spite of most of CR electrons lose their energy through IC interactions (Fig. 5.6), this shows that the subdominant synchrotron cooling process nevertheless appears to be a quasi-calorimetric tracer of the SFR, implying an almost linear slope of the FRC. Note that the overall change in q is comparably small in the 'CR diff' model and $\Delta q \leqslant 0.37$ for all considered effects. For a mean observed q of 2.21 in starburst galaxies (Helou et al., 1985), this is at most a 17 per cent effect.

In contrast to our 'CR diff' model, galaxies of our 'CR adv' model (right-hand panel in Fig. 5.7) exhibit a contribution of secondaries that is almost independent of SFR. This is because neglecting diffusion losses increases the importance of hadronic losses, which are faster than escape losses $\tau_\pi \ll \tau_{\mathrm{esc}}$. As a result, the ratio of primaries to secondaries does not depend on the gas density or the SFR, but only depends on $K_{\mathrm{ep}}^{\mathrm{inj}}$ and α_{p} (see Eq. 5.6), and is hence approximately constant across the range of SFRs probed by our set of simulations that only accounts for CR advection. Furthermore, as discussed in Section 5.4.2, the ν_{c}-effect can only significantly affect secondary electrons in the model accounting for energy dependent CR diffusion, which results in an SFR-dependence of the secondary contribution to the total radio synchrotron emission and hence explains the decrease of Δq_{sec} with increasing SFR in the 'CR diff' model.

5.5 Radio spectra

As pointed out by Thompson et al. (2006), the calorimetric assumption must hold for starburst galaxies like Arp 220. Here, the large photon energy density implies a short IC cooling time scale:

$$\tau_{\mathrm{IC}} \sim 4 \times 10^3 \,\mathrm{yr} \left(\frac{\varepsilon_{\mathrm{ph}}}{10^{-6}\,\mathrm{erg\,cm^{-3}}} \right)^{-1} \left(\frac{B}{3\,\mathrm{mG}} \right)^{1/2} . \tag{5.37}$$

In order for escape losses to be faster, unphysical wind velocities of order $\sim 20,000\,\mathrm{km\,s^{-1}}$ would be required for CR electrons to be advected from the compact star-bursting region of size ~ 100 pc. Consequently, losses due to IC emission must be larger than escape losses and we would expect

Table 5.2: This table summarises the properties of our simulated galaxies, that resemble the observed galaxies NGC 253, M82 and NGC 2146 in terms of their SFRs and total radio luminosities. The observed radio luminosity is derived from the observed flux density at the frequency bin that is closest to $\nu = 1.4$ GHz using the data shown in Figs. 5.8 and 5.9 and from the distances summarised below. We use the simulated radio luminosities with the observationally determined inclination angle ϕ and adopt $\delta = 0.3$. The central radius $R_{\rm central}$ and the constant fraction $\xi_{\rm e}$ of the electron density provided in our pressurised ISM model (Springel & Hernquist, 2003) are parameters used to construct the radio emission spectra from the simulations, including thermal free-free emission and absorption.

Galaxy	SFR (obs.[1]/sim.) [$M_\odot$ yr^{-1}]	Distance[2] [Mpc]	$L_{1.4\,\rm GHz}$ (obs./sim.) [erg s Hz^{-1}]	$R_{\rm central}$(obs./sim.) [kpc]	ϕ(obs.[3]/sim.)	$\xi_{\rm e}$	Simulation M_{200} [$M_\odot$], t [Gyr]
NGC 253	5.03 ± 0.76	3.3	7.67×10^{28}	0.15 - 0.25	74°	-	-
	4.110	-	3.87×10^{28}	0.15	74°	0.8	$M_{200} = 3 \times 10^{11}$, $t = 1.1$
M82[4]	10.4 ± 1.6	3.7	1.21×10^{29}	0.45	80°	-	-
	6.457	-	1.62×10^{29}	1.50	80°	1.0	$M_{200} = 10^{12}$, $t = 2.3$
NGC 2146	14.0 ± 0.5	15.2	3.02×10^{29}	-	63°	-	-
	25.520	-	5.55×10^{29}	0.30	63°	0.5	$M_{200} = 10^{12}$, $t = 0.7$

[1] Kornecki et al. (2020)
[2] NGC 253: Mouhcine et al. (2005); M82: Vacca et al. (2015); NGC 2146: Gao & Solomon (2004).
[3] NGC 253: Iodice et al. (2014); M82: Lynds & Sandage (1963), McKeith et al. (1995); NGC 2146: Della Ceca et al. (1999).
[4] This snapshot is shown in Figs. 5.1, 5.2, 5.10, 5.11 and 5.13.

steep radio spectra. This is because an IC-cooled steady-state CR electron spectrum with $\alpha_e = 3.2$ implies a synchrotron spectral index of $\alpha_\nu = (\alpha_e - 1)/2 = 1.1$, which is larger than the observed spectral indices of ~ 0.5 to 0.8. The same argument holds, if synchrotron losses dominate the cooling of CR electrons, due to the identical energy dependence of synchrotron and IC losses.

In order to solve this tension, we analyse in the following three possible mechanisms that could be responsible for flattening the radio spectra, in comparison to the steep radio spectra that are expected if IC and synchrotron cooling dominate. First, a non-negligible contribution of thermal free-free emission to the radio emission could have an influence on the radio spectral shape. Second, because bremsstrahlung losses have a weaker energy dependence, i.e. $b_{\rm brems} \propto E \ln E$ (Eq. 5.14), in comparison to IC and synchrotron losses with $b_{\rm IC/syn} \propto E^2$, they could lead to electron spectra that reflect the injected spectral index and hence lead to flatter radio spectra, if they are faster than IC and synchrotron losses, i.e. $\tau_{\rm brems} < (\tau_{\rm IC}^{-1} + \tau_{\rm syn}^{-1})^{-1}$. Similarly, Coulomb cooling could affect the radio spectral shape because $b_{\rm Coul} \approx$ const. for $\gamma_e \gg 1$. A third possibility for maintaining flat electron spectra and hence yielding flat emitted synchrotron spectra is advection. Because advection losses do not depend on energy, the injected electron spectral index of 2.2 would be maintained in the regions where those losses are dominant. We test these possibilities in the following sections.

So far, in our fiducial model we adopted an energy dependence of the diffusion coefficient $D \propto E^\delta$ where $\delta = 0.5$. In order to be consistent with our findings in Paper II, where we found that a shallower dependence of $\delta = 0.3$ enables better matches to the observed gamma-ray spectra of NGC 253, M82 and NGC 2146, we adopt in the following $\delta = 0.3$ for the calculation of the radio spectra.[3]

5.5.1 Thermal and non-thermal radio emission

Figures 5.8 and 5.9 show the radio spectra of the three star-forming galaxies NGC 253, M82 and NGC 2146. We compare observations by Kapińska et al. (2017), Adebahr et al. (2013) and Klein et al. (2018) to radio spectra derived from our simulated galaxies that resemble the observed ones in terms of their SFRs and radio luminosities, respectively (see Table 5.2). We show the observed and simulated total spectra (top panels) and the spectra from the central regions (middle panels). The flux density is inferred from our modeling of the intensity I_ν, as it would be observed from a galaxy with an inclination angle ϕ at a luminosity distance d (see Eqs. 2.95 and 5.42). Below the

[3]The energy dependence of the diffusion coefficient does not significantly change the radio spectra of these galaxies because radiative losses of CR electrons beat their diffusive losses which is different for CR protons that do not suffer radiative losses. For the considered snapshots, the effect of changing $\delta = 0.5 \rightarrow 0.3$ only changes $L_{1.4\,\rm GHz}$ by less than 8 per cent.

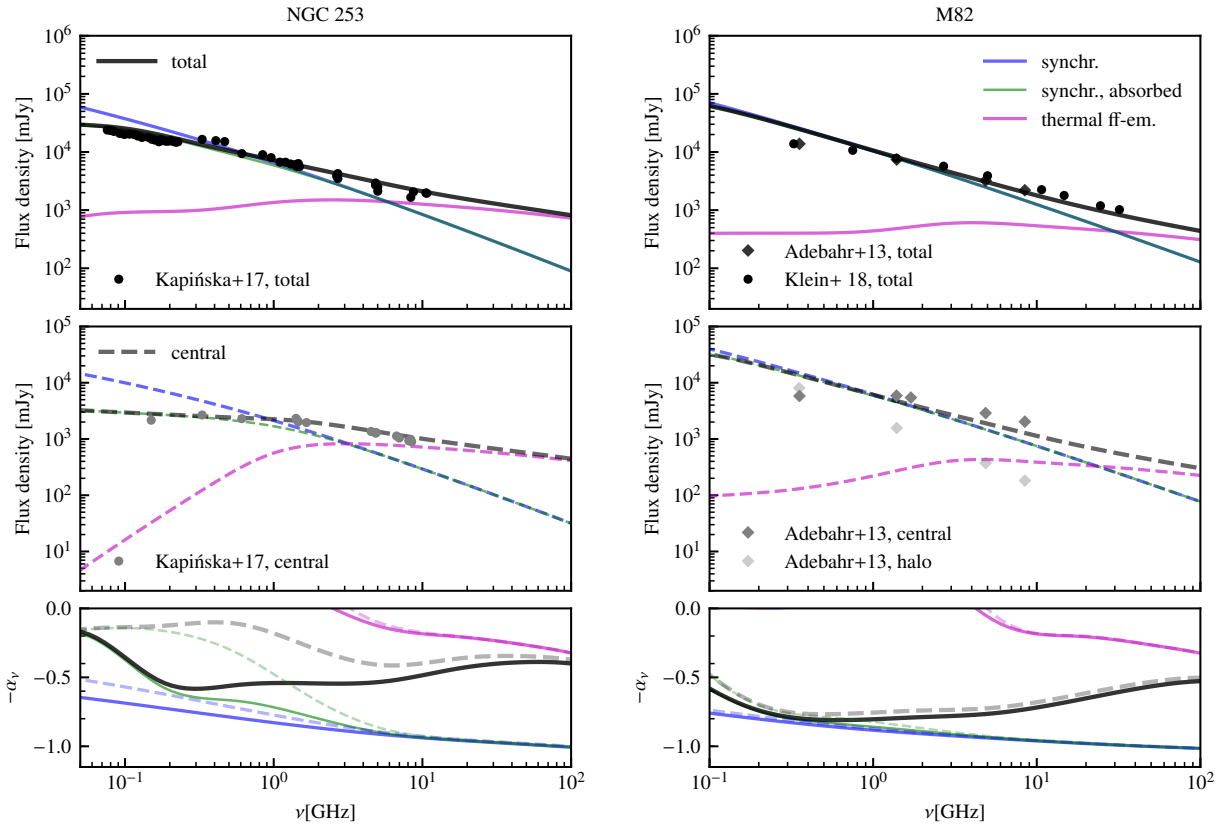

Figure 5.8: Spectra of synchrotron emission (blue lines) and thermal free-free emission (magenta lines) of our simulations that are similar to NGC 253 and M82 in terms of SFR and total radio luminosity (see Table 5.2). The spectra are computed for inclination angles $\phi = 74°$ for NGC 253 (Iodice et al., 2014) and $\phi = 80°$ for M82 (Lynds & Sandage, 1963; McKeith et al., 1995). The upper panels show the spectra for the whole galaxies, whereas for the middle panels, we cut out a region around the galactic center with a radius $R_{\rm central}$ (see Table 5.2; dashed lines), resembling the observed central regions, respectively. To allow a comparison with the spectral shapes of the observed spectra, the simulated spectra are re-normalised by $L_{1.4\rm GHz,obs}/L_{1.4\rm GHz,sim}$ (see Table 5.2). Thermal free-free absorption affects the synchrotron spectra at low frequencies (green lines) and is strongest for the central spectra, due to the high central gas density. For NGC 253 and M82, we plot the total (black points) and central (grey points) observed radio spectrum by Kapińska et al. (2017), Klein et al. (2018) and Adebahr et al. (2013), as indicated in the legend. The light grey points in the middle right-hand panel correspond to the spectrum of the halo, i.e. the difference between the total and central spectrum, which matches the spectral shape of our synchrotron component. Bottom panels: the solid (dashed) lines show the spectral indices of our total (central) simulated radio spectra for synchrotron, thermal free-free and total emission, respectively. For a variation of $R_{\rm central}$, see App. 5.8.

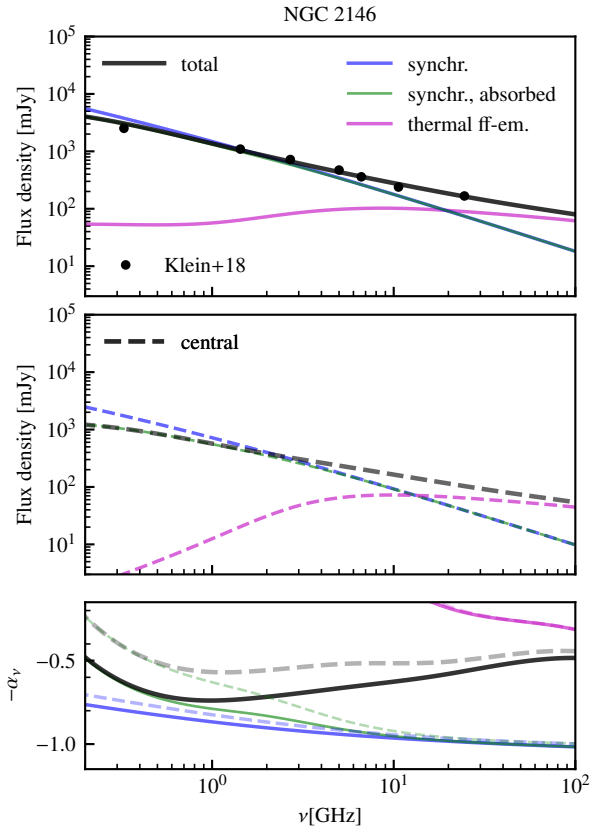

Figure 5.9: Top panel: we compare the observed total radio spectrum of NGC 2164 (Klein et al., 2018) to simulated spectra of synchrotron and thermal free-free emission of a simulation that matches NGC 2164 in terms of SFR and total radio luminosity (see Table 5.2). Here, we adopt an inclination angle of $\phi = 63°$ (Della Ceca et al., 1999). The middle panel shows the spectra in the central region (within $R_{\rm central} = 0.3\,{\rm kpc}$) while the bottom panel shows the spectral index of our simulated radio spectra for synchrotron, thermal free-free and total emission, respectively.

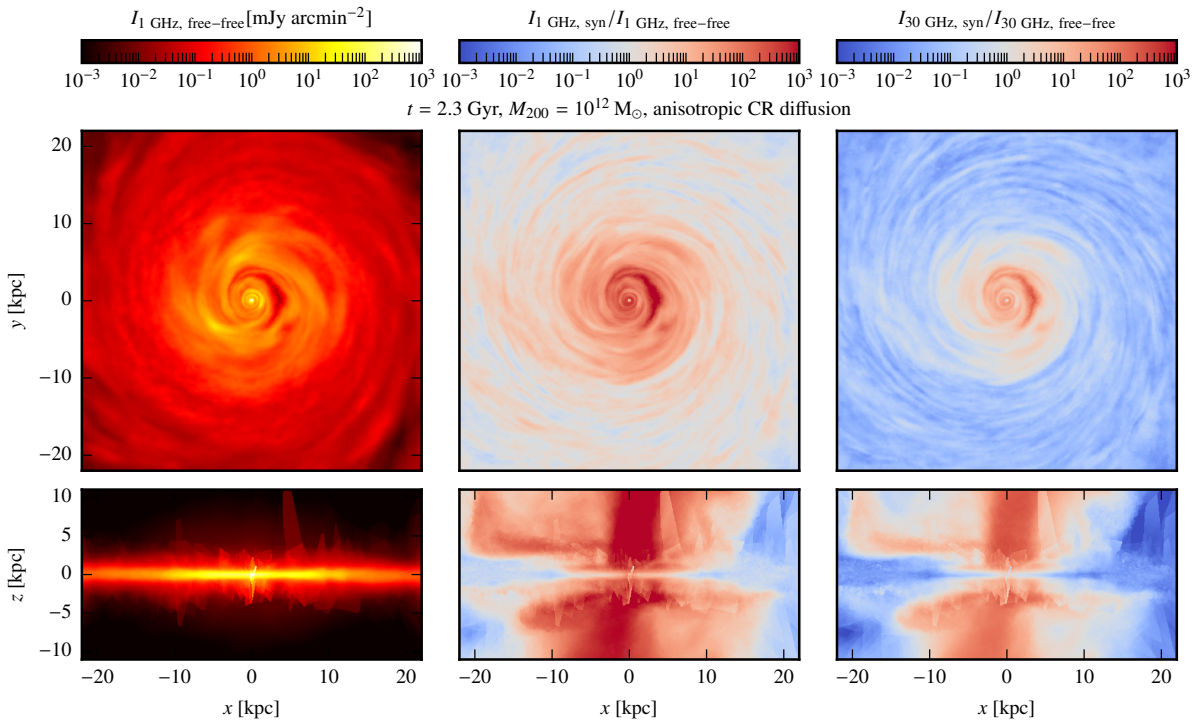

Figure 5.10: Face-on and edge-on maps of the projected thermal free-free emission at 1 GHz (left-hand panels) of our simulation with $M_{200} = 10^{12}\,\mathrm{M}_\odot$ at $t = 2.3$ Gyr. The middle and right-hand panels show the ratio of the synchrotron emission to the thermal free-free emission at 1 and 30 GHz, respectively.

total and central radio spectra, we show the spectral indices of the differently modeled components that are computed via

$$\alpha_\nu = -\frac{\mathrm{d}\log F_\nu}{\mathrm{d}\log \nu}. \tag{5.38}$$

We find that the total radio synchrotron spectra exhibit spectral indices from 0.6 to 1.1 for radio frequencies ranging from 0.1 to 100 GHz. Those are significantly steeper than the observed radio spectra at frequencies larger than a few GHz. However, our modeling of the thermal free-free emission (see Section 5.2.4) is able to flatten the total spectra so that they approach the observed values also at frequencies $\nu \gtrsim 1$ GHz. This has also been found for the starburst galaxies NGC 253, M82 and Arp220 in Peretti et al. (2019), although in contrast to our results, they find that the radio emission is dominated by secondary emission.

The spectrum of the central region of a simulated galaxy is obtained by computing the intensity $I_\nu(\boldsymbol{r}_\perp)$ within a circle around the center with the radius R_{central} (see Table 5.2) that approximately corresponds to the radius of the observed central region. Only for M82, we adopt a larger radius to match the total observed flux from the central region with our model. Interestingly, we find that the central data both of NGC 253 and M82 show an even flatter radio spectrum in comparison to the total spectrum, with particularly strong free-free absorption at small frequencies. This is convincingly explained by the higher electron density in central regions of galaxies, as it is also manifested within our model of NGC 253. It also becomes clear from the observations of M82, that the flattening of the radio spectra is a feature that is predominantly originating from the central region of the galaxy. The observations by Adebahr et al. (2013) of the central ~450 pc of M82 clearly show a flat radio spectrum, whereas the halo spectrum (i.e. the total spectrum minus the central data) is similarly steep in comparison to our radio synchrotron component. Hence, the flat component of the radio spectrum must result from the central region and can be reconciled with the steep radio synchrotron spectra.

In Fig. 5.10, we show modeled free-free emission maps at 1 GHz of our M82-like galaxy to illustrate the dependence of the thermal emission on the observed region and also on the viewing angle. Observing a galaxy edge-on leads to a higher column density along the line of sight, which enhances the thermal free-free emission in the mid-plane. Furthermore, the ratios of radio synchrotron to thermal free-free emission at two radio frequencies shown in the middle and right-hand panels of Fig. 5.10 highlight our conclusion drawn from the radio spectra as discussed above: while the synchrotron emission dominates at low frequencies, thermal free-free emission prevails towards higher frequencies.

Similarly to NGC 253 and M82, the observed spectrum of NGC 2146 is flatter than the radio synchrotron emission of our simulated galaxy. However, adding a thermal free-free component enables us to reproduce the flat observed spectrum at frequencies above $\sim$ 10 GHz. In the case of NGC 2146, there are no published data of the central region. We chose to show the central spectrum of NGC 2146 from a region with radius of 0.3 kpc, where we find a pronounced flattening of the central spectrum at low frequencies due to free-fee absorption.

We furthermore note that the radio luminosities given in Table 5.2 for our simulations include radio synchrotron emission and thermal free-free emission, whereas the luminosities adopted in our analysis of the FRC are only the non-thermal radio synchrotron luminosities. We determine the contribution of the thermal free-free emission to the total luminosity at 1.4 GHz to 24.7, 6.3 and 5.7 per cent for NGC 253, M82 and NGC 2146, respectively. Except from NGC 253, this is in agreement with thermal fractions at 1.5 GHz derived from observations of 61 nearby galaxies in Tabatabaei et al. (2017).

5.5.2 Can bremsstrahlung or Coulomb losses yield flat radio spectra?

In order to assess the possibility that bremsstrahlung cooling can lead to flatter radio spectra in comparison to the case when IC and synchrotron losses dominate, we first show in Fig. 5.11 a slice through the disc of the bremsstrahlung cooling timescale at an energy of 10 GeV, which is typically acting on timescales of $50-200$ Myr and is shortest in high-density regions (see Eq. 5.14). However, synchrotron cooling is faster in the central few kpc and in the outflow, where the magnetic field is strong. In the regions where bremsstrahlung losses are faster than synchrotron cooling, IC cooling kicks in (right-hand panel of Fig. 5.11). Therefore, bremsstrahlung losses are subdominant in most regions of this galaxy and are not able to significantly shape the electron spectra at the considered electron energy. Consequently, they cannot be responsible for flattening these at the corresponding frequencies. Instead, IC and synchrotron losses steepen the injected electron spectra by unity, yielding $\alpha_\nu = 1.1$ in the fully-cooled limit.

However, as can be seen from the radio spectral index shown in the bottom panels of Fig. 5.8 and 5.9, α_ν only approaches this limit of very high frequencies $\nu \gtrsim 10$ GHz. One reason for this is the fact that we include diffusive losses in our steady state equation[4], which only steepen the spectra by $\delta = 0.3$ (or 0.5). This implies that we obtain radio spectral indices ranging from 0.75 (or 0.85) if diffusion losses dominate, to 1.1 if IC or synchrotron losses prevail. Furthermore, in regions with particularly large magnetic field strengths, we observe lower-energetic electrons (due

[4]The influence of advection losses in outflows is discussed in Section 5.5.3.

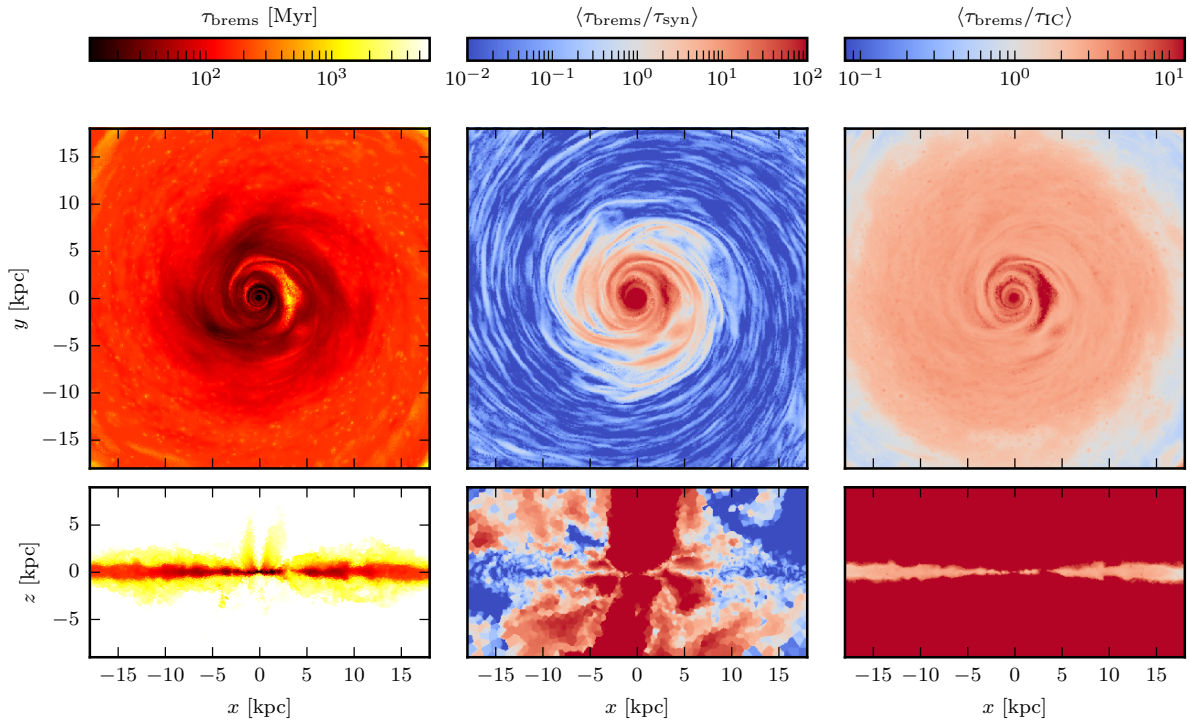

Figure 5.11: Face-on and edge-on maps of the timescale of bremsstrahlung cooling, $\tau_{\rm brems}$ (left-hand panels), as well as the ratio of $\tau_{\rm brems}$ to the cooling timescale due to synchrotron and IC emission (middle and right-hand panels, respectively) at an electron energy of 10 GeV. The maps are shown for our fiducial halo with $M_{200} = 10^{12}\,{\rm M}_\odot$ at 2.3 Gyr and the ratios are averaged over slices with a thickness of 0.5 kpc.

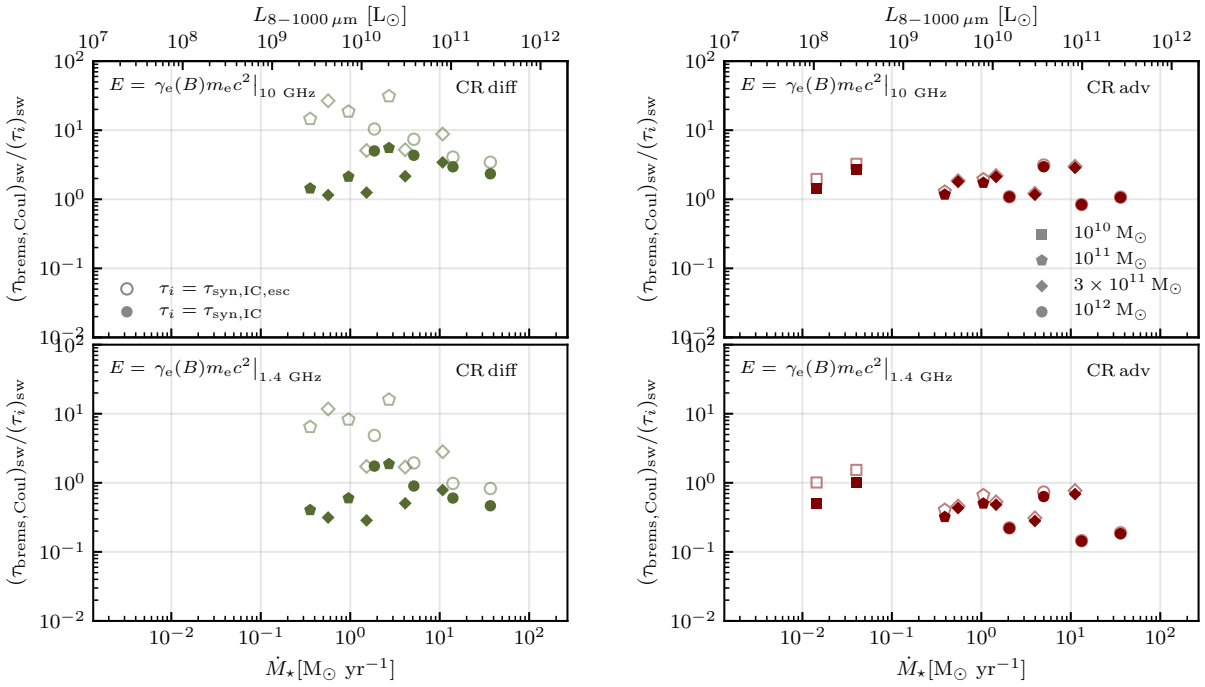

Figure 5.12: Ratios of the synchrotron-weighted timescales of bremsstrahlung and Coulomb cooling $\tau_{brems,Coul}$ (Eq. 5.39) to the timescale of synchrotron and IC cooling $\tau_{syn,IC}$ (as well as to that of radiative cooling and escape losses $\tau_{syn,IC,esc}$, open symbols; see Eqs. 5.40 and 5.41) for our 'CR diff' model (left-hand panels) and 'CR adv' model (right-hand panels). The timescales of each snapshot are calculated by averaging over the corresponding cooling rates (i.e. τ^{-1}) from all cells while weighting them with the synchrotron luminosity. The timescales are computed at the typical electron energy responsible for radio synchrotron emission at $\nu = 10$ GHz (top panels) and $\nu = 1.4$ GHz (lower panels), given the magnetic field in each cell (see Eq. 5.8).

to the ν_c-effect), which are more affected by Coulomb and bremsstrahlung cooling in comparison to high-energy electrons, where IC and synchrotron losses steepen the spectra.

To quantify this effect and to assess the importance of bremsstrahlung cooling in flattening radio spectra for galaxies along the SFR sequence, we show in Fig. 5.12 the ratio of the combined timescale of bremsstrahlung and Coulomb cooling

$$\tau_{\rm brems,Coul} = (\tau_{\rm brems}^{-1} + \tau_{\rm Coul}^{-1})^{-1} \tag{5.39}$$

to the combined synchrotron and IC timescale, i.e.,

$$\tau_{\rm syn,IC} = (\tau_{\rm syn}^{-1} + \tau_{\rm IC}^{-1})^{-1}, \tag{5.40}$$

as well as to the combined timescale of synchrotron, IC and escape losses,

$$\tau_{\rm syn,IC,esc} = (\tau_{\rm syn}^{-1} + \tau_{\rm IC}^{-1} + \tau_{\rm esc}^{-1})^{-1} \tag{5.41}$$

In order to show the cooling timescale ratios in regions that are relevant for synchrotron emission, we weight the corresponding cooling rates (τ^{-1}) with the synchrotron luminosity of each cell when averaging them over the whole galaxy. In both, our 'CR diff' and 'CR adv' models, we find cooling via bremsstrahlung and Coulomb losses to be slower than IC and synchrotron cooling for electron with energies $E_{\rm e} = \gamma_{\rm e}(B) m_{\rm e} c^2\big|_{10\ \rm GHz}$, i.e. electrons that are typically responsible for the emission of synchrotron radiation at 10 GHz, depending on the ambient magnetic field (see Eq. 5.8).[5]

However, if we consider synchrotron-emitting electrons at $\nu = 1.4$ GHz we find that bremsstrahlung and Coulomb losses are not at all negligible in comparison to IC and synchrotron losses in most of our snapshots, but instead, $\tau_{\rm brems,Coul} \lesssim \tau_{\rm syn,IC}$ at electron energies $E_{\rm e} = \gamma_{\rm e}(B) m_{\rm e} c^2\big|_{1.4\ \rm GHz}$. This is due to the fact that we typically probe lower energetic electrons when observing radio synchrotron emission at a lower frequency, given the same magnetic field. The mean Lorentz factor of electrons emitting at 1.4 GHz averaged over all cells ranges between $\gamma_{\rm e} = 10^4$ and 2×10^4 for all SFRs, corresponding to $E_{\rm e} = 5$ to 10 GeV. By contrast, the average $\gamma_{\rm e}$ weighted with the synchrotron luminosity in each cell decreases from 10^4 at small SFRs down to 10^3 in our starburst galaxies. Hence, the synchrotron emission at $\nu = 1.4$ GHz in starburst galaxies with their high magnetic field strengths probes electrons with energies down to $E_{\rm e} = 0.5$ GeV.

[5]For simplicity, we use in the estimation of the characteristic electron energy entering the calculation of the timescales in Fig. 5.12 the total magnetic field of each cell here. Adopting $B_\perp$ and calculating the resulting timescale ratios for edge-on and face-on configurations, respectively, changes the ratios shown in Fig. 5.12 by at most a factor of 2.

The additional inclusion of escape losses (open symbols in Fig. 5.12) that become increasingly more important for decreasing SFRs in our 'CR diff' model shows that only highly star-forming galaxies are able to maintain $\tau_{\rm brems,Coul} \lesssim \tau_{\rm syn,IC,esc}$ at the relevant energies, determined by $\gamma_{\rm e}(B)$ (Eq. 5.8). This is in accordance with our results from Section 5.4.4, where we found that neglecting bremsstrahlung and Coulomb losses increases the radio luminosity at 1.4 GHz for an increasing SFR. In the 'CR adv' model, we observe a similar trend in comparison to the 'CR diff' model: at high electron energies (e.g., at 10 GeV), bremsstrahlung and Coulomb losses are subdominant while they become relevant if we account for the $\nu_{\rm c}$-effect, where we typically probe lower energetic electrons. If we additionally include escape losses (i.e., only advection losses in this model), they do not significantly influence the considered timescale ratios.

In summary, we conclude that the synchrotron emission at 1.4 GHz in highly star-forming galaxies probes electrons with $\gamma_{\rm e} \sim 10^3$ which are mostly affected by bremsstrahlung and Coulomb losses. By contrast, electrons at higher energies are dominated by synchrotron and IC cooling and consequently, at higher frequencies, the radio synchrotron spectra are steepened by those cooling processes. Only the modeling of a thermal free-free component as discussed in Section 5.5.1 is thus able to flatten the radio spectra towards high frequencies in starbursts. We furthermore find an increasing relevance of energy dependent diffusion losses of CR electrons with decreasing SFRs. At the same time, observations at 1.4 GHz probe higher energetic electrons ($\gamma_{\rm e} \sim 10^4$) at low SFRs so that bremsstrahlung and Coulomb losses do not strongly affect the radio synchrotron luminosity towards low SFRs (see Fig. 5.7).

5.5.3 Can outflows in projection yield flat radio spectra?

We show in Fig. 5.13 maps of the projected synchrotron emissivity $I_{1.4\,\rm GHz}$ resulting from primary (left-hand panels) and secondary electrons (middle panels) for our fiducial halo with $M_{200} = 10^{12}\,{\rm M}_\odot$ at $t = 2.3\,$Gyr. Because the simulation shown here includes anisotropic diffusion, the radio luminosity from primary electrons dominates over the secondary contribution (as discussed in Section 5.4.2). From top to bottom, we show projected views of the simulated galaxy, changing the galaxy inclination from a face-on to an edge-on view in steps of 30°. The right-hand panels show spectral index maps of the total synchrotron emission between 1 and 3 GHz.

As discussed above, the spectral index of the steady-state electron population remains unchanged, if advection is the dominant loss process, i.e. $\alpha_{\rm e} = \alpha_{\rm inj} = 2.2$. Hence, the radio spectral index is $\alpha_\nu = (\alpha_{\rm e} - 1)/2 = 0.6$ in the outflows, where CRs predominantly are advected with the gas into the halo. By contrast, the observed spectral index maps of the radio emission of starburst

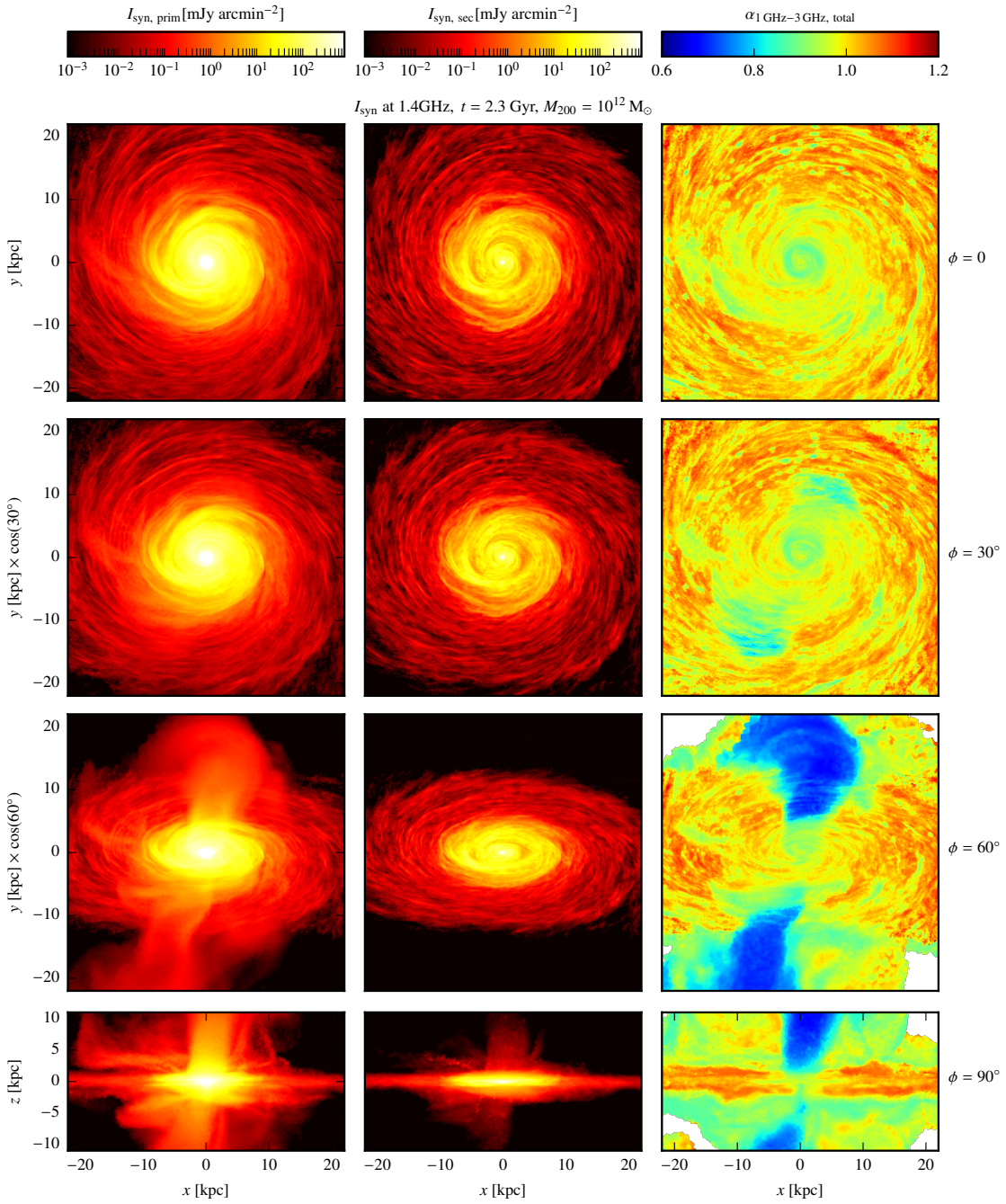

Figure 5.13: From top to bottom, we show projected maps of the radio synchrotron intensity (Eq. 5.9) arising from primary (left-hand panels) and secondary electrons (middle panels) observed from different inclination angles (0, 30, 60 and 90 degrees) for our fiducial galaxy with M_{200} = 10^{12} M$_\odot$ at t = 2.3 Gyr. The right hand panels show the corresponding maps of the spectral index of the total radio synchrotron emission (i.e. the primary plus secondary contribution) between frequencies of 1 GHz and 3 GHz.

galaxies like M82 (Adebahr et al., 2013), show flat spectral indices mainly in their central regions. We conclude that CR advection in combination with galaxy inclination cannot be responsible for the observed flat radio spectral indices because regions with flat spectral indices (due to advection losses) are seen off-center and only for inclinations larger than about 45°.

5.6 Discussion and conclusions

In this work, we model for the first time the radio emission of galaxies in three-dimensional MHD simulations, which evolve the energy density of CR protons self-consistently. To this end, we determine the steady-state spectra of CR protons, primary and secondary electrons in post-processing and assess the relative importance of primaries versus secondaries for models with and without anisotropic CR diffusion. The detailed modeling of the synchrotron and free-free radio emission of star-forming galaxies enables new insight into the underlying physics of the FRC over a broad range of SFRs. In particular, this novel approach sheds light on the long-standing puzzle whether the almost linear FRC implies electron calorimetry and how this compares to the observed flat radio spectra.

While in simulations that only account for CR advection ('CR adv') the secondary electron population is responsible for most of the radio synchrotron emission and independent of SFR, we find in our model that additionally includes anisotropic CR diffusion ('CR diff') that primary electrons dominate the total radio luminosity at 1.4 GHz (see Fig. 5.3). The main reason for this difference is the steepening of the steady-state CR proton spectra due to energy-dependent diffusion, which modifies the shape of the secondary electron source function. Thus, in steady state, the secondary CR electron spectra differ from the primary electron spectra (see Fig. 5.4). As a result, due to their steeper spectra, secondary electrons are more affected by the ν_c-effect, which means that the observed radio synchrotron emission at a given frequency probes lower electron energies for larger magnetic field strengths that are realised in highly star-forming galaxies. This leads to an increasing contribution of secondary emission to the total radio luminosity with SFR in the 'CR diff' model, in contrast to the 'CR adv' model, where this trend is absent.

To test electron calorimetry, we determine the fraction of available injected CR electron luminosity that is actually converted into synchrotron emission. This calorimetric synchrotron fraction $\eta_{\rm syn}$ varies from 0.03 to 0.67 among all our simulations with an increasing trend towards larger SFRs (see Fig. 5.6). The galaxies in the 'CR adv' model show overall larger calorimetric fractions with a weaker dependence on SFR in comparison to the 'CR diff' model, where diffusive losses and a weaker saturated magnetic field strength in dwarfs (in comparison to the thermal energy den-

sity, Pfrommer et al., 2021) decrease $\eta_{\rm syn}$ towards smaller SFRs. We anticipate that an improved ISM model (e.g., Rathjen et al., 2021) in combination with an improved two-moment CR transport scheme (e.g., Thomas & Pfrommer, 2019) within a cosmological setting that exhibits several epochs of accretion-driven star-forming phases can further amplify the magnetic field strength in these systems via star-formation and accretion-driven turbulence as well as modulate the influence of CR transport on the magnetic dynamo amplification via a more consistent self-generated CR diffusion coefficient. This is expected to weaken the dependence of $\eta_{\rm syn}$ on SFR. Generally, we find that CR electrons with energies $\gtrsim$ 10 GeV lose most of their energy through IC interactions with starlight and CMB photons in comparison to synchrotron losses and thus are approximately in the calorimetric limit. However, we also find that the contribution to IC cooling is on average largely independent of SFR at fixed observed radio frequency and hence, enables to use the synchrotron emission as a quasi-calorimetric measure of the SFR (see Fig. 5.7).

Furthermore, we show that the increasing secondary contribution to the total radio luminosity in starbursts is balanced by increasing bremsstrahlung and Coulomb losses, that diminish the radio synchrotron luminosity with increasing densities in those systems (see Fig. 5.7). This finding is in accordance with one-zone models by Lacki et al. (2010). However in our model, the effect is not as strong: Lacki et al. (2010) find an increase in the logarithm of the TIR-to-radio luminosity ratio q of 0.5 to 0.6 if secondaries are not included in starbursts, as well as a corresponding decrease if secondaries are included but non-synchrotron losses are disregarded. By contrast, our 'CR diff' model predicts a change of q of about 0.2 in our highest star-forming galaxy when we neglect the secondary radio emission. If non-synchrotron cooling is disregarded, q changes by 0.2 to 0.4. Note that we refrain from analysing this effect as a function of gas surface density, because this observable strongly depends on the viewing angle of the galaxy, whereas the SFR is a more robust global quantity.

Finally, we examine three possible solutions for the problem of the discrepancy between the observed flat radio spectra and the theoretically expected steep radio synchrotron spectra in the calorimetric limit, i.e. that CR electrons lose their energy primarily to radiative (synchrotron and IC) processes before they can escape from the galaxies.

1. Bremsstrahlung and Coulomb cooling processes are only able to affect low-energy electron spectra, and hence, yield flat radio spectra at low frequencies. However, these processes only play a minor role in the observed spectral flattening because (diffusive) escape losses are more important, especially at lower SFRs (see Fig. 5.12).

2. We also find that advection losses cannot be primarily responsible for the observed low

spectral indices because they only generate hard CR electron spectra in outflows. This implies flat radio spectra off-center, which is in direct conflict with the observed flat *central* radio spectra (see Fig. 5.13).

3. Our preferred solution is thermal free-free emission that starts to dominate the total radio spectrum at frequencies of several to tens of GHz and flattens the observed radio spectrum (see Figs. 5.8 and 5.9). Thermal free-free emission is not only able to flatten the radio spectra of our simulated galaxies similar to NGC 253, M82 and NGC 2146 at high frequencies, but the involved absorption process, i.e. free-free absorption, coincides with the spectral flattening of the central spectrum of NGC 253.

This interpretation of thermal free-free emission being the main driver for flattening the radio spectra at high frequencies is corroborated by the observed spectrum of the central $\sim$ 450 pc of M82: subtracting this central emission region from the total spectrum yields a spectrum that is as steep as the radio synchrotron spectrum resulting from CR electrons close to the fully cooled limit, with spectral indices up to 1.1. Consequently, the flattening of the spectra at high frequencies must mainly originate from the central region of starbursts and can be reconciled with steep radio synchrotron spectra, that dominate the emission outside the dense, central starburst region and the total spectrum at lower frequencies, i.e., below $\sim$3, 10 or 20 GHz in our modeling of NGC 253, NGC 2146 and M82, respectively.

These insights into the radio emission from galaxies and the physics of the FRC necessarily require a spectral modelling of the different CR populations in full three-dimensional MHD-CR simulations, which demonstrates the power of this approach. While we confirm several findings of one-zone models (e.g., Lacki et al., 2010), our approach exhibits less free parameters and thus can be considered to be more predictive. Most importantly, because these simulations evolve the magnetic field and the CR energy density, we can use this modeling to link the simulated radio emission to observational data to quantify the effect of CR feedback on galaxy formation.

Clearly, the presented radio analysis of steady-state CR spectra need to be complemented by full spectral-dynamical simulations of CR protons (Girichidis et al., 2020b) and electrons (Winner et al., 2019, 2020; Ogrodnik et al., 2021). Moreover, the employed one-moment approach for CR transport (Pfrommer et al., 2017a) will be improved with a two-moment CR hydrodynamics model that is coupled to the Alfvén wave energy density, which delivers a realistic (spatially and temporally varying) CR diffusion coefficient in the self-confinement picture (Thomas & Pfrommer, 2019; Thomas et al., 2021; Thomas & Pfrommer, 2022). Finally, pursuing MHD-CR simulations of galaxy formation in a cosmological setting (Buck et al., 2020; Hopkins et al., 2021b) will be

required to obtain realistic (bursty) star-formation histories. These have different epochs of turbulent driving, which can potentially amplify the magnetic field in dwarf galaxies furthermore to come into equipartition with the thermal energy density so that it does not saturate at a sub-equipartition level (Pfrommer et al., 2021) and reaches the FRC.

5.7 Appendix: Thermal free-free emission and absorption

Here, we present the remaining parts of the appendix published in Werhahn et al. (2021c), whereas the description of the radiation processes can be found in Section 2.3.3.

In practice, we solve Eq. (2.95) by computing j_ν on slices that are oriented perpendicular to the line of sight s and equidistantly spaced along s through the simulation cube and cumulatively add the optical depth. If we observe a simulated galaxy edge-on, for instance, $\mathrm{d}s = \mathrm{d}y$ and we obtain two-dimensional slices of the optical depth and the synchrotron emissivity in the $x-z$ plane, i.e. $\tau(x,z)$ and $j_\nu(x,z)$. This results in a two-dimensional projection of the intensity $I_\nu(x,z)$ after adding up the slices from the front to the back of the simulation. This procedure also allows us to construct the absorbed spectrum from a different viewing angle by initially rotating the cube around the x-axis, which yields $I_\nu(\boldsymbol{r}_\perp)$, where $\boldsymbol{r}_\perp$ is the vector in the plane perpendicular to the line of sight. The observed flux density from an object emitting at a luminosity distance d is then obtained by integrating over the area A and solid angle Ω

$$F_\nu = \frac{1}{4\pi d^2}\int_\Omega\int_A I_\nu(\boldsymbol{r}_\perp)\mathrm{d}^2 r_\perp \mathrm{d}\Omega. \tag{5.42}$$

5.8 Appendix: Radio spectra for different central radii

The radio spectra of the central regions of our analysed galaxies shown in the middle panels of Fig. 5.8 and 5.9 are calculated by adopting the radii summarised in Table 5.2. Here, we analyse the effect of choosing different central radii on the spectral shape of free-free-absorbed synchrotron spectra and the spectra of free-free emission. As an example, we show the central spectrum of NGC 253 in Fig. 5.14. Decreasing the radius of the central region of the galaxy yields a lower synchrotron flux, which additionally suffers from more absorption losses due to the higher central gas densities, leading to a stronger turn-over at low frequencies.

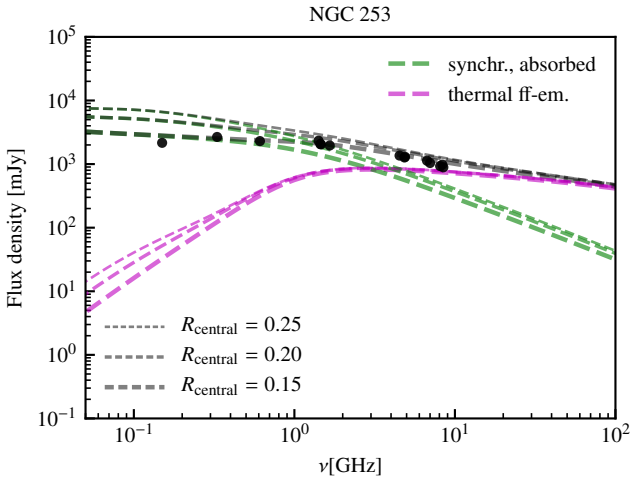

Figure 5.14: We compare the central radio spectrum of our simulated NGC 253-like galaxy (see Table 5.2) to observational data by Kapińska et al. (2017) of the central region. We compare the spectra within three different radial regions (as indicated in the legend) and show the resulting thermal free-free emission (magenta) and radio synchrotron spectrum (green).

5.9 Appendix: Parameter variation of the FRC

In Fig. 5.15, we show the FRC with variations of the parameters of the model discussed in Section 5.4, where we adopt $\zeta_{\rm SN} = 0.05$ and $B_0 = 10^{-10}$ G (see Fig. 5.3). Instead, the simulations shown in the top panels of Fig. 5.15 have an initial magnetic field of $B_0 = 10^{-12}$ G. Still, the observed FRC is reproduced both in our 'CR diff' and 'CR adv' models, respectively. There is only one outlier in the 10^{12} $M_\odot$ halo mass simulation in the 'CR diff' model, that overshoots the FRC beyond the observed scatter, at a SFR of 4.6 $M_\odot$ yr^{-1}. This illustrates the different dynamo actions taking place in the different simulations. As shown in Pfrommer et al. (2021), after $t \approx 1$ Gyr, the averaged magnetic energy density of a simulation with $M_{200} = 10^{12}$ $M_\odot$ initiated with a lower magnetic field of $B_0 = 10^{-12}$ G manages to overtake the simulations that started with a higher initial magnetic field of $B_0 = 10^{-10}$ G. However, for smaller halos, the magnetic field grows at a smaller rate in the simulations with $B_0 = 10^{-12}$ G (Pfrommer et al., 2021) and hence, they tend to fall short of the FRC.

The lower panels of Fig. 5.15 show the FRC of the simulation model with $B_0 = 10^{-12}$ G, but where CRs are injected with a higher acceleration efficiency and obtain a fraction of $\zeta_{\rm SN} = 0.10$ of the SN explosion energy, that is a factor of two larger than in our fiducial model. The combination of a lower initial magnetic field, but on the other hand a higher acceleration efficiency of CRs at

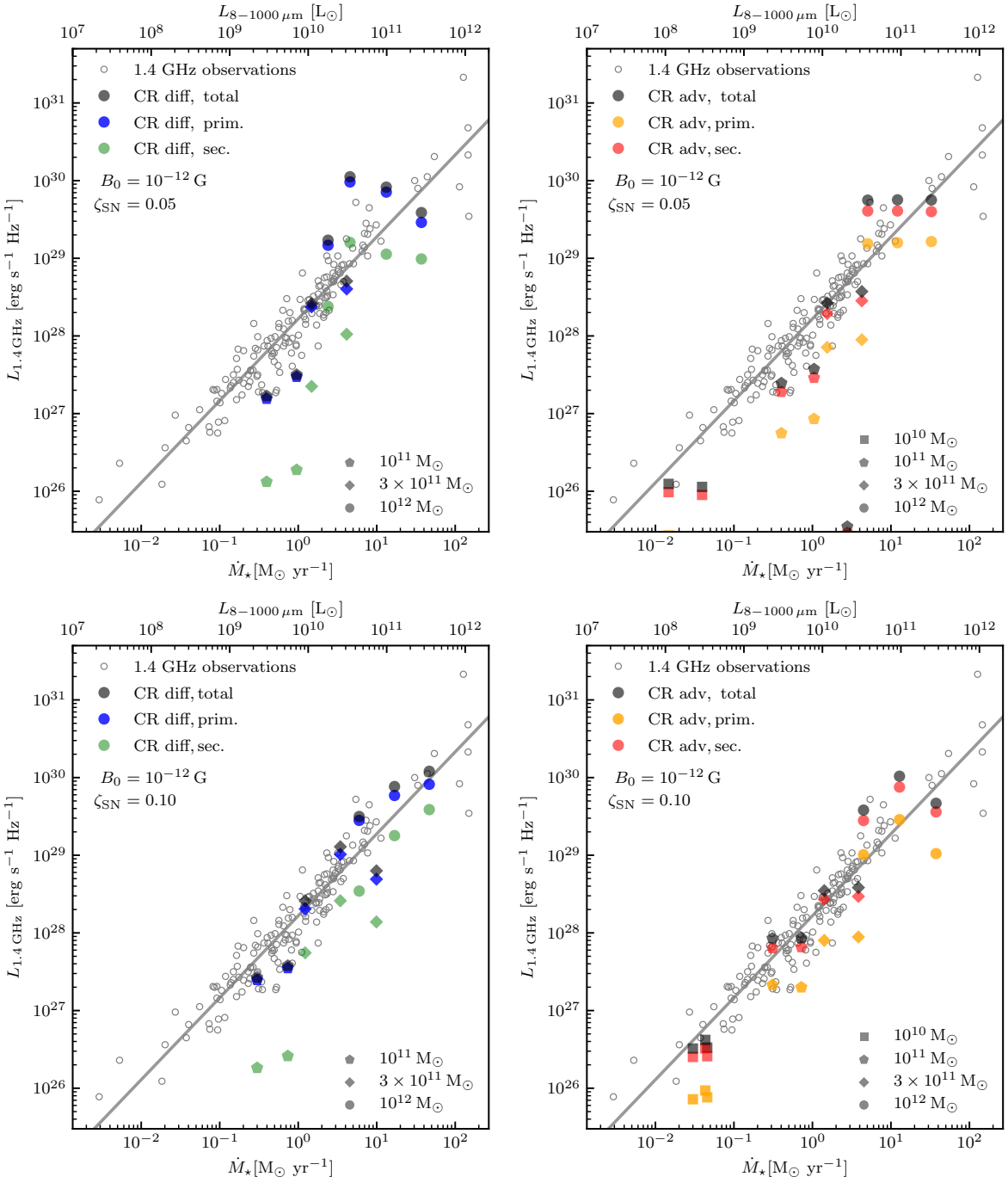

Figure 5.15: Parameter variation of the FRC. In contrast to Fig. 5.3, here we adopt a lower initial magnetic field strength $B_0 = 10^{-12}$ G (top panels). In the bottom panels, we additionally increase the CR injection efficiency by a factor of two, $\zeta_{SN} = 0.1$. Generally, our radio luminosities match the observed scatter.

SNe yields very similar results in comparison to our fiducial model and also matches the FRC within the observed scatter. However, we found in Paper II that this acceleration efficiency of 10 per cent is inconsistent with the observed FIR-gamma-ray relation, because it over-predicts the gamma-ray luminosity $L_{0.1-100\ \mathrm{GeV}}$ in both the 'CR diff' and 'CR adv' models. This highlights the importance of comparing theoretical models with observations across all accessible electromagnetic frequencies.

6. Gamma-ray emission from spectrally resolved cosmic rays in galaxies

This chapter is based on a paper draft that will be submitted to MNRAS.

The ubiquity of cosmic rays (CRs) in the interstellar medium (ISM) of nearby galaxies can be indirectly inferred through their emission processes. In particular, observations of gamma-ray emission from neutral pion decay constrain the interaction of CR protons with the ISM as well as their transport properties. To identify observational signatures from spectrally resolved CR transport, we analyse the gamma-ray emission arising from CR protons whose particle distribution functions are accurately modelled in every computational cell within magneto-hydrodynamical (MHD) simulations of isolated galaxies. The inclusion of energy-dependent spatial diffusion of CRs leads to a more extended emission of high-energy gamma-rays at 100 GeV in comparison to the emission resulting from a steady-state modelling of the spectra in all our simulated halos. This effect is especially visible in the maps and radial profiles of high-energy gamma-ray emission. However, the total gamma-ray spectra of the spectrally resolved CR model can still be represented by a steady-state configuration but requires in some cases a different energy dependence of the diffusion coefficient. Finally, our results reproduce the observed spectral indices and gamma-ray spectra of nearby star-forming galaxies and coincide with recent observations of the far infrared (FIR)-gamma-ray relation. We find that the spectrally resolved model yields smaller luminosities with decreasing star-formation rates (SFRs) in comparison to grey simulations of CRs. Our work highlights the importance of modelling spectrally resolved CR transport for an accurate prediction of spatially resolved high-energy gamma-ray emission, which will be probed by the future Cherenkov Telescope Array observatory.

6.1 Introduction

The unexpected low efficiency of galaxies to form stars is still one of the biggest puzzles in galaxy formation (e.g. Fukugita et al., 1998; Moster et al., 2010). It requires the existence of so-called feedback mechanisms that are able to quench star-formation by, e.g., expelling the gas from the disk via galactic winds. While active galactic nuclei (AGNs) have been suggested to be an influential feedback mechanism in very massive galaxies and galaxy clusters (Croton et al., 2006), feedback from stellar winds, radiation fields and/or supernovae might be relevant in galaxies with masses of the order of the Milky Way and below. One of the potential mediators of this feedback are cosmic rays (CRs), a non-thermal relativistic population of charged particles, which have been found to be in rough equipartition with the thermal, magnetic and turbulent energy densities in the interstellar medium (ISM) of the Milky Way (Boulares & Cox, 1990).

Because the main acceleration site of these particles are shocks that form at remnants of supernovae (SNRs), whose occurrence are closely connected to the star formation activity of a galaxy, we expect a close connection between the SFR and CR content of a galaxy. This can be indirectly constrained via the observation of non-thermal emission processes from CRs that arise across a wide range of frequencies. While the radio band traces the underlying CR electron population through synchrotron radiation and tightly correlates with the SFR (van der Kruit, 1971, 1973; Bell, 2003; Molnár et al., 2021), drawing inferences about the CR population using this band is often complicated as radio emission depends on properties of the galactic magnetic field that needs to grow via a galactic dynamo (Werhahn et al., 2021c; Pfrommer et al., 2022) and whose observed properties often have large uncertainties surrounding them. By contrast, the gamma-ray regime mainly probes the interaction of CR protons with the ambient gas, which leads to the emission of gamma-ray photons through the decay of neutral pions. If CR protons efficiently lose all of their energy due to this process, the galaxy would be a CR proton calorimeter (Pohl, 1994). This would in turn imply that CRs cannot escape the galaxy and thus are not able to play a significant role in driving galactic winds. Consequently, an accurate modelling of the CR proton population in the formation and evolution of galaxies in combination with the resulting non-thermal emission is required in order to constrain the relevance of CR feedback in galaxies.

There are a number of observations that provide constraints on this modelling. The gamma-ray emission of nearby star-forming galaxies has been observed by, e.g., the VERITAS Collaboration et al. (2009) collaboration, the H. E. S. S. Collaboration et al. (2018) and the Fermi-LAT Collaboration et al. (2022). Through these, a strong correlation between the gamma-ray luminosities and SFRs (or equivalently the FIR luminosity, which is a good tracer of star-formation) has been found

(Ackermann et al., 2012b; Rojas-Bravo & Araya, 2016; Ajello et al., 2020; Kornecki et al., 2020) as was predicted in earlier work (Thompson et al., 2007). This suggests that the calorimetric model holds for starburst galaxies, while other losses of CR protons lead to a deviation from this relation towards smaller SFRs (Thompson et al., 2007; Lacki et al., 2011; Martin, 2014; Pfrommer et al., 2017b; Kornecki et al., 2020; Werhahn et al., 2021b). In particular, CR transport like advection and/or diffusion might be responsible for diminishing gamma-ray emission. Another benchmark for theoretical models are observed gamma-ray spectra from individual galaxies, which provide a more detailed constraint on the underlying distribution of CR protons as shaped by the interplay of cooling and escape losses. Even before their detection, gamma-ray emission from individual galaxies has been predicted by a number of works (e.g. Torres, 2004; Domingo-Santamaría & Torres, 2005; Persic et al., 2008; de Cea del Pozo et al., 2009; Rephaeli et al., 2010) and confirmed by subsequent observations and models (e.g. Lacki et al., 2011; Yoast-Hull et al., 2013; Yoast-Hull & Murray, 2019; Peretti et al., 2019; Ambrosone et al., 2022).

Most of these approaches, however, adopt one-zone models where free parameters are fit to the observed data. Indeed, only recently has gamma-ray emission from CRs been explored using full MHD simulations of isolated galaxies (Pfrommer et al., 2017b; Chan et al., 2019; Buck et al., 2020; Werhahn et al., 2021b; Nuñez-Castiñeyra et al., 2022). In these simulations, CRs are coupled to the MHD equations as a relativistic fluid with an effective transport coefficient and cooling rates that assume a steady-state spectrum evolving only the CR energy density (Pfrommer et al., 2017a). We refer to this approach throughout the rest of the paper as the grey approach. In contrast, Girichidis et al. (2020b) introduced a novel implementation in the moving-mesh code Arepo where the spectral CR energy distribution is represented by a full spectrum in each computational cell. This treatment enables a dynamical coupling of CRs with the gas while evolving the full CR spectrum in time, as well as including cooling and spectrally resolved transport of CRs by means of energy-dependent spatial diffusion. To identify the observational signatures of this approach, we calculate in this work the gamma-ray emission from neutral pion decay from spectrally resolved CR MHD simulations of isolated galaxies. We then compare this to steady-state models of CR spectra that we apply to the spectrally resolved simulations as well as to simulations that include CRs in the grey approximation. Furthermore, we verify our results against several observations in the gamma-ray regime.

Our work is structured in the following way. We first explain our numerical methods and the simulation setup in Section 6.2. We then analyse the morphological features arising from the spectrally resolved CR simulations in comparison with the steady-state and grey modelling approaches in Section 6.3. In Section 6.4, we analyse the differences in the CR proton and

gamma-ray spectra in detail. In Section 6.5, we compare our results with recent data for nearby star-forming galaxies, including their gamma-ray spectra and the FIR-gamma-ray relation, where we additionally analyse the interpretation of the energy dependence of the diffusion coefficient. Finally, in Section 6.6, we discuss our results and conclude.

6.2 Numerical methods and simulations

6.2.1 Spectrally resolved CR treatment

The simulations underlying this work where performed with the second-order accurate, moving mesh code Arepo (Springel, 2010; Pakmor et al., 2016a; Weinberger et al., 2020) and follow the evolution of magnetic fields using the ideal MHD approximation. We employ the method of cell-centred magnetic fields in Arepo (Pakmor et al., 2011) with an HLLD Riemann solver (Miyoshi & Kusano, 2005) to compute fluxes and the Powell 8-wave scheme (Powell et al., 1999a) for divergence cleaning (Pakmor & Springel, 2013). We also include the one-moment CR hydrodynamics solver (Pfrommer et al., 2017a) that was extended to include spectrally resolved CR hydrodynamics developed by Girichidis et al. (2020b) and linked to Arepo in Girichidis et al. (2022). We briefly review the numerical method and physical processes in the following but refer to Girichidis et al. (2020b, 2022) for a more detailed description.

The spectral code solves the Fokker-Plank equation for CRs

$$\frac{\partial f^{(3\mathrm{D})}}{\partial t} = -\boldsymbol{v}\cdot\nabla f^{(3\mathrm{D})} + \nabla\cdot[\mathbf{D}\cdot\nabla f^{(3\mathrm{D})}] + \frac{1}{3}(\nabla\cdot\boldsymbol{v})\frac{\partial f^{(3\mathrm{D})}}{\partial p} \tag{6.1}$$

$$+ \frac{1}{p^2}\frac{\partial}{\partial p}\left(p^2 b_l f^{(3\mathrm{D})}\right) + j, \tag{6.2}$$

which describes the evolution of the isotropic part of the distribution function $f^{(3\mathrm{D})} = f^{(3\mathrm{D})}(\boldsymbol{x},\boldsymbol{p},t) = \mathrm{d}N/(\mathrm{d}p^3\mathrm{d}x^3)$ as a function of time t and $p = |\boldsymbol{p}| = P/(m_\mathrm{p}c)$ denotes the absolute value of the normalised particle momentum to the proton mass m_p times the speed of light c. Here, we neglect diffusion in momentum space and assume anisotropic spatial CR diffusion along the magnetic field using the discretisation of Pakmor et al. (2016b) with the spatial diffusion tensor $\mathbf{D} = D\boldsymbol{b}\boldsymbol{b}$, where $\boldsymbol{b} = \boldsymbol{B}/B$ denotes the direction of the magnetic vector field $\boldsymbol{B}$ with field strength $B = \sqrt{\boldsymbol{B}^2}$ and $D = D(p)$ is the parallel diffusion coefficient with the momentum dependence given by

$$D(p) = 10^{28} p^{\delta}\mathrm{cm}^2\,\mathrm{s}^{-1}, \tag{6.3}$$

where we choose $\delta = 0.3$. Furthermore, $\boldsymbol{v}$ is the mean velocity of the thermal gas and j and $b_l = \mathrm{d}p/\mathrm{d}t$ are source and loss terms, respectively. For the latter, losses due to Coulomb and hadronic interactions of CR protons with the ambient medium are taken into account. In addition, we account for streaming losses using the simplified approach by Pfrommer et al. (2017a); Buck et al. (2020), in which streaming drains energy from the CRs at a rate proportional to the Alfvén speed $\mathbf{v}_\mathrm{A}$ and the CR pressure gradient ∇P_cr, $\Lambda_\mathrm{cr} = |\mathbf{v}_\mathrm{A} \cdot \nabla \mathbf{P}_\mathrm{cr}|$. We apply the cooling to the total CR energy and rescale the spectrum uniformly to match the cooled total CR energy.

The particle distribution function is discretised in momentum space, where it is represented by a piece-wise power law in each bin. This provides two degrees of freedom: the normalisation and the slope of the spectrum in each momentum bin. The first two moments of the distribution function are chosen to be evolved in time, i.e. the CR number and energy density of each momentum bin.

6.2.2 Simulation setup

We simulate the formation of galaxies with the moving-mesh code Arepo, with the same setup as described in Girichidis et al. (2022), but varying some of the parameters. We start with a dark matter halo that is characterised by an NFW profile and a concentration parameter $c_{200} = 7$, where we vary the halo mass $M_{200} = \{10^{10}, 10^{11}, 3 \times 10^{11}, 10^{12}\}\,\mathrm{M}_\odot$. It contains gas that is initially in thermodynamic equilibrium but as soon as we start the simulation and switch on cooling, it collapses and forms a disk. Stars form in a stochastic manner following the Springel & Hernquist (2003) ISM model, where an effective equation of state is adopted based on the assumption that the hot and cold phase are in equilibrium. We inject CRs with an efficiency of 10 per cent of the canonical SN energy of 10^{51} erg.

We run all setups with two models of CR transport, respectively: First, we adopt the 'grey' approach, where we only follow the evolution of the CR energy density in the advection-diffusion approximation as introduced in Pfrommer et al. (2017a). In addition, we run a set of the same simulations but now apply the novel spectrally resolved CR hydrodynamics solver coupled to Arepo as summarised in the previous section (Girichidis et al., 2022). Here, we discretise the spectrum in twelve equally spaced logarithmic momentum bins ranging from 100 MeV c^{-1} to 100 TeV c^{-1}. In the vicinity of newly formed star particles, we inject CRs with an injection spectrum $f^{(3\mathrm{D})}(p) \propto p^{-4.2}$. Our set of simulations is summarised in Table 6.1.

In order to contextualise the novel approach of a spectral treatment of CR proton transport and to interpret the resulting gamma-ray emission in comparison to the grey approach in combination with the steady-state modelling of CR spectra, we follow three different approaches. We apply

Table 6.1: Overview of the simulations.

M_{200} [$M_\odot$]	CR model	D [$cm^2 s^{-1}$]	name
10^{10}	grey	10^{28}	`M1e10-grey`
10^{11}	grey	10^{28}	`M1e11-grey`
3×10^{11}	grey	10^{28}	`M3e11-grey`
10^{12}	grey	10^{28}	`M1e12-grey`
10^{10}	spectrally resolved	Eq. (6.3)	`M1e10-spec`
10^{11}	spectrally resolved	Eq. (6.3)	`M1e11-spec`
3×10^{11}	spectrally resolved	Eq. (6.3)	`M3e11-spec`
10^{12}	spectrally resolved	Eq. (6.3)	`M1e12-spec`

three models in post-processing to the simulations:

- Model 'grey': First, we apply the cell-based steady-state approach as introduced in Werhahn et al. (2021a) (see Section 6.2.3) on the grey runs.
- Model 'spec': Second, we directly take the CR spectra of the spectrally resolved CR runs and compute their resulting gamma-ray emission from neutral pion decay.
- Model 'steady on spec': Third, we apply the cell-based steady-state model (see Section 6.2.3) to the novel spectrally resolved CR runs to obtain steady-state CR proton spectra from the exact same simulations.

The last step is constructive because it enables a direct comparison between a steady-state modelling and the new spectrally resolved simulations of CRs. Because this novel treatment has a dynamical impact on the global evolution of the galaxy in comparison to the grey approach, solely comparing the spectrally resolved CRs to the grey simulations with steady-state spectra would dilute the interpretation of potential differences.

6.2.3 Steady-state modelling

For the steady-state solution, we apply the model introduced in Werhahn et al. (2021a), which we summarise now. We solve the diffusion-loss equation in post-processing in each computational cell

(see e.g. Ginzburg & Syrovatskii, 1964; Torres, 2004) for the one-dimensional distribution function $f(E_\mathrm{p}) = f(p)\mathrm{d}p/\mathrm{d}E_\mathrm{p} = 4\pi p^2 f^{(3\mathrm{D})}(p)\mathrm{d}p/\mathrm{d}E_\mathrm{p}$ that reads

$$\frac{f(E_\mathrm{p})}{\tau_\mathrm{esc}} - \frac{\mathrm{d}}{\mathrm{d}E_\mathrm{p}}\left[f(E_\mathrm{p})b(E_\mathrm{p})\right] = q(E_\mathrm{p}), \tag{6.4}$$

with source and loss terms q and b. The escape losses due to advection or diffusion are quantified by an escape timescale $\tau_\mathrm{esc}^{-1} = \tau_\mathrm{diff}^{-1} + \tau_\mathrm{adv}^{-1}$, where the diffusion and advection timescales are estimated via

$$\tau_\mathrm{diff} = \frac{L_\mathrm{CR}^2}{D(E_\mathrm{p})} \propto E_\mathrm{p}^{-\delta}, \qquad \tau_\mathrm{adv} = \frac{L_\mathrm{CR}}{v_z}, \tag{6.5}$$

where $L_\mathrm{CR} = \varepsilon_\mathrm{CR}/|\nabla\varepsilon_\mathrm{CR}|$ estimates the diffusion length in each cell and v_z is the z-component of the velocity of the gas cell. This estimate assumes that the advection is effectively only happening in z-direction implying that all fluxes in the azimuthal direction in and out of the cell compensate each other (see figure 6 of Werhahn et al., 2021a, corresponding to Fig. 3.6 in this work). As a source term, we assume a power law in momentum $q(p) = q[p(E_\mathrm{p})]\mathrm{d}E_\mathrm{p}/\mathrm{d}p$ with an exponential cut-off

$$q(p)\mathrm{d}p = C_0\, p^{-\alpha_\mathrm{inj}} \exp[-p/p_\mathrm{cut}]\mathrm{d}p, \tag{6.6}$$

with a cut-off momentum at $p_\mathrm{cut} = 1\,\mathrm{PeV}/mc$ (Gaisser, 1990) if not mentioned otherwise. The normalization C_0 is determined such that the integral over the equilibrium distribution function f eventually matches the CR energy density ε_CR of each cell, i.e. $\int E_\mathrm{kin}(p) f(p)\mathrm{d}p = \varepsilon_\mathrm{CR}$, where $E_\mathrm{kin} = (\sqrt{(p^2+1)} - 1)m_\mathrm{p}c^2$.

6.2.4 Gamma-ray emission

We calculate the gamma-ray emission from hadronic interactions of CR protons with the ambient gas of the simulations with the same approach as in Werhahn et al. (2021b). The source function of gamma-ray emission from neutral pion decay $q_E = \mathrm{d}N_\gamma/(\mathrm{d}V\,\mathrm{d}t\,\mathrm{d}E)$ is computed by adopting the parametrization by Kafexhiu et al. (2014) for large proton kinetic energies (above 10 GeV) and the model by Yang et al. (2018b) for energies from the threshold of pion production up to 10 GeV. From this, we obtain the specific luminosity as an integral over the volume V, i.e. $L_E = \int q_E(\boldsymbol{r})\mathrm{d}V$.

The spectral surface brightness S_E and the spectral flux F_E are defined via

$$S_E(\boldsymbol{r}_\perp) = \int_{-\infty}^{\infty} q_E(\boldsymbol{r}) \mathrm{d}l, \quad \text{and} \quad F_E = \frac{1}{4\pi d^2} \int q_E(\boldsymbol{r}) \mathrm{d}V, \tag{6.7}$$

where $\boldsymbol{r}_\perp$ is the radius vector in the plane orthogonal to the projection direction and d denotes the luminosity distance. We furthermore define the integrated luminosity in the energy range from E_1 to E_2 via

$$L_{E_1-E_2} = \int_\Omega \mathrm{d}V \int_{E_1}^{E_2} E q_E \, \mathrm{d}E. \tag{6.8}$$

6.3 Morphological differences

We first show the most striking effect of the spectrally resolved CR treatment on the gamma-ray emission from our simulated galaxies. In the upper six panels of Fig. 6.1, we present maps of the gamma-ray emission from neutral pion decay as obtained from the spectrally resolved CRs of our simulation `M3e11-spec` (model 'spec'), whilst in the middle six panels, we show the emission from the steady-state model as applied to the same simulation (model 'steady on spec'). The projected maps are shown face-on and edge-on, rotated by 25 degrees, for gamma-ray emission at 1, 10 and 100 GeV, respectively. Due to the inclusion of spectrally resolved CR transport, high-energy CRs are allowed to diffuse faster than low-energy ones and hence, in this model the GeV-gamma-rays are more centrally concentrated than the emission from the steady-state model. On the other hand, gamma-rays with energies of 10 or 100 GeV extend to larger radii in the spectrally resolved CR model. This is because comparing gamma-ray maps at 1 and 100 GeV probes CR protons that typically have energies of 100 MeV and 10 GeV, respectively, which have an increased diffusion coefficient by a factor of $100^{0.3} \approx 4$. This allows the 100 GeV emission to have a much greater radial extent in the face-on maps. Similarly, the nearly edge-on maps reveal more extended emission at 10 and 100 GeV from the spectrally resolved CR model in comparison to the corresponding steady-state approach.

The lower six panels of Fig. 6.1 show the simulation `M3e11-grey`, where the gamma-ray emission has been calculated from the steady-state model (model 'grey'). There is no explicit energy-dependent diffusion in our grey simulations, and subsequently the high-energy CRs do not diffuse to the same extent as in the 'spec' model. This leads to a much more concentrated high-energy gamma-ray emission at 100 GeV in this model (compare the right-hand panels in Fig. 6.1). The steady-state approach yields this result for both the steady-state applied to the grey simulations

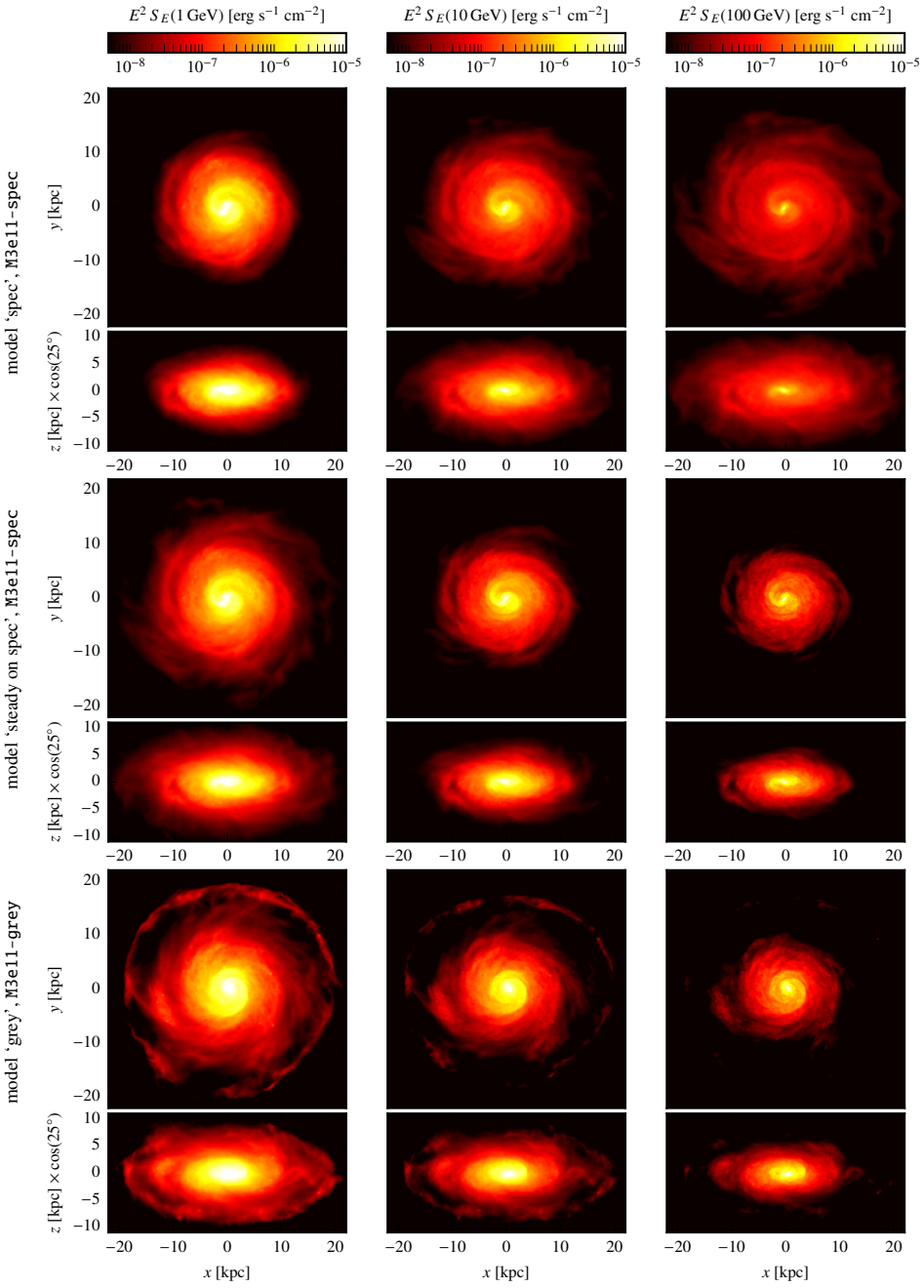

Figure 6.1: Gamma-ray emission from neutral pion decay of spectrally resolved CR protons (`M3e11-spec`, upper six panels), where energy dependent diffusion is included explicitly, and the emission resulting from steady-state CR spectra of the same simulation (middle six panels) at 1, 10 and 100 GeV (left-, middle and right-hand panels), respectively, at time t =1 Gyr. We show projected maps face-on (first, third and fifth row) as well edge-on views that are rotated by 25 degrees (second, forth and sixth row). The lower six panels show the same maps calculated from steady-state CRs of a simulation performed with the grey approach (`M3e11-grey`).

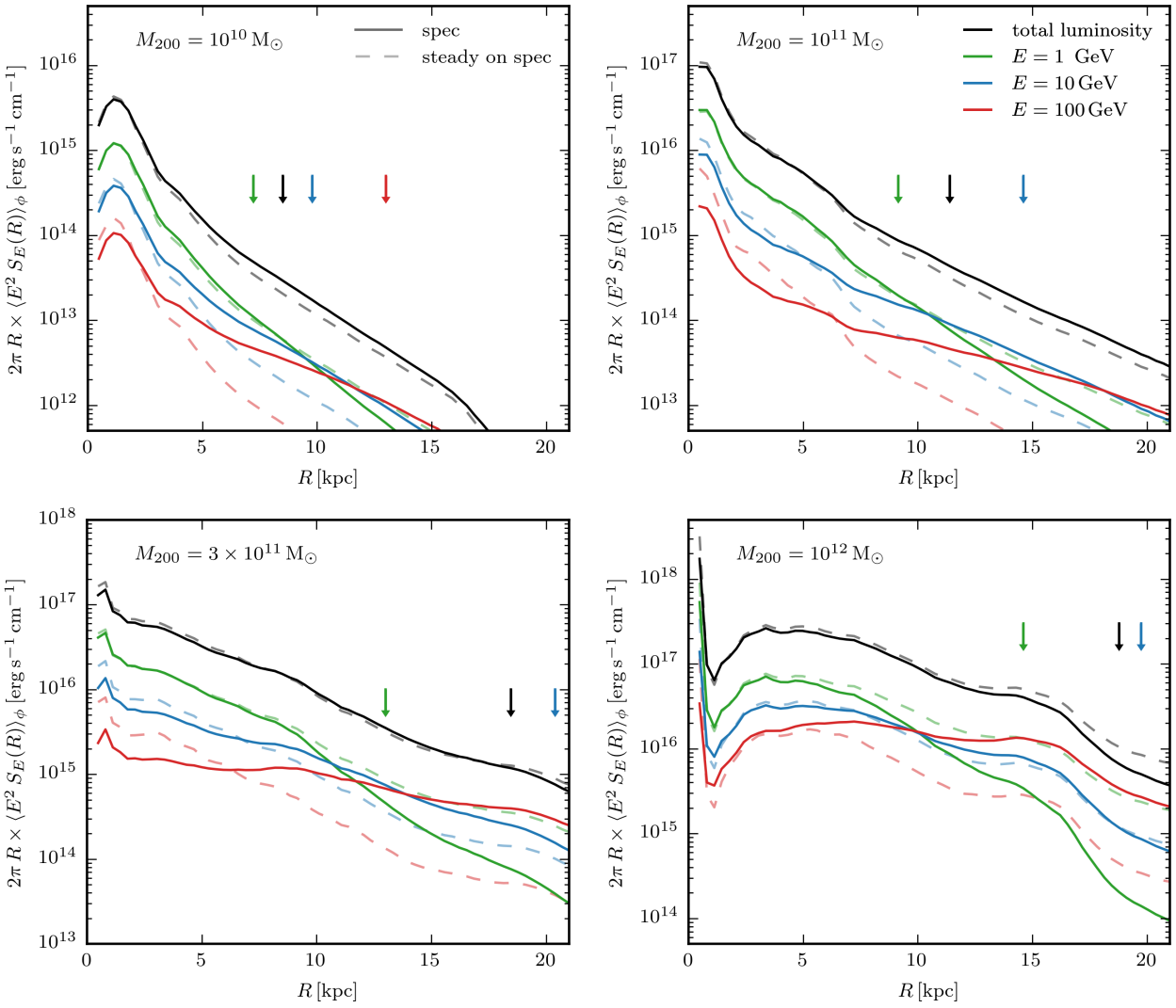

Figure 6.2: Radial profiles of the differential contribution to the gamma-ray emission for the different halo masses at $t = 1$ Gyr for the spectrally resolved CR runs (solid lines) and the steady-state model applied to the same simulations (dashed lines). The different colours show $E^2 \mathrm{d}L_E/\mathrm{d}R = 2\pi R \times \langle E^2 S_E(R)\rangle_\phi$ at different gamma-ray energies E as indicated in the legend in the upper right-hand panel. The differential contribution for the integrated luminosity $L_{0.1-100\mathrm{GeV}}$ is shown in black, where 99 per cent of this luminosity is included within a radius that is represented by the black arrow for each halo, respectively. The radius where 99 per cent of the specific luminosity L_E at a given energy is included is indicated by a vertical arrow in the corresponding colour for each E in the 'spec' model.

and applied to the spectral runs. We only find slightly varying distributions in gas density.

To quantify the morphological differences, we compute the differential contribution to the specific gamma-ray luminosity via

$$E^2 \frac{\mathrm{d}L_E}{\mathrm{d}R} = E^2 \frac{d}{dR} \int_{\mathrm{d}\Omega} q_E R \, \mathrm{d}R \, \mathrm{d}\phi \, \mathrm{d}z = 2\pi R \times \langle E^2 S_E(R) \rangle_\phi, \tag{6.9}$$

where the azimuthally averaged surface brightness is defined via

$$\langle E^2 S_E(R) \rangle_\phi = \frac{E^2}{2\pi} \int_{-\infty}^{\infty} q_E \mathrm{d}\phi \, \mathrm{d}z \tag{6.10}$$

and for the integrated gamma-ray luminosity

$$\frac{\mathrm{d}L_{0.1-100\mathrm{GeV}}}{\mathrm{d}R} = \frac{d}{dR} \int_{E_1}^{E_2} \int_{\mathrm{d}\Omega} E q_E R \, \mathrm{d}R \, \mathrm{d}\phi \, \mathrm{d}z \mathrm{d}E \tag{6.11}$$

$$= 2\pi R S_{0.1-100\mathrm{GeV}}(R), \tag{6.12}$$

where R denotes the cylindrical radius, $E_1 = 0.1\,\mathrm{GeV}$ and $E_2 = 100\,\mathrm{GeV}$. We show this as a function of radius in Fig. 6.2 for all four of our spectrally resolved CR runs with different halo masses after 1 Gyr of evolution. While applying the steady-state model to the simulations leads to a very similar radial contribution to the gamma-ray emission at all shown energies E, the spectrally resolved CR treatment differs substantially from this. Here, the distribution of gamma-ray emission varies for different energies due to the different diffusion efficiencies of CRs with different energies. This effect is in principle visible for all halo masses. However, while in our smaller galaxies `M1e10-spec` and `M1e11-spec` we find that 100 GeV gamma-rays only become dominant outside of the radius where 99 per cent of the total gamma-ray luminosity is included (black arrows), it already contributes substantially below that radius for larger halo masses. In particular, in our most massive halo with $M_{200} = 10^{12}\,\mathrm{M}_\odot$, 100 GeV gamma-rays dominate over all lower gamma-ray energies already at radii $\sim$10 kpc, while 99 per cent of the total, integrated gamma-ray luminosity are contained within $R \lessapprox 19$ kpc.

In contrast to the profiles of the specific luminosities at different energies, the radial distribution of the total gamma-ray luminosity in (black lines in Fig. 6.2) follow closely the profiles from a steady-state configuration in all considered halo masses. This is because the (momentum-integrated) CR energy densities of both models are identical in each cell by construction and consequently, integrating the gamma-ray emission over a large enough energy interval (that is powered by the

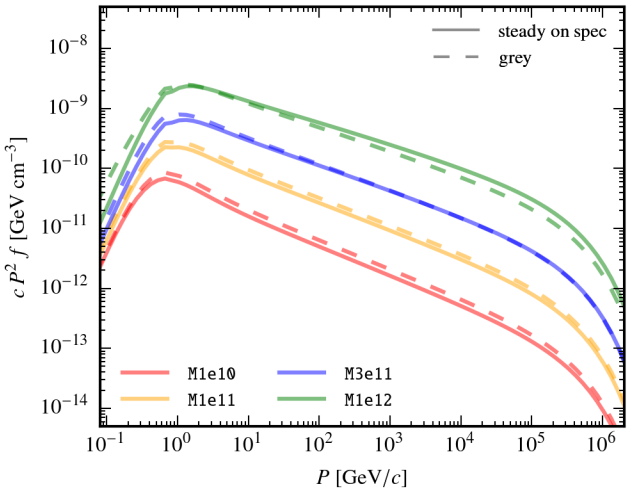

Figure 6.3: Steady-state CR proton spectra of all spectrally resolved (solid lines) and grey runs (dashed lines) after $t = 1$ Gyr. For all halo masses (shown in different colors as indicated in the legend), the steady-state CR proton distributions (averaged over a cylinder with $R = 20$ kpc and a height $h = 1$ kpc above and below the midplane) are almost identical.

majority of pressure-carrying CR particle energies) must reflect this. Hence, we conclude that while the radial distribution of the total gamma-ray luminosity is not sensitive to the underlying model of the CR spectra, the spatial gamma-ray distributions at different energy bands vary substantially and require to resolve spectral CR transport to accurately capture their distribution.

6.4 Spectral differences

After exploring the spatial signatures of spectrally resolved CR transport, we now examine the spectral differences by analysing first the CR proton spectra, before dissecting the gamma-ray spectra.

6.4.1 CR proton spectra

Steady-state and grey approach

First, we compare the same steady-state model applied to our grey and our spectral CR runs. Figure 6.3 shows the steady-state proton spectra of all our simulated halos after an evolution of 1 Gyr averaged within a cylinder with $R = 20$ kpc and a height $h = 1$ kpc above and below the

midplane, respectively. While we found some morphological differences in the distribution of gamma-ray emission from both steady-state models (see middle and lowest panels of Fig. 6.1) due to the moderately different dynamical impact of spectrally resolved CR hydrodynamics (Girichidis et al. in prep.), the averaged steady-state CR proton spectra are almost identical for the grey and spectrally resolved runs for each halo mass. This corroborates our forthcoming procedure of comparing the spectrally resolved CRs directly to the steady-state approach applied to the same runs, instead of comparing them to the grey simulations. Note that however, there are differences in morphology and star-formation histories which will be analysed in more detail in another paper (Girichidis et al. in prep.), while we will focus here mainly on the properties of the emerging gamma-ray emission.

Spectrally resolved CR protons vs. steady-state

The differences in the morphology of the gamma-ray emission found in Fig. 6.1 of spectrally resolved CRs in comparison to the corresponding steady-state can be traced back to differences in the underlying CR proton distribution. To enable a detailed comparison of the spectrally resolved CR approach with a steady-state, we show in the left-hand panels of Fig. 6.4 the CR proton spectra averaged in radial bins for our different halo masses, respectively. The averaged spectra are obtained from the spectrally resolved CR simulations by first averaging the CR energy and number density in each momentum bin over the region of interest and then reconstructing the normalization and slope for each bin. The steady-state spectra are computed in post-processing in every computational cell of the same simulations (see Section 6.2.3) by assuming the same energy scaling of the diffusion coefficient ($\delta = 0.3$) and an identical injected spectral index of CR protons. The average spectra are calculated via

$$\langle f \rangle_i = \frac{1}{V_i} \int f_i \, \mathrm{d}V_i \tag{6.13}$$

in each radial bin i with volume V_i, respectively. There are only very few cases where we find the spectrally resolved treatment to yield a spectrum that resembles the corresponding steady-state spectrum in the left-hand panels of Fig. 6.4. Only in the case of our dwarf galaxy with $M_{200} = 10^{10}\,\mathrm{M}_\odot$ in the radial region 1 kpc $\lesssim R \lesssim$ 3 kpc, the CR spectra exhibit similar slopes to the steady-state model but show a different cut-off at low momenta. This is due to the explicit modelling of cooling as the spectra evolve as a function of time, while the steady-state approach assumes injection and cooling to be in equilibrium at the time of the snapshot. Apart from this case, the CR spectra in all other regions are not found to be close to a steady-state configuration.

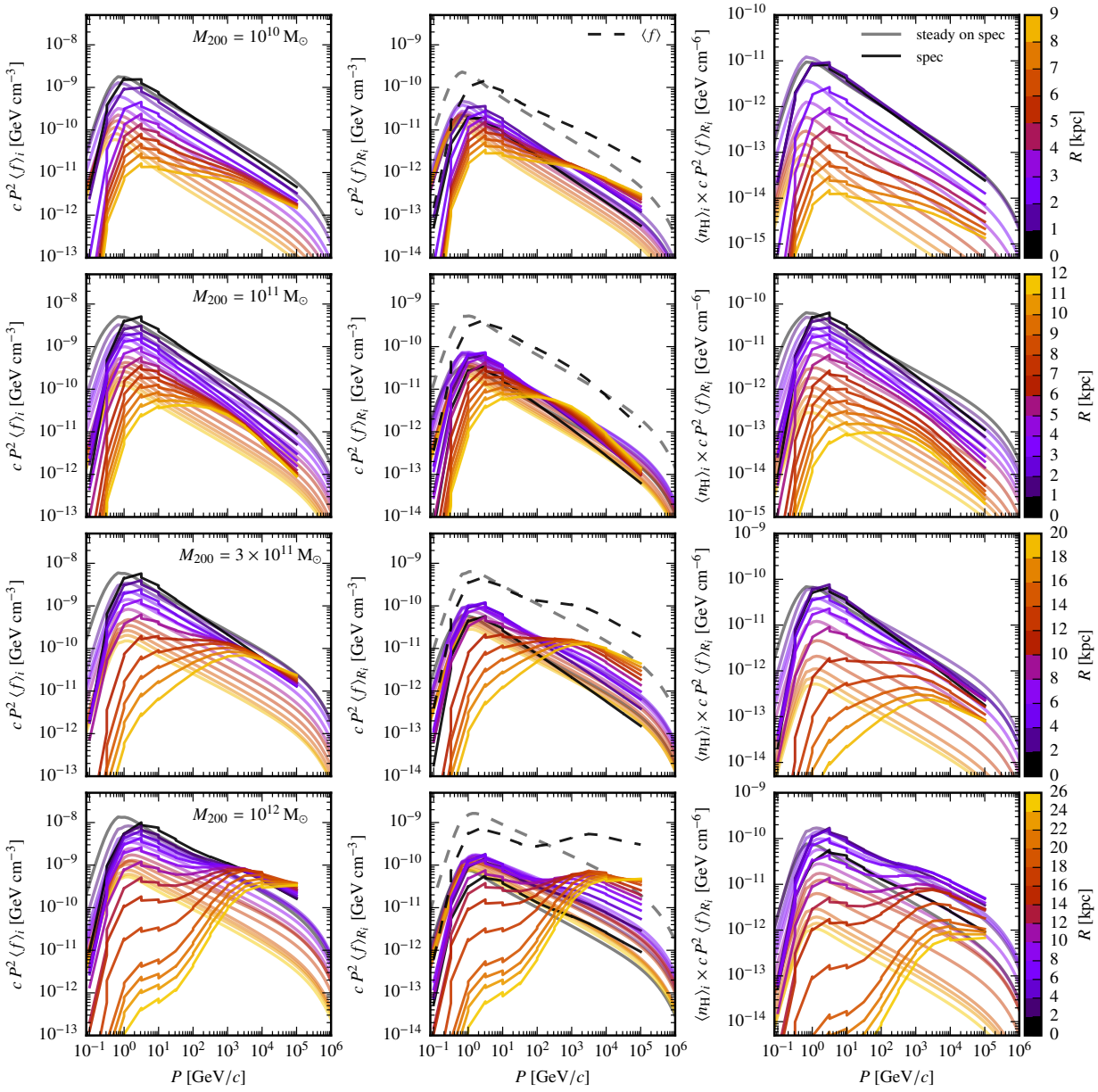

Figure 6.4: CR proton spectra for the different halo masses (increasing from top to bottom) at $t = 1$ Gyr in concentric, cylindrical bins, where we define a maximum radius such that the CR energy density has decreased approximately by four e-foldings. The left-hand panels show the CR spectra averaged in radial bins (Eq. 6.13), while the middle panels show the contribution of each radial bin to the total spectrum (Eq. 6.14). In order to study the contribution of different radii to the total gamma-ray emission, we multiply the spectra in the right-hand panels by the averaged gas density of each radial bin.

Instead, they either have a similar shape with a steeper slope or a completely different distribution. The former is predominantly occurring in the central regions of all but the most massive simulated galaxy. After an initial injection of CRs in the central regions due to the high SFRs there, high energy CRs are allowed to diffuse out very quickly in the spectral code which leads to steep central spectra, while they diffuse into the outskirts where the CR injection rate is lower. This leads to flatter spectra at large radii as compared to the steady-state model, where injection and cooling are always assumed to balance each other. This effect is particularly strong in the `M1e12-spec` simulation, where the spectra in the 'spec' model exhibit positive slopes in the outskirts of the galaxy in comparison to the negative slopes of the steady-state spectra (in the 'steady on spec' model) above ~ 1 GeV.

However, the left-hand panels of Fig. 6.4 only represent a volume-weighted average of the CR proton spectra in each radial bin, respectively, which does not reflect the actual contribution to the total spectrum. Hence, we additionally show the contribution to the total spectrum in radial bins R_i in the middle column of Fig. 6.4 where we calculate each contribution by

$$\langle f \rangle_{R_i} = \frac{1}{V} \int f_i \mathrm{d}V_i = \frac{2\pi}{V} \int_{R_{i-1/2}}^{R_{i+1/2}} f_i \; R_i \, \mathrm{d}R \, \mathrm{d}\phi \, \mathrm{d}z. \tag{6.14}$$

This definition ensures that the spectra fulfill $\Sigma_i \langle f \rangle_{R_i} = \langle f \rangle$ by construction, where the CR proton spectrum averaged over the total volume V is given by

$$\langle f \rangle = \frac{1}{V} \int f \mathrm{d}V. \tag{6.15}$$

Note that the definition of the average in Eq. (6.14) differs from that in Eq. (6.13) only by the normalising volume: in the latter case, the spectra are simple volume averages in the radial bins (left-hand panels of Fig. 6.4) while Eq. (6.14) computes the actual contribution of each radial bin to the total spectrum averaged over the whole volume (middle panels of Fig. 6.4). However, with increasing radius the gas density steeply decreases and hence, this representation does not reflect the radial contribution of the CR proton spectra to the total gamma-ray spectrum because the source function of gamma-ray emission from neutral pion decay is directly proportional to the gas density n_H. Consequently, we additionally consider the quantity $\langle n_\mathrm{H} \rangle \times \langle f \rangle_{R_i}$ in order to be able to identify the relevant spectral features that impact the gamma-ray emission. This is shown in the right-hand panels of Fig. 6.4 and will help us to interpret the differences in the gamma-ray emission in Section 6.4.2.

The comparison of the middle and right-hand panels of Fig. 6.4 reveals that the effect of high-energy CRs diffusing outwards more quickly (than expected in a steady-state) is visible in the total spectra of all halo masses (middle panels) but taking into account the gas density completely changes the picture (right-hand panels). In the latter, we clearly see that only the central few kpc will be relevant for the emerging gamma-ray emission, where the CR spectra of the `M1e10-spec` simulation closely resemble a steady-state, whereas the `M1e11-spec` simulation exhibits steeper CR spectra. In contrast, in the two most massive halos we expect an increasingly higher contribution from the relatively flat CR spectra due to energy-dependent diffusion. In particular, in the `M1e12-spec` simulation, this will substantially harden the gamma-ray spectra.

6.4.2 Gamma-ray spectra from spectrally resolved CRs

In this section, we aim to examine the effect of the spectrally resolved CR scheme on the resulting gamma-ray emission. First, we note that the steady-state modelling applied on the spectrally resolved simulations yields almost exactly the same spectral shapes in total gamma-ray emission than the steady-state applied to the grey runs for all halo masses at all times (see their corresponding CR proton spectra exemplified in Fig. 6.3 at $t = 1$ Gyr). There are only differences in the normalization of the total gamma-ray spectra and their morphologies due to variations in star-formation histories and different gas density distributions within the simulated disks resulting from the effect that spectrally resolved CR transport has on the dynamics of the whole system (Girichidis in prep.). Therefore, we again focus on the comparison of the emission from the spectrally resolved CRs to the steady-state approach applied to the same spectral runs in the following.

Temporal evolution of gamma-ray spectra

In Fig. 6.5 we show the temporal evolution of the gamma-ray spectra from neutral pion decay for all our simulated galaxies in the spectrally resolved runs from $t = 0.1$ to 2 Gyr of all simulated halos, respectively. The initial collapse of the gas cloud ignites a peak in star formation and hence results in a high injection of CRs which both decrease exponentially in time. This causes a decrease of the normalisation of the gamma-ray spectrum as a function of time in all simulations.

The comparison of the emission from the spectrally resolved CR protons with the steady-state model reveals that while the gamma-ray spectra only match a steady-state configuration (i.e. our steady-state approach adopted to the same simulations) in the simulations `M1e10-spec` and `M3e11-spec` at late times, all halos exhibit steeper spectra at early times. Additionally, the spectra of the `M1e11-spec` simulation continue to be steeper even at later times. In contrast, the gamma-

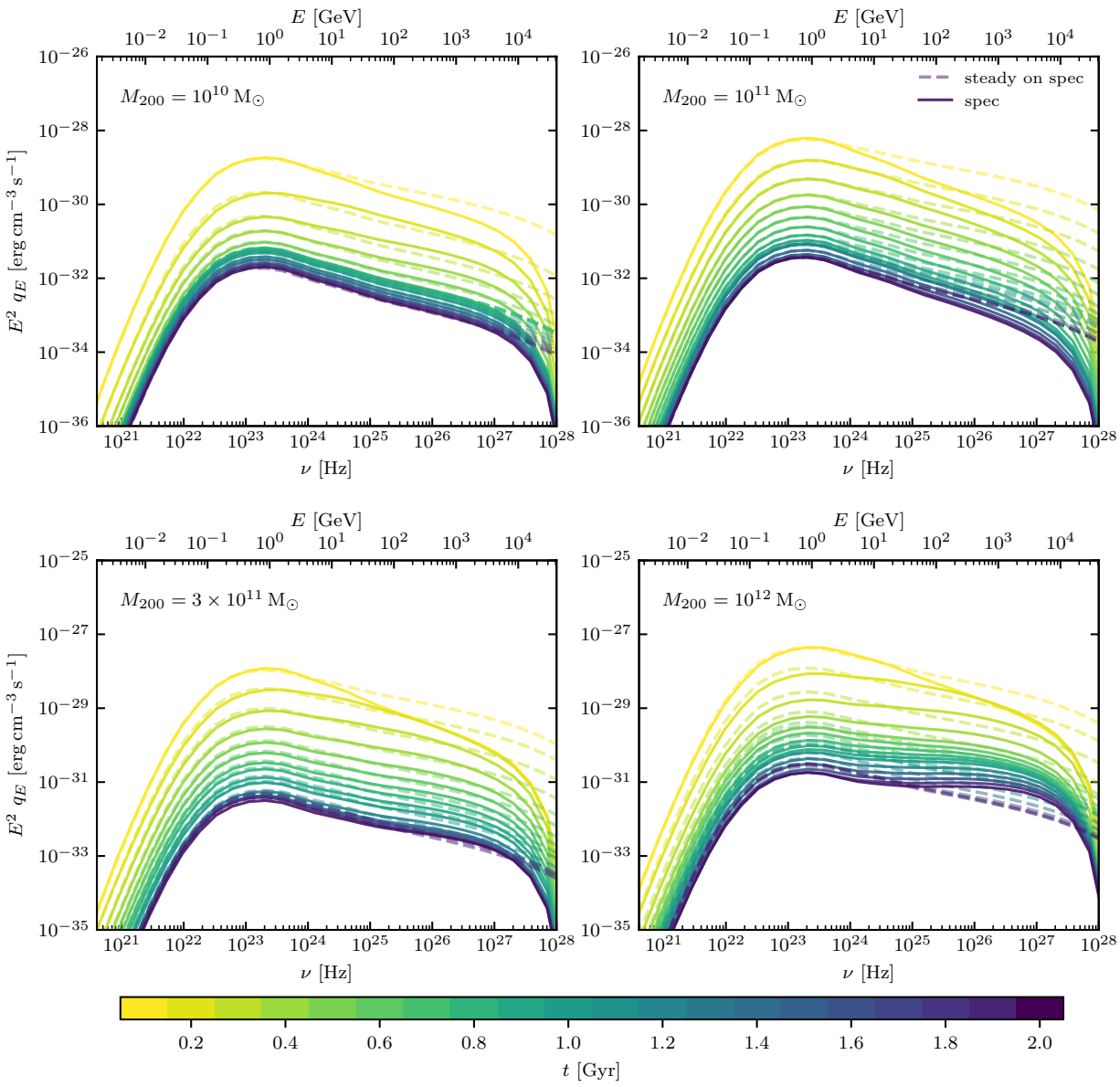

Figure 6.5: Time evolution of the total gamma-ray spectra from neutral pion decay of our simulated galaxies with different halo masses including spectrally resolved CRs (model 'spec', solid lines). In addition, the dashed lines show the resulting emission from the steady-state model applied to the same simulations (model 'steady on spec'). Note that the spacing between the plotted spectra is $\Delta t = 0.1$ Gyr up to 1 Gyr and $\Delta t = 0.2$ Gyr afterwards for better visibility.

ray spectrum of the `M1e12-spec` halo quickly hardens with time and exceeds the corresponding steady-state spectra above $\sim$ 10 GeV already after $\sim$ 0.3 Gyr of evolution.

To understand the reason for the deviations from a steady-state configuration outlined above, we examine the radial contributions to the total gamma-ray spectrum in the following.

Radial contribution to gamma-ray spectra

The effect of explicit energy-dependent diffusion on the CR spectra in the spectrally resolved model (as discussed in Section 6.4.1) is imprinted in the radial contribution to the total gamma-ray spectra and hence varies strongly with halo mass. This is illustrated in Fig. 6.6 where we show the gamma-ray spectra at $t = 1$ Gyr for all halo masses in the 'spec' model (solid lines) in radial bins together with the total spectrum obtained in the 'steady on spec' model (dashed lines). The range of the concentric radial bins is chosen such that at the maximum radius, the CR energy density has decreased by approximately four e-foldings (i.e. we use the same radial bins as in Fig. 6.4).

In the dwarf galaxy `M1e10-spec` we find the total gamma-ray spectrum to be dominated by the central region within $\sim$ 3 kpc, where the spectral shape of the gamma-ray emission is very close to the spectrum from a steady-state configuration. This reflects the agreement we found in the corresponding CR proton spectra in Fig. 6.4 in the central region. Only in the outskirts at larger radii, the gamma-ray spectra are much harder. However, the contribution from those large radii is sub-dominant due to the decreasing gas densities with radius. This is evident from comparing the middle and right-hand panels of the upper row in Fig. 6.4 where we multiplied the averaged CR spectra by the gas density (as discussed in Section 6.3).

However, the situation is very different in the simulation `M1e11-spec`. Here, the high-energy CRs diffuse outwards more quickly than they can be replenished from fresh injection, which means that no steady-state configuration can be achieved and consequently, the total gamma-ray spectrum is steeper than in a steady-state.[1] The outwards diffusing CRs lead to flatter CR proton spectra in the outskirts (see also Fig 6.4). But due to the decreasing gas density in these regions, the gamma-ray emission is too low in normalisation in order to be able to compensate for the very steep central spectra that dominate the total emission.

This is in contrast to the next more massive halo `M3e11-spec`. Here, we first have the same situation that CRs diffuse outwards very quickly which steepens the central CR proton and hence also the central gamma-ray spectrum (see Fig. 6.4 for the CR proton spectra). But here, the flat CR proton spectra in the outskirts arising from the outwards diffused CRs are in a region where

[1]Note, however, that we adopt here for the steady-state modelling the same energy dependence of the diffusion coefficient ($\delta = 0.3$) as in the spectrally resolved run but explore variations of δ in Section 6.5.1.

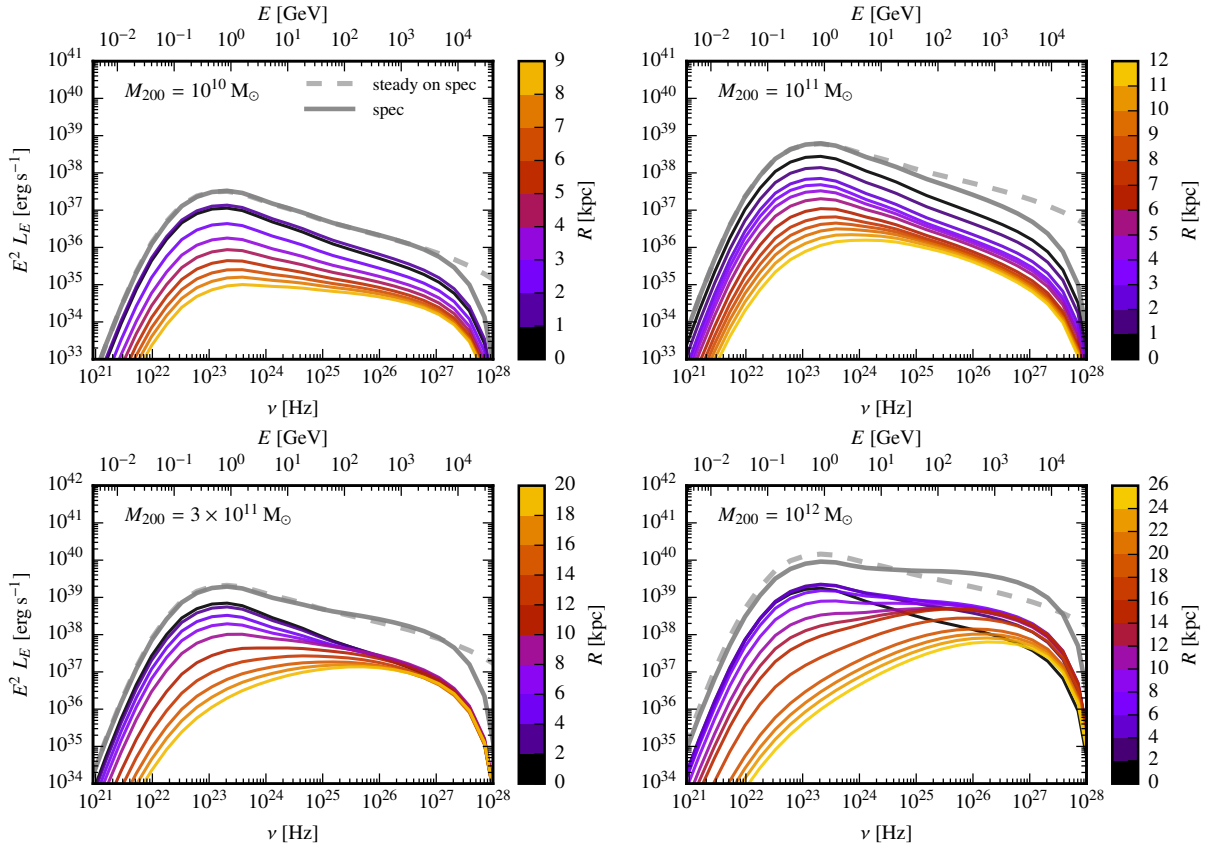

Figure 6.6: Gamma-ray spectra from neutral pion decay at $t = 1$ Gyr for different halo masses. The total gamma-ray spectra from the steady-state CRs (model 'steady on spec', dashed lines) are shown on top of the emission resulting from the spectrally resolved CR simulations (model 'spec', solid grey lines). Additionally, we show the differential contribution to the latter from different radial, concentric bins, where we define a maximum radius such that the CR energy density has decreased by four e-foldings (i.e. the same radial bins as shown in Fig. 6.4).

the gas density seems to be still high enough such that the resulting hard gamma-ray spectra from these regions exhibit a normalisation that is large enough to make a substantial contribution to the total emission. Interestingly, as a consequence, the total gamma-ray spectrum conspires to mimic a steady-state configuration if integrated over the whole galaxy. Only considering the different radial contributions to the total emission spectra reveals the effect of spectrally resolved CR diffusion, which does not resemble the emission from the corresponding steady-state spectra in any radial bin if considered individually.

In the simulation with the most massive halo `M1e12-spec`, the hard gamma-ray spectra from the quickly outwards diffusing high-energy CRs dominate the total spectrum. This leads to a harder total gamma-ray spectrum than expected from steady-state. Also, the gamma-ray spectra in the considered radial bins are in almost all regions harder than in a steady-state with the exception of the very central region ($R < 2$ kpc).

To enable a more detailed comparison of the effect of spectrally resolved CR transport on the spectral shape of the resulting hadronic gamma-ray emission, we will examine their spectral indices in the next section.

6.5 Comparison to observations and the interpretation of δ

6.5.1 Spectral index of gamma-ray emission

We calculate the spectral index of the hadronic gamma-ray spectrum at 5 and 100 GeV, respectively, for all simulated halos at all times and show the result as a function of SFR in Fig. 6.7 (the time of the simulations are indicated by the same colors as in Fig. 6.5). While we see a substantial evolution of the spectral indices at both energies shown for the spectrally resolved CR treatment (filled colored symbols), the steady-state model yields only a slight softening in the spectral index with time (i.e. decreasing SFR) for all halo masses.[2] Interestingly, we see an overall trend of a spectral hardening of α_γ at 5 GeV with increasing SFR in the spectral CR simulations, whereas there is almost no evolution in α_γ at 100 GeV for the small to intermediate halo masses. Only the two most massive halos (`M3e11-spec` and in particular `M1e12-spec`) exhibit a softening of the spectral index with increasing SFR, contrary to the general trend pointed out at 5 GeV. This has also been clearly visible in the temporal evolution (i.e. corresponding to a decreasing SFR with time, after the peak of SF) of the gamma-ray spectra shown in Fig. 6.5.

[2]Note that the steady-state model applied to the grey runs (model 'grey') yields almost identical spectral indices in comparison to the steady-state spectra from the spectrally resolved runs (model 'steady on spec').

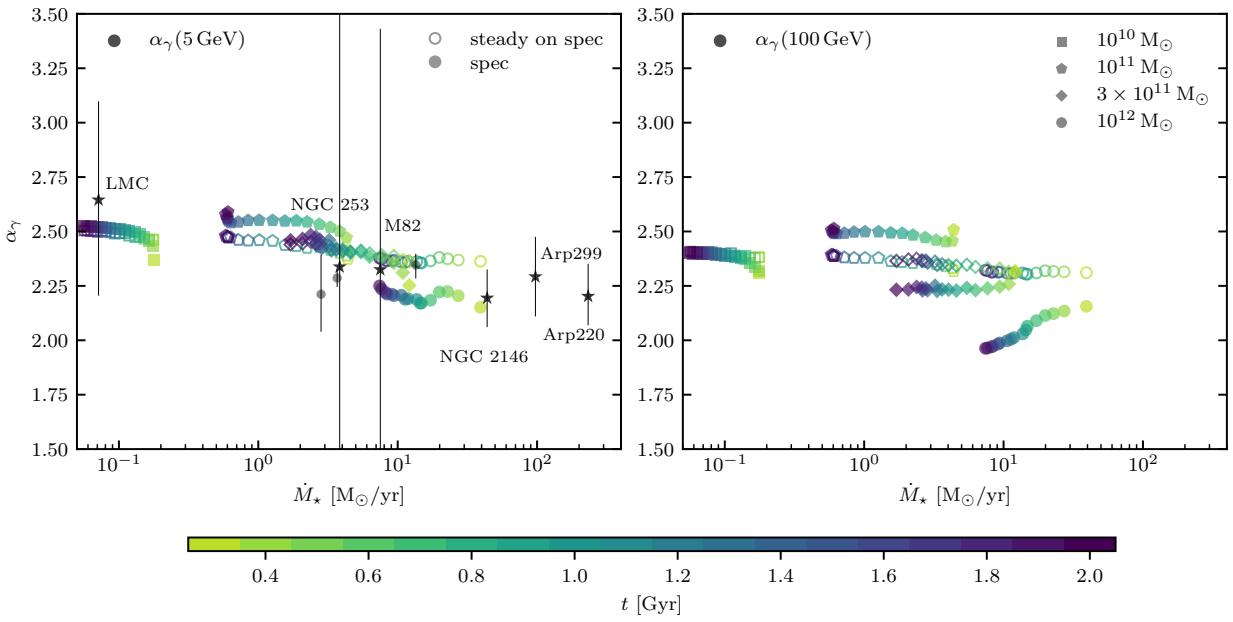

Figure 6.7: We show the spectral indices of the hadronic gamma-ray spectra α_γ at 5 GeV (left-hand panel) and 100 GeV (right-hand panel) of our simulated galaxies, where the colour indicates the time of evolution. The differnt symbols correspond to different halo masses. The left-hand panels additionally show the spectral indices of observed galaxies from Nuñez-Castiñeyra et al. (2022), where we differentiate between purely star-forming galaxies (star symbols) and galaxies with some potential AGN contribution to the gamma-ray emission (grey circles; see text for details). Filled symbols represent the spectral indices calculated from the spectrally resolved CR protons (model 'spec'), while open symbols represent our steady-state model applied to the same simulations (model 'steady on spec').

As a caveat, we note that while at 5 GeV the hadronic gamma-ray emission is expected to dominate over leptonic contribution from IC or bremsstrahlung emission, at 100 GeV we expect a potential contribution from IC emission to the spectrum, which we do not model here. Including this might modify the spectral shapes and dilute the strong variations in the spectral indices that we obtain from neutral pion decay alone. To account for this properly (beyond a steady-state approach as performed in Werhahn et al., 2021b) this requires a careful modelling of the time evolution of CR electron spectra, which goes beyond the scope of this paper and is left to future work.

In addition to our simulations, we show in Fig. 6.7 the spectral indices of a sample of nearby galaxies at 5 GeV from Nuñez-Castiñeyra et al. (2022). They extracted the spectral indices obtained from the most recent gamma-ray data from Fermi LAT, i.e. the DR3 version of the 4FGL catalogue (Fermi-LAT Collaboration et al., 2022).

While the gamma-ray emission from the LMC, NGC 253, M82, NGC 2146, Arp229 and Arp220 is probably dominated by emission resulting from their star-formation activity, we note that some galaxies of the sample have been suspected to exhibit some AGN activity. As pointed out in Ajello et al. (2020, and references therein), the gamma-ray emission from NGC 3424 exceeds the calorimetric limit which could potentially be due to an AGN contribution to the gamma-ray emission. Similarly, the gamma-ray emission from NGC 4945 and NGC 1069 might be partly arising from their central AGN (as discussed in Ajello et al., 2020). Consequently, we mark those galaxies in different symbols (grey circles) in Fig. 6.7. Overall, we find that the differences in the modelling of the CR proton spectra are still smaller than the constraints provided by observations, where the error bars of the sample of star-forming galaxies extend well beyond the differences arising from our various modelling of the CR spectra, i.e. the spectral treatment vs. a steady-state configuration. Only the observed α_γ of NGC 2146 slightly favours the 'spec' model that exhibits a harder spectrum in comparison to the steady-state approach. However, we caution that we expect this to strongly depend on the model choice of α and δ.

The deviations in the shapes of the gamma-ray spectra from spectrally resolved CR transport from a steady-state model suggest a re-interpretation of the energy dependence of the diffusion coefficient in a steady-state model. Thus, in Fig. 6.8 we vary δ in the 'steady on spec' model from 0.2 to 0.5 (the spectrally resolved CR runs have been performed with $\delta = 0.3$). We find that the simulated dwarf galaxy `M1e10-spec` matches a steady-state configuration with the same energy dependence ($\delta = 0.3$) in terms of the spectral shape of the gamma-ray emission both at 5 and 100 GeV, respectively. However, Fig. 6.8 clearly shows that the spectral index of gamma-ray emission from the `M1e11-spec` simulation is more closely represented by a steady-state with a stronger energy dependence (close to $\delta = 0.4$). In contrast, in the case of the most massive halo

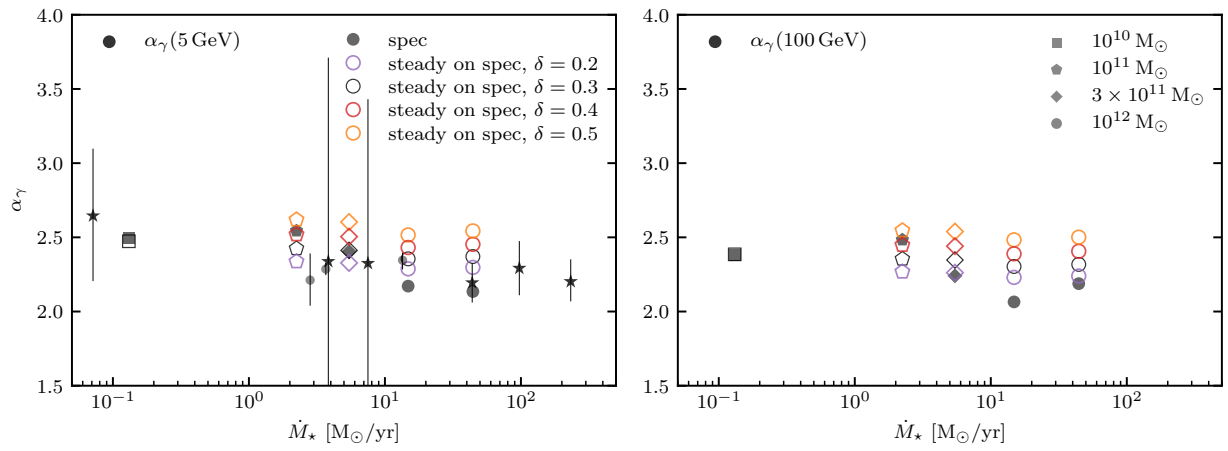

Figure 6.8: Same as Fig. 6.7, but only for a subset of the snapshots of our simulations for simplicity, i.e. snapshots at $t = 0.8$ Gyr and in addition a snapshot of the `M1e12-spec` simulation with a SFR close to NGC 2146. We show the effect of varying the energy dependence of the diffusion coefficient in the steady-state model ('steady on spec'), which we vary from $\delta = 0.2$ to $\delta = 0.5$ (see different colors in the legend) on top of the simulations that adopt explicit energy dependent diffusion with $\delta = 0.3$ (model 'spec').

`M1e12-spec` a shallower energy dependence of diffusion would be needed in order to reproduce the spectral shape of the more sophisticated spectrally resolved CR transport scheme.

Interestingly, the `M3e11-spec` simulation matches the steady-state model with $\delta = 0.3$. However, as discussed in Section 6.4.2, this is only the case if we consider the total emission, while there is no region that would individually resemble the steady-state configuration with the same adopted δ.

The differences are identical for the 5 and 100 GeV spectral indices in the 'steady on spec' model, while the 'spec' model differs slightly between the two energies. In particular, the 'spec' model of the `M3e11-spec` simulation exhibits a flatter spectral index in gamma-ray emission at 100 GeV in comparison to 5 GeV and resembles a steady-state with $\delta = 0.2$.

6.5.2 Gamma-ray spectra of starburst galaxies

Next, we compare our simulated spectra to observed gamma-ray spectra of the star-forming galaxies NGC 2145, M82 and NGC 253 in Figs. 6.9 and 6.10. For all three galaxies, we plot the observations by LAT (Ajello et al., 2020) and additionally include data from H. E. S. S. Collaboration et al. (2018) for NGC 253 and from VERITAS Collaboration et al. (2009) for M82. As summarized in Table 6.2, we chose snapshots from our simulations that lie close to the observed galaxies in terms

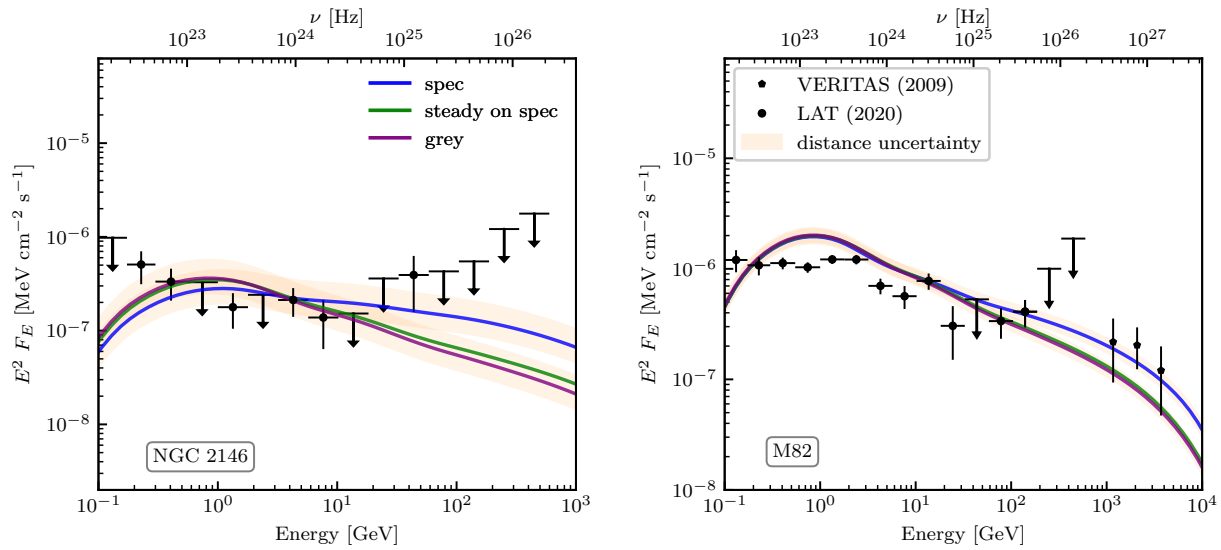

Figure 6.9: Observed gamma-ray spectra of NGC 2146 and M82 (black symbols, as indicated in the legend) together with the gamma-ray spectrum from neutral pion decay calculated from our simulations. For NGC 2146 (left-hand panel), we consider snapshots of the `M1e12-spec` and `M1e12-grey` simulations that are close in observed SFR (Nuñez-Castiñeyra et al., 2022, see Table 6.2). For the `M1e12-spec` simulation, we calculate the emission both from the spectrally resolved CR protons ('spec', blue line) and from our steady-state model applied to the same runs ('steady on spec', green line), while the resulting emission from the grey simulation is shown in purple. We proceed in the same way for M82 (right-hand panel) but for the `M3e11-spec` and `M3e11-grey` simulations, respectively (see Table 6.2). We assume a distance of $d = 18$ Mpc (Adamo et al., 2012) for NGC 2146 (with a distance uncertainty of 20 per cent) and for M82 a distance of $d = 3.53 \pm 0.25$ Mpc (Kourkchi et al., 2020) for calculating the fluxes. To enable a visual comparison we re-scaled the simulated spectra to reproduce the observed gamma-ray luminosities (given in Table 6.2).

Table 6.2: Summary of the starburst galaxies that we compare our simulated spectra to in Figs. 6.9 and 6.10. The SFRs by Kornecki et al. (2020) have been calculated using far UV (Gil de Paz et al., 2007; Cortese et al., 2012) and IRAS 25 µm data (Sanders et al., 2003), whereas Nuñez-Castiñeyra et al. (2022) combine the fluxes recorded in the four IRAS bands taken from the Sanders et al. (2003) and Moshir & et al. (1990) source catalogues. In the column L_γ(`spec`), we present the gamma-ray luminosities integrated from 0.1 to 100 GeV obtained from the 'spec' model as well as from the 'steady on spec' model.

Galaxy	SFR (obs) [$M_\odot$ yr^{-1}]	SFR (`spec`) [$M_\odot$ yr^{-1}]	SFR (`grey`) [$M_\odot$ yr^{-1}]	L_γ (obs) [10^{39}erg s^{-1}]	L_γ (`spec`) [10^{39}erg s^{-1}]	L_γ (`grey`) [10^{39}erg s^{-1}]	spectral simulation `name`, t [Gyr]	grey simulation `name`, t [Gyr]
NGC 2146	14.0 ± 0.5[1]	13.89	14.00	(88.6)[3]	46.35 / 59.20	45.12	`M1e12-spec`, 0.98	`M1e12-grey`, 1.15
	44.2 ± 12.6[2]	44.43	44.06	(86.2 ± 24.7)[2]	198.0 / 259.2	148.7	`M1e12-spec`, 0.27	`M1e12-grey`, 0.30
M82	10.4 ± 1.6[1]	10.40	10.22	(18.5)[3]	28.72 / 40.81	32.64	`M1e12-spec`, 1.48	`M1e12-grey`, 1.58
		10.45	10.43		26.61 / 30.40	34.57	`M3e11-spec`, 0.44	`M3e11-grey`, 0.45
	7.5 ± 0.7[2]	7.51	7.41	(8.80 ± 0.88)[2]	19.31 / 25.04	23.93	`M1e12-spec`, 1.97	`M1e12-grey`, 2.03
		7.51	7.55		16.33 / 18.82	23.76	`M3e11-spec`, 0.61	`M3e11-grey`, 0.61
NGC 253	5.03 ± 0.76[1]	5.07	5.04	(11.6)[3]	9.902 / 11.33	15.48	`M3e11-spec`, 0.84	`M3e11-grey`, 0.83
	3.8 ± 0.4[2]	3.83	3.82	(7.14 ± 0.71)[2]	7.005 / 7.948	11.49	`M3e11-spec`, 1.07	`M3e11-grey`, 1.02

[1] Kornecki et al. (2020).
[2] Nuñez-Castiñeyra et al. (2022)
[3] Ajello et al. (2020)

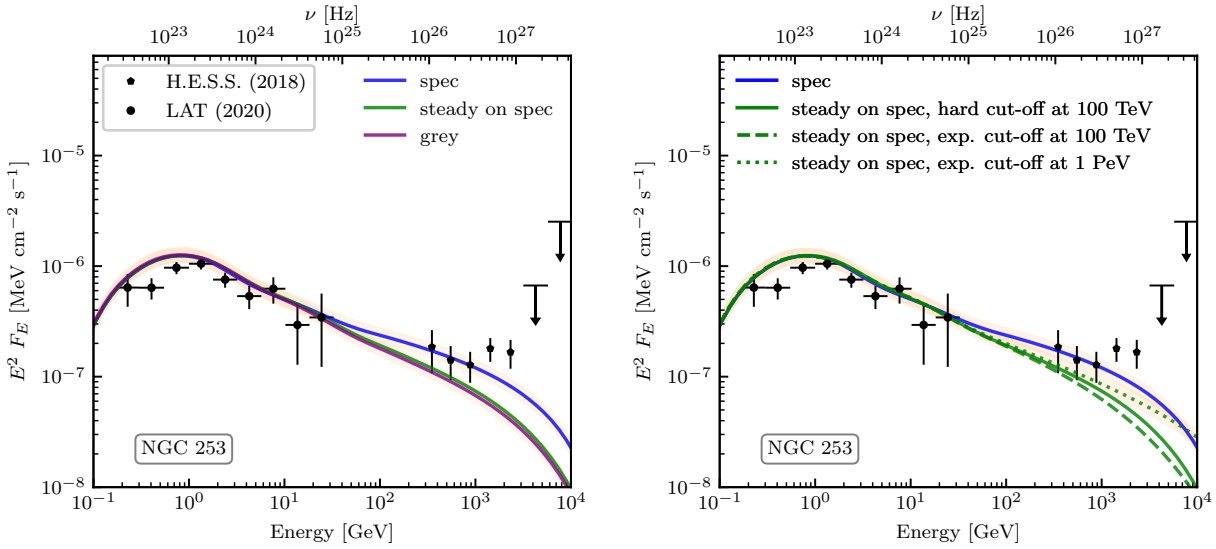

Figure 6.10: Same as Fig. 6.9, but for NGC 253 together with the simulated spectra from snapshots of the `M3e11-spec` and `M3e11-grey` simulations that are chosen such that they have a similar SFR to NGC 253 (Nuñez-Castiñeyra et al., 2022, see Table 6.2). The right-hand panel shows the model 'steady on spec' for different cut-offs in the injected CR proton spectrum.

of their SFRs, where we both consider the values from Kornecki et al. (2020) and Nuñez-Castiñeyra et al. (2022), respectively. We analyse the spectrally resolved CR and the grey simulations. For the former, we additionally calculate the emission from the 'steady on spec' model. In all considered cases, we obtain total gamma-ray luminosities (integrated from 0.1 to 100 GeV) that deviate at most a factor of three from the observed values (see Table 6.2).

We re-scale the simulated gamma-ray spectra to the observed total luminosities in order to enable a direct comparison with the data in Figs. 6.9 and 6.10. Here, we chose the snapshots from Table 6.2 that resemble the SFRs cited in Nuñez-Castiñeyra et al. (2022). For NGC 2146, we under-predict the observations in the sub-GeV regime. This could potentially be due to our lack in modelling of a potential contribution from non-thermal bremsstrahlung emission (see Werhahn et al., 2021b). However, we obtain an excellent agreement of our spectrally resolved CR simulation with the observed spectrum of NGC 253 (left-hand panel of Fig. 6.10), while the steady-state model (both applied to the spectral and grey runs) is softer towards the TeV regime. Similarly, the spectrum of M82 is almost perfectly reproduced from our spectrally resolved CR proton simulation `M3e11-spec` (right-hand panel of Fig. 6.9), where again the steady-state spectra are softer at high gamma-ray energies. However, we find that the observed spectrum of M82 is only matched with our `M3e11-spec` simulation but not with a corresponding snapshot of the more massive halo `M1e12-spec` where the simulated galaxy exhibits a hard spectrum above ~ 10 GeV in contradiction to the data. An estimation of the stellar mass of M82 via the relation obtained from Cappellari (2013) (which assumes that the dynamical mass within the observed region is $\approx M_\star$) by means of the K-band apparent magnitude $m_K = 4.665$ (Skrutskie et al., 2006) and a distance of 3.5 Mpc (3.7 Mpc) yields a stellar mass of $M_\star \approx 4.1 \times 10^{10}\,\mathrm{M}_\odot$ ($4.5 \times 10^{10}\,\mathrm{M}_\odot$) and a halo mass of $\approx 1.4 \times 10^{12}\,\mathrm{M}_\odot$ ($1.6 \times 10^{12}\,\mathrm{M}_\odot$), where we used the relation by Moster et al. (2010). However, Greco et al. (2012) estimate the dynamical mass of M82 (out to a radius of 4 kpc) to be only $\approx 10^{10}\,\mathrm{M}_\odot$. If one assumes this to be an estimate for the stellar mass, this would imply a much smaller halo mass of $\approx 4.5 \times 10^{11}\,\mathrm{M}_\odot$.

In this section, we used for the source function in the 'steady on spec' and the 'grey' models underlying the calculation of the gamma-ray emission a hard-cutoff in momentum space at 100 TeV to be consistent with the spectrally resolved method. Therefore, in the right-hand panel of Fig. 6.10 we examine the effect of different cut-off momenta and shapes of the injected spectrum of CR protons on the resulting gamma-ray emission spectrum. This is important because the novel spectrally resolved scheme is computationally expensive and hence only allows for a limited number of momentum bins that are chosen to range from 100 MeV c^{-1} to 100 TeV c^{-1}. To assess the robustness of the thereby introduced hard cut-off in momentum space, we consider two different

functional forms of the source function for CR protons as a toy model in our steady-state approach. In addition to the exponential cut-off with $q(p) \propto p^{-\alpha_{\rm inj}} \exp(-p/p_{\rm cut})$ (see Eq. 6.6), we now also calculate the spectra by assuming a hard cut-off where $q(p) \propto p^{-\alpha_{\rm inj}} \theta(p_{\rm cut} - p)$, with the Heaviside step function $\theta(p)$.

Clearly, the shape of the cut-off (either exponential or hard) only has a minor effect on the resulting gamma-ray spectrum if the same cut-off momentum $p_{\rm cut} = 100$ TeV c^{-1} is assumed. However, the choice of a higher proton cut-off momentum at $p_{\rm cut} = 1$ PeV c^{-1} leads to a harder gamma-ray spectrum that starts to deviate at gamma-ray energies $\gtrsim$ TeV from the spectrum we obtained from adopting $p_{\rm cut} = 100$ TeV c^{-1}. Hence, the gamma-ray spectrum of the spectrally resolved model with a hard proton momentum cut-off at 100 TeV c^{-1} is robust for calculating gamma-ray emission up to $\sim$ TeV energies, whereas the artificial cut-off in momentum space softens the spectrum at higher gamma-ray energies. Therefore, we anticipate that including further momentum bins above 100 TeV c^{-1} in the proton spectra of our spectrally resolved simulations would potentially slightly harden the resulting gamma-ray spectra above TeV energies.

However, the gamma-ray spectrum of extreme starbursts like Arp 220 has been suggested to soften above TeV energies because of pair production from the interaction of gamma-rays with infrared photons from the intense radiation field in the nucleus (Torres, 2004; Yoast-Hull et al., 2015; Peretti et al., 2019). Therefore, for a detailed modelling of very high-energy emission above a few TeV energies within such extreme environments, this effect should additionally be taken into account.

6.5.3 The FIR-gamma-ray relation

Finally, we compare the gamma-ray luminosities from neutral pion decay of all our simulated galaxies, which we obtain from Eq. (6.8), to observed data integrated over different energy bands in Fig. 6.11.

Observational data

Ajello et al. (2020) analysed 10 years of Fermi LAT data in the energy band from 0.1 – 100 GeV, while more recent work by Nuñez-Castiñeyra et al. (2022) extracted gamma-ray luminosities in the 0.5 – 50 GeV band from 12 years of observations with Fermi LAT. The energy range of the latter is chosen to reduce potential leptonic contributions to the gamma-ray emission, i.e. from bremsstrahlung and IC emission from CR electrons at low and high gamma-ray energies, respectively. Besides the different energy integration ranges and data collection time, both data sets

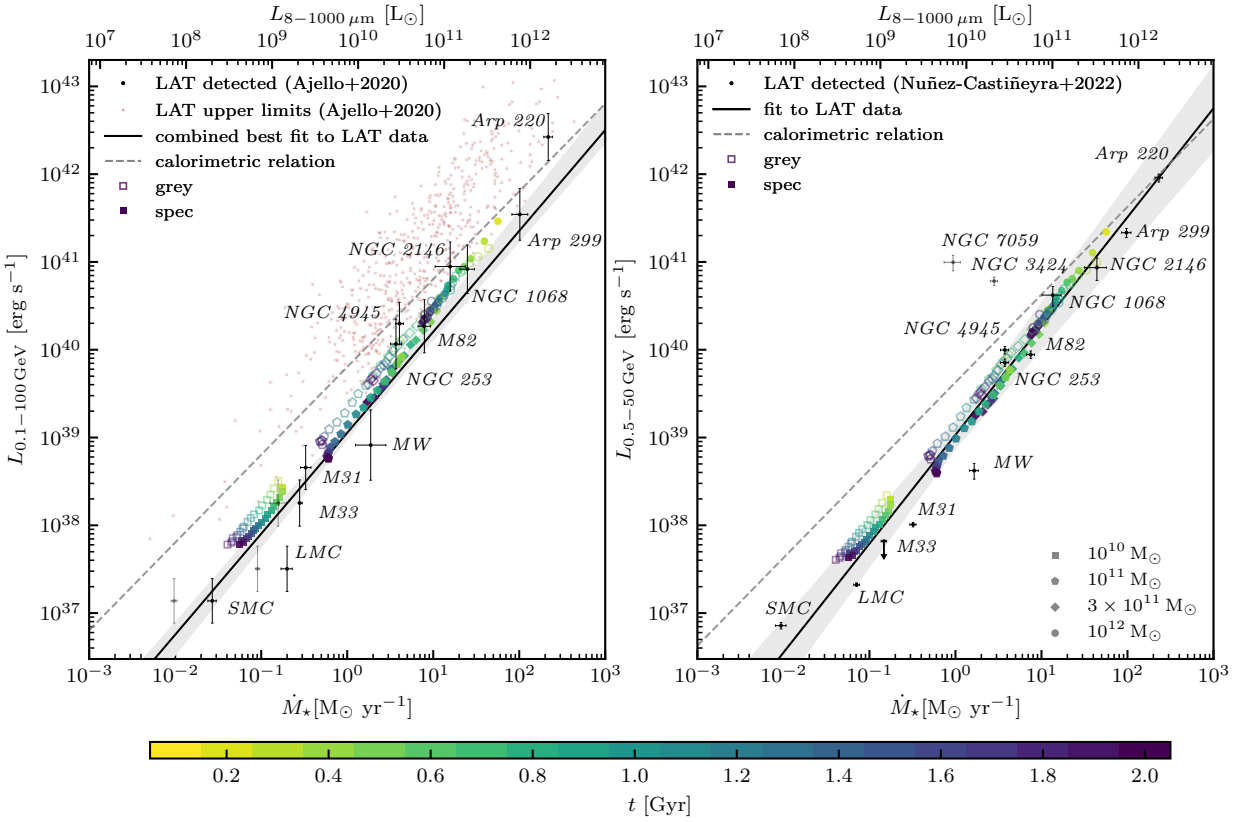

Figure 6.11: Relation between the SFR and gamma-ray luminosity in different energy bands. The left-hand panel shows $L_{0.1-100\,\mathrm{GeV}}$ from neutral pion decay of our simulated galaxies (coloured symbols) together with the LAT data from Ajello et al. (2020), whereas the right-hand panel shows the luminosities for a narrower energy band $L_{0.5-50\,\mathrm{GeV}}$ in order to compare it to more recent LAT observations from Nuñez-Castiñeyra et al. (2022). We show the luminosities from the 'grey' (open coloured symbols) and 'spec' model (filled coloured symbols) for all simulated halo masses (see the corresponding symbols in the legend) that are colour-coded by the time of the snapshot, starting from the peak of SFR in time intervals of 0.1 Gyr, respectively. From the snapshot with the highest SFR, we normalise the calorimetric relation (dashed line) via $L_{E_1-E_2}/\eta_{\mathrm{cal,p}}$ for $[E_1, E_2] = [0.1, 100]$ GeV and $[0.5, 50]$ GeV, respectively, where $\eta_{\mathrm{cal,p}}$ is calculated from equations (9) and (10) of Werhahn et al. (2021b) (corresponding to Eqs. 4.9 and 4.10 in this work).

use different distances in some cases and the inferred FIR-luminosities and SFRs deviate for some of the observed galaxies. Therefore, we compare our simulations to both approaches separately in Fig. 6.11. Because Ajello et al. (2020) only analyse the relation between the FIR and gamma-ray luminosities of their sample of star-forming galaxies, while we plot the gamma-ray luminosities against the SFRs of our simulated galaxies, we convert the observed FIR luminosities to SFRs via the Kennicutt (1998) relation. For low-SFR galaxies like the SMC, the LMC and M33, this relation is expected to break down (as discussed in Kornecki et al., 2020). Therefore, we additionally show their SFRs as obtained separately by Thirlwall et al. (2020) for M33 ($0.28^{+0.02}_{-0.01}\,\mathrm{M_\odot yr^{-1}}$) and by Kornecki et al. (2020) for the LMC ($0.20 \pm 0.03\,\mathrm{M_\odot yr^{-1}}$) and the SMC ($0.027 \pm 0.003\,\mathrm{M_\odot yr^{-1}}$) in the left-hand panel of Fig. 6.11. Nuñez-Castiñeyra et al. (2022) provide a fit to the SFR-gamma-ray relation (right-hand panel of Fig. 6.11) where they derive the SFRs of their sample also via the Kennicutt (1998) relation. Therefore, the same uncertainties hold here for the SMC, LMC and M33. They derive their fit to the data from all observed galaxies but excluding NGC 7059 whose association with the observed LAT source has been doubted (Nuñez-Castiñeyra et al., 2022). We note that Ajello et al. (2020) additionally exclude NGC 3424 from their bonafide sample because it has been claimed to host an AGN (Gavazzi et al., 2011) and shows some evidence of variability (Peng et al., 2019).

Simulated gamma-ray to SFR relation

In addition to the observational data, we present in Fig. 6.11 our simulated gamma-ray luminosities versus the SFRs of our simulated galaxies. We show all snapshots with a time difference of $\Delta t = 0.1$ Gyr for all halo masses of both the spectral and grey simulations (filled and open symbols, respectively). While we slightly overestimate the gamma-ray luminosities $L_{0.1-100\,\mathrm{GeV}}$ in comparison to the LAT data from Ajello et al. (2020), we obtain an excellent agreement with the observed luminosities $L_{0.5-50\,\mathrm{GeV}}$ by Nuñez-Castiñeyra et al. (2022). In both cases, we find that the 'spec' model exhibits almost identical luminosities to the 'grey' model at high SFRs, while it deviates towards lower gamma-ray luminosities with decreasing SFRs and halo masses. However, the differences are small in comparison to the observed scatter in the relation. We note that we adopt an acceleration efficiency of CRs at SNRs of $\zeta_{\mathrm{SN}} = 0.10$, while Werhahn et al. (2021b) previously found that an injection efficiency of $\zeta_{\mathrm{SN}} = 0.05$ in their grey simulations better reproduces the observed relation from Ajello et al. (2020). But in their approach, they model in addition to CR protons the steady-state spectra of CR electrons and calculate their resulting bremsstrahlung and IC emission. The contribution of neutral pion decay to the total gamma-ray luminosity $L_{0.1-100\,\mathrm{GeV}}$ in Werhahn et al. (2021b) is around 60 per cent at $\dot{M}_\star \gtrsim 1\,\mathrm{M_\odot yr^{-1}}$ and decreases to ~40 per

cent at $\dot{M}_\star \sim 10^{-2}$ $M_\odot yr^{-1}$. The choice of a narrower energy band of 0.5-50 GeV is expected to reduce the leptonic contribution further. Nevertheless, we conclude that our hadronic gamma-ray luminosities in both the 'grey' and 'spec' models are probably uncertain by roughly a factor of two due to the choice of $\zeta_{SN} = 0.10$ and the lack of accounting for leptonic gamma-ray emission in this work. However, both uncertainties have an opposite effect on the gamma-ray luminosities and hence might approximately cancel each other.

We furthermore analyse the calorimetric relation in comparison to the observed and simulated FIR-gamma-ray relations in Fig. 6.11. This relation is supposed to represent the limit where CR protons would lose all of their energy due to neutral pion decay. In order to estimate the normalisation of the calorimetric relation from our simulations, we calculate the calorimetric fraction $\eta_{cal,p}$ from the snapshot with the highest SFR according to equations (9) and (10) of Werhahn et al. (2021b) (i.e. Eqs. 4.9 and 4.10 in this work). This definition takes into account that only a fraction of the CR proton population is able to produce gamma-rays in the considered energy range, denoted as the bolometric energy fraction ζ_{bol}. While they found for the range 0.1 – 100 GeV $\zeta_{bol} \approx 0.6$, we find $\zeta_{bol} \approx 0.4$ in the energy range 0.5 – 50 GeV. This results in a calorimetric fraction of our snapshot with the highest SFR and gamma-ray luminosity in the 'spec' model of $\eta_{cal,p} = 0.81$ ($\eta_{cal,p} = 0.92$) for the energy band 0.1 – 100 GeV (0.5 – 50 GeV), suggesting that the energy range 0.1 – 100 GeV of emitted gamma-ray photons is less calorimetric than the narrower band. This is because the broader band up to 100 GeV traces higher energetic CR protons which are more affected by diffusive losses.

For both relations, we find that consistent with the observed data, highly SF galaxies are close to the calorimetric relation, whereas the luminosities deviate from the relation for galaxies with decreasing SFRs. This has also been found in previous work (Thompson et al., 2007; Lacki et al., 2011; Ackermann et al., 2012b; Martin, 2014; Pfrommer et al., 2017b; Kornecki et al., 2020; Werhahn et al., 2021b).

6.6 Discussion and conclusion

In this work, we study observational signatures of the gamma-ray emission from neutral pion decay resulting from spectrally resolved CR MHD simulations of isolated galaxies. To this end, we perform simulations using the moving-mesh code Arepo of isolated galaxies with halo masses ranging from 10^{10} to 10^{12} $M_\odot$ where we include a novel extension of the code that accounts for spectrally resolved CR transport (Girichidis et al., 2020b, 2022). Instead of only following the evolution of the momentum-integrated energy density as adopted in the grey approximation, this

method represents the CR distribution function by a piece-wise power law in momentum space in every computational cell and allows for energy-dependent diffusion.

To identify the observational signatures of this novel treatment, we compare the hadronic gamma-ray emission predicted by the spectrally resolved simulations (model 'spec') with that predicted by a steady-state model applied to the same simulations (model 'steady on spec') and on simulations using the grey approximation (model 'grey'). For the latter, only the CR energy density is evolved within the simulations which has a moderate effect on the SFR and dynamics of the system (Girichidis et al. in prep.). This leads to a minor variation in the spatially resolved spectra and gamma-ray emission resulting from our 'grey' and 'steady on spec' models (see Fig. 6.1). These models are, however, almost identical when averaged over the whole disk (see Fig. 6.3). We therefore focus on the differences between our 'steady on spec' and 'spec' models in our conclusions. We find that:

- The spatial distribution of the total gamma-ray luminosity is almost identical in the 'steady on spec' and 'spec' models. However, the distribution of the specific luminosities at various energy bands is significantly different (see Figs. 6.1 and 6.2). In particular, due to the explicit modelling of spectrally resolved CR transport, high-energy CRs diffuse faster into the outskirts of the disk and hence, the radial distribution of the high-energy gamma-ray emission is much more extended in the 'spec' model compared to the steady-state approach.

- While in the central regions of the simulated galaxies the 'spec' model yields steeper CR spectra at all halo masses in comparison to the corresponding 'steady on spec' model, outwards diffusing high-energy CRs lead to much flatter spectra in the outskirts of the galaxy (see Fig. 6.4). In the most extreme case of our largest simulated galaxy (with a halo mass of $10^{12}\,\mathrm{M}_\odot$), the CR spectra in the outskirts rise as a function of P in the 'spec' model above $\sim$ 1 GeV, whilst the spectral slope is negative for the steady-state model. But due to varying gas distributions in the different galaxies, these hard CR spectra at large radii only contribute to the gamma-ray emission in the 'spec' model of the two most massive halos, i.e. the `M3e11-spec` and `M1e12-spec` simulations, respectively. In the former, the combination of steep central and flat outer spectra coincide to closely resemble the total gamma-ray spectra of the corresponding 'steady on spec' model, whereas in the most massive halo, the 'spec' model yields much harder gamma-ray spectra already after short times of evolution (see Figs. 6.5 and 6.6).

- Overall, we find a good agreement between the spectral indices of gamma-ray emission α_γ at 5 GeV of the different models with the observed data of nearby star-forming galaxies

within the observational errors (see Fig. 6.7). This implies that the observations are not yet constraining enough to discriminate between our different modelling of the CR spectra.

- Furthermore, we find that the shape of the gamma-ray emission (i.e. the spectral index α_γ) from the 'spec' model at a fixed energy can be represented by a steady-state configuration if one allows for a variation in the energy dependence of the diffusion coefficient δ (see Fig. 6.8). For example, the `M1e11-spec` simulation with $\delta = 0.3$ can be reproduced globally by adopting a steady-state model with a stronger energy dependence of ~ 0.4, whereas the spectral shapes of the total gamma-ray emission of the `M1e12-spec` simulation requires $\delta < 0.2$ in the 'steady on spec' model to reproduce the results from the 'spec' model.

- The total gamma-ray spectra of the star-forming galaxy NGC 2146 is largely consistent with the hadronic emission from our 'spec' model. Moreover, the observed spectra of NGC 253 and M82 are in excellent agreement with our 'spec' model, while the 'steady on spec' and 'grey' models exhibit softer spectra at TeV energies than suggested by the observed data (see Fig. 6.9 and 6.10).

- In the FIR-gamma-ray relation (Fig. 6.11), we find that the 'spec' model yields similar gamma-ray luminosities to the 'grey' model at high SFRs but smaller values at SFRs $\lesssim 10\,\mathrm{M_\odot yr^{-1}}$. The relation obtained from the 'spec' model coincides particularly well with the most recent observations by Fermi LAT of the gamma-ray luminosities $L_{0.5-50\ \mathrm{GeV}}$ of nearby star-forming galaxies (Nuñez-Castiñeyra et al., 2022).

We caution, however, that we do not include leptonic contributions to the gamma-ray emission in this work. Including non-thermal bremsstrahlung and IC emission might flatten the gamma-ray spectra below the pion decay bump but their contribution has been found to be subdominant for the total emission of star-forming galaxies (e.g. Domingo-Santamaría & Torres, 2005; Thompson et al., 2007; Persic et al., 2008; de Cea del Pozo et al., 2009; Paglione & Abrahams, 2012; Yoast-Hull et al., 2013) and in the Milky Way up to energies of $\sim$ 10 GeV (Strong et al., 2010). In contrast, IC emission might become more relevant at higher energies, in particular in galaxies with smaller SFRs like the SMC (Werhahn et al., 2021b). We leave the analysis of this parameter space to future studies. An accurate modelling of the CR electron population beyond the steady-state modelling is needed to account for a detailed calculation of bremsstrahlung and IC emission, the latter being particularly sensitive to the high-energy shape of the CR electron spectrum. We postpone the modelling of live CR electron spectra to future work with the CREST code (Winner et al., 2019). Coupling this to the non-thermal emission code CRAYON+, described in Werhahn

et al. (2021a,b,c) will enable a detailed calculation of the leptonic contribution to the gamma-ray emission of star-forming galaxies.

Another caveat of this work is the fixed value of the energy dependence of the diffusion coefficient δ, which we chose to be 0.3 in all spectrally resolved simulations analysed here. Variations may be particularly required for a proper comparison to observations from the Milky Way, where the detected ratios of beryllium isotopes suggest $\delta = 0.5$ (Evoli et al., 2020b). We aim to explore a variation of δ in the 'spec' model in future work. This will additionally require running the simulation with a Milky Way-like halo mass to much later times where the SFR has sufficiently decreased to the observed value of $1.7\,\mathrm{M}_\odot\mathrm{yr}^{-1}$ (Chomiuk & Povich, 2011).

Furthermore, it is worthwhile to mention another caveat of the macroscopic picture of CR transport at hand, where the energy equation for CRs is coupled to the MHD equations and where CR diffusion is modelled by means of a constant diffusion coefficient that is not directly coupled to the physics of turbulence. It has been previously shown that the excitation of turbulence by the streaming instability has a non-linear effect on the escape and confinement of CRs in the region around their sources (see e.g., Bell, 2004; Bell et al., 2013; Marcowith et al., 2021, and references therein). This self-excited magnetic turbulence can reduce the diffusion coefficient which is particularly important in the vicinity of CR sources (Reville et al., 2008; Schroer et al., 2021; Recchia et al., 2022), but this depends on the properties of the ISM surrounding the source (Reville et al., 2007; Nava et al., 2016, 2019; Reville et al., 2021). Additionally, it can also impact the phase-space structure of star-forming regions so that it prevents local fragmentation even in cases when the disk is unstable and maintains a regular grand-design spiral structure (Semenov et al., 2021). Consequently, a further improvement in our modelling could be achieved by adopting a refined model of CR transport in the two-moment approach that accounts for a temporarily and spatially varying diffusion coefficient in the self-confinement picture (Thomas & Pfrommer, 2019; Thomas et al., 2021; Thomas & Pfrommer, 2022). This could potentially transform the morphology of our high-energy emission maps at ~ 100 GeV to become more source dominated.

To summarise, we conclude that the steady-state approach is a good approximation to calculate the gamma-ray emission from star-forming galaxies if, and only if, analysed globally. For each halo mass and stage of temporal evolution there exists a mapping of the parameters that are needed to closely resemble the total emission spectra of the spectrally resolved treatment with a steady-state approach at a fixed energy. Additionally, this mapping only slightly varies with energy. However, the spatial distribution of the gamma-ray emission at various energies is significantly different when modelling the energy dependent diffusion of CRs explicitly. Hence, we conclude that accounting for spectrally resolved CR transport is essential for an accurate prediction of the spatial distribution of

high-energy hadronic gamma-ray emission of star-forming galaxies, which will be highly relevant for future observations with the future Cherenkov Telescope Array observatory.

7. Further applications

The code developed in this work has been applied to various astrophysical studies. Besides the first-author publications presented in the Chapters 3, 4 and 5, as well as the paper draft presented in Chapter 6, it has been of use for other studies, which are summarized in the following.

7.1 Modelling of the multi-frequency emission of SNRs

The creation of CRs via diffusive shock acceleration (as discussed in section 2.1) can be directly probed by observations of the non-thermal emission processes that arise from the freshly accelerated CR population at SNRs. These enable direct constraints on theoretical models of obliquity-dependent shock acceleration, the magnetic field strength and configuration as well as the injection efficiency of CRs at shocks.

Pais et al. (2020) modelled the TeV gamma-ray emission from the two SNRs Vela Jr and SN1006 in order to constrain the magnetic coherence scale of the ISM. To this end, Pais et al. (2020) performed MHD simulations of the Sedov-Taylor phase of a SNR with the moving-mesh code Arepo. For both Vela Jr and SN1006, they injected energy into a periodic box containing 200^3 Voronoi cells. This consequently drives the expansion of a spherically symmetric strong shock where CR protons get injected into the downstream (Pfrommer et al., 2017a) and where the acceleration efficiency is assumed to be dependent on the obliquity of the shock. Consequently, CRs are advected with the gas and cool adiabatically. They vary the morphology of the magnetic field within the box from a homogeneous to a turbulent distribution in order to test the effect of different magnetic field configurations on the morphology of the resulting gamma-ray emission.

Furthermore, in order to shed light on the origin of the observed gamma-ray spectra of both SNRs within a one-zone model, I provided my code Crayon+ for the calculation of the multi-frequency emission from CRs ranging from the radio to the high-energy gamma-ray regime by accounting for synchrotron, IC and gamma-ray emission from neutral pion decay. The first author,

Matteo Pais, then applied this code to the integrated CR proton and electron population of the simulations while varying the electron-to-proton ratio $K_{\rm ep}$ at 10 GeV from 10^{-2} to 10^{-3}. For IC scattering, the ambient radiation field was assumed to consist of the CMB for SN1006, while for Vela Jr an additional stellar contribution with an energy density of $5 \times u_{\rm CMB}$ was assumed to mimic the location of Vela Jr within a star-forming region. The resulting multi-frequency spectra (see Fig. 1 of Pais et al., 2020) show that both the hadronic and the mixed hadronic/leptonic models provide a viable explanation for the observed gamma-ray spectra in both considered SNRs, depending on the assumed electron-to-proton ratio of the underlying CR population.

In order to allow for a more realistic and detailed modelling of the CR electron population, in comparison to the one-zone model by Pais et al. (2020) where CR electrons are simply attached to CR protons that are evolved within the MHD simulations, Winner et al. (2020) performed 3D MHD simulations of SN1006 while additionally following the temporal evolution of CR electrons. In order to obtain a spatially and temporally resolved representation of the CR electron spectrum, the CREST code (Cosmic Ray Electron Spectra that are evolved in Time; Winner et al., 2019) solves the Fokker-Planck equation on Lagrangian tracer particles that are passively evolved within the MHD simulation while tracking all relevant physical quantities that are needed for evolving the spectra in post-processing. To mimic Fermi-I acceleration, a power-law spectrum is injected at shocks where a fraction of the dissipated energy is attributed to CR electrons. They consequently cool via adiabtic and Coulomb losses as well as radiative losses due to synchrotron, IC and bremsstrahlung emission. Furthermore, Winner et al. (2020) investigate the effect of obliquity-dependent acceleration of CR electrons on the morphology of the resulting non-thermal emission. This is enabled by the wealth of observational data of SN1006 in radio, X-ray and gamma-ray wavebands.

For the calculation of all relevant emission processes from the simulated CR electron spectra by CREST, my non-thermal radiation code CRAYON+ was adjusted by the main author Georg Winner to read in the electron spectra calculated with CREST. This facilitated the production of detailed maps and radial emission profiles of the simulated emission in different wavebands as well as the multi-frequency spectrum of SN1006. From the CREST CR electron spectra, the synchrotron, bremsstrahlung and IC emission was calculated with my code in addition to the hadronic emission resulting from the CR population whose energy density is evolved consistently within the MHD simulation and is assumed to be represented by a power-law in momentum.

By comparing the morphologies of the emission maps from the simulated SNR with the observed maps, Winner et al. (2020) conclude that quasi-parallel shock acceleration of CR electrons is required, in contrast to quasi-perpendicular shock acceleration that fails to reproduce all observations simultaneously. Furthermore, Winner et al. (2020) find that the multi-frequency spectrum of

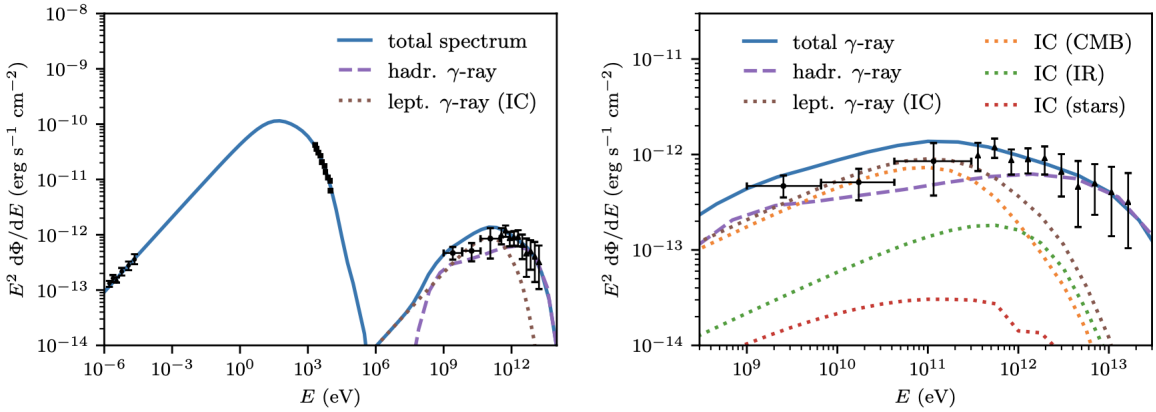

Figure 7.1: Multi-frequency spectrum of SN1006 as shown in Fig. 3 of Winner et al. (2020). The observations (black data points) are best fit with a mixed hadronic-leptonic model. The gamma-ray spectrum (right-hand panel) is dominated by leptonic IC emission up to ∼100 GeV, whereas hadronic emission from neutral pion decay is responsible for gamma-ray emission at higher energies.

SN1006 is matched in a mixed leptonic-hadronic model, where both, IC scattering of CR electrons off of an ambient radiation field as well as hadronic gamma-ray emission from neutral pion decay contribute to the observed GeV to TeV spectrum (see Fig. 7.1). The radial emission profiles are reproduced in their best fit model while assuming a volume-filling, turbulently amplified magnetic field.

7.2 Missing gamma-ray halos

By interacting with the intergalactic infrared background, TeV photons from AGN jets produce electron-positron pairs that can then Compton-up-scatter CMB photons into the 1-100 GeV regime. Since there has not been found any evidence of forward-beamed GeV emission from blazars, a lower limit on the intergalactic magnetic field (IGMF) of $> 3 \times 10^{-13}$ G has been proposed that would lead to the deflection of the produced electrons and positrons out of the line of sight. However, no extended emission around neither individual nor stacked gamma-ray observations of blazars has been found either. While blazars are AGN with their jets pointed towards the observer, the jets of oblique AGN are offset from the line of sight and hence, the predicted IC halos due to the presence of an IGMF should be detected with a high significance. To test this prediction, Broderick et al. (2018) select radio jet sources and align them according to the orientation of their

jets. Consequently, they stack the correspondingly oriented *Fermi* observations. By doing so, no extended gamma-ray halos are detected placing an upper limit on the IGMF strength of $< 10^{-15}$ G. Hence, Broderick et al. (2018) raise the question of an additional physical process that either leads to the suppression of very high-energy gamma-ray emission from blazars (i.e. above 100 GeV) before the electron-positron pairs are produced or that interferes with the IC cooling of the pairs.

In order to investigate the possibility that lack of the high-energy IC emission is due to the Klein-Nishina suppression of the Compton cross section, I provided my non-thermal radiation code CRAYON+ to calculate the IC emission including this effect (see Eq. 2.73 and 2.74). I calculated the emitted spectrum for various black-body radiation fields that serve as seed photons for IC scattering of an electron population with a distribution that is $\propto E^{-2.1}$, including the Klein-Nishina cross section. This implies that provided the energy of the scattered photon in the electron's rest frame is larger than the electron's rest mass energy, i.e. $\gamma_e h\nu_{\rm init} \gtrsim m_e c^2$, the cross section is severely suppressed. Assuming an incident photon of energy $E_{\rm init}$ =1 eV, this applies to electrons with $\gamma_e \gtrsim 5 \times 10^5$, i.e. energies of $\gtrsim$ 250 GeV and hence, only affects up-scattered photons with energies of $E_\gamma \approx 500$ GeV (where the maximum energy of the up-scattered photon was estimated to be $2\gamma_e^2 E_{\rm init}$). In general, the suppression of the IC cross section occurs if $E_\gamma E_{\rm init} \approx 2m_e^2c^4$ and consequently at an energy $E_\gamma \approx 500(E_{\rm init}/1{\rm eV})^{-1}$ GeV. However, we find that the shape of the emitted IC spectrum only slowly roles over in a sub-exponential way that can be fitted with a function $\propto E_\gamma^b \exp\left[-(E/E_c)^{0.25}\right]$ (see the dashed line in Fig. 7.2), where $b = 1 - (\alpha_e - 1)/2 = 0.45$ and where $\alpha_e = 2.1$ corresponds to the electron spectral index. Adopting a black-body distribution with $h\nu_{\rm peak} = 5$ eV gives $E_c = 2$ GeV (see Broderick et al. (2018)). This critical energy becomes higher for seed photon distributions that peak at lower energies, as shown in Fig. 7.2, above which it starts to decline only sub-exponentially. Thus, we conclude that the Klein-Nishina suppression of the Thomson cross section does not offer an alternative explanation for the absence of the expected IC halos from blazars.

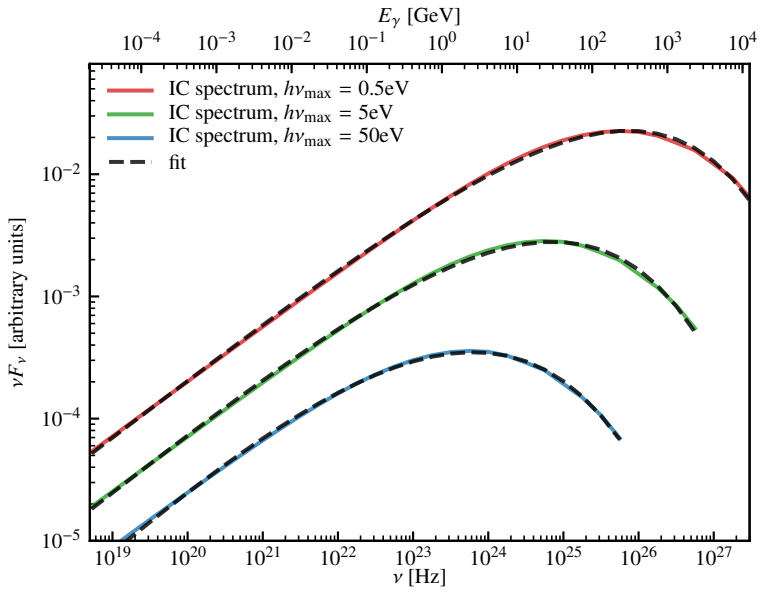

Figure 7.2: IC emission spectra from an electron population with $f_{\rm e} \propto E^{-2.1}$ that up-scatters photons from a black-body distributions peaking at different energies into the high-energy gamma-ray regime. The spectra are fitted by a function that is $\propto E_\gamma^b \exp\left[-(E/E_c)^{0.25}\right]$. This implies that they roll-over only sub-exponentially starting at energies $E_c = \{44, 2, 0.02\}$ GeV for the incident black body radiation fields with $h\nu_{\rm max} = \{0.5, 5, 50\}$ eV, respectively.

8. Conclusion

This work provides new insights into the non-thermal emission properties from CRs in star-forming galaxies. Since CRs have been found to play an important role in driving galactic winds and regulating star-formation, they have been modelled in various ways. These range from 1D flux tube models (e.g. Breitschwerdt et al., 1991; Recchia et al., 2016) over 3D simulations of the ISM (e.g. Hanasz et al., 2013; Girichidis et al., 2016) to hydrodynamic simulations of isolated galaxies (e.g. Jubelgas et al., 2008; Pakmor et al., 2016c) or even in cosmological settings (e.g. Buck et al., 2020; Hopkins et al., 2020, see Section 3.1 for more references). The modelling of the non-thermal emission properties from CRs has mainly been approached within one-zone models of galaxies (e.g. Torres, 2004; Persic et al., 2008; Lacki et al., 2010, 2011; Yoast-Hull et al., 2013; Eichmann & Becker Tjus, 2016) where the physical properties of a galaxy such as its magnetic field strength or the CR energy density are treated as free parameters. Furthermore, parametrized source functions and prescribed magnetic field distributions have been adopted in more detailed flux tube models (Breitschwerdt et al., 2002) or 2D axisymmetric models (Martin, 2014; Buckman et al., 2020). Hence, the logical next step was to model CRs in self-consistent, full 3D MHD simulations of galaxies together with their non-thermal emission spectra.

One of the main goals of this work is to understand the underlying physics of non-thermal emission processes in star-forming galaxies that lead to the emergence of the observed FRC, as well as the FIR-gamma-ray relation. Assuming calorimetry, i.e. that CRs lose most of their energy due to emission processes, these relations emerge naturally (Völk, 1989; Pohl, 1994; Lisenfeld et al., 1996; Lacki et al., 2010). However, because this explanation implies steeper radio spectra in comparison to observations and in the high-density environments of starburst galaxies other effects come into play, this assumption might not be fulfilled. In order to dissect these processes, I developed the code CRAYON+ to calculate steady-state spectra of CRs including all relevant cooling and escape losses and compute their resulting multi-frequency spectra, from the radio up to the TeV energy regime. This comprises synchrotron, bremsstrahlung, IC emission and gamma-ray emission from neutral

pion decay, as well as the production of secondary electrons and positrons. To apply this to galaxies, I performed high-resolution 3D MHD simulations of isolated galaxies using the moving-mesh code Arepo with self-consistent CR physics. This implies that the dynamics of the system is coupled to CRs that are injected at remnants of SNe and subsequently transported through the galaxy via advective and diffusive processes. By applying my steady-state model in post-processing, I was able to obtain CR proton, primary and secondary electron spectra that allowed for a detailed calculation of their emerging non-thermal emission in various wavebands. For the first time, this yields detailed emission maps, luminosities and non-thermal spectra of simulated galaxies, that range from dwarfs to Milky Way analogues to starburst galaxies, at different evolutionary stages. From this work, three published first-author papers emerged, where the main results are summarised in the following.

Consistent with Voyager-1 and AMS-02 data, our models reproduce the inversion of CR proton to electron spectra and match the shape of the positron fraction up to 8 GeV (Paper I). The simulated galaxies follow the observed FIR-gamma-ray relation, where the gamma-ray emission of highly SF galaxies is dominated by neutral pion decay (Paper II) and the gamma-ray spectra of starburst galaxies like NGC 253 are reproduced. The observed FRC of SF galaxies is recovered within the simulations, where we find differences in the contributions of primary and secondary electrons to the total radio luminosity depending on the adopted CR transport model (Paper III). Furthermore, we uncovered the underlying processes that enable the FRC to be maintained even in starburst galaxies and find that thermal free-free-emission naturally explains the observed radio spectra in SF galaxies like M82 and NGC 253, thus solving the riddle of flat radio spectra and a tight FIR-radio correlation.

Lastly, we calculate and analyse the hadronic gamma-ray emission from spectrally resolved CR protons in MHD simulations. On the one hand, we find that the gamma-ray spectra of our simulated galaxies with different halo masses and evolutionary stages can be closely reproduced by a steady-state approach if one allows for a different energy dependence of the diffusion coefficient in some cases. On the other hand, there are distinct morphological signatures from spectrally resolved CR transport visible in the high-energy gamma-ray emission maps and emission profiles. In particular, the high-energy gamma-ray emission at 100 GeV is more extended in the spectrally resolved model due to the inclusion of energy-dependent spatial diffusion of CRs in comparison to a grey approach. In addition, our results compare well with the most recent observations of the FIR-gamma-ray relation of nearby star-forming galaxies. However, the observed gamma-ray spectra of individual galaxies and in particular their spectral indices are not yet constraining enough to discriminate between spectrally resolved CR transport in contrast to a steady-state modelling and the grey treatment of CRs. Our work underlines the importance of modelling spectrally resolved

CR transport in order to be able to achieve accurate predictions of spatially resolved high-energy gamma-ray emission, which will be highly relevant for upcoming observations by the Cherenkov Telescope Array observatory (CTA).

Outlook

In order to explain a multitude of new, spatially resolved multi-messenger data of CR spectra, at gamma-rays and in the radio, more work is needed in terms of developing more sophisticated theoretical models and translating them to observational space. Since the steady-state assumption breaks down in highly dynamical regions such as near SNRs and in outflows, the next step is to overcome this assumption and model the spectral evolution of CR electrons in galaxy simulations in unprecedented detail, compare it to the steady-state approach and eventually to observables. To this end, we will make use of the code CREST (Winner et al., 2019) that accurately evolves CR electron spectra on Lagrangian tracer particles and which is coupled to Arepo. It offers plenty of possible applications to astrophysical problems: from SNRs to isolated galaxies up to cosmological simulations. It treats all important aspects of spectral CR electron evolution such as adiabatic expansion and compression, Coulomb losses, radiative losses, diffusive shock acceleration and re-acceleration, as well as Fermi-II re-acceleration (see Winner et al., 2019, 2020). Coupled with a spectral treatment of CR protons (Girichidis et al., 2020b, 2022), this will enable robust constraints on CR feedback in galaxy formation and evolution.

In addition to the analysis of radio intensity, another possibility to compare different approaches of modelling CR transport in galaxy formation to observations is to produce radio polarisation maps from simulated galaxies. The realistic modelling of this would be on the one hand enabled by including a better model for the multi-phase ISM in Arepo simulations to potentially obtain small-scale turbulence resulting from SF activity (e.g. Gutcke et al., 2021). Another potential driver of turbulence is a more realistic, bursty star-formation history, which will be obtained by performing cosmological MHD-CR simulations of galaxy formation (Buck et al., 2020; Hopkins et al., 2021a). In addition, we anticipate in a cosmological setting a further amplification of the magnetic field in dwarf galaxies due to the additional turbulence. So far, the magnetic energy densities in our simulated dwarf galaxies saturate below equipartition with the thermal energy density and fall short of the observed FRC (Pfrommer et al., 2021), but they could potentially reach the FRC within an improved setting. As a consequence, we will have the ability to exploit the physical processes leading to the observed tight FRC that is even maintained within dwarf galaxies and so far has only been analysed in simplified one-zone models (Lacki et al., 2010). Furthermore, the detailed modelling of CR electrons in galaxy simulations will make predictions

about future X-ray observations. In this regime the detection of IC emission could delimit the leptonic contribution to the total gamma-ray emission, which will provide further constraints on hadronic interactions and thus our modelling of CR transport. As a whole, this contributes to a highly relevant connection of the theory of emission processes in SF galaxies with observations. In this context the radio band is particularly interesting since it is ideal for accurate estimations of SFRs of local and distant galaxies (up to intermediate redshifts) without being biased by dust and thus enabling us to better constrain the star formation history of the Universe. On the other hand, making predictions for future observations in the X-ray band will offer yet another window to constrain our theoretical modelling.

A further application of a more detailed modelling of CR electrons is to unveil the physical processes that illuminate one of the largest features in the gamma-ray sky, i.e. the Fermi bubbles. This could be done by testing different injection scenarios of CRs, their transport and possible conditions for re-acceleration in outflows. Outflows in galaxies are a ubiquitous phenomenon and have been found to play an important role in determining the evolution of galaxies, in particular by affecting their star formation histories. Even in our own Galaxy, we observe evidence of a nuclear wind, in form of giant bubbles observed in gamma-rays, X-rays, microwave emission as well as radio polarisation. This nearby example offers the unique possibility to study the morphology, kinematics, chemical abundances and other properties of nuclear feedback processes such as its effect on the CGM in close detail. Despite already being discovered more than a decade ago, the origin the Fermi bubbles is still under debate (see e.g. Yang et al., 2018a, for a review). Is the observed gamma-ray emission of hadronic or leptonic nature? What energetic event caused the acceleration of protons and/or electrons, a nuclear starburst or AGN activity in the Galactic center? Or are CRs accelerated in situ, due to shocks or turbulence? A clear picture of the physics in place is still missing, that is able to reproduce all observational constraints at the same time. In addition, future observations in the upcoming years in the MeV and TeV regime (e.g. by instruments such as AdEPT, AMEGO, e-Astrogam and CTA) will provide further constraints on the multi-frequency emission and neutrino observations with IceCube-Gen 2 will give further implications on the efficiency of hadronic interactions in place. Hence, we need to investigate the hydrodynamic structure of the Fermi bubbles: is there a reverse shock? Are the bubble edges a contact discontinuity or a forward shock? What conditions are needed for efficient re-acceleration of CRs in situ? These questions can be addressed by including CREST within our 3D MHD simulations of isolated galaxies and, as a next step, also in cosmological simulations.

The recently discovered large-scale X-ray bubbles (eROSITA bubbles, Predehl et al., 2020) have been suggested to be causally connected to the Fermi bubbles. If these are indeed features due

to an energetic event from the Galactic nucleus, they prove the existence of a feedback mechanism in an apparently quiescent galaxy such as the Milky Way (Predehl et al., 2020). Hence, the question arises if and how galactic outflows effect the CGM, e.g. by re-heating the plasma. It has been shown that the density and temperature distribution of the CGM can be affected by an additional CR pressure component, making the CGM cooler and smoother (Buck et al., 2020). The emission and absorption lines of galaxies and their CGM are influenced by the temperature-density distribution of the gas as well as its ionisation state. Hence, accounting for a non-thermal pressure component could change our picture of understanding observational features of the CGM of galaxies, such as Lyman-alpha halos that have been revealed by MUSE observations (Wisotzki et al., 2016; Arrigoni Battaia et al., 2019). Also, it has been shown that including a spectral treatment for CR protons affects the morphology and SFR of simulated galaxies as well as the structure and strength of their outflows (Girichidis et al., 2022). Hence, including this novel scheme within cosmological simulations and additionally accounting for CR electrons with CREST could reveal new insights into the interplay of galactic outflows and their environments. This will also offer the possibility to constrain CR feedback further by coupling the simulations to the CRAYON+ code in order to calculate the multi-frequency emission from CR protons and electrons and thus predict more observable quantities that will be relevant for future observations with SKA and CTA in the upcoming years.

9. Commented Publication List

Here, I collect an overview of all my publications so far and state my contributions as well as the contributions of the co-authors to the papers that have been presented in this work. Furthermore, I briefly summarize my contribution to other publications.

Publications presented in this thesis

Some underlying concepts of the first three publications in the following list have been presented in my master thesis. There, I started developing the CR steady-state and non-thermal emission code and applied it to four snapshots of low-resolution simulations of galaxies. Subsequently, after finishing my master thesis, I intensively improved the numerical efficiency of the code, e.g. by adopting the Message Passing Interface (MPI) method in python in order to enable numerical calculations on multiple processors on clusters and supercomputers in parallel. Only then I was able to apply the code to a large number of higher resolution simulations with ten times more cells. Furthermore, we improved on various underlying assumptions of the steady-state approach such as the definition of the injected source function, the ratio of primary to secondary electrons and the estimation of the diffusion and advection timescales. These further improvements on the technical as well as conceptual side had a significant impact on the conclusions and enabled further analysis of the CR spectra, the gamma-ray and radio emission in much more detail and enabled the publication of three extensive papers.

- Cosmic rays and non-thermal emission in simulated galaxies - I. Electron and proton spectra compared to Voyager-1 data
  Maria Werhahn, Christoph Pfrommer, Philipp Girichidis, Ewald Puchwein, Rüdiger Pakmor - 2021
  Monthly Notices of the Royal Astronomical Society, Volume 505, Issue 3, pp.3273-3294

I ran the simulations for this work, developed the numerical code for modelling of the CR spectra, made the figures and prepared the manuscript with the help of CP, who also helped to conceptualize the manuscript. CP and RP provided the initial conditions for the simulations and the general simulation setup. PG assisted in conceptualizing the manuscript and the code development, while EP provided the tree code that was used in this work. All authors contributed to the discussion and conclusion.

- Cosmic rays and non-thermal emission in simulated galaxies - II. γ-ray maps, spectra, and the far-infrared-γ-ray relation
  Maria Werhahn, Christoph Pfrommer, Philipp Girichidis, Georg Winner - 2021
  Monthly Notices of the Royal Astronomical Society, Volume 505, Issue 3, pp.3295-3313

  I developed the numerical code for the modelling of the CR spectra and their non-thermal emission, made the figures and prepared the manuscript. CP helped to conceptualize the manuscript and in the preparation of the manuscript. PG and GW assisted by improving the efficiency of the code. All authors contributed to the discussion and conclusion.

- Cosmic rays and non-thermal emission in simulated galaxies - III. Probing cosmic-ray calorimetry with radio spectra and the FIR-radio correlation
  Maria Werhahn, Christoph Pfrommer, Philipp Girichidis - 2021
  Monthly Notices of the Royal Astronomical Society, Volume 508, Issue 3, pp.4072-4095

  I developed the numerical code for the modelling of the CR spectra and their non-thermal emission, made the figures and prepared the manuscript. CP helped to conceptualize the manuscript and all authors contributed to the discussion and conclusion.

Further publications during my doctoral studies

- Simulating radio synchrotron emission in star-forming galaxies: small-scale magnetic dynamo and the origin of the far infrared-radio correlation
  Christoph Pfrommer, **Maria Werhahn**, Rüdiger Pakmor, Philipp Girichidis, Christine M. Simpson - 2021
  arXiv:2105.12132 - accepted by Monthly Notices of the Royal Astronomical Society (2022)

  I used my numerical code for the modelling of the CR spectra and their radio emission and helped in deriving the analytical equation for the FRC. I made the figures in Appendix C that show the numerical convergence of the modelling.

My contributions to the following three publications have been summarized in Chapter 7.

- Evolution and observational signatures of the cosmic ray electron spectrum in SN 1006
  Georg Winner, Christoph Pfrommer, Philipp Girichidis, **Maria Werhahn**, Matteo Pais - 2020
  Monthly Notices of the Royal Astronomical Society, Volume 499, Issue 2, pp.2785-2802

- Constraining the coherence scale of the interstellar magnetic field using TeV gamma-ray observations of supernova remnants
  Matteo Pais, Christph Pfrommer, Kristian Ehlert, **Maria Werhahn**, Georg Winner - 2020
  Monthly Notices of the Royal Astronomical Society, Volume 496, Issue 2, pp.2448-2461

- Missing Gamma-Ray Halos and the Need for New Physics in the Gamma-Ray Sky
  Broderick, Avery E.; Tiede, Paul; Chang, Philip; Lamberts, Astrid; Pfrommer, Christoph; Puchwein, Ewald; Shalaby, Mohamad; **Werhahn, Maria** - 2018
  The Astrophysical Journal, Volume 868, Issue 2, article id. 87, 17 pp.

Further publications during my bachelor and master thesis

- The MUSE-Wide Survey: survey description and first data release Urrutia, T.; Wisotzki, L.; Kerutt, J.; Schmidt, K. B.; Herenz, E. C.; Klar, J.; Saust, R.; **Werhahn, M.**; Diener, C.; Caruana, J.; Krajnović, D.; Bacon, R.; Boogaard, L.; Brinchmann, J.; Enke, H.; Maseda, M.; Nanayakkara, T.; Richard, J. ; Steinmetz, M. ; Weilbacher, P. M. - 2019
  Astronomy & Astrophysics, Volume 624, id.A141, 24 pp.

- The MUSE-Wide survey: A first catalogue of 831 emission line galaxies
  Edmund Christian Herenz, Tanya Urrutia, Lutz Wisotzki, Josephine Kerutt, Rikke Saust, **Maria Werhahn**, Kasper Borello Schmidt, Joseph Caruana, Catrina Diener, Roland Bacon, Jarle Brinchmann, Joop Schaye, Joop and Michael Maseda, Peter M. Weilbacher - 2017
  Astronomy & Astrophysics, Volume 606, id.A12, 23 pp.

Acknowledgments

I would like to thank everyone who supported me during my PhD. First of all, special thanks go to my supervisor Christoph Pfrommer for his extensive support throughout the years. I am very grateful for your open door and ear, for always believing in me, for your invaluable scientific input and for inspiring me with your constant enthusiasm. Furthermore, I would like to thank my mentor Else Starkenburg for the valuable discussions during our thesis committee meetings and the encouraging support. Next, I would like to thank my former office mates Philipp Girichidis and Georg Winner. I am very grateful for all your advice, time, patience and support in all matters. Moreover, I felt very welcome and supported by the whole Cosmology Section at the AIP and enjoyed all interesting discussions, besides of course the nice social gatherings like the wine-and-cheese-evenings or the BBQs. Thanks to Thomas Berlok, Tobias Buck, Martin Sparre, Joe Whittingham, Simon Pfeiffer, Matthias Weber, Mohamad Shalaby, Laura Keating, Alexander Scherrmann, Timon Thomas, Kristian Ehlert and everyone else from the group who made this time so enjoyable. Furthermore, my thanks go to Rüdiger Pakmor for his help with Arepo, his highly appreciated input and his and Matthias Steinmetz' support with my applications, as well as Laura Keating and Tobias Buck for their help.

I also owe my thanks to all my friends and family, who always encouraged me to keep going and who constantly believed in me. In particular my sisters Julia, Sarah, Katharina, Theresia, my brother Raphael and my parents, who were there for me at all times, from the frustrating to the enthusiastic ones. In addition, I am very grateful for the support of my friends Eva, Iva and all other friends from Stammtić and Ischen, as well as Mira, Lavonna and Yannick. Without your constant support, listening, cheering up and making me enjoy life outside the PhD I would not have been able to finish this work and further pursue in astrophysics.

Bibliography

AMS-01 Collaboration et al., 2007, Physics Letters B, 646, 145

Abdo A. A., et al., 2010, A&A, 523, A46

Abeysekara A. U., et al., 2017, Science, 358, 911

Abramowitz M., Stegun I. A., eds, 1965, Handbook of Mathematical Functions with Formulas, Graphs and Mathematical Tables. Dover Publications, Inc., New York

Accardo L., et al., 2014, Phys. Rev. Lett., 113, 121101

Ackermann M., et al., 2012a, Phys. Rev. Lett., 108, 011103

Ackermann M., et al., 2012b, ApJ, 755, 164

Ackermann M., et al., 2016, A&A, 586, A71

Adamo A., et al., 2012, MNRAS, 426, 1185

Adebahr B., Krause M., Klein U., Weżgowiec M., Bomans D. J., Dettmar R. J., 2013, A&A, 555, A23

Adriani O., et al., 2009, Nature, 458, 607

Agostinelli S., et al., 2003, Nuclear Instruments and Methods in Physics Research A, 506, 250

Aguilar M., et al., 2013, Phys. Rev. Lett., 110, 141102

Aguilar M., et al., 2014a, Phys. Rev. Lett., 113, 121102

Aguilar M., et al., 2014b, Phys. Rev. Lett., 113, 221102

Aguilar M., et al., 2015, Phys. Rev. Lett., 114, 171103

Aguilar M., et al., 2016, Phys. Rev. Lett., 117, 231102

Aharonian F. A., Atoyan A. M., 2000, A&A, 362, 937

Aharonian F. A., Kelner S. R., Prosekin A. Y., 2010, Pys. Rev. D, 82, 043002

Ajello M., Di Mauro M., Paliya V. S., Garrappa S., 2020, ApJ, 894, 88

Allison J., et al., 2006, IEEE Transactions on Nuclear Science, 53, 270

Amato E., Blasi P., 2018, Advances in Space Research, 62, 2731

Ambrosone A., Chianese M., Fiorillo D. F. G., Marinelli A., Miele G., 2022, arXiv e-prints, p. arXiv:2203.03642

Arrigoni Battaia F., Hennawi J. F., Prochaska J. X., Oñorbe J., Farina E. P., Cantalupo S., Lusso E., 2019, MNRAS, 482, 3162

Axford W. I., Leer E., Skadron G., 1977, in International Cosmic Ray Conference. p. 132

Baier V. N., Fadin V. S., Khoze V. A., 1967, Soviet Phys. JETP, 24, 760

Baring M. G., Ellison D. C., Reynolds S. P., Grenier I. A., Goret P., 1999, ApJ, 513, 311

Basu A., Beck R., Schmidt P., Roy S., 2015, MNRAS, 449, 3879

Beatty J. J., et al., 2004, Phys. Rev. Lett., 93, 241102

Bell A. R., 1978, MNRAS, 182, 147

Bell E. F., 2003, ApJ, 586, 794

Bell A. R., 2004, MNRAS, 353, 550

Bell A. R., Schure K. M., Reville B., Giacinti G., 2013, MNRAS, 431, 415

Beringer J., et al., 2012, Phys. Rev. D, 86, 010001

Bethe H., Heitler W., 1934, Proceedings of the Royal Society of London Series A, 146, 83

Białłas A., Bleszyński M., Czyż W., 1976, Nuclear Physics B, 111, 461

Blandford R., Eichler D., 1987, Phys. Rep., 154, 1

Blandford R. D., Ostriker J. P., 1978, ApJ, 221, L29

Blasi P., 2010, MNRAS, 402, 2807

Blasi P., Amato E., Serpico P. D., 2012, Phys. Rev. Lett., 109, 061101

Blom J. J., Paglione T. A. D., Carramiñana A., 1999, ApJ, 516, 744

Blumenthal G. R., Gould R. J., 1970, Reviews of Modern Physics, 42, 237

Boezio M., et al., 2001, Advances in Space Research, 27, 669

Booth C. M., Agertz O., Kravtsov A. V., Gnedin N. Y., 2013, ApJ, 777, L16

Boulares A., Cox D. P., 1990, ApJ, 365, 544

Breitschwerdt D., McKenzie J. F., Voelk H. J., 1991, A&A, 245, 79

Breitschwerdt D., Dogiel V. A., Völk H. J., 2002, A&A, 385, 216

Broderick A. E., Tiede P., Chang P., Lamberts A., Pfrommer C., Puchwein E., Shalaby M., Werhahn M., 2018, ApJ, 868, 87

Buck T., Pfrommer C., Pakmor R., Grand R. J. J., Springel V., 2020, MNRAS, 497, 1712

Buckman B. J., Linden T., Thompson T. A., 2020, MNRAS, 494, 2679

Bullock J. S., Kolatt T. S., Sigad Y., Somerville R. S., Kravtsov A. V., Klypin A. A., Primack J. R., Dekel A., 2001, MNRAS, 321, 559

Calzetti D., Armus L., Bohlin R. C., Kinney A. L., Koornneef J., Storchi-Bergmann T., 2000, ApJ, 533, 682

Cappellari M., 2013, ApJ, 778, L2

Caprioli D., Spitkovsky A., 2014, ApJ, 783, 91

Cerri S. S., Gaggero D., Vittino A., Evoli C., Grasso D., 2017, J. Cosmology Astropart. Phys., 2017, 019

Chabrier G., 2003, ApJ, 586, L133

Chan T. K., Kereš D., Hopkins P. F., Quataert E., Su K. Y., Hayward C. C., Faucher-Giguère C. A., 2019, MNRAS, 488, 3716

Cholis I., Hooper D., 2013, Phys. Rev. D, 88, 023013

Chomiuk L., Povich M. S., 2011, AJ, 142, 197

Choudhuri A., Choudhuri P., 1998, The Physics of Fluids and Plasmas: An Introduction for Astrophysicists. Cambridge University Press, https://books.google.de/books?id=i_kufpYwkpQC

Condon J. J., 1992, ARA&A, 30, 575

Cortese L., et al., 2012, A&A, 544, A101

Crain R. A., McCarthy I. G., Frenk C. S., Theuns T., Schaye J., 2010, MNRAS, 407, 1403

Crocker R. M., Jones D. I., Aharonian F., Law C. J., Melia F., Ott J., 2011a, MNRAS, 411, L11

Crocker R. M., Jones D. I., Aharonian F., Law C. J., Melia F., Oka T., Ott J., 2011b, MNRAS, 413, 763

Croton D. J., et al., 2006, MNRAS, 365, 11

Cummings A. C., et al., 2016, ApJ, 831, 18

Dashyan G., Dubois Y., 2020, A&A, 638, A123

Della Ceca R., Griffiths R. E., Heckman T. M., Lehnert M. D., Weaver K. A., 1999, ApJ, 514, 772

Dermer C. D., 1986a, A&A, 157, 223

Dermer C. D., 1986b, ApJ, 307, 47

Di Mauro M., et al., 2017, ApJ, 845, 107

Domingo-Santamaría E., Torres D. F., 2005, A&A, 444, 403

Drury L. O., 1983, Reports on Progress in Physics, 46, 973

Eichmann B., Becker Tjus J., 2016, ApJ, 821, 87

Everett J. E., Zweibel E. G., Benjamin R. A., McCammon D., Rocks L., Gallagher John S. I., 2008, ApJ, 674, 258

Evoli C., Gaggero D., Grasso D., Maccione L., 2008, J. Cosmology Astropart. Phys., 2008, 018

Evoli C., Gaggero D., Vittino A., Di Bernardo G., Di Mauro M., Ligorini A., Ullio P., Grasso D., 2017, J. Cosmology Astropart. Phys., 2017, 015

Evoli C., Blasi P., Morlino G., Aloisio R., 2018, Phys. Rev. Lett., 121, 021102

Evoli C., Aloisio R., Blasi P., 2019, Phys. Rev. D, 99, 103023

Evoli C., Morlino G., Blasi P., Aloisio R., 2020a, Phys. Rev. D, 101, 023013

Evoli C., Blasi P., Amato E., Aloisio R., 2020b, Phys. Rev. Lett., 125, 051101

Farber R., Ruszkowski M., Yang H. Y. K., Zweibel E. G., 2018, ApJ, 856, 112

Feng L., Kang Z., Yuan Q., Yin P.-F., Fan Y.-Z., 2020, Journal of Cosmology and Astroparticle Physics, 2020, 031

Fermi-LAT Collaboration et al., 2022, ApJS, 260, 53

Fletcher R. S., Gaisser T. K., Lipari P., Stanev T., 1994, Phys. Rev. D, 50, 5710

Franco V., Glauber R. J., 1966, Physical Review, 142, 1195

Freedman W. L., et al., 2001, ApJ, 553, 47

Fukugita M., Hogan C. J., Peebles P. J. E., 1998, ApJ, 503, 518

Gabici S., 2022, arXiv e-prints, p. arXiv:2203.14620

Gabici S., Evoli C., Gaggero D., Lipari P., Mertsch P., Orlando E., Strong A., Vittino A., 2019, International Journal of Modern Physics D, 28, 1930022

Gaisser T. K., 1990, Cosmic rays and particle physics. Cambridge University Press

Gao Y., Solomon P. M., 2004, ApJ, 606, 271

Gavazzi G., Savorgnan G., Fumagalli M., 2011, A&A, 534, A31

Génolini Y., et al., 2019, Phys. Rev. D, 99, 123028

Gil de Paz A., et al., 2007, ApJS, 173, 185

Ginzburg V. L., Syrovatskii S. I., 1964, The Origin of Cosmic Rays. Pergamon Press

Girichidis P., et al., 2016, ApJ, 816, L19

Girichidis P., et al., 2020a, Space Sci. Rev., 216, 68

Girichidis P., Pfrommer C., Hanasz M., Naab T., 2020b, MNRAS, 491, 993

Girichidis P., Pfrommer C., Pakmor R., Springel V., 2022, MNRAS, 510, 3917

Glauber R. J., 1955, Physical Review, 100, 242

Glauber R. J., Matthiae G., 1970, Nuclear Physics B, 21, 135

Golden R. L., et al., 1996, ApJ, 457, L103

Golokhvastov A. I., 2001, Physics of Atomic Nuclei, 64, 1841

Gould R., 1972a, Physica, 58, 379

Gould R., 1972b, Physica, 60, 145

Greco J. P., Martini P., Thompson T. A., 2012, ApJ, 757, 24

Grenier I. A., Black J. H., Strong A. W., 2015, ARA&A, 53, 199

Gutcke T. A., Pakmor R., Naab T., Springel V., 2021, MNRAS, 501, 5597

H. E. S. S. Collaboration et al., 2018, A&A, 617, A73

Hanasz M., Lesch H., Naab T., Gawryszczak A., Kowalik K., Wóltański D., 2013, ApJ, 777, L38

Harris J., Zaritsky D., 2009, AJ, 138, 1243

Haug E., 1975a, Zeitschrift Naturforschung Teil A, 30, 1099

Haug E., 1975b, Sol. Phys., 45, 453

Haug E., 1997, A&A, 326, 417

Hayakawa S., Ito K., Terashima Y., 1958, Progress of Theoretical Physics Supplement, 6, 1

Heesen V., Brinks E., Leroy A. K., Heald G., Braun R., Bigiel F., Beck R., 2014, AJ, 147, 103

Heesen V., Dettmar R.-J., Krause M., Beck R., Stein Y., 2016, MNRAS, 458, 332

Heesen V., et al., 2019, A&A, 622, A8

Heitler W., 1954, Quantum theory of radiation. 3rd edn. Clarendon Press, Oxford

Helou G., Soifer B. T., Rowan-Robinson M., 1985, ApJ, 298, L7

Hooper D., Blasi P., Serpico P. D., 2009, Journal of Cosmology and Astroparticle Physics, 2009, 025

Hopkins P. F., et al., 2020, MNRAS, 492, 3465

Hopkins P. F., Chan T. K., Ji S., Hummels C. B., Kereš D., Quataert E., Faucher-Giguère C.-A., 2021a, MNRAS, 501, 3640

Hopkins P. F., Squire J., Chan T. K., Quataert E., Ji S., Kereš D., Faucher-Giguère C.-A., 2021b, MNRAS, 501, 4184

Iodice E., Arnaboldi M., Rejkuba M., Neeser M. J., Greggio L., Gonzalez O. A., Irwin M., Emerson J. P., 2014, A&A, 567, A86

Jacob S., Pakmor R., Simpson C. M., Springel V., Pfrommer C., 2018, MNRAS, 475, 570

Jokipii J. R., Morfill G. E., 1985, ApJ, 290, L1

Jones F. C., 1968, Physical Review, 167, 1159

Jubelgas M., Springel V., Enßlin T., Pfrommer C., 2008, A&A, 481, 33

Kafexhiu E., 2016, Phys. Rev. C, 94, 064603

Kafexhiu E., Aharonian F., Taylor A. M., Vila G. S., 2014, Phys. Rev. D, 90, 123014

Kalmykov N. N., Ostapchenko S. S., 1993, Physics of Atomic Nuclei, 56, 346

Kalmykov N. N., Ostapchenko S. S., Pavlov A. I., 1997, Nuclear Physics B Proceedings Supplements, 52, 17

Kapińska A. D., et al., 2017, ApJ, 838, 68

Kelner S. R., Aharonian F. A., Bugayov V. V., 2006, Phys. Rev. D, 74, 034018

Kennicutt Jr. R. C., 1998, ARA&A, 36, 189

Kissmann R., 2014, Astroparticle Physics, 55, 37

Klein U., Lisenfeld U., Verley S., 2018, A&A, 611, A55

Kornecki P., Pellizza L. J., del Palacio S., Müller A. L., Albacete-Colombo J. F., Romero G. E., 2020, A&A, 641, A147

Kourkchi E., et al., 2020, ApJ, 902, 145

Krymskii G. F., 1977, Akademiia Nauk SSSR Doklady, 234, 1306

Lacki B. C., Thompson T. A., 2010, ApJ, 717, 196

Lacki B. C., Thompson T. A., 2013, ApJ, 762, 29

Lacki B. C., Thompson T. A., Quataert E., 2010, ApJ, 717, 1

Lacki B. C., Thompson T. A., Quataert E., Loeb A., Waxman E., 2011, ApJ, 734, 107

Lebedev A. M., Slavatinskii S. A., Tolkachev B. V., 1963, Soviet Phys. JETP, 19, 1452

Linden T., 2017, Phys. Rev. D, 96, 083001

Lipari P., 2014, arXiv e-prints, p. arXiv:1407.5223

Lisenfeld U., Voelk H. J., Xu C., 1996, A&A, 306, 677

Lopez L. A., Auchettl K., Linden T., Bolatto A. D., Thompson T. A., Ramirez-Ruiz E., 2018, The Astrophysical Journal, 867, 44

Lynds C. R., Sandage A. R., 1963, ApJ, 137, 1005

Mannheim K., Schlickeiser R., 1994, A&A, 286, 983

Marcowith A., van Marle A. J., Plotnikov I., 2021, Physics of Plasmas, 28, 080601

Martin P., 2014, A&A, 564, A61

Matthews A. M., Condon J. J., Cotton W. D., Mauch T., 2021, ApJ, 914, 126

Maurin D., 2020, Computer Physics Communications, 247, 106942

McDaniel A., Jeltema T., Profumo S., 2019, Phys. Rev. D, 100, 023014

McKeith C. D., Greve A., Downes D., Prada F., 1995, A&A, 293, 703

Mertsch P., Vittino A., Sarkar S., 2020, arXiv e-prints, p. arXiv:2012.12853

Miniati F., 2001, Computer Physics Communications, 141, 17

Miskolczi A., et al., 2019, A&A, 622, A9

Miyoshi T., Kusano K., 2005, J. Comput. Phys., 208, 315

Molnár D. C., et al., 2021, MNRAS, 504, 118

Morganti R., 2017, Frontiers in Astronomy and Space Sciences, 4, 42

Mori M., 1997, ApJ, 478, 225

Moshir M., et al. 1990, IRAS Faint Source Catalogue, p. 0

Moster B. P., Somerville R. S., Maulbetsch C., van den Bosch F. C., Macciò A. V., Naab T., Oser L., 2010, ApJ, 710, 903

Mouhcine M., Ferguson H. C., Rich R. M., Brown T. M., Smith T. E., 2005, ApJ, 633, 810

Nava L., Gabici S., Marcowith A., Morlino G., Ptuskin V. S., 2016, MNRAS, 461, 3552

Nava L., Recchia S., Gabici S., Marcowith A., Brahimi L., Ptuskin V., 2019, MNRAS, 484, 2684

Navarro J. F., Frenk C. S., White S. D. M., 1997, ApJ, 490, 493

Novikov I. D., Thorne K. S., 1973, in Black Holes (Les Astres Occlus). pp 343–450

Nuñez-Castiñeyra A., Grenier I. A., Bournaud F., Dubois Y., Kamal Youssef F. R., Hennebelle P., 2022, arXiv e-prints, p. arXiv:2205.08163

Ogrodnik M. A., Hanasz M., Wóltański D., 2021, ApJS, 253, 18

Orth C. D., Buffington A., 1976, ApJ, 206, 312

Ostapchenko S., 2006, Phys. Rev. D, 74, 014026

Paglione T. A. D., Abrahams R. D., 2012, ApJ, 755, 106

Pais M., Pfrommer C., 2020, MNRAS, 498, 5557

Pais M., Pfrommer C., Ehlert K., Pakmor R., 2018, MNRAS, 478, 5278

Pais M., Pfrommer C., Ehlert K., Werhahn M., Winner G., 2020, MNRAS, 496, 2448

Pakmor R., Springel V., 2013, MNRAS, 432, 176

Pakmor R., Bauer A., Springel V., 2011, MNRAS, 418, 1392

Pakmor R., Springel V., Bauer A., Mocz P., Munoz D. J., Ohlmann S. T., Schaal K., Zhu C., 2016a, MNRAS, 455, 1134

Pakmor R., Pfrommer C., Simpson C. M., Kannan R., Springel V., 2016b, MNRAS, 462, 2603

Pakmor R., Pfrommer C., Simpson C. M., Springel V., 2016c, ApJ, 824, L30

Pakmor R., et al., 2017, MNRAS, 469, 3185

Pakmor R., Guillet T., Pfrommer C., Gómez F. A., Grand R. J. J., Marinacci F., Simpson C. M., Springel V., 2018, MNRAS, 481, 4410

Pakmor R., et al., 2020, MNRAS, 498, 3125

Peng F.-K., Zhang H.-M., Wang X.-Y., Wang J.-F., Zhi Q.-J., 2019, ApJ, 884, 91

Peretti E., Blasi P., Aharonian F., Morlino G., 2019, MNRAS, 487, 168

Persic M., Rephaeli Y., Arieli Y., 2008, A&A, 486, 143

Pfrommer C., 2005, PhD thesis, Ludwig-Maximilians-Universität München, http://nbn-resolving.de/urn:nbn:de:bvb:19-46051

Pfrommer C., Enßlin T. A., 2004, A&A, 413, 17

Pfrommer C., Pakmor R., Schaal K., Simpson C. M., Springel V., 2017a, MNRAS, 465, 4500

Pfrommer C., Pakmor R., Simpson C. M., Springel V., 2017b, ApJ, 847, L13

Pfrommer C., Werhahn M., Pakmor R., Girichidis P., Simpson C. M., 2021, submitted to MNRAS, p. arXiv:2105.12132

Pfrommer C., Werhahn M., Pakmor R., Girichidis P., Simpson C. M., 2022, MNRAS, arXiv:2105.12132,

Pohl M., 1994, A&A, 287, 453

Potgieter M. S., 2013, Living Reviews in Solar Physics, 10, 3

Powell K. G., Roe P. L., Linde T. J., Gombosi T. I., De Zeeuw D. L., 1999a, J. Comput. Phys., 154, 284

Powell K. G., Roe P. L., Linde T. J., Gombosi T. I., De Zeeuw D. L., 1999b, Journal of Computational Physics, 154, 284

Predehl P., et al., 2020, Nature, 588, 227

Ptuskin V. S., Soutoul A., 1998, Space Sci. Rev., 86, 225

Ptuskin V. S., Voelk H. J., Zirakashvili V. N., Breitschwerdt D., 1997, A&A, 321, 434

Rathjen T.-E., et al., 2021, MNRAS, 504, 1039

Recchia S., Blasi P., Morlino G., 2016, MNRAS, 462, 4227

Recchia S., Galli D., Nava L., Padovani M., Gabici S., Marcowith A., Ptuskin V., Morlino G., 2022, A&A, 660, A57

Rephaeli Y., Arieli Y., Persic M., 2010, MNRAS, 401, 473

Reville B., Kirk J. G., Duffy P., O'Sullivan S., 2007, A&A, 475, 435

Reville B., O'Sullivan S., Duffy P., Kirk J. G., 2008, MNRAS, 386, 509

Reville B., Giacinti G., Scott R., 2021, MNRAS, 502, 4137

Robishaw T., Quataert E., Heiles C., 2008, ApJ, 680, 981

Rojas-Bravo C., Araya M., 2016, MNRAS, 463, 1068

Romero G. E., Torres D. F., 2003, ApJ, 586, L33

Ruszkowski M., Yang H. Y. K., Zweibel E., 2017, ApJ, 834, 208

Rybicki G. B., Lightman A. P., 1986, Radiative Processes in Astrophysics. Wiley, New York

Salem M., Bryan G. L., 2014, MNRAS, 437, 3312

Salem M., Bryan G. L., Hummels C., 2014, ApJ, 797, L18

Samui S., Subramanian K., Srianand R., 2010, MNRAS, 402, 2778

Sanders D. B., Mazzarella J. M., Kim D. C., Surace J. A., Soifer B. T., 2003, AJ, 126, 1607

Schleicher D. R. G., Beck R., 2013, A&A, 556, A142

Schlickeiser R., 1989, ApJ, 336, 243

Schober J., Schleicher D. R. G., Klessen R. S., 2016, ApJ, 827, 109

Schroer B., Pezzi O., Caprioli D., Haggerty C., Blasi P., 2021, ApJ, 914, L13

Semenov V. A., Kravtsov A. V., Gnedin N. Y., 2018, ApJ, 861, 4

Semenov V. A., Kravtsov A. V., Caprioli D., 2021, ApJ, 910, 126

Serpico P. D., 2012, Astroparticle Physics, 39, 2

Shalaby M., Thomas T., Pfrommer C., 2021, ApJ, 908, 206

Simpson C. M., Pakmor R., Marinacci F., Pfrommer C., Springel V., Glover S. C. O., Clark P. C., Smith R. J., 2016, ApJ, 827, L29

Sjöstrand T., Mrenna S., Skands P., 2006, Journal of High Energy Physics, 2006, 026

Sjöstrand T., Mrenna S., Skands P., 2008, Computer Physics Communications, 178, 852

Skilling J., 1975, MNRAS, 172, 557

Skrutskie M. F., et al., 2006, AJ, 131, 1163

Springel V., 2010, MNRAS, 401, 791

Springel V., Hernquist L., 2003, MNRAS, 339, 289

Stecker F. W., 1971, NASA Special Publication, 249

Stephens S. A., Badhwar G. D., 1981, Ap&SS, 76, 213

Strauss R. D., Potgieter M. S., Ferreira S. E. S., Fichtner H., Scherer K., 2013, ApJ, 765, L18

Strong A. W., Moskalenko I. V., 1998, ApJ, 509, 212

Strong A. W., Moskalenko I. V., Ptuskin V. S., 2007, Annual Review of Nuclear and Particle Science, 57, 285

Strong A. W., Porter T. A., Digel S. W., Jóhannesson G., Martin P., Moskalenko I. V., Murphy E. J., Orlando E., 2010, ApJ, 722, L58

Tabatabaei F. S., et al., 2017, ApJ, 836, 185

Tatischeff V., Gabici S., 2018, Annual Review of Nuclear and Particle Science, 68, 377

Thirlwall J. J., Popescu C. C., Tuffs R. J., Natale G., Norris M., Rushton M., Grootes M., Carroll B., 2020, Monthly Notices of the Royal Astronomical Society

Thomas T., Pfrommer C., 2019, MNRAS, 485, 2977

Thomas T., Pfrommer C., 2022, MNRAS, 509, 4803

Thomas T., Pfrommer C., Enßlin T., 2020, ApJ, 890, L18

Thomas T., Pfrommer C., Pakmor R., 2021, MNRAS, 503, 2242

Thompson T. A., Quataert E., Waxman E., Murray N., Martin C. L., 2006, ApJ, 645, 186

Thompson T. A., Quataert E., Waxman E., 2007, ApJ, 654, 219

Torres D. F., 2004, ApJ, 617, 966

Uhlig M., Pfrommer C., Sharma M., Nath B. B., Enßlin T. A., Springel V., 2012, MNRAS, 423, 2374

VERITAS Collaboration et al., 2009, Nature, 462, 770

Vacca W. D., et al., 2015, ApJ, 804, 66

Vink J., 2012, A&ARv, 20, 49

Völk H. J., 1989, A&A, 218, 67

Völk H. J., Aharonian F. A., Breitschwerdt D., 1996, Space Sci. Rev., 75, 279

Vollmer B., Soida M., Beck R., Powalka M., 2020, A&A, 633, A144

Weinberger R., Springel V., Pakmor R., 2020, ApJS, 248, 32

Werhahn M., Pfrommer C., Girichidis P., Puchwein E., Pakmor R., 2021a, MNRAS, 505, 3273

Werhahn M., Pfrommer C., Girichidis P., Winner G., 2021b, MNRAS, 505, 3295

Werhahn M., Pfrommer C., Girichidis P., 2021c, MNRAS, 508, 4072

Winner G., Pfrommer C., Girichidis P., Pakmor R., 2019, MNRAS, 488, 2235

Winner G., Pfrommer C., Girichidis P., Werhahn M., Pais M., 2020, MNRAS, 499, 2785

Wisotzki L., et al., 2016, A&A, 587, A98

Wojaczyński R., Niedźwiecki A., 2017, ApJ, 849, 97

Yanasak N. E., et al., 2001, ApJ, 563, 768

Yang H. Y., Ruszkowski M., Zweibel E., 2018a, Galaxies, 6, 29

Yang R.-z., Kafexhiu E., Aharonian F., 2018b, A&A, 615, A108

Yin P.-F., Yuan Q., Liu J., Zhang J., Bi X.-J., Zhu S.-H., Zhang X., 2009, Phys. Rev. D, 79, 023512

Yoast-Hull T. M., Murray N., 2019, MNRAS, 484, 3665

Yoast-Hull T. M., Everett J. E., Gallagher J. S. I., Zweibel E. G., 2013, ApJ, 768, 53

Yoast-Hull T. M., Gallagher J. S., Zweibel E. G., 2015, MNRAS, 453, 222

Yun M. S., Reddy N. A., Condon J. J., 2001, ApJ, 554, 803

Zirakashvili V. N., Aharonian F., 2007, A&A, 465, 695

Zirakashvili V. N., Breitschwerdt D., Ptuskin V. S., Voelk H. J., 1996, A&A, 311, 113

Zweibel E. G., 2013, Physics of Plasmas, 20, 055501

Zweibel E. G., 2017, Physics of Plasmas, 24, 055402

de Cea del Pozo E., Torres D. F., Rodriguez Marrero A. Y., 2009, ApJ, 698, 1054

van der Kruit P. C., 1971, A&A, 15, 110

van der Kruit P. C., 1973, A&A, 29, 263